Light Induced Dynamics in Quantum Matter

Thesis by
Swati Chaudhary

In Partial Fulfillment of the Requirements for the
Degree of
Doctor of Philosophy

CALIFORNIA INSTITUTE OF TECHNOLOGY
Pasadena, California

2021
Defended 25 May 2021

ACKNOWLEDGEMENTS

I would like to start with a deep obeisance to Goddess Saraswati, the patron of music, arts, and knowledge. She is the ultimate embodiment of creative powers which guide us from darkness to light, from ignorance to absolute truth, from death to immortality, and from indifference to compassion.

This PhD would have not been possible without the unconditional support of many people. First, my heartfelt gratitude to my advisor. I am indebted to my adviser Gil Refael for helping me to grow as a physicist. His constant support and encouragement has kept my spirit buoyed even when my mind tried its best to dampen it with its pessimistic tendencies. I have benefited immensely from his unique insights about physics. I also thank him for providing me an opportunity to TA his solid state class which I never knew could be that much fun. I am very grateful to my collaborators, Arbel Haim, Yang Peng, Alon Ron, Christina Knapp, and Cyprian Lewandowski who not only taught me a lot of great physics, but also showed me efficient ways to do research. I enjoyed learning from discussions with other group members, Michael Buchhold and Christopher David White who were always generous with their time. I feel very lucky to have had a chance to learn from two very successful and inspiring experimentalists, Manuel Endres and David Hsieh. I will constantly strive to emulate their level of perfection and clarity for the rest of my life.

I would be amiss if I did not extend a very special thanks to Loly Ekmekjian whose positive vibes always kept the CMP group's happiness index much higher than the Caltech average. I sincerely acknowledge her efforts to bring us all together on different occasions of celebration. I found a great friend in her who never minded being inundated with my irrational worries, and constantly encouraged me to go to yoga classes. I would also like to thank Alice Sogmonian at the Caltech Health center for helping me to navigate difficult periods during many recurring episodes of Ulcerative Colitis. I am very grateful to Dr. Charisma Bartlett at Caltech Counselling Center who time and again helped me a lot to get rid of paralyzing negative thoughts.

Outside of Caltech, at first I would like to thank all the wonderful people and families I met in Alhambra Sikh temple. The divine current of that place has changed the course of my life. I am humbled beyond measure by the magnanimity and philanthropy of the Southern California Sikh community. I would like to thank all my friends from "Monument Valley Group" and "Chai Peene wale log" for all the wonderful trips and for always being there for me. I am grateful to all my undergraduate friends from St. Stephens College and IIT Kanpur whose encouragement and support has proved to be vital in this journey. I would also like to thank my friends from the Sunday reading group who have inspired me to learn more about the history and the reality of this world.

This journey of PhD had begun way before I came to Caltech. I am indebted to my high school teacher, Mr. Pushpender Singh who inspired me to dream big. I cannot thank enough to my undegraduate college professors Dr. Sanjay Kumar and Dr. Bikram Phookun who went out of their way to know my personal story, and guided me accordingly to pursue a career in physics. I am also very grateful to Prof. Anand Kumar Jha at IIT Kanpur for his constant encouragement and for providing me an opportunity to work in his quantum optics lab.

Most importantly, none of this could have been possible without the unconditional love and support from my wonderful family who sacrificed a lot for my health and education, and went against the flow of their society by allowing me to fly alone in an open sky both literally and figuratively.

ABSTRACT

This thesis presents studies of different schemes to probe and manipulate quantum matter using light with an aim to discover novel routes to efficiently control the properties of quantum materials. A special focus is placed on developing new schemes utilizing light-matter interactions (1) to modify exchange interactions in magnetic insulators, and (2) to probe and modify band topology in quantum matter.

In part II, new schemes are presented to probe local band topology of Bloch bands. First, we study the effects of time-dependent band topology on adiabatic evolution of a Bloch wavepacket. We find that it results in an electric-field analog in semi-classical equation of motion, and can be demonstrated in a honeycomb lattice by varying the sublattice offset energy. We then extend these methods to include non-adiabatic processes, and found interesting connections between the anomalous drift during band excitation and a quantum geometric quantity known as shift-vector. We generalize the concept of shift-vector to include different kinds of band transition protocols beyond light induced dipole transitions. The idea of electric-field analog and the shift-vector are then combined to develop a novel charge pumping scheme. Motivated by these interesting consequences of band topology in non-adiabatic processes, we study shift-current response in moiré materials, and find that the highly topological nature of flat bands along with their very large unit cells significantly enhances these shift-vector related effects. This response also displays a strong dependence on interaction induced changes in band structure and quantum geometric quantities. These results suggest that shift-current response can possibly serve as a very reliable probe for interactions in twisted bilayer graphene. In addition to studying consequences of band topology on single-particle transport, we also consider Berry curvature effects on exciton transport. We find that the non-trivial band topology of underlying electron and hole bands allows us to manipulate excitons with a uniform electric field. We examine the conditions necessary to observe such transport and propose that transition metal dichalcogenide heterobilayers with moiré structure can prove an ideal platform for these effects.

In part III, we propose novel drive protocols based on manipulating orbital and lattice degrees of freedom in quantum materials with light. We found that light induced changes in orbital hybridization and their electronic energies results in a significant change in exchange interactions in quantum magnets. We also accounted for the role of ligands in periodically driven quantum magnets, and found that the predictions

made by the minimal model based on direct-hopping can be wrong in certain regimes of drive parameters. This understanding of light induced modifications in ligand-mediated exchange interactions was used to explain the phase shift observed in coherent phonon oscillations of $CrSiTe_3$ upon the onset of short-range spin correlations. We also demonstrate that light induced coherent lattice vibrations can provide a new route to realize space-time symmetry protected topological phases. Our results suggest that manipulating additional degrees of freedom (not included in commonly employed minimal models of periodically driven systems) with light can provide novel routes for ultrafast control of quantum materials.

PUBLISHED CONTENT AND CONTRIBUTIONS

[1] **Swati Chaudhary**, Cyprian Lewandowski, and Gil Refael. “Interaction-enhanced shift current in twisted bilayer graphene”. In: (Preparation).
This work is in preparation. S.C. participated in the conception of the project, carried out calculations and numerical simulations, and participated in the writing of the manuscript.

[2] **Swati Chaudhary**, Christina Knapp, and Gil Refael. “Anomalous exciton transport in response to a uniform in-plane electric field”. In: *Phys. Rev. B* 103 (16 Apr. 2021), p. 165119. DOI: `10.1103/PhysRevB.103.165119`.
S.C. participated in the conception of the project, carried out calculations and numerical simulations, and participated in the writing of the manuscript.

[3] **Swati Chaudhary**, Alon Ron, David Hsieh, and Gil Refael. “Controlling ligand-mediated exchange interactions in periodically driven magnetic materials”. In: (2020). arXiv: `2009.00813`.
S.C. participated in the conception of the project, carried out calculations and numerical simulations, and participated in the writing of the manuscript.

[4] **Swati Chaudhary**, Arbel Haim, Yang Peng, and Gil Refael. “Phonon-induced Floquet topological phases protected by space-time symmetries”. In: *Phys. Rev. Research* 2 (4 Dec. 2020), p. 043431. DOI: `10.1103/PhysRevResearch.2.043431`.
S.C. participated in the conception of the project, carried out calculations and numerical simulations, and participated in the writing of the manuscript.

[5] A. Ron, **S. Chaudhary**, G. Zhang, H. Ning, E. Zoghlin, S. D. Wilson, R. D. Averitt, G. Refael, and D. Hsieh. “Ultrafast enhancement of ferromagnetic spin exchange induced by ligand-to-metal charge transfer”. In: *Phys. Rev. Lett.* 125 (19 Nov. 2020), p. 197203. DOI: `10.1103/PhysRevLett.125.197203`.
S.C. participated in providing theoretical explanations for the observed experimental results, carried out theory calculations and participated in the writing of the manuscript.

[6] **Swati Chaudhary**, David Hsieh, and Gil Refael. “Orbital Floquet engineering of exchange interactions in magnetic materials”. In: *Phys. Rev. B* 100 (22 Dec. 2019), p. 220403. DOI: `10.1103/PhysRevB.100.220403`.
S.C. participated in the conception of the project, carried out calculations and numerical simulations, and participated in the writing of the manuscript.

[7] **Swati Chaudhary**, Manuel Endres, and Gil Refael. “Berry electrodynamics: Anomalous drift and pumping from a time-dependent Berry connection”. In: *Phys. Rev. B* 98 (6 Aug. 2018), p. 064310. DOI: `10.1103/PhysRevB.98.064310`.

S.C. participated in the conception of the project, carried out calculations and numerical simulations, and participated in the writing of the manuscript.

TABLE OF CONTENTS

II Probing Non-trivial Band Geometry 49

LIST OF ILLUSTRATIONS

Number *Page*

LIST OF TABLES

Part I

Introduction

Chapter 1

GENERAL INTRODUCTION

"Light, as a radiant energy of creation, started the ring-dance of atoms in a diminutive sky, and also the dance of the stars in the vast, lonely theatre of time and space."– Rabindranath Tagore

The last two decades have witnessed an exponential growth in the field of quantum simulations, quantum control, and quantum materials. On the one hand, artificial solids, especially the field of ultracold atomic gases has matured to a stage where it can be used to reliably simulate quantum many-body systems with unprecedented precision. The increased ability to manipulate atoms with light has enabled us to realize and study quantum phase transitions in a highly controllable manner. This progress has proved immensely beneficial for understanding and realizing topological phases of matter, many of which were previously considered inaccessible. On the other hand, the zoo of quantum materials is expanding rapidly, and heralds the promise of highly manipulable platforms with immense functionalities. These materials provide an exceptional platform to study a wide range of symmetry-broken, topological, and quantum many body phenomena [354]. The properties of these quantum materials are dictated by the interplay of electronic kinetic energy and interactions between spin, charge, lattice, and orbital degrees of freedom. In order to exploit quantum advantages of these materials in next generation technology, it is imperative to develop an in-depth understanding of interactions between the underlying degrees of freedom and discover new routes to control and tune their properties on demand. Many of their properties can be tuned by chemical doping, heterostructuring, or by applying static external perturbations like pressure, strain, or electrostatic gating [21]. Such methods are commonly employed to induce superconductivity and study metal-insulator phase transitions [385]. However, the slow time-scales and cumbersome experimental setups needed to execute these methods limit their applications in high-speed technologies. With the advent of powerful lasers capable of reaching E field as high as $10^8 - 10^9\ Vm^{-1}$ in THZ frequency range, ultrafast control of quantum materials with light is emerging as another promising route to control and understand these materials. Light-matter interactions have been used extensively for coherent manipulation of quantum many-body systems in optical lattices which have led to realization of many inaccessible phases. Motivated by this success of the AMO community, condensed matter physicists are now on a quest to discover new schemes to restructure the energy landscape and quantum states in solids by leveraging light-matter interactions.

1.1 Probing band topology

In addition to electronic kinetic energy and interactions between different degrees of freedom, the quantum geometry of the electronic wavefunctions is another aspect which is playing an increasingly important role in predicting the properties of quantum materials [377]. Non-trivial band topology of Bloch bands can manifest in many different signatures like the Quantum Hall effect (QHE) in the absence of a magnetic field, precise quantization of some transport coefficients, robust gapless edge modes or zero-energy corner modes. The anomalous Hall transport is a very well-established and a very prominent signature of non-trivial band signature. It relies on non-zero Berry curvature which can be considered an analog of magnetic field in momentum space. This naturally raises the question of whether we can define an analog of other electrodynamics quantities. In Chapter 4, we extend this analogy to define an electric field analog in reciprocal space which arises from the time-dependent Berry connection. We explore the term in the semiclassical equation of motion that gives rise to this phenomenon, and show that it can lead to anomalous drift in wave-packet motion. We then propose that such an effect can be demonstarted in graphene by varying the sublattice offset energy in an adiabatic manner. This anomalous drift arising from the change in band-topology inspired us to explore the consequences of time-dependent band population when a wavepacket is excited from one band to another. As a result, we extended these methods to include non-adiabatic processes, and found that the anomalous drift during band excitation was directly proportional to a quantum geometric quantity known as shift-vector. This quantity depends on the difference of Berry connection in two bands involved in the transition. We generalize the concept of shift-vector to include different kinds of band transition protocols and find that the nature of drive is also an important deciding factor for the shift-vector. We then combine this idea of electric-field analog and the shift-vector to develop a novel charge pumping scheme based on a cycle comprised of adiabatic and non-adiabatic steps.

Most of the signatures of quantum geometry depend on global band topology, and quite often cannot be revealed without breaking the time-reversal symmetry. However, in two-dimensional quantum materials like graphene or transition-metal dichalcogenide (TMDs) monolayers and bilayers, there are regions of non-trivial quantum geometry in momentum space even though the global band topology characterized by Chern number in these setups is trivial. This makes them insensitive to commonly employed topology probes based on QHE or gapless edge states. As a result, the non-trivial quantum geometry of these materials is revealed only when illuminated by circularly polarized, which breaks time-reversal symmetry [254, 257]. One can ask if the aforementioned shift-vector based anomalous drift can be used to probe non-trivial band topology in TRS preserving systems. It was shown in Ref. [317] that the shift-vector can have important implications on second-order optical responses. Recently, it has been found responsible for the giant bulk photovoltaic effect in many materials.The effect arising from this shift-vector manifests in second-order optical response, and is commonly known as shift-current. The magnitude of this quantity depends on the size of unit cell in real space, and thus can lead to a large response in moiré materials. We pursue this direction in Chapter 5 and study how this shift-current response is affected by different parameters and electron-electron interactions of twisted bilayer graphene.

Furthermore, quantum geometry signatures are not limited to single-particle transport, but can have important consequences for collective excitations like excitons and plasmons as well [327, 191, 329, 406]. The non-trivial quantum geometry of underlying Bloch bands can manifest as non-hydrogenic features in exciton spectra of TMDs [329, 406]. It can also give rise to the anomalous Hall effect of excitons in the presence of non-uniform electric fields. With the ever-expanding field of highly controllable VdW heterostructures, we can engineer different kinds of band structures and band topologies. We show in Chapter 6 that certain band structures can offer the possibility to transport transport excitons with a uniform electric field. We posit that this effect can be demonstrated for intervalley excitons in systems with a narrow electronic bandwidth and a large unit cell in real space, and found that moiré TMDs might be an ideal candidate for such studies.

1.2 Ultrafast control of quantum matter

A central goal of condensed matter physics is to discover new pathways to control and understand the properties of materials around us. The intense research activity in the field of quantum materials and recent advancements in light based technology are paving the way for utilizing light-matter interactions to manipulate quantum materials. Light-induced changes in solids can be either thermal like simple melting of thermal states by laser-induced heating or non-thermal like carrier excitations between different bands, coherent resonant excitation of collective lattice or charge density vibrations, dynamical modification of hopping parameters, etc. One particular class of non-thermal phenomena which can be described by a time-periodic perturbation has found immense applications in coherent manipulation of quantum many-body systems. It is commonly known as Floquet engineering.

Floquet engineering has been touted as a very powerful technique to control and tune the properties of quantum matter. At the basis of this scheme is the modification of electronic or atomic wavefunctions through photon dressing. In the last decade, it has been used extensively to manipulate quantum matter in optical lattices [89]. It has been invoked in a variety of contexts like achieving dynamical localization [91], engineering artificial gauge fields for neutral atoms [243, 149, 332, 9], demonstrating dynamical phase transitions [397], and most successfully in realizing topological phases like the Haldane model in optical lattices with no equilibrium counterparts [155]. These methods are now gaining popularity in solid state physics [21, 257], and this enthusiasm to adopt Floquet engineering is further boosted by recent experimental realization [226] of light-induced topological phase in graphene. Although, we can use the simple toy models as periodically driven optical lattices in certain cases, quantum materials are significantly more complicated. There are many intertwined degrees of freedom like spin, charge, lattice, or orbital degree of freedom, and they couple to EM fields in different ways. One of the main goals of this thesis is to understand how we can manipulate these additional degrees of freedom with light to control the properties of quantum materials. As an example, we consider the case of light induced modifications of exchange interactions in transition metal based magnetic insulators. The minimal model for antiferromagnetic exchange modification assumes direct hopping between neighboring sites and considers only one orbital on each spin site. We extend the minimal model based on direct-hopping modification [227] to include ligand-mediated exchange processes. In Chapter 8, we explore the possibility of manipulating the ligand orbital degree of freedom with light. We demonstrate that the light-induced orbital hybridization can result in a significant change in exchange interactions with drive requirement similar to the direct-hopping models. It is well known that multi-orbital nature of d orbitals on TM ion sites can have significant ramifications on electronic and magnetic properties of transition metal compounds. We demonstrate that exciting a coherent lattice vibration can mix d orbitals which in turn allow us to control exchange interactions. These effects can be observed at somewhat weaker drive amplitudes, and hence pave the way for more efficient driving schemes.

Another very interesting aspect of periodically driven systems is that the temporal degree of freedom can act as an artificial spatial dimension. It was first shown in Ref. [221], that this analogy can be exploited to construct a higher dimensional Floquet system from a low dimensional static system. Similar ideas were invoked to demonstrate that Floquet Hamiltonian can also exhibit space-time symmetries which expand the topological classification [270]. This allows for the existence of novel topological phases with no static counterparts. These Floquet topological phases rely on the symmetry promotion action of drive, and hence are different from traditional Floquet schemes where the drive breaks certain non-spatial symmetries. Although, these ideas have been existing for a while but a toy model for realization of such phases using the ingredients offered by typical quantum materials was lacking. In Chapter 7, we present how a coherent phonon mode can be used to realize such phases by promoting a reflection symmetry to a time-glide symmetry.

One important feature of Floquet engineering is that the "engineered Hamiltonian" exists only when the drive is on, and can be tuned in real-time by modifying the drive parameters. However, there are other light-induced phenomena where the irradiated system cannot be simply described by a time-periodic Hamiltonian. For instance, if the light is resonant with some electronic transitions, it can change the charge distribution in the quantum material which can change the system in a more complicated way when interactions are involved. This kind of modification can affect several properties of the quantum materials. In Chapter 10, we applied this approach to predict a novel route for non-thermal modification of exchange interactions in magnetic insulator $CrSiTe_3$. In this transition metal trichalcogenide, light-induced charge transfer transition can excite electrons from d orbitals of Cr ion to p orbital in Te. Using a molecular toy model, we calculate its effect on ferromagentic (FM) exchange interactions between two Cr ions, and show that this charge transfer excitation results in a significant enhancement of FM coupling. The exchange striction arising from modified magnetic coupling manifests as a phase change in phonon oscillations which were detected experimentally in a time-resolved coherent phonon spectroscopy [294].

Chapter 2

QUANTUM GEOMETRY

"The surprise in everything is that quantum mechanics is so much richer than we ever dreamed." - Duncan Haldane

About 60 years ago, Panchratnam made a surprising discovery that decades later changed the course of solid-state physics. He observed that when the polarization state of a light beam was varied in a cyclic manner, it resulted in a phase shift which depended purely on the geometric properties of the path traced by the polarization state on the Poincaré sphere [265]. Two decades later Sir Michael Berry discovered a similar phase change for the adiabatic and cyclic evolution of a quantum state and popularized this concept of geometric phases in quantum systems [33]. This phase, which later came to be known as Berry phase, soon found applications in many other fields including atomic and molecular physics, cosmology, nuclear physics, optics, and solid state physics. A fortuitous meeting between Barry Simon and Michael Berry inspired Simon to investigate the connection of this phase to abstract mathematical concepts in algebraic topology. Barry Simon found that the Berry phase has a very elegant explanation in terms of the connection of fiber bundles representing the wavefunction of quantum states and could be interpreted as the holonomy of this Hermitian line bundle [316]. On the basis of this newly found link between math and physics, Barry Simon also explained the connection between Berry phase and quantized Hall conductance [349]. This elegant mathematical framework not only explained the ubiquity of geometric phases in quantum mechanics, but also provided a new basis for the classification of quantum matter. Most importantly, these concepts of quantum geometry, when applied to electronic wavefunctions in quantum matter, led to a paradigm shift in our understanding of crystalline materials. Additionally, these quantum geometrical aspects can drastically alter the physical properties of quantum materials [377]. In order to predict and harness these quantum geometrical aspects, we need new probes to extract more information about these features.

In the first part of this thesis, we explore different methods in which local band geometry can be probed using light. In this part, we mainly look into probes which depend on time-dependence of such phases or the signatures of quantum geometry in non-equilibrium processes.

In this chapter, we provide the theoretical background needed to understand how light can be used as a probe to study quantum geometric properties of Bloch bands. We discuss the significance of the quantum geometry of wavefunction on material properties. We start by focusing on the simplest manifestation of quantum geometry, i.e, Berry phase. We then proceed to identify the mathematical and physical aspects of quantum geometry in Bloch bands.

This chapter draws heavily upon the references [377, 361, 266]. Henceforth, they will not be explicitly cited unless necessary.

2.1 Background

The Berry phase is the geometric phase accumulated during the adiabatic and cyclic evolution of a quantum state. In order to understand how this phase arises in quantum mechanics, let us consider a system described by Hamiltonian

$$H = H(\boldsymbol{\lambda}) \tag{2.1}$$

where $\lambda = (\lambda_1, \lambda_2, ...\lambda_N)$ is a set of N time-dependent parameters. The instantaneous eigenstates of this Hamiltonian satisfy

$$H(\boldsymbol{\lambda}) \left| n_{\boldsymbol{\lambda}} \right\rangle = \varepsilon_n(\boldsymbol{\lambda}) \left| n_{\boldsymbol{\lambda}} \right\rangle . \tag{2.2}$$

If the system starts in a non-degenerate eigenstate and these parameters are changed in a cyclic and adiabatic manner, the system remains in the same instantaneous eigenstate, i.e.,

$$\left| \Psi_n(t) \right\rangle = e^{i\phi(t)} \left| n_{\boldsymbol{\lambda}} \right\rangle \tag{2.3}$$

where the time-dependent phase $\phi(t)$ has two kinds of contributions

$$\phi(t) = \phi_{\text{dyn}} + \gamma. \tag{2.4}$$

The first term is known as the dynamical phase factor which depends on time-evolution of energy eigenvalue and is given by

$$\phi_{\text{dyn}} = -\frac{1}{\hbar} \int_0^t \varepsilon_n(t') dt' \tag{2.5}$$

and the second term is of purely geometric origin which depends only on the path traced by $\boldsymbol{\lambda}$ in parameter space and satisfies:

$$\frac{d\gamma_n}{dt} = i \left\langle n_{\boldsymbol{\lambda}} \right| \nabla_{\boldsymbol{\lambda}} \left| n_{\boldsymbol{\lambda}} \right\rangle \cdot \frac{d\boldsymbol{\lambda}}{dt}. \tag{2.6}$$

The geometric phase accumulated during a cyclic process can be expressed as a path integral in $\boldsymbol{\lambda}$ parameter space

$$\gamma_n = \oint_C d\boldsymbol{\lambda} \cdot \mathbf{A}^n(\boldsymbol{\lambda}) \tag{2.7}$$

where $\mathbf{A}^n = \langle n_{\boldsymbol{\lambda}} | \nabla_{\boldsymbol{\lambda}} | n_{\boldsymbol{\lambda}} \rangle$ is known as Berry connection. It is a gauge-dependent quantity with transformation given by

$$|n_{\boldsymbol{\lambda}}\rangle \rightarrow e^{i\alpha(\lambda)} |n_{\boldsymbol{\lambda}}\rangle \implies \mathbf{A} \rightarrow \mathbf{A} - \frac{\partial}{\partial \boldsymbol{\lambda}} \alpha. \tag{2.8}$$

This phase can be considered an analog of the Aharanov-Bohm (AB) phase [4] which appears when a charged particle is moved around a closed loop with non-zero magnetic flux. In the case of AB phase, the acquired phase can be calculated either from the line integral of the EM vector potential or from the magnetic flux threading the loop. This analogy can thus be exploited to express the geometric phase in terms of a gauge-field tensor (analog of magnetic field) quantity derived from the Berry connection

$$\Omega^n_{ij} = \frac{\partial}{\partial \lambda^i} A^n_j(\boldsymbol{\lambda}) - \frac{\partial}{\partial \lambda^j} A^n_i(\boldsymbol{\lambda}). \tag{2.9}$$

This field is known as the Berry curvature, and by applying the Stoke's theorem, we can express geometric phase as

$$\gamma_n = \int_S d\lambda^i \wedge d\lambda^j \frac{1}{2} \Omega^n_{ij}(\boldsymbol{\lambda}). \tag{2.10}$$

The Berry curvature is a gauge invariant quantity which is local in parameter space. Its locality implies that its effects are not limited to cyclic adiabatic processes and can manifest non-cyclic processes as well.

Simple example of Berry phase

So far, we considered the geometric phase and related quantities in a very abstract manner for a generic parameter space $\boldsymbol{\lambda}$. Physically, these phases arise in a multilevel system with non-degenerate eigenstates when the Hamiltonian is tuned adiabatically in a continuous manner. One simple and very illustrative example is the time-evolution of a Spin-1/2 particle in a slowly varying uniform magnetic field. Let us consider that the magnetic field strength remains fixed and its direction $\hat{\mathbf{n}}$ is changing with time. The dynamics of this system is governed by

$$H = -g\mathbf{B} \cdot \mathbf{S} \tag{2.11}$$

where g is the gyromagnetic ratio, $\mathbf{B} = B\hat{\mathbf{n}(t)}$, $\mathbf{S} = \hbar\boldsymbol{\sigma}/2$ is the spin, and σ_j are the Pauli matrices. The instantaneous eigenstates of this Hamiltonian are given by

$$|\uparrow_{\mathbf{n}}\rangle = \begin{pmatrix} \cos\frac{\theta}{2} \\ \sin\frac{\theta}{2}e^{i\phi} \end{pmatrix}, \text{ and } |\downarrow_{\mathbf{n}}\rangle = \begin{pmatrix} \sin\frac{\theta}{2}e^{-i\phi} \\ -\cos\frac{\theta}{2} \end{pmatrix} \tag{2.12}$$

where $\hat{\mathbf{n}} = (\sin\theta\cos\phi, \sin\theta\sin\phi, \cos\theta)$ and can be visualized as a vector pointing in $\hat{n}$ on Bloch sphere. If the system starts in eigenstate $|\uparrow_{\mathbf{n}}\rangle$ and $\hat{\mathbf{n}}$ is varied along a closed loop C parameterized by λ, then the Berry phase accumulated during this process can be expressed as

$$\mathbf{A} = i\,\langle\uparrow_{\hat{\mathbf{n}}}|\,\nabla_{\hat{\mathbf{n}}}\,|\downarrow_{\hat{\mathbf{n}}}\rangle = -\frac{1}{\sin\theta}\sin^2\left(\frac{\theta}{2}\right)\hat{\phi}. \tag{2.13}$$

Now, the geometric phase is

$$\gamma = \oint_C \mathbf{A}\cdot d\hat{l} \tag{2.14}$$

where on curve C, $d\hat{l} = d\theta\,\hat{\theta} + \sin\theta d\phi\,\hat{\phi}$, and, the Berry curvature is given by

$$\Omega = \frac{1}{\sin\theta}\left(\sin\theta A_\phi\right) = \frac{1}{2}\hat{r}. \tag{2.15}$$

We can also write

$$\gamma_n = \frac{1}{2}\int\int d\theta\sin\theta d\phi = \frac{1}{2}\left(\text{Solid angle subtended by curve } C \text{ w.r.t origin}\right). \tag{2.16}$$

This expression further reveals the geometric origin of this phase as it depends only on the area enclosed by curve C. Similar phases can arise in classical systems, for example, the geometric phase picked up by polarization vector as it moves along a closed loop on Poincare Sphere. This connection between two very unrelated systems has a simple interpretation in terms of anholonomy angle acquired during the parallel transport of a vector on a curved sphere. Another important point to notice is that such phases can arise only if the system has at least a two-dimensional Hilbert space at each point on curve C. For spin-1/2, it is just the spin degree of freedom, and for the case of light, it is the polarization degree of freedom. This two-dimensional vector space associated with these degrees of freedom allows for the possibility of picking a non-zero geometric phase during a cyclic process.

Quantum geometry beyond Berry phase

The Berry phase was a remarkable discovery which brought to light the geometric aspects of quantum evolution. However, Berry's phase was just a special case of more general quantum geometrical aspects. Soon after Berry's work, it was realized that adiabaticity and cyclicity were not necessary to study such quantum geometric features. The concept of Berry's phase was generalized to non-adiabatic processes by Aharanov and Anandan [3] who presented the geometric phase in terms of the properties of the quantum state rather than of the parameters of Hamiltonian. It was further generalized to approximately cyclic processes by Berry himself [34] and to the non-cyclic case by Samuel and Bhandari [302]. In fact, the local quantity Berry curvature does not capture the entire geometric structure of quantum evolution, but it is the imaginary part of the more general quantity known as quantum geometric tensor (QGT) [69] defined as

$$\chi^n_{\mu\nu}(\boldsymbol{\lambda}) = \left\langle \frac{\partial n(\boldsymbol{\lambda})}{\partial \lambda_\mu} \middle| \frac{\partial n(\boldsymbol{\lambda})}{\partial \lambda_\nu} \right\rangle - \left\langle \frac{\partial n(\boldsymbol{\lambda})}{\partial \lambda_\mu} \middle| n(\boldsymbol{\lambda}) \right\rangle \left\langle n(\boldsymbol{\lambda}) \middle| \frac{\partial n(\boldsymbol{\lambda})}{\partial \lambda_\nu} \right\rangle . \tag{2.17}$$

The real part of this QGT, $\mathrm{Re}(\chi^n_{\mu\nu}(\boldsymbol{\lambda})) = g_{\mu\nu}$ is the Fubini-Study metric, which can be interpreted as the distance between states in the parameter space and the imaginary part, $\mathrm{Im}(\chi^n_{\mu\nu}(\boldsymbol{\lambda})) = \Omega_{\mu\nu}/2$ where $\Omega_{\mu\nu}$ is the Berry curvature.

Berryology of the Brillouin Zone

Until a few decades ago, condensed matter physicicsts were quite satisfied with their understanding of non-interacting electrons in periodic potentials. Most properties of such crystalline solids could be explained very well from the knowledge of energy-momentum dispersion of electrons. Soon after Berry's seminal work, it was obvious that the band structure of crystals naturally provides an interesting platform to study Berry phase effects. In this part, we aim to understand how this Berry phase can impact the properties of electrons in crystalline solids and how it can provide a new framework to classify the quantum matter. For non-interacting electrons in a crystalline solid, the motion of electrons in such solids is governed by Hamiltonian which satisfies

$$H(\mathbf{r} + \mathbf{a}_i) = H(\mathbf{r}) \tag{2.18}$$

where $\mathbf{a}_i$'s are Bravais lattice vectors. The eigenstates of this Hamiltonian are given by Bloch wavefunctions:

$$|\psi_n\rangle = e^{i\mathbf{k}\cdot\mathbf{r}} |u_n(\mathbf{k})\rangle \tag{2.19}$$

where $|u_k\rangle$ is the cell periodic part and $|u_k\rangle(\mathbf{r} + \mathbf{a}_i) = |u_k\rangle(\mathbf{r})$. This cell periodic part can be interpreted as the eigenstate of Bloch Hamiltonian $H(\mathbf{k}) = e^{-i\mathbf{k}\cdot\mathbf{r}} H e^{i\mathbf{k}\cdot\mathbf{r}}$. Now, this $H(k)$ usually has a multiband structure and its eigenstates $|u_k\rangle$ change with k which can have important implications on many physical properties. The information about how these eigenstates change with k in encapsulated in quantum geometric tensor described in Eq. 2.17. We can understand most of the features of the Bloch band geometry in terms of Berry connection and Berry curvature defined in k space

$$\mathbf{A}^n(\mathbf{k}) = i \langle u_n(\mathbf{k}| \nabla_{\mathbf{k}} |u_n(\mathbf{k})\rangle \tag{2.20}$$

$$\boldsymbol{\Omega}^n = \nabla_{\mathbf{k}} \times \mathbf{A}^n(\mathbf{k}). \tag{2.21}$$

As also mentioned earlier, Berry curvature is local in parameter space and in this case, it becomes an intrinsic property of the Bloch band. We will see in the next section that non-zero Berry curvature can have profound effects on transport. Also, these effects can appear even when the quantum evolution is non-cyclic and non-adiabatic. In two dimensions, there is only one component in Berry curvature, $\boldsymbol{\Omega}^n = \Omega^n \hat{z}$ which points in a direction perpendicular to the two-dimensional k space.

Symmetry properties of Berry curvature

We have discussed all these quantum geometric quantities like Berry connection and Berry curvature in a very abstract manner. Now, we can ask when are these quantities non-zero and under what circumstances we can safely ignore all such quantities. In order to address these questions, let us briefly consider the consequences of some spatial and non-spatial symmetries on Berry curvature. We are going to focus only on two cases for now:

1. *Inversion Symmetry*: If the Bloch Hamiltonian is inversion symmetric, $H(\mathbf{k}) = H(-\mathbf{k})$, then $\boldsymbol{\Omega}^n(\mathbf{k}) = \boldsymbol{\Omega}^n(-\mathbf{k})$.
2. *Time-reversal Symmetry*: If the system has time-reversal symmetry described by $H(\mathbf{k}) = H^*(-\mathbf{k})$, then, $\boldsymbol{\Omega}^n(\mathbf{k}) = -\boldsymbol{\Omega}^n(-\mathbf{k})$.

As a consequence of these properties, Berry curvature is non-zero only if at least one of these symmetries is broken. It indicates that Berry curvature effects come into picture only for non-centrosymmetric or magnetic systems. Another extremely important aspect of quantum geometry stems from the fact that the parameter space for Bloch Hamiltonians is a closed 2D manifold. Since the Berry curvature is the curvature of the fiber bundle representing the Bloch wavefunctions, by applying Gauss-Bonnett theorem it can be shown that

$$\int_{\mathrm{BZ}} dk_x dk_y\, \Omega^n(\mathbf{k}) = 2\pi C \tag{2.22}$$

where C is an integer known as Chern number. The geometric nature of Berry curvature allows us to associate a topological invariant with Bloch bands and provide a new method to classify Hamiltonians on the basis of their topological properties. This invariant for a given band cannot be changed without closing the gap, and hence it is very robust. We notice that using the above symmetry properties of Berry curvature, it is evident that C can be non-zero only if TRS is broken. The Chern number was an example of a topological invariant for a two-dimensional system on the basis of TRS. Similarly, the absence or presence of other non-spatial symmetries (particle-hole, chiral) divide quantum matter into different classes based on other topological invariants. This topology-based analysis provided a new framework for classification of quantum matter famously known as ten-fold way [11].

Berry curvature hotspots

We discussed how a non-zero Berry curvature can lead to non-trivial band geometry. We also noticed that such a situation can be realized if TRS or inversion is broken. However, so far we never mentioned what decides the Berry curvature profile in a Bloch band. Since the Berry curvature depends on how the eigenstates of a Bloch Hamiltonian change with $\mathbf{k}$, we can expect that avoided crossings would serve as Berry curvature hotspots. As an example, let us consider a linearized two-band model in the vicinity of an avoided crossing in a two-dimensional parameter space (k_x, k_y) described by

$$H_{\text{Dirac}}(\mathbf{k}) = \Delta\sigma_z + \hbar v_F \mathbf{k} \cdot \boldsymbol{\sigma} \tag{2.23}$$

where σ matrices represent some spin, orbital, or pseudospin degree of freedom. It can be realized in a variety of systems like graphene, TMD monolayers, TMD bilayers, etc. around gapped Dirac points. It also resembles the Hamiltonian of spin-1/2 particle in an external magnetic field, but the role of $\mathbf{B}$ is replaced by vector $\mathbf{d}(\mathbf{k}) = (\hbar v_F k_x, \hbar v_F k_y, \Delta)$. Now, we can calculate the Berry connection and Berry curvature for the two eigenstate of this Hamiltonian using the following gauge for $\Delta > 0$

$$|u_+\rangle = \begin{pmatrix} \cos\frac{\theta}{2} \\ \sin\frac{\theta}{2}e^{i\phi} \end{pmatrix}, \text{ and } |u_-\rangle = \begin{pmatrix} \sin\frac{\theta}{2}e^{-i\phi} \\ -\cos\frac{\theta}{2} \end{pmatrix} \tag{2.24}$$

where

$$\cos\theta = \frac{\Delta}{\sqrt{\Delta^2 + (\hbar v_F k)^2}}, \text{ and } \phi = \tan^{-1}\left(\frac{k_y}{k_x}\right). \tag{2.25}$$

This gives Berry connection and Berry curvature

$$\mathbf{A}^{\pm} = \mp\frac{1}{2k}\left(1 - \frac{\Delta}{\sqrt{\Delta^2 + \hbar^2 v_F^2 k^2}}\right)\hat{k}_{\phi}, \text{ and } \mathbf{\Omega}^{\pm} = \pm\frac{\hbar^2 v_F^2 \Delta}{2(\Delta^2 + \hbar^2 v_F^2 k^2)^{3/2}}\hat{z}. \qquad (2.26)$$

Now, there are a few noticeable and interesting properties of these quantities in Dirac Hamiltonians. In the limit, $\hbar v_F k \ll \Delta$, we can approximate

$$\mathbf{A}^{\pm} \approx \mp\frac{\hbar^2 v_F^2 k}{4\Delta^2}\hat{k}_{\phi}, \text{ and } \mathbf{\Omega}^{\pm} \approx \pm\frac{\hbar^2 v_F^2}{2\Delta^2}\hat{z} \qquad (2.27)$$

which results in a constant Berry curvature and a linear in k Berry connection. If we now calculate the Berry flux through a small loop of radius k centered around the Dirac point, it is directly proportional to the area of loop. On the other hand, in the opposite limit, $\hbar v_F k \gg \Delta$

$$\mathbf{A}^{\pm} \approx \mp\frac{1}{2k}\hat{k}_{\phi}, \text{ and } \mathbf{\Omega}^{\pm} \approx \pm\frac{\Delta}{2\hbar v_F k^3}\hat{z} \qquad (2.28)$$

and the Berry flux, $\Phi_{\text{Berry}} = \int_{\phi=0}^{\phi=2\pi} \mathbf{A}^{\pm} \cdot k d\phi = \mp\pi$ associated with a loop of large radius k saturates to a value of π. This indicates that if a Bloch state is moved around a closed loop of radius $k \gg \Delta/(\hbar v_F)$ around a Dirac point, it gains a Berry phase of $\pm\pi$. The Berry curvature is roughly spread out in a circular region of radius $\Delta/(\hbar v_F)$, and thus increasing the gap results in a broader distribution of Berry curvature. In the limit, $\Delta \to 0$, these Dirac points act as Berry curvature monopoles. In two-dimensional systems, these Dirac points always occur in pairs. In TRS preserving systems, the total Berry flux is zero as the Berry flux from two DPs in each pair is equal and opposite. However, when TRS is broken (which can be done even without a magnetic field [128]), the two DPs in pair have the same sign for Berry flux which results in a total flux equal to an integer multiple of 2π and such systems with non-trivial topology are known as Chern insulators.

2.2 Manifestations of quantum geometry (QG) in quantum matter

So far, we focused on the description of quantum geometric quantities arising from the non-trivial structure of Bloch eigenstates. These quantities are important not only from a theoretical perspective, but can also affect the behavior of Bloch electrons significantly. In the last decade, there has been a lot of focus on probing and utilizing these quantum geometric properties of solids to build more robust and efficient quantum devices. In order to understand how these geometric features can be probed and exploited, below we discuss some of the very important manifestations of quantum geometry in crystalline solids.

Pumping from Berry phase

One of the very interesting and extensively studied consequence of Berry phase in crystalline solids is the Berry phase induced transport or pumping effect. A remarkable example of this effect is the quantized adiabatic transport in a one-dimensional (1D) band insulator, first studied by Thouless [348]. He studied the particle transport in a gapped 1D periodic Hamiltonian subjected to a time-periodic perturbation varying slowly in time, i.e

$$H(t) = H(t+T). \tag{2.29}$$

This Hamiltonian remains periodic in space for all time, thus its eigenstates are given Bloch wavefunctions $e^{ikx}\left|u_k^n(t)\right\rangle$. If the system starts in n^{th} state, then apart from an overall phase factor, the wavefunction of the system is given by:

$$\left|u_k^n\right\rangle - i\hbar \sum_{m\neq n} \frac{\left|u_k^m\right\rangle \langle u^m|\partial u^n/\partial t\rangle}{\varepsilon_n - \varepsilon_m}. \tag{2.30}$$

We can now calculate the adiabatic current induced by this time periodic perturbation. The velocity operator has the form $v = \partial H/\hbar\partial(k)$ which gives the average velocity for the above state

$$v^n(k) = \frac{\partial\varepsilon^n(k)}{\hbar\partial k} - i\sum_{m\neq n}\left[\frac{\langle u^n|\,\partial H/\partial k\,|u^m\rangle\,\langle u^n|\partial u^m/\partial t\rangle}{\varepsilon_n - \varepsilon_m} - \text{c.c}\right] \tag{2.31}$$

which can be re-expressed as

$$v^n(k) = \frac{\partial\varepsilon^n(k)}{\hbar\partial k} - i\left[\left\langle\frac{\partial u^n}{\partial k}\middle|\frac{\partial u^n}{\partial t}\right\rangle - \left\langle\frac{\partial u^n}{\partial t}\middle|\frac{\partial u^n}{\partial k}\right\rangle\right]. \tag{2.32}$$

Here, the second term is the Berry curvature $\Omega^n + kt$ in two-dimensional parameter space (k,t), thus the average velocity expression is simplified to

$$v^n(k) = \frac{\partial\varepsilon^n(k)}{\hbar\partial k} - \Omega^n_{kt}. \tag{2.33}$$

The perturbation induced adiabatic current can be obtained by integrating the above expression over full BZ. The first term vanishes, and the second term gives the total current from the n^{th} band

$$j^n(t) = -\frac{1}{2\pi}\int_{BZ}\Omega^n_{kt}\,dk. \tag{2.34}$$

Now, the charge transport over one full cycle is given by

$$q^n = -\frac{1}{2\pi}\int_0^T dt\int_{BZ}\Omega^n_{kt}\,dk. \tag{2.35}$$

The parameter space (k, t) of this Hamiltonian is torus, thus the Berry curvature integral over full BZ is quantized in units of 2π which gives

$$q^n = -C \tag{2.36}$$

where C is the Chern number of the n^{th} band.

This kind of adiabatic transport (also known as adiabatic pumping) induced by time-periodic perturbation can generate a DC current I proportional to Chern number and that too in the absence of a voltage bias as recently demonstrated in Ref. [248]. This DC current is present only if the Chern number in parameter space (k, t) is non-zero which makes it a direct signature of band topology. Similar pumping based arguments can be applied to understand the precise quantization of conductance in quantum Hall experiment [15].

Berry phase effects on electron dynamics

The above example demonstrated that non-zero Berry curvature can have important implications for particle transport. Now, we can ask how it affects the dynamics of Bloch electrons in presence of other perturbations like DC electric field, magnetic field or EM fields.

Let us first consider the motion of Bloch electrons under the influence of a weak uniform electric field. According to any standard solid state textbook, this dynamics can be extracted simply from the group velocity obtained from the band dispersion. In this simple picture, the velocity of a k state in n^{th} band is simply given by:

$$\mathbf{v}^n(\mathbf{k}) = \frac{1}{\hbar}\frac{\partial \varepsilon_n(\mathbf{k})}{\partial \mathbf{k}} \tag{2.37}$$

and

$$\dot{\mathbf{k}} = -\frac{e}{\hbar}\mathbf{E}. \tag{2.38}$$

This description ignores the changes in the structure of Bloch wavefunction as it is moved in k space. As discussed in the previous subsection, the wavefunction of a given k state changes according to Eq. 2.30 when subjected to a time-dependent perturbation. In this case, it becomes

$$|\psi_n\rangle = \left|u_k^n\right\rangle - i\hbar \sum_{m \neq n} \frac{\left|u_k^m\right\rangle \left\langle u_k^m \middle| \nabla_{\mathbf{k}_k} u^n \right\rangle}{\varepsilon_n - \varepsilon_m} \cdot \dot{\mathbf{k}}, \tag{2.39}$$

and now following the same steps as the previous subsection, we get the expectation value of velocity operator $\cap \mathbf{v}(\mathbf{k}) = \frac{1}{\hbar}\nabla_{\mathbf{k}} H$

$$\mathbf{v}^n(\mathbf{k}) = \frac{1}{\hbar}\nabla_{\mathbf{k}}\varepsilon_n(\mathbf{k}) - i\left[\left\langle \nabla_{\mathbf{k}} u_n \middle| \dot{\mathbf{k}} \cdot \nabla_{\mathbf{k}} u_n \right\rangle - \left\langle \dot{\mathbf{k}} \cdot \nabla_{\mathbf{k}} u_n \middle| \nabla_{\mathbf{k}} u_n \right\rangle\right] \tag{2.40}$$

EM fields	Quantum geometry
Aharanov-Bohm Phase	Berry phase
Magnetic field	Berry curvature
Vector potential	Berry connection
Electric field	Time-derivative of Berry connection
$\left[k_\alpha, k_\beta\right] = -i\epsilon_{\alpha\beta\gamma}B_\gamma$	$\left[r_\alpha, r_\beta\right] = i\epsilon_{\alpha\beta\gamma}\boldsymbol{\Omega}_\gamma$

Table 2.1: Duality between EM and quantum geometric quantities.

$$\mathbf{v}_i^n(\mathbf{k}) = \frac{1}{\hbar}\frac{\partial \varepsilon_n(\mathbf{k})}{\partial k_i} - i\dot{k}_j\left[\left\langle\frac{\partial u_n}{\partial k_i}\middle|\frac{\partial u_n}{\partial k_j}\right\rangle - \left\langle\frac{\partial u_n}{\partial k_j}\middle|\frac{\partial u_n}{\partial k_i}\right\rangle\right] \tag{2.41}$$

which can be expressed as

$$\mathbf{v}_i^n(\mathbf{k}) = \frac{1}{\hbar}\frac{\partial \varepsilon_n(\mathbf{k})}{\partial k_i} - \epsilon_{ijl}\dot{k}_j\boldsymbol{\Omega}_l^n \tag{2.42}$$

where $\boldsymbol{\Omega}_l^n$ is the Berry curvature tensor. It shows that the dynamics of the electron is now described by

$$\mathbf{v}^n(\mathbf{k}) = \frac{1}{\hbar}\frac{\partial \varepsilon_n(\mathbf{k})}{\partial \mathbf{k}} - \dot{\mathbf{k}}\times\boldsymbol{\Omega}^n, \text{ with } \dot{\mathbf{k}} = -\frac{e}{\hbar}\mathbf{E}. \tag{2.43}$$

Here, this effect can be interpreted as Hall effect arising from a magnetic field analog in k space. For a non-trivial band the integral of Berry curvature is quantized, thus for a completely filled Bloch band, it results in a quantized Hall conductance proportional to Chern number of the band.

This analogy between EM and quantum geometric quantities (shown in Table 2.1) can be extended to include electric field. We can ask whether there are any pumping effects arising from an electric field analog. Is it possible to get such a DC current in topologically trivial systems with non-vanishing Berry curvature? If yes, under what conditions such an effect can survive. We answer these questions in Chapter 1 where we present a scheme to observe a pumping effect arising from the time-dependence of Berry connection.

Although our main focus in this thesis is to investigate novel quantum geometric signatures in presence of the electric field, a finite magnetic field can also engender many interesting quantum geometry induced effects. As shown in Ref. [59], a Bloch wavepacket may possess a self-rotation around its center of mass which depends on the structure of Bloch wavefunctions and endows it an angular momentum

$$\boldsymbol{m}(\mathbf{k}) = -\frac{e}{2\hbar}\left\langle\nabla_{\mathbf{k}}u\right|\times\left[H(\mathbf{k}) - \varepsilon(\mathbf{k})\right]\left|\nabla_{\mathbf{k}}u\right\rangle. \tag{2.44}$$

In the presence of magnetic field, this orbital angular momentum can contribute to energy dispersion which is now given by:

$$\varepsilon_{\mathbf{m}}(\mathbf{k} = \varepsilon(\mathbf{k}) - \mathbf{B} \cdot \boldsymbol{m}(\mathbf{k}) \tag{2.45}$$

which would inevitably affect the group velocity. The new equations of motion for semiclassical dynamics of wavepacket are

$$\mathbf{v}^n(\mathbf{k}) = \frac{1}{\hbar}\nabla_{\mathbf{k}} - \dot{\mathbf{k}} \times \boldsymbol{\Omega}^n(\mathbf{k}) \tag{2.46}$$

$$\dot{\mathbf{k}} = -e\mathbf{E} - e\mathbf{v}^n(\mathbf{k}) \times \mathbf{B}. \tag{2.47}$$

There is another very interesting manifestation of non-zero Berry curvature in the presence of a magnetic field. In addition to electron dynamics, the Berry curvature can also modify the electron density of states in the phase space [379]. Using the above equation of motion, it can be shown that the time evolution of volume element $\Delta V = \Delta\mathbf{r}\Delta\mathbf{k}$ is given by:

$$\frac{1}{\Delta V}\frac{\partial \Delta V}{\partial t} = \nabla_{\mathbf{r}} \cdot \dot{\boldsymbol{r}} + \nabla_{\mathbf{k}} \cdot \dot{\boldsymbol{k}} \tag{2.48}$$

and thus

$$\Delta V = \frac{V_0}{1 + e/\hbar\mathbf{B} \cdot \boldsymbol{\Omega}} \tag{2.49}$$

which is a function of $\mathbf{r}$ and $\mathbf{k}$ as $\mathbf{B} = \mathbf{B}(\mathbf{r})$ and $\boldsymbol{\Omega} = \boldsymbol{\Omega}(\mathbf{k})$. This results in a modified density of states. The Berry curvature can also modify the relaxation time if $\mathbf{B} \neq 0$ as the transition probability from $\mathbf{k}$ to k' also depends on the structure of Bloch wavefunction. All of these factors can drastically alter the magnetotransport in solids with non-zero Berry curvature.

Additionally, other perturbations like deformation in crystals or other slowing varying modifications in Hamiltonian can also give rise to anomalous transport in presence of Berry curvature. In fact, some of these external perturbations lead to modifications which introduce a time-derivative of Berry connection in semiclassical equation of motion and hence can be interpreted as an electric field analog in k space. We present one such scheme in our work in Chapter 1 and demonstrate that this electric field analog can be used to build a charge pump.

Non-linear response from quantum geometry

The effects arising from the magnetic field analog mentioned above require the breaking of time-reversal symmetry. However, as discussed earlier, it is possible to have non-zero Berry curvature profile even for TRS setups. One of the main questions that we pursue in this thesis is how to probe the quantum geometry of such systems. It has been shown in many previous works [238, 323] that quantum geometry effects are not limited to linear Hall response, but can also contribute to non-linear responses. Additionally, these band geometry signatures also reveal themselves in non-adiabatic processes involving excitations to different bands. The above two ideas naturally suggest that such quantum geometric signatures can also affect the optical responses like photocurrent, second-harmonic generation (SHG) etc. which has become the basis of new methods to reveal and harness the topological features of quantum materials [259, 217].

These quantum geometry induced non-linear responses can be broadly divided into two categories:

1. Low frequency regime: In this limit, the frequency of light is much smaller than gap and non-linear responses that come from intraband processes.
2. High frequency regime: In this limit, the frequency of EM field is comparable to gap and interband processes that dominate the non-linear response.

In both these limits, the magnitude of non-linear Hall coefficient is dictated by different quantum geometry-dependent terms. Let us first discuss the DC limit where a crystalline solid is exposed a weak EM field, $E(t) = \mathcal{E}e^{i\omega t} + \mathcal{E}^* e^{-i\omega t}$. It changes the occupation f of different k states and within the relaxation time approximation, the Boltzmann transport equation gives

$$f = f_0 + \tau \frac{eE_i}{\hbar} \frac{\partial f}{\partial k_i} - \tau \frac{\partial f}{\partial t}. \tag{2.50}$$

We are interested in second-order processes, so we can expand f up to second order: $f = f_0 + f_1 + f_2$ where $f_n \propto E^n$ and substituting in above equation

$$f_1 = f_1^{\omega} e^{i\omega t}, \;\; f_1^{\omega} = \frac{e\tau \mathcal{E}_i}{\hbar(1 + i\omega\tau)} \frac{\partial f}{\partial k_i} \tag{2.51}$$

$$f_2 = f_2^0 + f_2^{2\omega} e^{i2\omega t}, \;\; f_2^0 = \frac{(e\tau)^2 \mathcal{E}_i^* \mathcal{E}_j}{2\hbar^2(1 + i\omega\tau)} \frac{\partial^2 f}{\partial k_i \partial k_j}, \;\; f_2^{2\omega} = \frac{(e\tau)^2 \mathcal{E}_i \mathcal{E}_j}{2\hbar^2(1 + i\omega\tau)(1 + 2i\omega\tau)} \frac{\partial^2 f}{\partial k_i \partial k_j}. \tag{2.52}$$

Now, the electric current density in a d-dimensional solid is given by

$$j_i = -e \int \frac{d^d k}{(2\pi)^d} f(\mathbf{k}) v_i(\mathbf{k}) \tag{2.53}$$

where v_i is the physical velocity of Bloch electron with momentum k and it includes both the group velocity and the anomalous velocity, i.e

$$v_i(\mathbf{k}) = \frac{1}{\hbar}\frac{\partial \varepsilon(\mathbf{k})}{\partial k_i} + \epsilon_{ijl}\frac{e}{\hbar}\Omega_j E_l. \tag{2.54}$$

Using Eqs. 2.51-2.54, we can write current $j_i = \mathrm{Re}\left(j_a^0 + j_a^{2\omega}e^{2i\omega t}\right)$ where

$$\begin{aligned} j_i^0 &= \frac{e^2}{2\hbar}\int \frac{d^dk}{(2\pi)^d}\epsilon_{ijl}\Omega_j\mathcal{E}_l^* f_1^\omega - e\int \frac{d^dk}{(2\pi)^d}\frac{f_2^0}{\hbar}\frac{\partial\varepsilon(\mathbf{k})}{\partial k_i} \\ j_i^{2\omega} &= \frac{e^2}{2\hbar}\int \frac{d^dk}{(2\pi)^d}\epsilon_{ijl}\Omega_j\mathcal{E}_l f_1^\omega - e\int \frac{d^dk}{(2\pi)^d}\frac{f_2^{2\omega}}{\hbar}\frac{\partial\varepsilon(\mathbf{k})}{\partial k_i} \end{aligned} \tag{2.55}$$

where j_i^0 is the DC response and $j_i^{2\omega}$ is the second-harmonic. As we can see, there are two contributions to both components. The first-one depends on Berry curvature, and the second one is coming from the band dispersion. Now, within RTA, f_2^0 and $f_2^{2\omega}$ are both proportional to $\partial^2 f/(\partial k_i \partial k_j)$, and thus the second term in the above equation is odd under time reversal. Therefore, the second-order contributions to current density are purely dependent on Berry curvature and by expressing $j_i^0 = \chi_{\mathrm{ijl}}\mathcal{E}_j\mathcal{E}_l^*$, $j_i^{2\omega} = \chi_{\mathrm{ijl}}\mathcal{E}_j\mathcal{E}_l$ where

$$\chi_{\mathrm{ijl}} = \epsilon_{\mathrm{iml}}\frac{e^3\tau}{2\hbar^2(1+i\omega\tau)}\int \frac{d^dk}{(2\pi)^d}\frac{\partial f_0}{\partial k_j}\Omega_m = -\epsilon_{\mathrm{iml}}\frac{e^3\tau}{2\hbar^2(1+i\omega\tau)}\int \frac{d^dk}{(2\pi)^d}D_{jm}f_0 \tag{2.56}$$

where the quantity $D_{jm} = \frac{\partial\Omega_m}{\partial k_j}$ is a Berry curvature dependent quantity known as Berry curvature dipole. This contribution to second-order conductivity is mainly a Fermi surface property because of the presence of $\partial f_0/\partial k_j$, and hence vanishes when the Fermi level lies in a gap. This expression is valid only for small frequencies as we have ignored the EM field induced transitions. It is evident from the form of χ_{ijl}, that for a linearly polarized field, the current density has to be perpendicular to the direction of E field. As a result, this contribution can be interpreted as non-linear Hall response arising from Berry curvature dipole and has been recently observed in TMD bilayers [218]. However, this effect does not rely on the breaking of time-reversal symmetry, but Berry curvature dipole can be non-zero only if certain spatial symmetries are broken [323]. In two-dimensions, the largest symmetry that allows this effect is a single mirror line, and thus in certain materials like graphene it can be induced by applying a unaxial strain which reduces its symmetry. Additionally such non-linear effects can be generalized to higher-order processes which depends on Berry curvature quadrupole or its higher moments.

So far, the band geometry effects mentioned above were limited to ground-state properties where the band population remained constant. Now, we investigate how these band geometry signatures can affect the non-linear optical responses arising from band transitions. In intraband processes considered so far, the quantum geometry comes into picture because the structure of Bloch wavefunction is dependent on the k value. Similarly, when an electron is excited from one band to another, the structure of Bloch wavefunctions would be different in two bands and that can result in a real-space shift in the center of Bloch wavepacket. Next, we attempt to understand how this behavior can be understood in terms of different quantum geometric quantities.

The derivations below are based on Ref. [266, 317]

For the purpose of this section, we use independent particle approach which neglects electron-electron interaction. We can thus focus on each k state separately and study its dynamics in the presence of an EM field. In a static setup, the dynamics of a Bloch electron with momentum k is governed by Bloch Hamiltonian $H_0(\mathbf{k})$. When it is irradiated with light, within the minimal coupling approximation, its dynamics is described by the time-dependent Hamiltonian

$$H(\mathbf{k},t) = H_0\left(\mathbf{k} - \frac{e}{\hbar}\boldsymbol{\mathcal{A}}(t)\right) \tag{2.57}$$

where we have used the velocity gauge to incorporate the effects of the EM field and $\boldsymbol{\mathcal{A}}$ is the vector-potential associated with this field. Now, treating the EM part as a perturbation, we can write this time-dependent Hamiltonian as a Taylor series

$$H(\mathbf{k},t) = H_0(\mathbf{k}) + \frac{e}{\hbar}\boldsymbol{\mathcal{A}}(t)\cdot\nabla_{\mathbf{k}}H_0 + \frac{e^2}{2\hbar^2}\boldsymbol{\mathcal{A}}(t)\cdot\nabla_{\mathbf{k}}\left(\boldsymbol{\mathcal{A}}(t)\cdot\nabla_{\mathbf{k}}H_0\right) + .. \tag{2.58}$$

$$H(\mathbf{k},t) = H_0(\mathbf{k}) + \frac{e}{\hbar}\mathcal{A}^i(t)\partial_i H_0 + \frac{e^2}{2\hbar^2}\mathcal{A}^i(t)\mathcal{A}^j(t)\partial_i(\partial_j H_0) + .. \tag{2.59}$$

where $\partial_i = \partial/\partial k_i$. Although, at first it might seem that the above expression has nothing to do with quantum geometric quantities, but they are hidden in the velocity expression

$$\left\langle u_m\middle|\frac{\partial H_0}{\partial k_i}\middle|u_n\right\rangle = \frac{\partial\varepsilon_m}{\partial k_i}\delta_{mn} + (\varepsilon_m-\varepsilon_n)\left\langle u_m\middle|\frac{\partial u_n}{\partial k_i}\right\rangle = \frac{\partial\varepsilon_m}{\partial k_i}\delta_{mn} - i(\varepsilon_m-\varepsilon_n)A^i_{mn} \tag{2.60}$$

where $|u_\alpha\rangle$ are the cell-periodic part of Bloch wavefunctions (eigenstates of $H_0(\mathbf{k})$) and $\mathbf{A}_{mn} = i\langle u_m|\nabla_{\mathbf{k}}u_n\rangle$ is the Berry connection between m^{th} and n^{th} bands. This is a very interesting result and in fact can be generalized to any operator O

$$\left\langle u_m|\frac{\partial O}{\partial k_i}|u_n\right\rangle = \frac{\partial O_{mn}}{\partial k_i} - i\left[\mathbf{A^i}, O\right]_{mn} \tag{2.61}$$

where $O_{mn} = \langle u_m | O | u_n \rangle$ and $\mathbf{A}^i$ is the Berry connection matrix with its elements, $A^i_{mn} = i \left\langle u_m | \partial/\partial_{k_i} u_n \right\rangle$. Now, getting back to the Hamiltonian, we use a short-hand expression to write down the derivatives of Hamiltonian as follows

$$h^i = \frac{\partial H_0}{\partial k_i}, \ h^{ij} = \frac{\partial}{\partial k_i}\left(\frac{\partial H_0}{\partial k_j}\right), \ h^{ijm} = \frac{\partial}{\partial k_i}\left(\frac{\partial}{\partial k_j}\left(\frac{\partial H_0}{\partial k_m}\right)\right). \tag{2.62}$$

It simplifies Eq. 2.59 to

$$H(\mathbf{k},t) = H_0(\mathbf{k},t) + \frac{e}{\hbar}\mathcal{A}^i(t) h^i + \frac{e^2}{2\hbar^2}\mathcal{A}^i(t)\mathcal{A}^j(t) h^{ij} + .. = H_0 + V_E(t) \tag{2.63}$$

and the new velocity operator for the full Hamiltonian is now given by:

$$v^i_E(t) = \frac{\partial H_0}{\partial k_i} + \frac{\partial V_E(t)}{\partial k_i} = h^i + \frac{e}{\hbar} h^{ij}\mathcal{A}^j(t) + \frac{e^2}{2\hbar^2} h^{ijk}\mathcal{A}^j(t)\mathcal{A}^k(t) + ... \tag{2.64}$$

Now, for EM field , we can use $A(t) = \int d\omega e^{-i\omega t} A(\omega)$ and electric field $\mathbf{E}(\omega) = i\omega\boldsymbol{\mathcal{A}}(\omega)$ to rewrite

$$H(\mathbf{k},t) = \sum_{n=0}^{\infty} \frac{1}{n!}\left(\prod_{j=1}^{n} \int d\omega_j e^{i\omega_j t}\left(\frac{e}{\hbar\omega_j}\right) E^{\alpha_j}(\omega_j)\right) h^{\alpha_1\alpha_2\ldots\alpha_n} \tag{2.65}$$

$$v^{\mu}_E(t) = \sum_{n=0}^{\infty} \frac{1}{n!}\left(\prod_{j=1}^{n} \int d\omega_j e^{i\omega_j t}\left(\frac{e}{\hbar\omega_j}\right) E^{\alpha_j}(\omega_j)\right) h^{\mu\alpha_1\alpha_2\ldots\alpha_n}. \tag{2.66}$$

It is important to note that the EM field induced perturbation also introduces an explicit time-dependence in the velocity operator. We can now use these above expressions to calculate the current density which in this case can be expanded as

$$\left\langle \mathbf{J}^i \right\rangle(\omega) = \int d\omega_1 \sigma^i_j(\omega;\omega_1) E^j(\omega_1) + \int d\omega_1 d\omega_2 \sigma^i_{jm}(\omega;\omega_1,\omega_2) E^j(\omega_1) E^m(\omega_2) + ... \tag{2.67}$$

The partition function of the perturbed system c

$$\mathcal{Z}(\mathbf{E}) = \int \mathcal{D}c^{\dagger}\mathcal{D}c e^{-i\int H_A(t)dt'} \tag{2.68}$$

$$H_A(t) = \int [d\mathbf{k}] c^{\dagger}(\mathbf{k},t) H_0 c(\mathbf{k},t) + c^{\dagger}(\mathbf{k},t) V_E(t) c(\mathbf{k},t) \tag{2.69}$$

and the expectation value of current density can be obtained from

$$\left\langle J^i \right\rangle(t) = \frac{1}{\mathcal{Z}} \mathrm{Tr}\left[\mathcal{T} e v^i_E(t) e^{-i\int H_E(t')dt'}\right], \tag{2.70}$$

which can be used to calculate conductivity tensor in terms of functional derivatives

$$\sigma^{\mu}_{\alpha_1..\alpha_n} = \int \frac{dt}{2\pi} e^{i\omega t} \prod_{j=0}^{j=n} \frac{dt_j}{2\pi} e^{i\omega_j t_j} \frac{\partial}{\partial E^{\alpha_k}} \left\langle J^{\mu} \right\rangle(t) \Big|_{\mathbf{E}=0}. \tag{2.71}$$

This expression can be evaluated by using Feynman diagrams where we treat the photon as a classical background without any dynamics and the electron propagator is that of the free fermion. We ignore scattering and any other non-equilibriun processes like exciton formation. Within this simplified picture (more details of this calculation can be found in Ref. [266]), the second-order conductivity comes out to be

$$\begin{aligned}\sigma^{\mu}_{\alpha\beta}(\omega_Z,\omega_1,\omega_2) = -\frac{e^3}{\hbar^2\omega_1\omega_2}\sum_{a,b,c}\int d\mathbf{k}\, &\frac{1}{2}f_a h^{\mu\alpha\beta}_{aa} + \frac{1}{2}f_a h^{\mu\beta\alpha}_{aa} + f_{ab}\frac{h^{\alpha}_{ab}h^{\mu\beta}_{ba}}{\omega_1 + i\eta - \varepsilon_{ab}} \\ &+ f_{ab}\frac{h^{\beta}_{ab}h^{\mu\alpha}_{ba}}{\omega_2 + i\eta - \varepsilon_{ab}} + \frac{1}{2}f_{ab}\frac{h^{\alpha\beta}_{ab}h^{\mu}_{ba}}{\omega_Z + i\eta - \varepsilon_{ab}} + \frac{1}{2}f_{ab}\frac{h^{\beta\alpha}_{ab}h^{\mu}_{ba}}{\omega_Z + i\eta - \varepsilon_{ab}} \\ &+ \frac{h^{\alpha}_{ab}h^{\beta}_{bc}h^{\mu}_{ca}}{\omega_Z + i\eta - \varepsilon_{ca}}\left[\frac{f_{ab}}{\omega_1 + i\eta - \varepsilon_{ba}} + \frac{f_{cb}}{\omega_2 + i\eta - \varepsilon_{cb}}\right] \\ &+ \frac{h^{\beta}_{ab}h^{\alpha}_{bc}h^{\mu}_{ca}}{\omega_Z + i\eta - \varepsilon_{ca}}\left[\frac{f_{ab}}{\omega_2 + i\eta - \epsilon_{ba}} + \frac{f_{cb}}{\omega_1 + i\eta - \varepsilon_{cb}}\right].\end{aligned} \tag{2.72}$$

It can be further simplified to

$$\begin{aligned}\sigma^{\mu}_{\alpha\beta}(0,\omega,-\omega) = \frac{e^3}{\hbar^2\omega^2}\sum_{a,b,c}\int d\mathbf{k}\, &\frac{1}{2}f_a h^{\mu\alpha\beta}_{aa} + \frac{1}{2}f_a h^{\mu\beta\alpha}_{aa} + f_{ab}\frac{h^{\alpha}_{ab}h^{\mu\beta}_{ba}}{\omega_1 + i\eta - \varepsilon_{ab}} \\ &+ f_{ab}\frac{h^{\beta}_{ab}h^{\mu\alpha}_{ba}}{\omega_2 + i\eta - \varepsilon_{ab}} + \frac{1}{2}f_{ab}\frac{h^{\alpha\beta}_{ab}h^{\mu}_{ba}}{\omega_Z + i\eta - \varepsilon_{ab}} + \frac{1}{2}f_{ab}\frac{h^{\beta\alpha}_{ab}h^{\mu}_{ba}}{\omega_Z + i\eta - \varepsilon_{ab}} \\ &+ \frac{2\pi e^3}{\hbar^2}\int [d\mathbf{k}] f_{ab}|\mathbf{A}^{\alpha}_{ab}|^2\mathbf{S}^{\mu\alpha}_{ba}\delta(\omega - \epsilon_{ab})\end{aligned} \tag{2.73}$$

where $\mathbf{S}^{\mu\alpha}_{mn} = \mathbf{A}^{\mu}_{mm} - \mathbf{A}^{\mu}_{nn} - \partial_{\mu}(\mathrm{Arg}\mathbf{A}^{\alpha}_{mn})$ is the shift-vector and $\mathbf{A}_{mn}$ is the interband Berry connection. For a system described by a Hamiltonian linear in k, the shift-vector contribution is the only contribution that survives and the resulting current is know as shift-current. This shift-current has been at the center of attention as it provides an opportunity to harness quantum geometric effects to generate DC photocurrent from a linearly polarized EM field. Additionally, this shift-vector is a very interesting gauge-invariant quantum geometric quantity which captures the change in Bloch wavefunction when an electron is excited from one band to another. It can be non-zero even in a TRS system. In this case, we focused on a Hamiltonian perturbed by EM field, but it can be generalized to any form of perturbation as we show in Chapter 4 where we consider an oscillating sublattice energy offset in a graphene lattice. Furthermore, this quantity becomes very important when the size of real space unit cell is increased and hence can result in large second-order conductivity for moiré systems which we investigate in Chapter 5.

Berry phase effects on excitons

In previous subsections, we discussed how the quantum geometry of Bloch bands can affect the single-particle charge transport and optical responses within the independent electron picture. We neglected all electron-electron and electron-phonon interactions and thus also ignored any quasiparticle corrections and effects arising from collective excitations. The effects of QGT are not limited to single-particle transport and can have important consequences for excitons and plasmons as well [327, 191, 329, 406]. In the first part, we are interested in effects of QGT in band transition processes so we briefly the discuss the signatures of QGT in excitonic properties. Let us first consider the exciton spectra. The effective Hamiltonian for excitons is decided by the energy dispersion of bands involved in the formation of electron-hole bound pairs and Coulombic interactions between them. We have already seen that Berry curvature can affect the anomalous velocity of electrons in Bloch bands so thus including the structure of Bloch wavefunctions can alter the effective Hamiltonian for excitons. Below, we investigate how Berry curvature of underlying single-particle Bloch bands can affect the properties of excitons. There are many different approaches to incorporate the effect of Berry curvature on excitons. The most straighforward manifestation can be seen in Bethe-Salpeter equation for exciton wavefunction. For a two-band model, the excitonic wavefunction can be simply expressed as $\sum_{\mathbf{k}} C^n(\mathbf{k}) a^{\dagger}_{c,\mathbf{k}} a_{v,\mathbf{k}} |0\rangle = C^n(\mathbf{k}) |\mathbf{k}\rangle$ where $\mathbf{k}\rangle$ with $a_{c(v),\mathbf{k}}$ being the annihilation operator for a Bloch electron with wavefunction $\left|u_{c(v}(\mathbf{k})\right\rangle$ in the conduction (valence) band and $|0\rangle$ is the semiconductor vacuum. We have ignored intraband contributions. Now, the amplitudes $C^n(\mathbf{k})$ can be obtained by solving the eigenvalue equation $\sum_{\mathbf{k}'} \langle \mathbf{k}|H_0 + U|\mathbf{k}'\rangle C^n(\mathbf{k}') = \mathcal{E}^n C^n(\mathbf{k}')$ where $\langle \mathbf{k}|H_0|\mathbf{k}'\rangle = \delta_{\mathbf{k},\mathbf{k}'} (\varepsilon^c(\mathbf{k}) - \varepsilon^v(\mathbf{k}))$ which takes the following form

$$\varepsilon^{cv}(\mathbf{k}) C^n(\mathbf{k}) - \sum_{\mathbf{k}'} U(\mathbf{k}-\mathbf{k}') \langle u_c(\mathbf{k})|u_c(\mathbf{k}')\rangle \langle u_v(\mathbf{k})|u_v(\mathbf{k}')\rangle C^n(\mathbf{k}') = \mathcal{E}^n C^n(\mathbf{k}) \tag{2.74}$$

where $\varepsilon^{cv}(\mathbf{k}) = \varepsilon^c(\mathbf{k}) - \varepsilon^v(\mathbf{k})$ and $U(\mathbf{k}-\mathbf{k}') = \int d\mathbf{r}_e d\mathbf{r}_h\, U(\mathbf{r}_e - \mathbf{r}_h) e^{i(\mathbf{k}-\mathbf{k})\cdot(\mathbf{r}_e-\mathbf{r}_h)}$. We notice that Bloch wavefunctions are present in the second term in above equation and hence the Berry curvature of the single-particle Bloch bands can modify the properties of exciton. This equation can be solved numerically for any arbitrary dispersion and Berry curvature profile. However, in order to illustrate the consequences of Berry curvature, we can use a much simpler equation where we treat Berry curvature as k space magnetic field.

Let us consider an electron-hole pair interacting via Coulombic potential. If we assume a PH symmetric band structure and approximate the electron hole dispersion as quadratic in the vicinity of the band minima, the effective Hamiltonian for electron-hole pair can be written as:

$$H_{\text{eff}} = \frac{k^2}{2\mu} + U(\mathbf{r}_e - \mathbf{r}_h) \tag{2.75}$$

where μ is the reduced mas and $\mathbf{k} = \mathbf{k}_e = -\mathbf{k}_h$. Now, if we have finite Berry curvature (magnetic field in k space), then

$$H_{\text{eff}}(\mathbf{k}, \mathbf{r}_e, \mathbf{r}_h) \longrightarrow H_{\text{eff}}(\mathbf{k}, \mathbf{r}_e - \mathbf{A}^c(\mathbf{k}), \mathbf{r}_h - \mathbf{A}^v(\mathbf{k})) \tag{2.76}$$

where $\mathbf{A}^{c(v)}(\mathbf{k})$ is the Berry connection (vector potential analog) for Bloch electrons in conduction (valence) band. Here, we exploited the analogy with real space magnetic field whose effects are incorporated in the Hamiltonian by shifting $\mathbf{k} \rightarrow \mathbf{k} - e/\hbar\mathcal{A}$ where $\mathcal{A}$ is the vector potential associated with real space magnetic field. For simplicity, let us focus on a two-dimensional systems and consider a constant Berry curvature (exciton properties are decided by the dispersion at band minimas and these points also happen to be Berry curvature hotspots which changes very slowly around such points) which can be obtained from a vector potential $\mathbf{k} \times \Omega$. Now, we can express

$$H_{\text{eff}} = \frac{k^2}{2\mu} + U(\mathbf{r}_e - \mathbf{r}_h) + \frac{1}{2\hbar}(\mathbf{\Omega} \times \mathbf{k}) \cdot \nabla U + .., \tag{2.77}$$

where $\mathbf{\Omega} = \mathbf{\Omega}^c - \mathbf{\Omega}^v$. Clearly, there is an extra term in this Hamiltonian which gives rise to non-hydrogenic features. In this particular case, it lifts the degeneracy of exciton states with opposite angular momentum. This kind of physics can be realized in TMD monolayers where gapped Dirac points are Berry curvature hotspots. This non-zero Berry curvature results in valley-dependent splitting of exciton states with opposite orbital angular momentum [329, 406, 10, 138].

In addition to exciton spectra, Berry curvature can also affect the exciton dynamics. In the semiclassical picture, we can describe the dynamics of bounds electron and hole pair by the following equations:

$$\dot{\mathbf{k}}_{e/h} = -\nabla_{\mathbf{r}_{e/h}} U(\mathbf{r}_e - \mathbf{r}_h) + \mathbf{F}^{\text{ext}}_{e/h} \tag{2.78}$$

$$\dot{\mathbf{r}}_{e/h} = \partial_{\mathbf{k}_{e/h}} \varepsilon_{e/h}(\mathbf{k}_{e/h}) - \dot{\mathbf{k}}_{e/h} \times \mathbf{\Omega}^{c/v}_{e/h} \tag{2.79}$$

where e/h refers to electron and hole, respectively, $U(\mathbf{r}_e - \mathbf{r}_h)$ is the interaction potential, and $\varepsilon_{e/h}(\mathbf{k}_{e/h})$ is the dispersion of electron/hole band. In terms of relative and center-of-mass (COM) coordinates, it becomes

$$\dot{\mathbf{k}} = -\nabla_{\mathbf{r}} U(\mathbf{r}) + \frac{1}{2}(\mathbf{F}^{\text{ext}}_e - \mathbf{F}^{\text{ext}}_h),\ \dot{\mathbf{K}} = \dot{\mathbf{k}}_e + \dot{\mathbf{k}}_h = \mathbf{F}^{\text{ext}}_e + \mathbf{F}^{\text{ext}}_h \tag{2.80}$$

$$\dot{\mathbf{r}} = \partial_{\mathbf{k}_e} \varepsilon_e(\mathbf{k}_e) - \partial_{\mathbf{k}_h} \varepsilon_h(\mathbf{k}_h) - \dot{\mathbf{k}}_e \times \mathbf{\Omega}^c_e(\mathbf{k}_e) + \dot{\mathbf{k}}_h \times \mathbf{\Omega}^v_h(\mathbf{k}_h) \tag{2.81}$$

$$\dot{\mathbf{R}} = \frac{\partial_{\mathbf{k}_e} \varepsilon_e(\mathbf{k}_e) + \partial_{\mathbf{k}_h} \varepsilon_h(\mathbf{k}_h)}{2} - \dot{\mathbf{k}}_e \times \frac{\mathbf{\Omega}^c_e(\mathbf{k}_e)}{2} - \dot{\mathbf{k}}_h \times \frac{\mathbf{\Omega}^v_h(\mathbf{k}_h)}{2} \tag{2.82}$$

where $\mathbf{k}(\mathbf{K})$ and $\mathbf{r}(\mathbf{R})$ are relative (C.O.M) momentum and position of the exciton. If we consider the usual PH symmetric two-band picture where the Berry curvature of Bloch electrons in conduction and valence band is opposite, i.e $\mathbf{\Omega}^c_e(\mathbf{k}_e) = -\mathbf{\Omega}^v_e(\mathbf{k}_e)$ which corresponds to $\mathbf{\Omega}^c_e(\mathbf{k}_e) = \mathbf{\Omega}^v_h(-\mathbf{k}_e)$, then the above equation reduces to

$$\dot{\mathbf{r}} = \partial_{\mathbf{k}_e} \varepsilon_e(\mathbf{k}_e) - \partial_{\mathbf{k}_h} \varepsilon_h(\mathbf{k}_h) - 2\dot{\mathbf{k}} \times \mathbf{\Omega}^c_e(\mathbf{k}_e) \tag{2.83}$$

$$\dot{\mathbf{R}} = \frac{\partial_{\mathbf{k}_e} \varepsilon_e(\mathbf{k}_e) + \partial_{\mathbf{k}_h} \varepsilon_h(\mathbf{k}_h)}{2} - \dot{\mathbf{K}} \times \frac{\mathbf{\Omega}^c_e(\mathbf{k}_e)}{2}. \tag{2.84}$$

It shows that if the electron and hole part experience an opposite force (which is the case for an electric field or internal restoring force), the anomalous velocity affects only relative motion which manifests as non-hydrogenic features in exciton spectra. On the other hand, a net force on exciton COM can give rise to anomalous drift of exciton. This kind of force can arise for example in the presence of a non-uniform electric field which couples to the dipole moment of the exciton. It can lead to quantized anomalous valley Hall effect of excitons in non-centrosymmetric two-dimensional materials in the absence of magnetic field [184].

With the ever-expanding field of highly controllable two-dimensional quantum materials, we can engineer different kinds of band structures and can even realize a situation where the conduction minima and valence band maxima have the same sign for Berry curvature. Now, we can ask what happens if the Berry curvature of conduction and valence band is not opposite. As evident from Eq. 6.5, it can result in an anomalous drift of exciton COM even when the net force on COM is zero. This offers a possibility of manipulating a neutral particle with uniform electric field. However, this kind of force which acts oppositely on electron and hole part is counteracted by the restoring force arising from electron-hole interaction potential. The interplay of these forces is dictated by bandwidth, strength and nature of interactions, exciton binding energy, size of the Brillouin zone, etc. We investigate this dependence and explore the possibility and conditions necessary to observe this effect in two-dimensional materials. We study the dynamics of excitons using both a semiclassical and a full quantum mechanical analysis in a toy model in [64]. Our simulations indicate that twisted TMD heterobilayers can possibly provide an ideal platform to study the anomalous drift of excitons at reasonably small E fields without breaking them apart. This kind of neutral particle transport in presence of a uniform electric field can offer a possibility to get a thermoelectric transport with a very large thermopower.

2.3 Practical advantages of QG effects

Quantum geometry concepts not only transformed our understanding of electronic properties of solids, but are also paving the way for next generation quantum technology. These geometric effects allow many unconventional phenomena like persistent spin currents [215], dissipationless quantum transport [136], fractional statistics [367], chiral anomaly [408], etc. which are very advantageous for new quantum technologies. The signatures of band geometry in optical responses have lead to many astounding results like giant NLOR [374, 260], large anomalous Hall effect [125, 250], and are also finding advantages in photovoltaics [79]. Most of these effects occur in graphene or TMD bilayers and can be tuned by modifying the encapsulation environment or by applying external perturbations like strain [326, 389, 244, 206, 164] or electric field [383] which make them very promising for new technologies. These effects are even more pronounced for moiré materials [13] where the energy-momentum dispersion is almost flat and the real space unit cell is many times larger than conventional crystalline solids. These quantum geometry effects can have important consequences for non-adiabatic processes in such setups which are not that well studied yet. Additionally, the effects of interactions on quantum geometric features can be very prominent for moiré systems which makes it even more important to study different manifestations of quantum geometry in these systems.

Chapter 3

ULTRAFAST CONTROL OF QUANTUM MATTER

“I am one of those who think like Nobel, that humanity will draw more good than evil from new discoveries.”– Marie Curie

In the second part of this thesis, we study photo-induced phenomena with an aim to develop efficient driving schemes to manipulate the properties of quantum materials. The past decade has witnessed an explosion in the field of quantum materials [110]. The ever-expanding zoo of these materials along with their inexhaustible versatility heralds promises of more efficient and novel quantum technologies. In order to harness this immense potential, it is imperative to develop an in-depth understanding of their behavior and control their properties with unprecedented precision. In fact, it has become a central goal of modern condensed-matter physics to discover new pathways to manipulate these quantum materials. Using light-matter interactions to coherently control different properties of these materials is emerging as one such promising route [1, 21, 356]. Until very recently, the coherent manipulation of quantum systems with light was limited to the realms of atomic, molecular, and optical physics. New developments in the field of lasers and spectroscopy techniques are now paving the way for using light-matter interactions to manipulate quantum materials at ultrafast time-scales [41].

Light induced changes in solids can be either thermal like simple melting of thermal states by laser-induced heating or non-thermal like carrier excitations between different bands, coherent resonant excitation of collective lattice or charge density vibrations, dynamical modification of hopping parameters, etc. One particular class of non-thermal phenomena which can be described by a time-periodic perturbation has garnered significant attention in last few years. These phenomena occur only when the drive is switched on, and arise from the coherent dressing of quantum states by the EM field. This kind of periodic drive has been used extensively for coherent manipulation of quantum many-body systems realized with ultracold atomic gases in optical lattices. These methods have proved immensely successful in achieving precise control of these systems and also in experimental realization of systems without any equilibrium counterparts. However, it is only with the advent of more powerful lasers and spectroscopy techniques, such methods are gaining popularity in solid-state systems [399, 257]. This periodic drive-based approach to coherently manipulate the properties of a system is known as Floquet engineering. Below, we briefly review the theory and some well-established examples of Floquet engineering.

3.1 Floquet engineering

Floquet engineering has been touted as a very powerful technique for coherent control of quantum many-body systems. In the last decade, it has been used extensively to manipulate quantum matter in optical lattices [89]. It has been invoked in a variety of contexts like achieving dynamical localization [91], engineering artificial gauge fields for neutral atoms [243, 149, 332, 9], demonstrating dynamical phase transitions [397], and most successfully in realizing topological phases like the Haldane model with no equilibrium counterparts [155].

Floquet engineering theory

Consider a time-periodic Hamiltonian

$$H(t+T) = H(t) \tag{3.1}$$

with $T = 2\pi/\omega$, which can also be expressed in terms of its Fourier components

$$H(t) = \sum_m e^{im\omega t} H_m. \tag{3.2}$$

According to Floquet theorem, any solution of the Schrodinger equation, $i\partial_t |\Psi_t\rangle = H(t)|\Psi(t)\rangle$, for the above Hamiltonian can be decomposed into orthogonal solutions of the form:

$$|\Psi(t)\rangle = e^{-i\varepsilon_\alpha t} |\Phi_\alpha(t)\rangle \tag{3.3}$$

with $|\Phi_\alpha(t)\rangle = |\Phi_\alpha(t+T)\rangle$ which allows us to expand

$$|\Phi_\alpha(t)\rangle = \sum_m e^{im\omega t} \left|\Phi_\alpha^m\right\rangle \tag{3.4}$$

which satisfy

$$\sum_m (H_{n-m} - m\omega\delta_{mn}) \left|\Phi_\alpha^m\right\rangle = \varepsilon_\alpha \left|\Phi_\alpha^n\right\rangle. \tag{3.5}$$

We can thus treat this driven system in a time-independent manner by treating the temporal degree of freedom as an extra degree of freedom which now extends the Hilbert space to $\mathcal{H} \otimes \mathcal{T}$ also known as Sambe space, where $\mathcal{H}$ is the original Hilbert space of the system and $\mathcal{T}$ is the infinite-dimensional Hilbert space associated with the photon degree of freedom. In this new basis, we can express

$$||\Phi_\alpha(t)\rangle\rangle = \sum_m \left|\Phi_\alpha^m\right\rangle \otimes |m\rangle \tag{3.6}$$

with $\langle t|m\rangle = e^{im\omega t}$ which is now an eigenstate of

$$H = \begin{bmatrix} \ddots & \vdots & \vdots & \vdots & \vdots & \iddots \\ \dots & H_0+\omega & H_1 & H_2 & H_3 & \dots \\ \dots & H_{\bar{1}} & H_0 & H_1 & H_2 & \dots \\ \dots & H_{\bar{2}} & H_{\bar{1}} & H_0-\omega & H_1 & \dots \\ \iddots & \vdots & \vdots & \vdots & \vdots & \ddots \end{bmatrix} \tag{3.7}$$

with eigenvalue ε_α. Now, if we consider the state $|\Phi_\alpha(t+nT)\rangle$ for an integer n,

$$|\Phi_\alpha(t+nT)\rangle = \sum_m \left|\Phi_\alpha^m\right\rangle \otimes |m+n\rangle \tag{3.8}$$

which is an eigenstate of above Hamiltonian with eigenvalues $\varepsilon_\alpha - n\omega$. This periodicity in temporal degree of freedom translates to a quasi-periodicity in energy spectrum. This shows that in analogy with the Brillouin zone encountered in spatially-periodic Hamiltonian, we can define a concept of Floquet zone where the energies between two different Floquet zones differ by an integer multiple of ω and eigenstates are identical in the original Hilbert space of the static Hamiltonian.

Given, the translational symmetry of this Hamiltonian in temporal degree of freedom, it can be diagonalised and re-expressed as

$$H = \begin{bmatrix} \ddots & & & & \\ & H_F+\omega & & & \\ & & H_F & & \\ & & & H_F-\omega & \\ & & & & \ddots \end{bmatrix} \tag{3.9}$$

The time-evolution operator within a period can then be described as

$$U(T,0) = e^{-iH_F T} \tag{3.10}$$

where H_F is known as Floquet Hamiltonian.

We can think that the system now evolves according to the effective time-independent Hamiltonian H_F which can be very different from the static Hamiltonian. Its properties can be tuned by changing the drive parameters which allows us to modify and control the band topology, magnetic properties, etc. with a periodic drive. In certain cases, we can also realize models which have no counterparts in equilibrium systems.

Having discussed the basics of Floquet engineering, we can now ask how to calculate this effective Hamiltonian for a given system. In most general cases, it cannot be solved analytically, so we use numerical diagnolization of this full Hamiltonian truncated at some $n = \pm N$. However, in the limit of high frequency, where different photon sectors are well separated in energy, we can use van Vleck's perturbation theory to evaluate the effective Hamiltonian which gives

$$H_{\text{eff}} = H_0 + \sum_{m\neq 0}\left(\frac{[H_{\bar{m}}, H_m]}{2m\omega} + \frac{[[H_{\bar{m}}, H_0], H_m]}{2m^2\omega^2} + \sum_{n\neq 0,m}\frac{[[H_{\bar{m}}, H_{m-n}], H_n]}{3mn\omega^2}\right) + O\left(\frac{1}{\omega^3}\right). \tag{3.11}$$

In this thesis, we focus on engineering band topology and magnetic interactions with a periodic drive. For the first case, we can choose a generic non-interacting Hamiltonian which is periodic in both space and time, and for the second case we focus on a one-dimensional spin chains with on-site Coulombic interactions. Before, going into the details of the two systems of interest described above, let us consider a simple example of a driven system which can be solved analytically.

Example: Driven two-level system with Floquet formalism

We consider the well-established example of a driven two-level system which can be solved analytically in certain limits like RWA. We investigate this model using Floquet formalism which also provides some intuition about the role of counter rotating terms. This model can be described by the following Hamiltonian:

$$H = \frac{\Delta}{2}\sigma_z + 2A_x \cos\omega t \sigma_x + 2A_y \cos(\omega t - \phi)\sigma_y \tag{3.12}$$

where σ s are the three Pauli matrices for $|\uparrow\rangle$ and $|\downarrow\rangle$which in matrix-form becomes

$$\begin{aligned} H = \sum_m \left(\frac{\Delta}{2}\sigma_z + m\omega\mathbb{I}\right) |m\rangle \langle m| &+ (A_x\sigma_x + A_y e^{i\phi}\sigma_y)\big(\,|m\rangle \langle m+1|\,\big) \\ &+ (A_x\sigma_x + A_y e^{-i\phi}\sigma_y)\,(|m\rangle \langle m-1|) \end{aligned} \tag{3.13}$$

$$H = \begin{bmatrix} \ddots & \vdots & \vdots & \vdots & \vdots & \vdots & \vdots & \iddots \\ \cdots & \frac{\Delta}{2}+\omega & 0 & 0 & A_x - iA_y e^{-i\phi} & 0 & 0 & \cdots \\ \cdots & 0 & \frac{-\Delta}{2}+\omega & A_x + iA_y e^{-i\phi} & 0 & 0 & 0 & \cdots \\ \cdots & 0 & A_x - iA_y e^{i\phi} & \frac{\Delta}{2} & 0 & 0 & 0 & \cdots \\ \cdots & A_x + iA_y e^{i\phi} & 0 & 0 & -\frac{\Delta}{2} & A_x + iA_y e^{-i\phi} & 0 & \cdots \\ \cdots & 0 & 0 & 0 & A_x - iA_y e^{i\phi} & \frac{\Delta}{2}-\omega & 0 & \cdots \\ \cdots & 0 & 0 & A_x + iA_y e^{i\phi} & 0 & 0 & -\frac{\Delta}{2}-\omega & \cdots \\ \iddots & \vdots & \vdots & \vdots & \vdots & \vdots & \vdots & \ddots \end{bmatrix} \tag{3.14}$$

where the basis is $(\dots, |\uparrow, 1\rangle, |\downarrow, 1\rangle, |\uparrow, 0\rangle, |\downarrow, 0\rangle, |\uparrow, -1\rangle, |\downarrow, -1\rangle, \dots)$. This is an infinite matrix, but can be solved numerically after truncating at some $n = \pm N$ according to the precision required. It can be solved analytically under some special conditions. If $A_x - iA_y e^{-i\phi} = 0$ or the detuning $|\omega - \Delta| \ll \omega, \left|A_x - iA_y e^{-i\phi}\right|^2 / \omega$, then we can use rotating wave approximation (RWA), whicj allows us to approximate the above Hamiltonian as a block diagonal matrix

$$H = \begin{bmatrix} \ddots & \vdots & \vdots & \vdots & \vdots & \vdots & \vdots & \iddots \\ \cdots & \frac{\Delta}{2}+\omega & 0 & 0 & 0 & 0 & 0 & \cdots \\ \cdots & 0 & \frac{-\Delta}{2}+\omega & A_x + iA_y e^{-i\phi} & 0 & 0 & 0 & \cdots \\ \cdots & 0 & A_x - iA_y e^{i\phi} & \frac{\Delta}{2} & 0 & 0 & 0 & \cdots \\ \cdots & 0 & 0 & 0 & -\frac{\Delta}{2} & A_x + iA_y e^{-i\phi} & 0 & \cdots \\ \cdots & 0 & 0 & 0 & A_x - iA_y e^{i\phi} & \frac{\Delta}{2}-\omega & 0 & \cdots \\ \cdots & 0 & 0 & 0 & 0 & 0 & -\frac{\Delta}{2}-\omega & \cdots \\ \iddots & \vdots & \vdots & \vdots & \vdots & \vdots & \vdots & \ddots \end{bmatrix} \tag{3.15}$$

$$H = \begin{bmatrix} \ddots & \vdots & \vdots & \vdots & \vdots & \vdots & \vdots & \iddots \\ \cdots & \frac{\Delta}{2}+\omega & 0 & 0 & 0 & 0 & 0 & \cdots \\ \cdots & 0 & \frac{\Delta}{2}+\delta & \Omega & 0 & 0 & 0 & \cdots \\ \cdots & 0 & \Omega^* & \frac{\Delta}{2} & 0 & 0 & 0 & \cdots \\ \cdots & 0 & 0 & 0 & \frac{\Delta}{2}+\delta-\omega & \Omega & 0 & \cdots \\ \cdots & 0 & 0 & 0 & \Omega^* & \frac{\Delta}{2}-\omega & 0 & \cdots \\ \cdots & 0 & 0 & 0 & 0 & 0 & -\frac{\Delta}{2}-\omega & \cdots \\ \iddots & \vdots & \vdots & \vdots & \vdots & \vdots & \vdots & \ddots \end{bmatrix} \tag{3.16}$$

where $\delta = \omega - \Delta$ is the detuning and $\Omega = A_x + iA_y e^{-i\phi}$ is the drive term. Now, we can simply write this as

$$H = \sum_m \left(\frac{\Delta + \delta}{2} + m\omega\right) \mathbb{I} + 2\sqrt{\delta^2 + 4|\Omega|^2} \left(|+, m\rangle \langle +, m| - |-, m\rangle \langle -, m|\right) \tag{3.17}$$

where $|\pm, m\rangle = a_\pm |\uparrow, m\rangle + b_\pm |\downarrow, m + 1\rangle$ with

$$\begin{pmatrix} \frac{\delta}{2} & \Omega \\ \Omega^* & -\frac{\delta}{2} \end{pmatrix} \begin{pmatrix} a_\pm \\ b_\pm \end{pmatrix} = \pm\frac{1}{2}\sqrt{\delta^2 + 4|\Omega|^2} \begin{pmatrix} a_\pm \\ b_\pm \end{pmatrix} \tag{3.18}$$

We can see that all these states from different Floquet sectors are identical in Spin-1/2 Hilbert space, but the number of photons depend on the Floquet zone they belong to. The static system had two energy levels $|\uparrow, 0\rangle$ and $|\downarrow, 0\rangle$ separated by a gap of Δ, but the driven system has many energy levels with a gap of $\sqrt{\delta^2 + 4|\Omega|^2}$ between two levels in a Floquet zone and a gap of $\omega - \sqrt{\delta^2 + 4|\Omega|^2}$ at Floquet zone boundaries. When RWA is valid, we can describe the dynamics of the system very well with just four states, as each original energy level overlaps with only two eigenstates of full Floquet Hamiltonian and thus the driven system can be considered identical to a four-level system.

Let us get back to the two-level system and study what predictions we can make about this system on the basis of Floquet formalism. We started with a static system with a gap Δ, but the driven system has a gap of $4\sqrt{\delta^2 + 4|\Omega|^2}$ between its quasienergies. We can simply deduce the probability of finding the system in the excited state of the static Hamiltonian. If the system starts in the ground state $|\downarrow\rangle \equiv |\downarrow\rangle \otimes |0\rangle$, then we can see that it has a finite overlap with states $|\pm, -1\rangle$, then the time-evolved state of the system at any arbitrary time t is given by:

$$|\psi(t)\rangle = e^{i\mathcal{E}_0 t} \left(e^{i\mathcal{E}_+ t} b_+^* |+, -1\rangle + e^{i\mathcal{E}_+ t} b_-^* |-, -1\rangle\right) \tag{3.19}$$

with $\mathcal{E}_0 = \left(\frac{\Delta+\delta}{2} - \omega\right)$ and $\mathcal{E}_\pm = \pm\frac{1}{2}\sqrt{\delta^2 + 4|\Omega|^2}$, and the probabilities of finding the system in two-eigenstates of the undriven Hamiltonian are given by

$$|c_\downarrow|^2 = \left||b_+|^2 e^{i\mathcal{E}_+ t} + |b_-|^2 e^{i\mathcal{E}_- t}\right|^2 = 1 - \frac{2|\Omega|^2}{\sqrt{\delta^2 + 4|\Omega|^2}} \sin^2\left(\frac{\sqrt{\delta^2 + 4|\Omega|^2}}{2} t\right) \tag{3.20}$$

$$|c_\uparrow|^2 = \left|a_+ b_+^* e^{i\mathcal{E}_+ t} + a_- b_-^* e^{i\mathcal{E}_- t}\right|^2 = \frac{2|\Omega|^2}{\sqrt{\delta^2 + 4|\Omega|^2}} \sin^2\left(\frac{\sqrt{\delta^2 + 4|\Omega|^2}}{2} t\right) \tag{3.21}$$

which represent the Rabi oscillations of a near-resonant driven two-level system.

Thouless pump in the light of Floquet

We encountered Thouless pump in Ch. 2 where we described Berry phase induced transport from a time-periodic perturbation in a translationally invariant one-dimensional chain. The topological aspects of this model become more transparent if we treat this problem in Floquet formalism. As an example, we can consider the adiabatic charge pumping in a $2N$ site Rice-Mele model:

$$H(t) = \sum_{r=0}^{2N-2} (J + \delta_1 \cos \omega t (-1)^r) (|r+1\rangle \langle r| + \text{h.c}) - \delta_2 \sin \omega t \sum_{r=0}^{2N-1} (-1)^r |r\rangle \langle r| \tag{3.22}$$

where $|r\rangle$ denotes a state localized at site r on the one-dimensional chain. Let us denote even sites $|r = 2j\rangle$ by $|A_j\rangle$ and take odd sites $|r = 2j+1\rangle \equiv |B_j\rangle$.

$$\begin{aligned} H(t) = \sum_{j=0}^{N-1} v(t) \left(|B_j\rangle \langle A_j| + |B_j\rangle \langle A_j|\right) + w(t) \left(|A_{j+1}\rangle \langle B_j| + |B_j\rangle \langle A_{j+1}|\right) \\ +u(t) \sum_{j=0}^{N-1} \left(|B_j\rangle \langle B_j| - |A_j\rangle \langle A_j|\right) \end{aligned} \tag{3.23}$$

with $v(t) = J + \delta_1 \cos \omega t$, $w(t) = J - \delta_1 \cos \omega t$, $u(t) = \delta_2 \sin \omega t$. If we impose periodic boundary conditions, then it becomes

$$H = \begin{bmatrix} \delta_2 \sin \omega t & (J - \delta_1 \cos \omega t) + (J + \delta_1 \cos \omega t) e^{ik_x} \\ (J - \delta_1 \cos \omega t) + (J + \delta_1 \cos \omega t) e^{-ik_x} & -\delta_2 \sin \omega t \end{bmatrix} \tag{3.24}$$

It maps to a non-trivial SSH model at $t = nT$ and to a trivial SSH at $t = (n + 1/2)\, T$ which results in a charge-transfer during each cycle. Using the Floquet formalism, we can treat it as a two-dimensional setup where the second dimension arises from the photon degree of freedom. Now, each state can be described in the extended Hilbert space with two indices $|\alpha_j, m\rangle$ with $\alpha = A, B$ and m is the photon number. We can now interpret ωt as the momentum associated with the second direction, i.e., $\mathbf{k} = (k_x, \omega t)$. The time-dependence of k_y can be accounted for by considering a uniform E field in y direction. The equation of motion for a Bloch electron with momentum $\mathbf{k}$ in this space can thus be described by:

$$\dot{\mathbf{k}} = \omega \tag{3.25}$$

$$\dot{\mathbf{r}} = \mathbf{v}_{\text{group}} + \dot{\mathbf{k}} \times \mathbf{\Omega} \tag{3.26}$$

where $\mathbf{\Omega}$ is the Berry curvature of Bloch bands obtained from Eq. 3.24. The anomalous term arising from a non-zero Berry curvature results in a drift in x

direction. Now, if we consider a completely filled Bloch band, then the current density is given by:

$$\mathbf{j} = \frac{1}{T}\int_{BZ} dk_x dk_y \omega \mathbf{\Omega}^z(k_x, k_y) = \frac{1}{T} eC \tag{3.27}$$

where C is the Chern number of the filled band responsible for the quantized charge transport during each cycle.

This Floquet picture can be generalized further to systems which are not purely periodic. It was used for the case of two drives with incommensurate frequencies which resulted in two additional degrees of freedom in extended Hilbert space [221]. This analogy provides a novel route to extend the dimensionality of the system, and thus can be used to realize an analog of 2D topological models with a single qubit or even higher dimensional models.

3.2 Periodically driven topological systems

Floquet engineering has proved a very promising tool to realize and control topological phases [297]. It allows us to study topological phase transitions which can be controlled by the amplitude, frequency, or polarization of light. We now briefly review the very well-established example of topological phase transitions observed in graphene when irradiated with circularly polarized light [226].

Periodically driven graphene

The graphene Hamiltonian H_{graphene} consists of nearest-neighbor hopping on a honeycomb lattice, and, potentially, a substrate-induced mass term between the two sublattices. The vectors connecting one site to its three nearest neighbors are given by:

$$\mathbf{d}_1 = a\hat{y},\ \mathbf{d}_2 = a\left(\frac{\sqrt{3}}{2}\hat{x} - \frac{1}{2}\hat{y}\right),\ \mathbf{d}_3 = a\left(-\frac{\sqrt{3}}{2}\hat{x} - \frac{1}{2}\hat{y}\right), \tag{3.28}$$

where the lattice vectors of the underlying triangular lattice are

$$\mathbf{a}_1 = \frac{\sqrt{3}}{2}\left(-\hat{x} + \sqrt{3}\hat{y}\right),\ \mathbf{a}_2 = \frac{3}{2}\left(\hat{x} - \sqrt{3}\hat{y}\right). \tag{3.29}$$

We begin with the static Hamiltonian H_{graphene} for graphene with nearest neighbor hopping of electrons,

$$H_{\text{graphene}} = -t_0 \sum_{r_i, j=1,2,3} \left(b^\dagger_{\mathbf{r}_i+\mathbf{d}_j} a_{\mathbf{r}_i} + a^\dagger_{\mathbf{r}_i} b_{\mathbf{r}_i+\mathbf{d}_j}\right) + \Delta_0 \sum_{r_i} \left(a^\dagger_{\mathbf{r}_i} a_{\mathbf{r}_i} - b^\dagger_{\mathbf{r}_i+\mathbf{d}_1} b_{\mathbf{r}_i+\mathbf{d}_1}\right),$$

where the Fermionic operator $c_r(c_r^\dagger)$ annihilates (creates) an electron at position $\mathbf{r}$ with $c = a, b$ for sublattices A and B, respectively. The vectors $\mathbf{r}_i$ span sublattice A, and d_i are the position vectors to the three nearest neighbors around each A site of the hexagonal plaquette. The first term in H_{graphene} describes the hopping of electrons between the two sublattices A and B with tunneling strength t_0, and the second term accounts for a staggered sublattice symmetry breaking mass Δ_0.

When the graphene is irradiated with light, the effect of oscillating EM field can be incorporated via the Peierls' substitution, where the hopping between sites $\mathbf{r}_i$ and $\mathbf{r}_j$ are replaced by

$$t_{\mathbf{r}_i\mathbf{r}_j} \longrightarrow e^{ie\int_{\mathbf{r}_i}^{\mathbf{r}_j}\mathbf{A}\cdot d\mathbf{r}}\, t_{\mathbf{r}_i\mathbf{r}_j} \tag{3.30}$$

where $\mathbf{A}$ is the vector potential of the light used to irradiate the sample. For the case of circularly polarized light, the vector potential reads $\mathbf{A} = A_0 \cos\omega t\hat{x} + A_0 \sin\omega t\hat{y}$, and thus Peierls' phase takes the following form

$$e^{ie\left(\int_{\mathbf{r}_j}^{\mathbf{r}_i}\mathbf{A}\cdot d\mathbf{r}\right)} = e^{i\alpha\sin(\omega t+\beta)} \tag{3.31}$$

where $\alpha = eA_0$ and β is a phase which depends on the direction of $\mathbf{r}_i - \mathbf{r}_j$. Using Jacobi-Anger expression,

$$e^{i\alpha\sin(\omega t+\beta)} = \sum_n J_n(\alpha)e^{in\beta}e^{in\omega t}. \tag{3.32}$$

we can find the Fourier components of $H(t)$. Specifically, the real space H_0 and $H_{\pm1}$ are:

$$H_0 \quad = J_0(A)H_{\text{graphene}} \tag{3.33}$$

$$H_1 \quad = t_0 \sum_{r_i, j=1,2,3} J_1(A)e^{i\phi_j}\left(b^\dagger_{\mathbf{r}_i+\mathbf{d}_j}a_{\mathbf{r}_i} - a^\dagger_{\mathbf{r}_i}b_{\mathbf{r}_i+\mathbf{d}_j}\right) \tag{3.34}$$

$$H_{-1} \quad = t_0 \sum_{r_i, j=1,2,3} J_{-1}(A)e^{-i\phi_j}\left(b^\dagger_{\mathbf{r}_i+\mathbf{d}_j}a_{\mathbf{r}_i} - a^\dagger_{\mathbf{r}_i}b_{\mathbf{r}_i+\mathbf{d}_j}\right) \tag{3.35}$$

where $\phi_1 = \pi$, $\phi_2 = \frac{\pi}{3}$, $\phi_3 = -\frac{\pi}{3}$, and $A = \frac{eEa}{\omega}$. It can be shown that the commutation

$$[H_1, H_{-1}] = t_0^2(J_1(A))^2 \sum_{\mathbf{r}_i, d_k-d_j=\mathbf{a}_1,\mathbf{a}_2,\mathbf{a}_3} 2i\sin(\phi_k-\phi_j)\left(b^\dagger_{\mathbf{r}_i+\mathbf{d}_k}b_{\mathbf{r}_i+\mathbf{d}_j} - a^\dagger_{\mathbf{r}_i+\mathbf{d}_k-\mathbf{d}_j}a_{\mathbf{r}_i}\right) + \text{h.c} \tag{3.36}$$

where $\mathbf{a}_3 = -\mathbf{a}_1 - \mathbf{a}_2$ and $\mathbf{a}_1, \mathbf{a}_2$ are two lattice vectors described in Eq. 3.29. These terms represent complex next-nearest hopping, as $\phi_1 - \phi_2 = \phi_2 - \phi_3 = \phi_3 - \phi_1 = \frac{2\pi}{3}$.

Let us assume that the frequency of drive, $\omega \ll t_0, \Delta_0$. In this high-frequency regime, the effective Floquet Hamiltonian

$$H_F = H_0 + \sum_m \frac{[H_m, H_{\bar{m}}]}{m\omega} + O\left(\frac{1}{\omega^2}\right) \tag{3.37}$$

becomes identical to the static Haldane model with second-nearest neighbor amplitude, $t_2 \propto t_0^2 \frac{E}{w^3}$. In addition to this next-nearest neighbor hopping induced by the drive, the nearest hopping has also been suppressed by a factor of $J_0(\alpha)$. This kind of term is responsible for dynamical localization in one-dimensional tight-binding model when $J_0(\alpha) \to 0$.

Another much simpler way to understand these changes in band topology of irradiated graphene is to consider the k space picture in the vicinity of Dirac points

$$H(\mathbf{k}, t) = \Delta_0 \sigma_z + v_F \hbar (k_x + \frac{e}{\hbar} A_x(t))\sigma_x + \tau v_F \hbar (k_y + \frac{e}{\hbar} A_x(t))\sigma_y \tag{3.38}$$

where τ is the valley index. Now, we can see that

$$[H_1, H_{-1}] = \tau \frac{A^2}{\omega^2} \sigma_z \tag{3.39}$$

which results in a valley-dependent mass term similar to the mass term obtained in Haldane model from complex second-nearest neighbor hopping. Clearly, this kind of gap term is allowed only for circular polarized drive. This drive-induced non-trivial topology is thus allowed only if TRS is broken by the drive.

Band-inversion with resonant drive

In the irradiated graphene case considered above, the drive frequency was much larger than the bandwidth of the system, and thus there was no overlap between neighboring photon dressed bands of the original Hamiltonian which made it more amenable to Magnus series expansion. On the other hand, in the case of two-level system, we focussed on a near-resonant drive which resulted in an overlap of neighboring photon-dressed states of the static Hamiltonian. However, the drive term opened up a gap at these band crossings. In the limit where RWA was valid, we could simply study this system just by focusing on the inner 2×2 block of the truncated Hamiltonian

$$H_F = \begin{pmatrix} H_0 + \omega & H_1 \\ H_1^\dagger & H_0 \end{pmatrix}. \tag{3.40}$$

A similar approach can be used to obtain Floquet topological phases as first proposed in Ref. [207]. In Floquet picture, there is an overlap between the lower band of $H_0 + \omega$

and the upper band of H_0, and the drive couples these two bands significantly at resonant points. This mixing is responsible for band-inversion around avoided crossings which can result in a non-trivial gap opening depending on the properties of drive and the static system.

Floquet topological phases from drive-induced symmetry promotion

We discussed how a circularly polarized light can turn a trivial system into a non-trivial system. These drive-induced topological features can be attributed to the TRS symmetry breaking action of the drive which changes the Atland-Zirnbauer (AZ) [11] symmetry class of the system. This classification is decided on the basis of three *non-spatial* symmetries, i.e time-reversal $\mathcal{T}$, particle-hole $\mathcal{C}$, and chiral symmetry $\mathcal{S}$ described as:

$$\mathcal{T}H(\mathbf{k},t)\mathcal{T}^{-1} = H^*(-\mathbf{k},-t) \tag{3.41}$$

$$\mathcal{C}H(\mathbf{k},t)\mathcal{C}^{-1} = -H^*(-\mathbf{k},t) \tag{3.42}$$

$$\mathcal{S}H(\mathbf{k},t)\mathcal{S}^{-1} = -H(\mathbf{k},t) \tag{3.43}$$

for Bloch Hamiltonians $H(\mathbf{k})$. Most of the Floquet engineering schemes are based on some sort of *non-spatial* symmetry breaking action of the drive. However, there are additional symmetries which can have important consequences for topological classification. It is well-known that including *spatial* symmetries like reflection (given by some operator M) can expand the topological classification beyond ten AZ classes, and can even allow for the existence of higher-order topological phases. The topological features of such Hamiltonians depend not only on the presence or absence of certain symmetries, but also on the algebraic relations between spatial and non-spatial symmetries, i.e on commutation relations $[M,\mathcal{T}]_\pm$, $[M,\mathcal{C}]_\pm$,$[M,\mathcal{S}]_\pm$ where ± represents anti-commutation and commutation respectively. Furthermore, for the case of driven systems, the photon degree of freedom can be interpreted as an artificial dimension.

We can ask if there are any additional symmetries which come into picture because of the periodic drive. It was shown in Ref. [271], that in addition to spatial and non-spatial symmetries, the time-periodic Hamiltonians can also exhibit more exotic symmetries like *space-time* symmetries which have no equilibrium counterparts. In Floquet formalism, the symmetries of this effective time-independent Hamiltonian are given by effective symmetry operators. The algebraic relations between these effective symmetry operators can be quite different from their static counterparts. For example, for Floquet Hamiltonian of Eq. 3.40, the effective symmetry operators for time-reversal, particle-hole, and chiral symmetry are given by:

$$\mathscr{T} = \begin{pmatrix} \mathcal{T} & \\ & \mathcal{T} \end{pmatrix}, \mathscr{C} = \begin{pmatrix} & C \\ C & \end{pmatrix}, \text{ and } \mathscr{S} = \begin{pmatrix} & \mathcal{S} \\ \mathcal{S} & \end{pmatrix}, \tag{3.44}$$

respectively. Now, if the drive is such that the reflection symmetry of static Hamiltonian is promoted to a time-glide symmetry, then

$$\mathcal{M}H(\mathbf{k}, t)\mathcal{M} = H(-k_x, \mathbf{k}_{\parallel}, t + T/2). \tag{3.45}$$

For Floquet Hamiltonian H_F in Eq. 3.40, it becomes an effective reflection symmetry given by

$$\mathscr{M} = \begin{pmatrix} \mathcal{M} & \\ & -\mathcal{M} \end{pmatrix}. \tag{3.46}$$

On the basis of these effective symmetry operators, we can conclude that the following commutation relations are reversed for the driven system

$$[\mathcal{M}, C]_{\pm} = [\mathscr{M}, \mathscr{C}]_{\mp}], \ [\mathcal{M}, \mathcal{S}]_{\pm} = [\mathscr{M}, \mathscr{S}]_{\mp}] \tag{3.47}$$

which can change the topological classification. In Chapter 7, we demonstrate how such a set up can by realized by coherent excitations of lattice vibrations.

3.3 Periodically driven quantum magnets

In addition to band engineering described above for non-interacting models, light-matter interactions can also be used to control the properties of strongly correlated matter [21, 356]. In these materials, the energy landscape is dominated by different interactions which can be modified by light-induced charge redistribution. Such changes can alter charge, spin, or orbital ordering and interaction strength in these systems which can allow us to study phase transitions in these materials. This would not only improve our fundamental understanding of the interactions between different degrees of freedom, but are also paving the way for ultrafast quantum technologies. In the past few years, these ideas have found enormous applications in the field of light-induced superconductivity [97]. Now, these methods are gaining popularity in the context of quantum magnetism [228]. The magnetic properties of a system depend on a lot of factors like the nature of orbitals involved in exchange processes, nature of interactions, electronegativity of ligands, crystal structure, etc. In the second part of this thesis, we explore how light can be used to change magnetic properties by manipulating these different knobs. Here, we provide a brief background required to understand the ideas pesented there.

Exchange mechanism in magnetic insulators

This section draws heavily upon Ref. [267].

In this section, we briefly review different possible mechanisms for magnetic interactions in transition metal based magnetic materials. We focus on systems with localized spins, and would be ignoring itinerant magnets. We aim to understand how spin exchange interactions emerge in a strongly correlated material and what factors determine the nature of strength of these interactions.

Direct superexchange

We consider a simple two-site Fermi-Hubbard model at half-filling. We assume one orbital on each site with hopping described by

$$H_{\text{KE}} = -t \sum_{\sigma=\uparrow,\downarrow} \left(c^\dagger_{1\sigma} c_{2\sigma} + c^\dagger_{2\sigma} c_{1\sigma} \right) . \tag{3.48}$$

The electrons at each site experience the mutual Coulomb repulsion which is given by

$$H_{\text{int}} = U(n_{1\uparrow}n_{1\downarrow} + n_{2\uparrow}n_{2\downarrow}), \tag{3.49}$$

where $n_{i,\sigma} = c^\dagger_{i,\sigma} c_{i,\sigma}$. In the Mott regime, $t \ll U$, $S_z = 0$, the charge degree of freedom is almost frozen, and we can consider two situations:

1. Parallel alignment: both spins point in the same direction. In this case, the Hilbert space is spanned by

   $$|\uparrow, \uparrow\rangle = c^\dagger_{2\uparrow} c^\dagger_{1\uparrow} |0\rangle \, , \; |\downarrow, \downarrow\rangle = c^\dagger_{2\uparrow} c^\dagger_{1\uparrow} |0\rangle \, . \tag{3.50}$$

   In this case, both states are eigenstates of the full Hamiltonian $H_{\text{KE}} + H_{\text{int}}$ with energy zero.

2. Antiparallel alignment where the two spins on different sites point in opposite directions. In this case, the Hilbert space can be partitioned into two sectors: (1) Single occupancy denoted by subspace P, and (2) Double occupancy denoted by subspace Q. The states in subspace P

   $$|\uparrow, \downarrow\rangle = c^\dagger_{2\downarrow} c^\dagger_{1\uparrow} |0\rangle \tag{3.51}$$
   $$|\downarrow, \uparrow\rangle = c^\dagger_{2\uparrow} c^\dagger_{1\downarrow} |0\rangle \tag{3.52}$$

   and the states in subspace Q

   $$|\uparrow\downarrow, .\rangle = c^\dagger_{1\downarrow} c^\dagger_{1\uparrow} |0\rangle \tag{3.53}$$
   $$|., \uparrow\downarrow\rangle = c^\dagger_{2\downarrow} c^\dagger_{2\uparrow} |0\rangle \, . \tag{3.54}$$

Using these states, we can write the above Hamiltonian

$$H = \begin{pmatrix} 0 & 0 & -t & -t \\ 0 & 0 & t & t \\ -t & t & U & 0 \\ -t & t & 0 & U \end{pmatrix} \tag{3.55}$$

in the basis $|\uparrow, \downarrow\rangle, |\downarrow, \uparrow\rangle, |\uparrow\downarrow, .\rangle, |., \uparrow\downarrow\rangle$. It can be solved exactly, but we are more interested in its magnetic properties when $t \ll U$. In the absence of hopping, the two states in the subspace P (Q) are degenerate with energy zero (U), respectively. In this limit , we can treat H_{hop} as a perturbation to H_{int} and the low energy physics can be very well captured by

$$H_{\text{eff}} \approx \mathcal{P} H_0 \mathcal{P} + \frac{1}{U} \mathcal{P} H_{\text{hop}} \mathcal{Q} H_{\text{hop}} \mathcal{P} \tag{3.56}$$

where $\mathcal{P}(\mathcal{Q})$ is a projection operator for subspace $P(Q)$. In the basis of $|\uparrow, \downarrow\rangle, |\downarrow, \uparrow\rangle$, it takes the following form

$$H_{\text{eff}} \approx -\frac{2t^2}{U} \begin{pmatrix} 1 & -1 \\ -1 & 1 \end{pmatrix} \tag{3.57}$$

which results in a splitting of $E_t - E_s = 4t^2/U$ between singlet and triplet states of subspace P given by $|\psi_{s/t}\rangle = 1/\sqrt{2}\left(|\uparrow, \downarrow\rangle \mp |\downarrow, \uparrow\rangle\right)$. The triplet sector has the same energy as the parallel spin case and thus we can write this effective Hamiltonian as a spin Hamiltonian which becomes more evident when we use the second-quantization picture.

In the second-quantization picture, we can capture both cases described above with the effective Hamiltonian

$$\begin{aligned} H_{\text{eff}} &= -\frac{2t^2}{U}\left(c^\dagger_{2\uparrow} c^\dagger_{1\downarrow} c_{1\downarrow} c_{2\uparrow} - c^\dagger_{2\downarrow} c^\dagger_{1\uparrow} c_{1\downarrow} c_{2\uparrow} - c^\dagger_{2\uparrow} c^\dagger_{1\downarrow} c_{1\uparrow} c_{2\downarrow} + c^\dagger_{2\downarrow} c^\dagger_{1\uparrow} c_{1\uparrow} c_{2\downarrow}\right) \\ &= -\frac{2t^2}{U}\left(c^\dagger_{1\downarrow} c_{1\downarrow} c^\dagger_{2\uparrow} c_{2\uparrow} - c^\dagger_{1\uparrow} c_{1\downarrow} c^\dagger_{2\downarrow} c_{2\uparrow} - c^\dagger_{1\downarrow} c_{1\uparrow} c^\dagger_{2\uparrow} c_{2\downarrow} + c^\dagger_{1\uparrow} c_{1\uparrow} c^\dagger_{2\downarrow} c_{2\downarrow}\right) \end{aligned} \tag{3.58}$$

and on using

$$S_i^x = \frac{1}{2}\left(c^\dagger_{i\uparrow} c_{i\downarrow} + c^\dagger_{i\downarrow} c^\dagger_{i\uparrow}\right), \; S_i^y = \frac{1}{2}\left(c^\dagger_{i\uparrow} c_{i\downarrow} - c^\dagger_{i\downarrow} c^\dagger_{i\uparrow}\right), \; S_i^z = \frac{1}{2}\left(c^\dagger_{i\uparrow} c_{i\uparrow} + c^\dagger_{i\downarrow} c^\dagger_{i\downarrow}\right) \tag{3.59}$$

it becomes

$$H_{\text{eff}} = \frac{4t^2}{U}\left(\mathbf{S}_1 \cdot \mathbf{S}_2 - \frac{n_1 n_2}{4}\right) \tag{3.60}$$

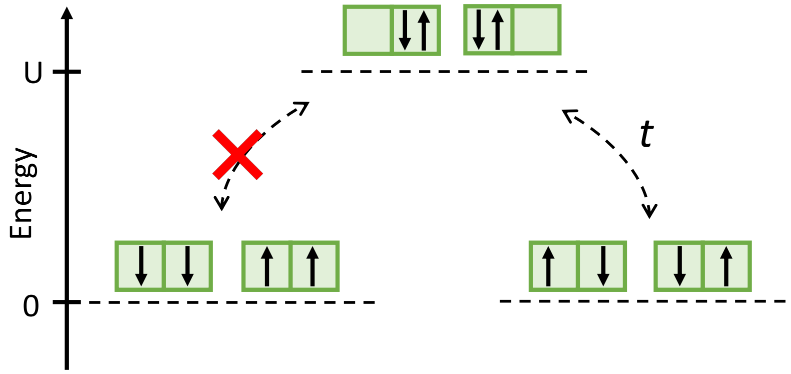

Figure 3.1: Virtual excitations to doubly-occupied sector responsible for lowering of energy in the singlet sector.

which gives exchange coupling, $J = 4t^2/U$, and shows that the ground state is antiferromagnetic. This effective spin Hamiltonian arises when we eliminate the higher-energy states from the full Hilbert space after accounting for the virtual excitations to these levels as shown in Fig. 3.1.

So far, we considered only a single orbital on each site and the effective spin coupling came out to be antiferromagnetic in nature. However, the superexchange mechanism can also give rise to ferromagnetic interactions which can show up only if we account for multi-orbital nature of TM. For example, if we consider a toy-model on each site with one spin on each site with inter-orbital hopping between neighboring sites. We notice that both FM and AFM states can reduce their energy through virtual excitations to doubly-occupied sectors. However, the energy associated with the virtual state of FM case is lower due to Hund's coupling between two orbitals at a given site which results in a ferromagnetic ground state. This shows that the multi-orbital nature of TM ions can have important implications on magnetic properties of magnetic materials.

Ligand-mediated superexchange interactions

The model discussed above can describe the magnetic properties of a system with localized spins on each site. It assumed direct hopping between magnetic sites and considered only a single orbital. There are very few real magnetic materials which can be described by the simple model considered above. In most transition metal-based quantum materials, the multi-orbital character of each magnetic site can have significant implications on their magnetic properties. Additionally, these *d* orbitals are highly localized and the direct hopping between *d* orbitals at neighboring sites is almost negligible. And quite often, the transition metal ions are separated by large non-magnetic ions known as ligand ions. These ligand ions usually have active *p* orbitals which have a finite overlap with the *d* orbitals of TM ions. These ligand ions can mediate exchange interactions between two TM ions even if there is no overlap between the *d* orbitals of these TM ions. The magnetic properties in such cases are strongly influenced by the properties of orbitals involved in the superexchange mechanism. A better understanding of the role of multi-orbital nature and ligand properties on the superexchange mechanism can open up novel routes to manipulate magnetic properties with external perturbations which is the basis of our work described in Ch 7-10. In this section, we try to develop an intuition about different aspects of ligand-mediated superexchange interactions.

We consider a simple situation where the hopping between two singly-occupied TM ions is mediated by one orbital of the ligand which sits between two TM ions. To understand superexchange in this model, we consider one *d* orbital on each TM site denoted by $i = 1$ and $i = 2$ with a completely filled *p* orbital of the ligand ion. This model can be described by the following Hamiltonian:

$$H = \sum_{i=1,2,\sigma} \Big((-t_{pd} c^\dagger_{i\sigma} c_{p\sigma} + \text{h.c}\ ) + E_d \hat{n}_{i\sigma} \Big) + \sum_{\sigma} E_p \hat{n}_{p\sigma} + U \sum_{i=1,2} \hat{n}_{i\uparrow} \hat{n}_{i\downarrow}, \tag{3.61}$$

where $E_{p/d}$ is the hopping between *d* orbitals of the TM ion and the ligand orbital, $E_{p/d}$ is the electronic energy of p/d orbitals, and U is the on-site Coulombic interaction on TM ion site. For the undriven case, the magnetic coupling strength can be obtained by using fourth-order perturbation theory which gives an exchange interaction:

$$\text{J=}4t_{pd}^4 \left(\frac{1}{(E_{dp} + U)^2 U} + \frac{1}{(E_{dp} + U)^3} \right), \tag{3.62}$$

where $E_{dp} = E_d - E_p$. These terms arise due to virtual excitations to high energy sectors and thus the exchange intereactions now depend on the orbital properties of ligands, their electronic energies, and the geoemtric arrangement of ligand and TM ions.

This model very well captures the superexchange in antiferromagnetic magnetic insulators like MnO, NiO, etc. where the spins at singly-occupied *d* orbitals of TM ion site can hop between two sites via neighboring oxygen ion located directly at the center of the line joining the two TM ions.

We noticed in the direct superexchange case that the models with more than one orbital on TM ion exhibit a much richer behavior. Similarly, if we consider two orbitals on the ligand or TM ion, the ligand-mediated superexchange can result in ferromagnetic interactions. We can consider a toy model with one ligand atom and two TM ions, where the ligand ion has two completely filled p orbitals but the electrons in different orbitals can hop only to d orbitals in different TM ions. In addition to the on-site interaction on each TM ion, the two orbitals on the ligand ion are interacting via Hund's coupling. This model can be described by:

$$\begin{aligned} H =& U\sum_{i=1,2}\left(\hat{n}_{i\uparrow}\hat{n}_{i\downarrow}+E_d(\hat{n}_{i\uparrow}+\hat{n}_{i\downarrow})\right)+J_H\sum_{\substack{\alpha=p_x,p_y,\\ \alpha\neq\alpha'}}c^\dagger_{\alpha\uparrow}c^\dagger_{\alpha'\downarrow}c_{\alpha\downarrow}c_{\alpha'\uparrow} \\ &+\sum_{\substack{\alpha=\{p_x,p_y\},\\ \sigma=\{\uparrow,\downarrow\}}}E_p\hat{n}_{\alpha\sigma}-\sum_{\substack{i=\{1,2\},\\ \alpha=\{p_x,p_y\}}}t_{i\alpha}(c^\dagger_{i\sigma}c_{\alpha\sigma}+c^\dagger_{\alpha\sigma}c_{i\sigma}) \end{aligned} \tag{3.63}$$

where J_H is Hund's coupling between two p orbitals and the hopping parameters, $t_{1p_x}=t_{2p_y}=t$, and $t_{2p_x}=t_{1p_y}=0$ as the spins at $i=1$, and at $i=2$ hop to orbitals p_x and p_y, respectively. In the limit, $t\ll U, U+E_{pd}$ and for singly-occupied d orbitals, the effective low-energy Hamiltonian takes the form of a spin Hamiltonian with exchange interactions given by:

$$\begin{aligned} J &= \frac{4t^4_{pd}}{(U+E_{dp})^2}\left(\frac{1}{2(U+E_{dp})+J_H}-\frac{1}{2(U+E_{dp})-J_H}\right) \\ &= -\frac{4t^4_{pd}}{(U+E_{dp})^2}\frac{2J_H}{4(U+E_{dp})^2-J_H^2} \end{aligned} \tag{3.64}$$

which is negative indicating their FM nature. This form can be understood from fourth order virtual processes which are allowed for both singlet and triplet sectors. However, one of the intermediate states results in one electron at each p_x and p_y orbitals and the contribution of Hund's term is positive (negative) for singlet (triplet) respectively which lowers the virtual excitation energy for the triplet sector. This indicates that including more than one orbital on the ligand ion can give rise to FM interactions which depend not only on t_{pd}, E_{pd}, and U like AFM case, but also on Hund's coupling. On the basis of these two simple toy models with one d orbital on each TM ion and a ligand with p orbitals, we can predict that for singly-occupied TM ion site, the ligand-mediated exchange interactions are AFM in 180° geometry and FM in 90° geometry. In most cases, $J_H\ll U, E_{dp}$, which indicates that FM exchange interaction given in Eq. 3.64 tends to be significantly weaker than AFM interaction in Eq. 3.62.

These were the two cases which involved only one orbital on each TM ion site. If we include other *d* orbitals on these TM ions, many different scenarios can arise and we can even get an AFM interaction in 180° geometry. For example, consider the case where each TM site has two *d* orbitals with opposite orbital ordering on two sites (for instance, this situation can arise in Jahn-Teller active materials) such that the ligand orbital overlaps with the half-filled orbital on one TM ion and with empty *d* orbital on the second TM ion. In this case, the Hund's coupling between *d* orbital electrons at TM site would result in a FM coupling. The nature of interactions in such cases involving multiple orbitals on TM ion or ligand ion can be predicted using Goodenough-Kanamori rules [115].

Ultrafast control of exchange interactions

In transitional metals based magnetic insulators with localized spins, exchange interactions depend on a lot of factors and some of them include:

1. Direct hopping between TM orbitals
2. Hopping between TM and ligand orbitals
3. Energy difference between ligand and TM orbitals
4. On-site Coulomb interaction and Hund's coupling
5. Orbital occupancies of ligand and TM orbitals

This dependence on different parameters can be leveraged to modify the exchange interactions by applying external perturbations like pressure or strain which have long been used to change the orbital overlap between neighboring sites. Similar changes can also be obtained in multiferroics with polarization and magnetization coupling, using static electric fields which modifies the metal-ligand separation resulting in a change in exchange interactions[224]. Some of these static methods are known for over a half century now, and have proved immensely successful, but the time-scales associated with these changes are much slower. In order to use quantum magnets for new generation technologies like high-speed spintronics and information processing, and quantum computation, we need new routes for direct manipulation of exchange interactions at ultra-fast time-scales. The new advancements in the field of lasers and quantum materials can possibly allow us to harness light-matter interactions to control magnetic properties at these timescales. Below, we discuss different possibilities of using light to modify exchange interactions.

Even in simple models considered above, an EM field can affect the exchange interactions via many different mechanisms depending on how different ingredients mentioned above are impacted by light. For example, an oscillating electric field can modulate the hopping between TM ions or it can result in a Stark shift of the energy levels involved in exchange processes. Additionally, in certain case, it can also induce transitions between different levels which can change the charge distribution. Furthermore, light can also give rise to coherent lattice vibrations which in turn can affect the energies of d orbitals or metal-ligand bond angles.

Floquet engineering is one such mechanism which is emerging as a powerful technique to coherently manipulate the exchange interactions. To gain some insight about Floquet engineering of exchange interactions, we briefly review the periodically driven one-dimensional Fermi-Hubbard model at half-filling in the Mott regime. In the presence of a time-dependent electric field, the full Hamiltonian of the Fermi-Hubbard model is given by:

$$H = -t \sum_i c^\dagger_{i\sigma} c_{i+1\sigma} + \text{h.c} + U \sum_i \hat{n}_{i\uparrow}\hat{n}_{i\downarrow} + e\mathcal{E}a \sum_{i,\sigma} \hat{n}_{i\sigma} i \cos(\omega t) \tag{3.65}$$

where $\mathcal{E}(t) = \mathcal{E}\cos\omega t$ is the time-dependent electric field from the laser. After Peierls' substitution, it becomes:

$$H' = -t \sum_i e^{i\left[\frac{e\mathcal{E}a}{\omega}\sin(\omega t)\right]} c^\dagger_{i\sigma} c_{i+1\sigma} + \text{h.c} + H_U = H'_t + H_{\text{int}}. \tag{3.66}$$

Using Jacobi-Anger expressions, this hopping term can be expressed in terms of Fourier components

$$H'_t = -\sum_n \sum_i t\mathcal{J}_n(\zeta) \sum_i c^\dagger_{i\sigma} c_{i+1\sigma} e^{in\omega t} + \text{h.c} \tag{3.67}$$

where $\mathcal{J}_n$ denotes n^{th} order Bessel function, and drive parameter

$$\zeta = \frac{e\mathcal{E}a}{\omega}, \tag{3.68}$$

which is known as Floquet parameter. Now, in Floquet picture, we can interpret this Hamiltonian in a time-independent manner where terms involving $e^{i\omega t}$ give rise to hopping between Floquet zones which differ by n photons. This photon-assisted hopping thus results in virtual excitations to sectors with energy $U - n\omega$. If the drive is off-resonant, we can again use the second perturbation theory in the extended Floquet basis which gives an exchange coupling:

$$J' = JU \sum_{n=-\infty}^{\infty} \frac{1}{U + n\omega} \mathcal{J}_n(\zeta)^2, \tag{3.69}$$

where, $J = \frac{4t^2}{U}$ is the magnetic coupling strength for the undriven case. In the presence of this periodic drive, spin-exchange interactions are affected mainly due to two factors: (a) change in the hopping parameter due to photon-assisted tunneling, and (b) virtual excitations between different Floquet sectors. The effective spin exchange interactions can thus be controlled by changing the frequency, polarization, or intensity of the laser. As we can notice from the form of this above equation, to modify J significantly, the Floquet parameter, $\zeta \approx 1$, and also the frequency ω should be comparable to U at least. For a typical lattice constant of few Å, this requires an Electric field amplitude , $\mathcal{E} \approx 1eV/\text{Å}$. This necessitates the use of very strong laser pulses which makes Floquet engineering of quantum magnets very challenging.

This model for Floquet engineering of exchange interactions assumed direct hopping and single orbital at each site. The effect of EM field was incorporated using minimal coupling only. However, as we have seen already for the static case, the presence of non-magnetic ligand ions and the multi-orbital nature of TM and ligand orbitals plays a crucial role in determining the exchange interactions. A strong EM field can affect these extra degrees of freedom in many different ways which cannot be captured in the minimal coupling picture employed above. In the second part of this thesis, we charter new routes to manipulate different knobs using light, and propose novel schemes for ultrafast control of exchange interactions.

In Chapter 8, we propose a scheme based on the manipulation of orbital degree of freedom with light. This scheme relies on the drive-induced energy shift and orbital hybridization of ligand or TM ion orbitals which affects the exchange interactions. In Chapter 9, we discuss the impact of ligands in periodically driven quantum magnets. This works shows that the direct hopping model can fail to capture the essential features of drive-induced changes in exchange interactions. Both of these works are addressed within the Floquet formalism, and we considered mainly the off-resonant case where the charge sector remains inert during the time when drive is on. This allows us to describe the effective Floquet Hamiltonian as a spin Hamiltonian. On the other hand, a resonant drive can modify the charge distribution by inducing charge transfer excitations from ligand to TM ions or vice-versa. This can significantly disrupt the exchange processes resulting in a very strong modification of exchange interactions. In Chapter 10, we apply these ideas to explain the phase shift observed in coherent phonon oscillations of $CrSiTe_3$ upon the onset of short-range spin correlations. This ligand-to-metal charge transfer induced modification of exchange interactions also gives rise to a new kind of phonon excitation mechanism which we refer to as spin-displacive excitation of coherent phonons.

Part II

Probing Non-trivial Band Geometry

Chapter 4

BERRY ELECTRODYNAMICS: ANOMALOUS DRIFT AND PUMPING FROM A TIME-DEPENDENT BERRY CONNECTION

“Scientific thought and its creation is the common and shared heritage of mankind.”
– Abdus Salam

The Berry curvature of a Bloch band can be interpreted as a local magnetic field in reciprocal space. This analogy can be extended by defining an electric field analog in reciprocal space which arises from the time-dependent Berry connection. In this chapter, we explore the term in the semi-classical equation of motion that gives rise to this phenomenon, and show that it can lead to anomalous drift in wavepacket motion. We also shown that a similar effect arises from changes in the band population due to periodic driving, where the resulting drift depends on the nature of the drive and can be expressed in terms of a shift vector. Finally, we combine these effects to build a pump with a net anomalous drift during a cyclic evolution in momentum space.

This chapter is based on the following reference:

Swati Chaudhary, Manuel Endres, and Gil Refael. “Berry electrodynamics: Anomalous drift and pumping from a time-dependent Berry connection.” Phys. Rev. B **98**, 064310 (2018).

4.1 Introduction

The non-trivial geometry of energy bands in lattice models often gives rise to non-zero Berry curvature, which can lead to Hall response and affect material properties significantly [33, 404, 277, 377]. Berry curvature can be interpreted as a local magnetic field in momentum space. Its effect on the semiclassical dynamics is well studied [278, 84]. The local nature is directly observed in many cold atom setups, where localized wave packets in momentum space can be generated and coherently controlled [376, 121, 155, 8]. In most of these experiments, the underlying band topology is revealed either by Aharanov-Bohm [4] effects in quasimomentum space [88, 200], or by Hall drift measurements [155, 82], while new methods even allow the reconstruction of the Berry curvature across the Brillouin zone (BZ) [98, 200]. Most of these methods exploit the analogy between the Berry curvature and a magnetic field, and measure its effect on the dynamics of a wavepacket moving adiabatically in one of the Bloch bands.

It is natural to ask what happens if we keep the wavepacket stationary in the BZ, but change the band geometry. What effects arise from a time-dependent band geometry as experienced by a wavepacket localized at some quasimomentum $\mathbf{q}$? This situation can be realized either by making the band geometry time dependent, or by changing the relative band population of two bands with opposite geometric properties. We recount how the rate of change of the Berry connection appears as an electric field analog in the semiclassical equation of motion for a wavepacket undergoing adiabatic evolution [1]. We connect this effect to the shift that a wavepacket undergoing Rabi oscillations between two bands with opposite geometric properties exhibits.

Our results extend earlier results for thought experiments involving electrons moving slowly in spatially varying magnetic fields [330], where the time dependence of a Berry flux gives rise to an analog of electromotive force and an associated motion. In addition, non-trivial band geometry can profoundly affect the non-linear optical responses of a solid [240, 245, 374, 343]. Inspired by the role of band geometry in these non-adiabatic processes, we also explore the consequences of a time varying average Berry connection arising due to excitations between bands.

Our main motivation is to explain how the Berry connection dynamics, both adiabatic and non-adiabatic could be used to control the motion of wavepackets. This is timely given the variety of experiments, particularly in the atomic and optical realm [200, 345, 88, 155, 369], which explore the motion of wavepackets rather than the transport properties of a whole Fermi sea, as is typical in solid-state systems. In our work, we explore the anomalous motion that such Berry-dynamics produces for a wave packet in a honeycomb lattice. Furthermore, we show how these processes can be combined to produce deterministic translations of a wave packet, including a pumping cycle. Given that the motion is due to geometric effects, it has the advantage that it is by and large detail-independent.

4.2 Background and summary of results

In order to understand the effects of a time-dependent band geometry, let us first review the effects of Berry curvature on the motion of a wavepacket in a Bloch band. The Berry curvature effects on the center of mass (COM) motion of a wavepacket

---

[1] This term is also mentioned in the review [377], but its effects on transport were not explored or used as far as we know

in the n^{th} Bloch band are well captured by the semiclassical equation of motion derived in Refs. [377, 337, 87]. For a wavepacket moving adiabatically in the n^{th} band, the COM velocity becomes:

$$\mathbf{v}^n(\mathbf{q}) = \nabla_{\mathbf{q}} E^n(\mathbf{q}) + \dot{\mathbf{q}} \times \mathbf{\Omega}^n, \tag{4.1}$$

where $E^n(\mathbf{q})$ is the energy of the n^{th} band, and $\mathbf{\Omega}^n(\mathbf{q})$ is the Berry curvature given by

$$\mathbf{\Omega}^n(\mathbf{q}) = \nabla \times \mathbf{A}_{\text{nn}}, \quad \text{where} \quad \mathbf{A}_{\text{nn}} = \langle u_n(\mathbf{q})| \, i\nabla_{\mathbf{q}} \, |u_n(\mathbf{q})\rangle \tag{4.2}$$

is the Berry connection, and $|u_n(\mathbf{q})\rangle$ is the space periodic part of n^{th} band eigenstate. This description shows that the COM velocity has a contribution from a Lorentz force analog in addition to the regular group velocity, and thus highlights the analogy between a magnetic field and the Berry curvature, in the sense of

$$\mathbf{B} \leftrightarrow \nabla \times \mathbf{A}_{\text{nn}} = \mathbf{\Omega}^n.$$

In our work, we recount how in a more general scenario, the COM velocity is given by (see App. A.1)

$$\mathbf{v}^n(\mathbf{q}) = \nabla_{\mathbf{q}} E^n(\mathbf{q}) + \dot{\mathbf{q}} \times \mathbf{\Omega}^n + \left(\frac{\partial \mathbf{A}_{\text{nn}}}{\partial t}\right)_{\mathbf{q}} - \nabla_{\mathbf{q}} \chi_n(t), \tag{4.3}$$

where

$$\chi_n(t) = i \langle u_n| \frac{\partial}{\partial t} |u_n\rangle . \tag{4.4}$$

The last two terms in Eq. (4.3) arise when the band structure is changed adiabatically. In the absence of a force, these terms can be treated as a correction due to the time dependence of the Berry connection, and hence as an analog of the electric field, in the sense of

$$\mathbf{E} \leftrightarrow \frac{\partial}{\partial t}(\mathbf{A}_{\text{nn}}) - \nabla_{\mathbf{q}} \chi_n(t).$$

Our extension to time-varying band-structures suggest an interpretation of $\mathbf{A}_{\text{nn}}$ as vector potential and χ as the electric potential. Note that the term $\frac{\partial}{\partial t}(\mathbf{A}_{\text{nn}}) - \nabla_{\mathbf{q}} \chi_n(t)$ is gauge invariant (see App. A.1). We show that this additional term can give rise to an anomalous drift which is studied in Sec. 4.3. We note that a essentially the same term is also derived in the review [377], Eq. 6.9, for general changes in a band structure, its effect on transprot, however, have been so far unexplored. In particular, we see that the Berry connection is simply playing the role of a shift of the wavepacket center.

These time-dependent Berry connection effects also depend on the band occupation. Intuitively, one would expect that the process of band switching (in a static band structure) should also be considered as an effective time-dependent change in the Berry-connection seen by a wavepacket, which could lead to similar results. Indeed, we show that for a wavepacket starting in one band and undergoing Rabi oscillations between two bands with different geometric properties, the COM velocity is given by (see App. A.2):

$$\mathbf{v} = \left\langle \nabla_{\mathbf{q}} E_n \right\rangle + \frac{\partial}{\partial t} \left\langle \mathbf{A}_{\mathrm{nn}} \right\rangle + \frac{\partial}{\partial t} \left\langle \nabla_{\mathbf{q}}(\phi_n) \right\rangle, \tag{4.5}$$

where

$$\phi_1 = -\phi_2 = (\mathrm{Arg}\langle u_1 | H' | u_2 \rangle)/2 \tag{4.6}$$

is the phase of the matrix element connecting the two bands via the perturbation Hamiltonian H' inducing the Rabi oscillation. For any quantity O, we define the average $\langle O_n \rangle = P_1 O_1 + P_2 O_2$ with P_1 and P_2 the occupation probabilities for the two bands. The first term in Eq. (4.5) is the average group velocity, and the last two terms can be considered as an anomalous correction arising due to the change in the average Berry connection, and the q dependence of the phase of the transition matrix element. In this case, the electric field analogy is

$$\mathbf{E} \leftrightarrow \frac{\partial}{\partial t} \left\langle \mathbf{A}_{nn} \right\rangle + \frac{\partial}{\partial t} \left\langle \nabla_{\mathbf{q}}(\phi_n) \right\rangle .$$

We show gauge independence in App. A.2. Depending on the nature of the drive, which modifies $\frac{\partial}{\partial t} \left\langle \nabla_{\mathbf{q}}(\phi_n) \right\rangle$, the electric field term can lead to an anomolous drift (Sec. 4.4).

Most importantly, we show in Sec. 4.5 how to construct a charge pump by combining and repeating adiabatic and non-adiabatic steps. An alternative scheme for a pump, combining non-adiabatic processes with and without anamolous drift, is presented in App. A.4.

4.3 Anomalous drift from adiabatic changes of the band structure

Consider a Hamiltonian $H(\mathbf{q}, \mathbf{G}(t))$ which depends on quasimomentum $\mathbf{q}$ and a set of time-dependent parameters denoted by $\mathbf{G}(t)$. When the parameters $\mathbf{G}$ are varied in an adiabatic manner, the COM velocity of a wavepacket initialized in the n^{th} Bloch band is given by:

$$\mathbf{v}(q) = \nabla_{\mathbf{q}} E_n(q) + i \frac{\partial G_\mu}{\partial t} \left[\left\langle \frac{\partial u_n}{\partial G_\mu} | \nabla_{\mathbf{q}} u_n \right\rangle - \left\langle \nabla_{\mathbf{q}} u_n | \frac{\partial u_n}{\partial G_\mu} \right\rangle \right] \tag{4.7}$$

where $|u_n\rangle$ is the space-periodic part of Bloch wave function for n^{th} band (see App. A.1). This reduces to Eq. (4.3) with $\dot{\mathbf{q}} = 0$, where the last two terms can be interpreted as an electric field analog.

We demonstrate this effect by studying the honeycomb lattice. We consider a wavepacket localized at quasimomentum $\mathbf{q} = q_0\hat{x}$ as measured from the nearest Dirac point. In the vicinity of a Dirac point, the Bloch Hamiltonian for the lowest two bands in A-B basis is

$$H = \frac{3}{2}J \begin{bmatrix} \Delta(t) & \tau_z q_x + i q_y \\ \tau_z q_x - i q_y & -\Delta(t) \end{bmatrix}, \tag{4.8}$$

where $\tau_z = \pm 1$ for the two Dirac points $\mathbf{K}_\pm$, and $\mathbf{q} = \mathbf{k} - \mathbf{K}_\pm$ [54]. The sublattice offset-energy $\Delta(t)$, which can be a function of time t, is measured in units of $\frac{3J}{2}$, where J is the hopping amplitude, and quasi-momentum $\mathbf{q}$ in units of $\frac{1}{a}$, where a is the lattice constant.

Consider a wavepacket in the lower Bloch band, and localized at $\mathbf{q} = q_0\hat{x}$ in the vicinity of a Dirac point with $\tau_z = 1$. For a time-dependent sublattice offset-energy $\Delta(t)$, the Berry connection is given by

$$\mathbf{A}_{\mathrm{gg}} = \frac{1}{2q_0}\left(\frac{\Delta}{\sqrt{\Delta^2 + q_0^2}} - 1\right)\hat{y}, \tag{4.9}$$

where the gauge is chosen such that $\nabla_{\mathbf{q}}(\chi) = 0$.

Changes of the Band structure are induced by varying $\Delta(t)$ linearly from $-\Delta_0$ to Δ_0 in time T. Then in the semiclassical picture, the group velocity and the anomalous velocity are given by:

$$\mathbf{v}_g = \nabla_{\mathbf{q}} E_- = -\frac{\mathbf{q}}{\sqrt{\Delta^2 + q_0^2}}, \tag{4.10}$$

and

$$\mathbf{v}_a = \frac{\partial \mathbf{A}}{\partial t} - \nabla_{\mathbf{q}}\chi_n(t) = \frac{\partial \Delta}{\partial t}\frac{q_0}{2(q_0^2 + \Delta^2)^{3/2}}\hat{y} \tag{4.11}$$

with $\Delta(t) = \frac{2\Delta_0}{T}(t - \frac{T}{2})$. When $\nabla_{\mathbf{q}}(\chi) = 0$, the anomalous drift depends only on the change in the Berry connection which is shown in Fig. 4.1, and it is significant only in the vicinity of a Dirac point.

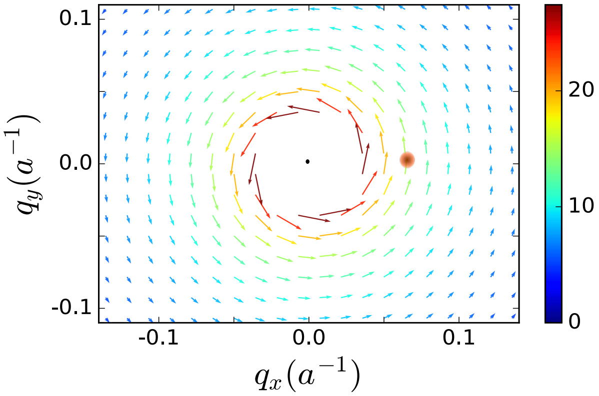

Figure 4.1: This vector plot shows the difference in Berry connection (Eq. (4.9)) for the lower band eigenstate around a Dirac point when the sublattice offset-energy is changed adiabatically from $-\Delta_0$ to Δ_0. The color bar on the side represents the magnitude of this difference. The wavepacket position is marked by a red circle. Here, the gauge is chosen such that $\nabla_{\mathbf{q}}\chi$ in Eq. (4.11) vanishes and thus the anomalous drift after the adiabatic evolution is the same as the change in the Berry connection vector at the position of wavepacket.

The total anomalous displacement could be integrated, as it is simply:

$$\begin{aligned}\delta_a =& \int_{-\infty}^{\infty} dt\mathbf{v}_a = A_{gg}(t=\infty) - A_{gg}(t=-\infty)\\ =&\frac{1}{q_0}\frac{\Delta}{\sqrt{\Delta^2+q_0^2}}.\end{aligned} \tag{4.12}$$

This formula in particular establishes the Berry connection as simply a shift of the center of the wavepacket, and makes it significantly less abstract.

Adiabaticity is crucial for this result. Here, the adiabaticity condition is decided by Landau-Zener parameter, $\Gamma = \frac{|v_{12}|^2}{\partial\mathcal{E}/\partial t}$, where $|v_{12}|$ is the gap at the level crossing, and $\mathcal{E}$ is the energy gap between two levels far from the level crossing [296]. When Δ is changed linearly in time from a large negative to a large positive value, the energy gap $|v_{12}| = q$, $\frac{\partial\mathcal{E}}{\partial t} = 2\frac{\partial\Delta}{\partial t}$, and thus the Landau-Zener parameter $\Gamma = \frac{q^2}{\Delta_0/T}$. This process is adiabatic if $\Gamma >> 1$.

To compare with the semi-classical expression, we numerically simulated the motion of a wavepacket centered at quasimomentum q_0 with spread σ_q, in a honeycomb lattice for the following set of parameters: $q_0 = \pi/50$, $\sigma_q = 0.02$, T=$700\hbar/J$, $\Delta_0 = 0.4$. The observed transverse drift, as shown in Fig. 4.2, is in good agreement with Eq. (4.11). For the given set of parameters, the motion is almost adiabatic.

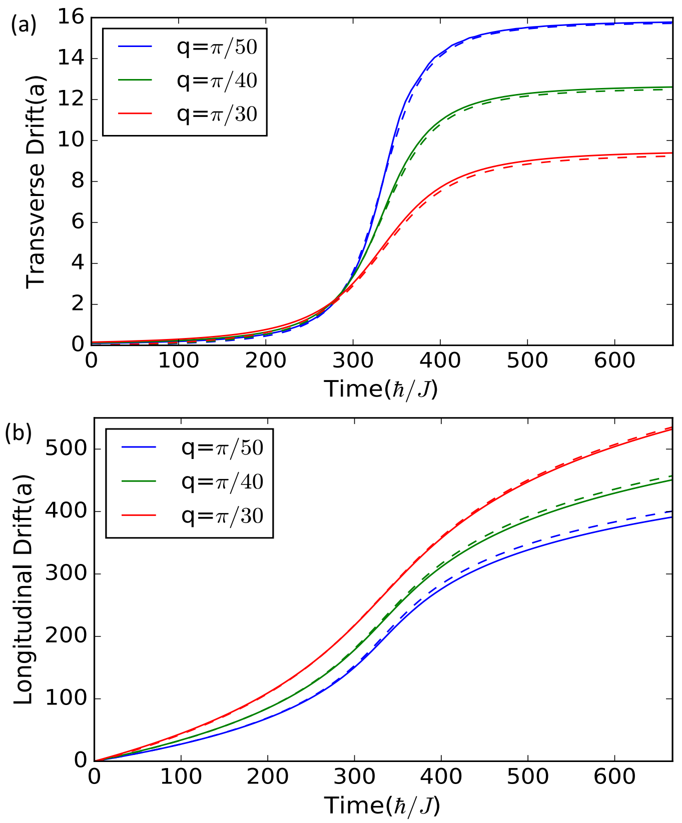

Figure 4.2: COM displacement vs time when Δ is changed linearly in time from -0.4 to 0.4 (a) Transverse drift (units of a), (b) COM displacement due to the group velocity term. Dashed lines depict the results from the semiclassical theory, and solid lines are from numerics.

Indeed, for the numbers used we find at the center of the wavepacket, $\Gamma = 2.59$, and excitation probability averaged over the gaussian wavepacket , $P_e \approx \left\langle e^{-2\pi\Gamma} \right\rangle = 0.0007$. Accordingly, we observe from numerics that the excitation probability $P_e \approx 0.08\%$ for $q = \frac{\pi}{50}$.

The anomalous drift observed in this section has a similar origin as the quantized particle transport in the Thouless pump [348]. In both cases, the transport properties are related to the adiabatic changes in the band geometry. An important difference is that we study these effects for a wavepacket, and thus the anomalous drift depends only on the changes in the band geometry near the wavepacket center. In contrast, the Thouless pump is geared towards driving a completely filled band where its action is quantized. Therefore, the Thouless pump relies more on global topological properties of cyclically driven band structures.

4.4 Anomalous drift from changes in the band population

Non-adiabatic processes, involving bands with different geometry, can have various interesting consequences, e.g., effects originating from the shift in the charge center upon excitation [317, 393, 187, 19, 188]. In many non centro-symmetric crystals, the difference between the Berry connection of the valence and conduction bands can give rise to a bulk photovoltaic effect during the optical transitions [101, 152, 398]. This kind of response can be expressed in terms of a shift vector [19, 317], which appears naturally in the study of shift current photovoltaic and photo galvanic effects [344, 188]. This shift vector highlights the role of the band geometry in many non-linear optical processes [172, 240, 239]. In these works, transitions are mainly induced by light, but in a more general scenario, one can consider any time-periodic perturbation which changes the band population. As we show below, the shift vector depends not only on the Berry connection of the two bands, but also on the phase of the transition matrix elements. We illustrate this effect by discussing two types of band switching processes stemming from sub-lattice offset modulation or a sinusoidal force. We discuss the relation of our work to previous works [317, 393, 187, 19, 188, 101, 152, 398, 344, 172, 240, 239] at the end of the section.

The changes in the average Berry connection affect the motion of a wavepacket undergoing coherent interband Rabi oscillations. For a wavepacket localized in momentum space, and evolving under a time-dependent and space-periodic Hamiltonian, the wavefunction is:

$$|\Psi(\mathbf{r},t)\rangle = \int d\mathbf{q}\, \phi(q(t),q_0)\, e^{i\mathbf{r}.\mathbf{q}}\, |\Phi(\mathbf{q},t)\rangle\,, \tag{4.13}$$

where $\phi(\mathbf{q}(t),q_0)$ is localized around $\mathbf{q}_0$, and

$$|\Phi(\mathbf{q},t)\rangle = A(t)\,|g(\mathbf{q})\rangle + B(t)\,|e(\mathbf{q})\rangle \tag{4.14}$$

is the superposition of the energy eigenstates $|g(\mathbf{q})\rangle$ and $|e(\mathbf{q})\rangle$ in the two bands. In the absence of an external force and for a translationally-invariant Hamiltonian, $\phi(q(t),q_0) = \phi(q(t=0),q_0)$ can be taken as real, and the displacement in real space is given by:

$$\langle\mathbf{r}\rangle = \int_{BZ} d\mathbf{q}|\phi(\mathbf{q},\mathbf{q}_0)|^2\, \langle\Phi(\mathbf{q},t)|\, i\nabla_{\mathbf{q}}\, |\Phi(\mathbf{q},t)\rangle\,. \tag{4.15}$$

This expression is also valid in the presence of a weak and time-periodic force, but captures only the average displacement as shown in App. A.2. We consider a perturbation H' of the form:

$$\begin{aligned} H(\mathbf{q},t) &= H_0 + H' \\ &= \begin{bmatrix} E_g(\mathbf{q}) & 0 \\ 0 & E_e(\mathbf{q}) \end{bmatrix} + \begin{bmatrix} 0 & \frac{|V|}{2}e^{i\Theta}e^{i\omega t} \\ \frac{|V|}{2}e^{-i\Theta}e^{-i\omega t} & 0 \end{bmatrix} \end{aligned} \tag{4.16}$$

in the basis $\{|g(\mathbf{q})\rangle, |e(\mathbf{q})\rangle\}$, where $|g(\mathbf{q})\rangle$ and $|e(\mathbf{q})\rangle$ are lower and upper band energy eigenstates with eigenvalues E_g and E_e, respectively. For the near resonance condition, $\omega \approx E_e(\mathbf{q}_0) - E_g(\mathbf{q}_0)$, it is useful to express $|\Phi(\mathbf{q},t)\rangle$ as:

$$|\Phi(\mathbf{q},t)\rangle = a(t)e^{i\frac{\omega t}{2}}|g(\mathbf{q})\rangle + b(t)e^{-i\frac{\omega t}{2}}|e(\mathbf{q})\rangle, \tag{4.17}$$

where $a(t)$ and $b(t)$ are slowly varying functions of time. Assuming that at $t = 0$, a wavepacket tightly localized at $\mathbf{q} = \mathbf{q}_0$ starts in the lower band, and if one ignores the terms oscillating at frequency ω, the COM velocity as given by Eq. (4.5), now becomes

$$\mathbf{v} = \mathbf{v}_g + \mathbf{v}_a, \tag{4.18}$$

where the average group velocity is

$$\mathbf{v}_g = P_g \nabla_{\mathbf{q}} E_g(\mathbf{q})|_{\mathbf{q}_0} + P_e \nabla_{\mathbf{q}} E_e(\mathbf{q})|_{\mathbf{q}_0} = -\cos(2\Omega_{\text{eff}}t)\nabla_{\mathbf{q}} E_0, \tag{4.19}$$

and the anomalous correction is given by

$$\begin{aligned} \mathbf{v}_a &= \frac{\partial}{\partial t}\left(P_g \mathbf{A}_{\text{gg}} + P_e \mathbf{A}_{\text{ee}}\right) - \frac{1}{2}\frac{\partial}{\partial t}\left(P_g \nabla_{\mathbf{q}}\Theta - P_e \nabla_{\mathbf{q}}(\Theta)\right) \\ &= \sin(2\Omega_{\text{eff}}t)\left(\mathbf{A}_{\text{ee}} - \mathbf{A}_{\text{gg}} - \nabla_{\mathbf{q}}\Theta\right)\Omega_{\text{eff}}|_{\mathbf{q}_0}, \end{aligned} \tag{4.20}$$

with phase $\phi_1 = -\phi_2 = \Theta/2$, defined in Eq. (4.16), probability $P_e = 1 - P_g = |b(t)|^2 = \sin^2(\Omega_{\text{eff}}t)$, and Ω_{eff} is the effective Rabi frequency.

The anomalous velocity in Eq. (4.20) depends on the difference in the Berry connection of the two bands, and the $\mathbf{q}$ space gradient of the phase of the drive. We used a fixed basis to express $|\Phi(\mathbf{q},t)\rangle$ in Eq. (4.17), and both of these contributions are gauge-dependent, but the overall gauge dependence cancels. As a result, the anomalous velocity is proportional to a gauge-invariant quantity, $\mathbf{A}_{\text{ee}} - \mathbf{A}_{\text{gg}} - \nabla_{\mathbf{q}}\Theta$, which is known as the shift vector in the context of non-linear optical processes [317]. Importantly, because of its dependence on the phase Θ of the drive, the resulting anomalous velocity $\mathbf{v}_a$ can differ significantly, as shown in Fig. 4.3.

Comparing the semi-classical result with the exact dynamics of a very narrow wavepacket (see Fig. 4.3), we notice that apart from the fast oscillations in COM motion, the dynamics is captured very well by Eq. (4.5). These fast oscillations arise from the non-zero inter-band Berry connection as shown in Eq. (A.45) of App. A.2. It is worth mentioning that for a large wavepacket in quasimomentum space, finite detuning effects can cause significant deviation from the semi-classical theory, and the dependence on wavepacket size is discussed in App. A.3.

We now consider two different mechanisms to switch band population for a wavepacket in a honeycomb lattice, and show how the nature of drive decides the anomalous shift during the transition.

Band switching with Δ modulation

We first consider switching the bands by modulating the sublattice offset-energy, and the Hamiltonian for this process is given by

$$\begin{aligned} H &= H_0 + H' \\ &= \begin{bmatrix} \Delta_0 & q e^{-i\phi} \\ q e^{i\phi} & -\Delta_0 \end{bmatrix} + \begin{bmatrix} \Delta_0 a_m \cos \omega_r t & 0 \\ 0 & -\Delta_0 a_m \cos \omega_r t \end{bmatrix} \end{aligned} \tag{4.21}$$

in A-B Basis. Now, expressing this Hamiltonian in energy eigenstate basis of H_0, and comparing it to Eq. (4.16), we find, for $a_m << 1$:

$$V = |V| e^{i\Theta} = \Delta_0 a_m \frac{q_0}{\sqrt{\Delta_0^2 + q_0^2}}, \tag{4.22}$$

when the lower and upper band eigenstates are expressed in the same gauge. Using the same gauge to find $\mathbf{A}_{\mathrm{ee}}$ and $\mathbf{A}_{\mathrm{gg}}$, we find from Eq. (4.20), that the anomalous velocity is given by:

$$\mathbf{v}_a = -\sin(2\Omega_{\mathrm{eff}} t) \left(\frac{1}{q_0} \frac{\Delta_0}{\sqrt{\Delta_0^2 + q_0^2}} \right) \Omega_{\mathrm{eff}}. \tag{4.23}$$

We simulate the dynamics of a very narrow wavepacket for $\sigma_q = 0.01$, $a_m = 0.14$, $q_0 = \pi/50.0$, $\Delta_0 = 0.5$, and $\omega_r = 2\sqrt{\Delta_0^2 + q_0^2}$, and the observed transverse drift is in good agreement with Eq. (4.23) as shown in Fig. 4.4. In this case, the effective Rabi frequency, Ω_{eff} is very small, and the resonance condition is satisfied only at the center of the wavepacket. This results in a small discrepancy between numerics and theory, which can be attributed to the finite detuning for a fraction of the wavepacket.

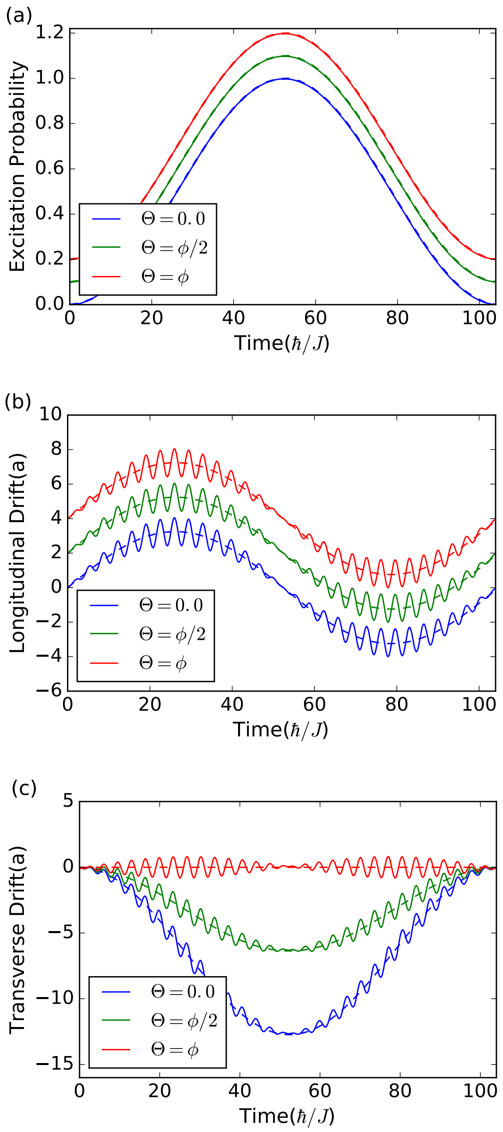

Figure 4.3: Dynamics during Rabi oscillations for a general drive: (a) Transition probability as a function of time, (b) Longitudinal drift, (c) Transverse Drift for the time evolution by H (solid lines) in Eq. (4.16) and from expressions (dashed lines) in Eq. (4.19) and (4.20), respectively, for $q_0 = \pi/40$, $\Delta_0 = 0.6$, $V = 0.04$, $\sigma_q = 0.01$ and $\omega = 2E_0$ and different drive phases Θ where $\phi = \tan^{-1}(q_y/q_x)$. For illustration purposes, the quantities on the y axis in (a) and (b) are shifted by a constant value for different Θ.

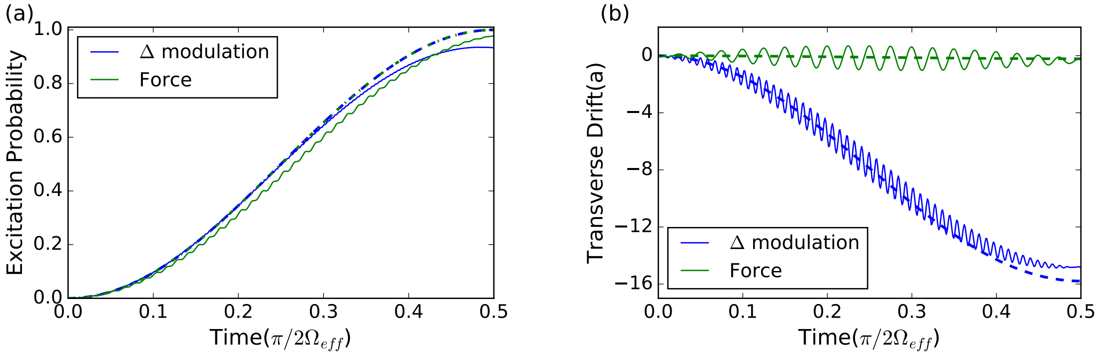

Figure 4.4: Dynamics during non-adiabatic processes: (a) Transition probability and (b) Transverse drift as a function of time for two non-adiabatic schemes from numerics (solid line) and from theory (dashed lines). Results for Δ modulation are shown in blue color, and we observe a significant drift during the band switching process as expected from Eq. (4.23). On the other hand, when band switching is achieved by applying a sinusoidal force, anomalous drift (shown in green color) is vanishingly small and is in good agreement with Eq. (4.25).

Band switching with sinusoidal force

We further consider applying a time-periodic force on the wavepacket. We consider a weak external sinusoidal force, $\mathbf{F} = \mathbf{F}_0 \sin \omega t$. If $|\mathbf{F}_0 \cdot \mathbf{A}_{\rm ge}| \ll \omega$ (see Eq. (A.35) in App. A.2 and Ref. [121]), the perturbation H' is given by:

$$H' = \cos(\omega t) \begin{bmatrix} \mathbf{F} \cdot \mathbf{A}_{\rm gg} & \mathbf{F} \cdot \mathbf{A}_{\rm ge} \\ \mathbf{F} \cdot \mathbf{A}_{\rm eg} & \mathbf{F} \cdot \mathbf{A}_{\rm ee} \end{bmatrix}. \tag{4.24}$$

Within rotating-wave approximation, we find from Eq. (4.20) and (4.24) that the anomalous velocity is given by:

$$\mathbf{v}_a = \sin(2\Omega_{\rm eff} t) \left(\mathbf{A}_{\rm ee} - \mathbf{A}_{\rm gg} - \nabla_{\mathbf{q}} (\mathrm{Arg}(\mathbf{F} \cdot \mathbf{A}_{\rm ge})) \right) \Omega_{\rm eff}. \tag{4.25}$$

Here, the anomalous term has two kinds of contributions, one from the change in Berry connection, and the other from the phase of the drive. Interestingly, for the specific case of a wavepacket close to a Dirac point and a linear force, these two contributions are equal. Hence, the wavepacket is excited to the upper band without any significant transverse drift unlike the sublattice offset-energy modulation case (see Fig. 4.4). We also simulate the dynamics of a wavepacket for $\mathbf{q}_0 = \pi/40\hat{x}$, $\Delta_0 = 0.6$ in the presence of a sinusoidal force $\mathbf{F} = \omega_r \Delta_0/20 \cos(\omega_r t)\hat{y}$. The observed transverse drift and the transition probability are in good agreement with the analytical treatment (Fig. 4.4). The finite size of wavepacket results in

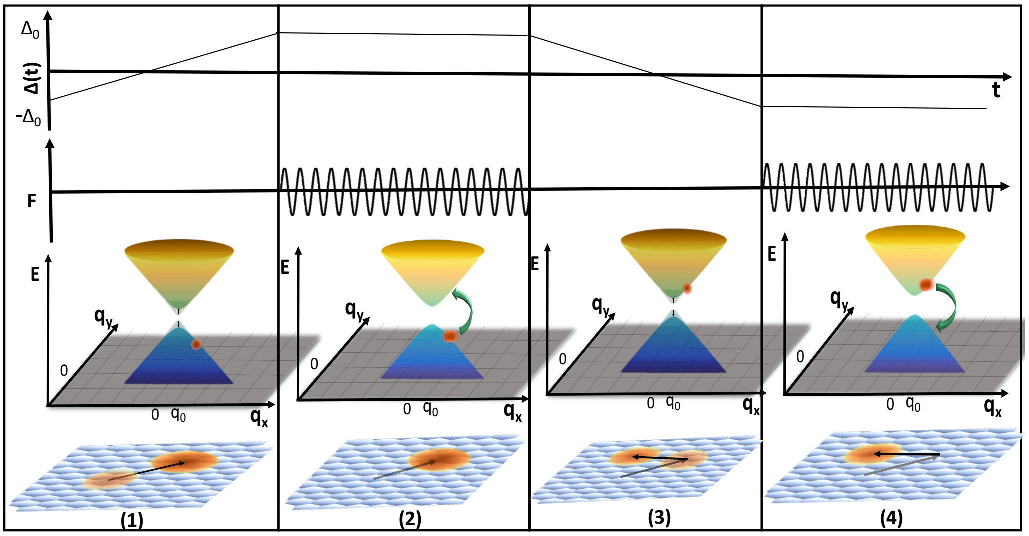

Figure 4.5: Scheme for amplification of the anomalous drift due to electric field analog. One cycle mainly consists of four steps: (1) Δ is changed from $-\Delta_0$ to Δ_0 adiabatically, (2) Δ is kept constant and a weak sinusoidal force is applied to achieve band switching, (3) Δ ramped adiabatically in the opposite direction, (4) Again a π pulse using a sinusoidal force. Upper two panels show how the sublattice offset-energy and external force is changed in time for different steps in the cycle. In the third panel, we show the schematic for wavepacket localized in the vicinity of a Dirac point during the cycle. The lowermost panel illustrates the motion in real space. During each adiabatic step, the wavepacket center shifts significantly with transverse drift in the same direction. On the other hand, the time average displacement during the process of band switching is negligible. This results in an overall transverse drift during one cycle.

some detuning effects as the resonance condition is fulfilled only the center of the wavepacket. This gives rise to a small discrepancy in numerics and theory. Also, we neglected the terms oscillating at frequency ω in Eq. (A.45), and hence the oscillations in COM motion are not captured by Eq. (4.20).

Relation to previous shift-currents work

During the band switching process, we came across interesting connections between the anomalous drift and the shift vector, $\mathbf{A}_{ee} - \mathbf{A}_{gg} - \nabla_{\mathbf{q}}\Theta$. This shift vector also appears in the study of many other optoelectronic processes in solids. It is responsible for the shift current bulk photovoltaic effect [317, 188, 187, 240, 239] and for the large nonlinear optical response in many non-centrosymmetric crystals. In these shift current calculations, one considers a completely filled valence band,

and a continuous pumping to the conduction band gives rise to a shift current. In these materials, continuous pumping arises from relaxation processes; in contrast, the schemes proposed here are based on fully coherent quantum dynamics. The contribution from different k points in BZ is proportional to the shift vector, and the proportionality constant depend on many other factors like amplitude and frequency of drive, temperature, etc. Since, the shift current is obtained by summing up this contribution from all k points in a BZ, and thus it is non-zero only for crystals without an inversion center. Furthermore, the polarization of light directly affects the phase Θ of the transition matrix elements, and thus can change the shift vector significantly.

The effect for localized wavepackets depends only on the shift vector at the wavepacket center. Also, while electrons in crystals were treated through the Fermi golden rule, the wave packet we are considering exhibits coherent oscillations between the bands, and the observed anomalous drift oscillates in the same manner as the relative band population. Most importantly, the transition matrix we consider is general, and does not apply only to optical transitions or nonlinear optical processes [317, 393, 187, 240, 239]. In the context of the optoelectronic processes discussed in these references, the shift vector depends on the interband Berry connection, and is given by $\mathbf{A}_{\mathrm{ee}} - \mathbf{A}_{\mathrm{gg}} - \nabla_{\mathbf{q}}(\mathrm{Arg}(\mathbf{F} \cdot \mathbf{A}_{\mathrm{ge}}))$. This dependence originates from the fact that the transition is induced by a time-periodic force, and thus according to Eq. (4.24), $\Theta = \mathrm{Arg}(\mathbf{F} \cdot \mathbf{A}_{\mathrm{ge}})$. Hence, our work generalizes the shift-current expression to $\mathbf{A}_{\mathrm{ee}} - \mathbf{A}_{\mathrm{gg}} - \nabla_{\mathbf{q}}\Theta$, where Θ is the phase of the matrix element connecting the two bands, and the previous results appear as a special case.

4.5 Application: Pump from electric field analog

Our primary goal is to show how time-dependent Berry connections could be used to control particle motion. Indeed, the two mechanisms to achieve an anomalous drift from time-dependent geometric properties as discussed above can be combined to produce a pumping effect on a wavepacket. During the adiabatic evolution (Sec. 4.3), the sign of transverse drift depended on the band index, and the rate of change of Δ. For the non-adiabatic case, we mentioned two schemes for band transition, and it was observed that the wavepacket displacement was negligible when a linear and time-periodic force was applied. These effects can be combined to produce an amplified transverse drift (Fig. 4.5), with the following steps:

1. The wavepacket is initialized in the lower band, and the sublattice offset-energy Δ is changed adiabatically from -Δ_0 to Δ_0. This results in a transverse drift.

2. A π pulse is realized by applying a weak external sinusoidal force on the wavepacket. The wavepacket ends up in the upper band after this pulse with the same q distribution as before. There is no significant transverse drift during this step.

3. Now, Δ is changed in the opposite direction. The transverse drift during this step is expected to be the same as in the step one because both, the band index, and the rate of change of Δ have opposite sign.

4. Another π pulse is applied, and the wavepacket returns to the lower band.

After these four steps, the wavepacket shifts by a finite distance in the transverse direction but returns back to the ground band with the same q-distribution. Importantly, also the lattice parameters are back to their initial values, which makes it possible to repeat these steps in a pump cycle. We discuss an alternative scheme only involving band transfer (but no adiabatic changes) in App. A.4.

The overall transverse drift after one complete cycle can also be associated with the total phase picked up by the state in this non-adiabatic but cyclic process. We notice that after a full cycle of the scheme shown in Fig. 4.5, the space-periodic part of Bloch wavefunction in Eq. (4.13) changes from $|\Phi(\mathbf{q},t)\rangle = |g(\mathbf{q})\rangle$ at $t = 0$ to $|\Phi(\mathbf{q},t)\rangle = e^{i\theta(\mathbf{q})}\,|g(\mathbf{q})\rangle$, where $\theta(\mathbf{q})$ has contribution both from dynamical and geometrical terms. Interestingly, in the scheme described above, the overall dynamical phase vanishes, and thus the phase picked up in one cycle can be interpreted as Aharanov-Anandan phase [3]. Now, according to Eq. (4.15), the COM displacement is given by:

$$\langle \mathbf{r} \rangle = \nabla_{\mathbf{q}} \theta(\mathbf{q})|_{\mathbf{q}_0}, \tag{4.26}$$

for an extremely narrow wavepacket located at $\mathbf{q} = \mathbf{q}_0$. Here, the transverse after one cycle, depends solely on Aharanov-Anandan phase, and is thus non-zero only for those cyclic processes where the state picks up a non-trivial geometric phase.

We explained above how this phase depends on the nature of H', and there is no $\mathbf{q}$ dependent overall phase when band switching is obtained by modulating the sublattice offset-energy. On the other hand, for the weak sinusoidal force case, in the limit $|\Delta| >> q_0$, and for the same gauge choice,

$$\theta(\mathbf{q}) \approx \mathrm{Arg}(\mathbf{F} \cdot \mathbf{A}_{\mathrm{ge}}(\Delta_0)) + \mathrm{Arg}(\mathbf{F} \cdot \mathbf{A}_{\mathrm{eg}}(-\Delta_0)) \approx 2\phi, \tag{4.27}$$

where $\phi = \tan^{-1}(q_y/q_x)$, and thus we expect the displacement after one cycle to be $< \mathbf{r} >= 2/q_0\hat{y}$.

We simulate the motion of wavepacket for one full cycle in Fig. 4.5 (see Fig. A.4 in Appendix for multiple cycles), and observe that the obtained transverse drift shown in Fig. 4.6 is in close agreement with Eq. (4.26). In this case, it was also observed that the wavepacket first expands in real space during the first adiabatic step, and then contracts during the second adiabatic step. It is mainly because the dispersion relation is opposite for two bands, and thus the wavepacket shows a breathing behavior. Hence, at the end of each cycle, we can achieve a significant transverse drift without any spreading of wavepacket in real space.

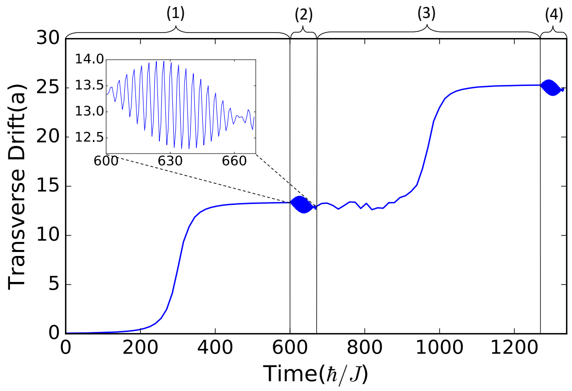

Figure 4.6: Transverse drift for one cycle in scheme shown in Fig. 4.5. We observe a transverse drift during the adiabatic evolution when the sublattice offset is varied from $-\Delta_0$ to Δ_0 in step 1. Next, the wavepacket is excited to the upper band without any significant drift when a sinusoidal force is applied during the step 2. In step 3, it is displaced in the same direction during the adiabatic evolution in the opposite band when sublattice offset is changed in the opposite direction. Again, the wavepacket returns to the lower band without any insignificant displacement during step 4. In this case, the offset was changed very slowly from -0.6 to 0.6 in $T = 600$ to satisfy the adiabaticity condition. The schematics of wavepacket dynamics in q space is shown in Fig. 4.5.

4.6 Discussion and conclusions

In this manuscript, we explored the time dependence of the Berry connection as a means of controlling a wavepacket in a Bloch band. Indeed, there are many ways to control a particle moving in a confined potential. It could be subject to a force, or it could be subject to a variety of quench protocols. A change of a geometric quantity such as the Berry connection, however, is more likely to result in a universal response. Furthermore, we demonstrated that the time derivative of the Berry connection appears as an anomalous velocity in the semiclassical equation of motion for a wavepacket, and can be considered as a momentum space analog of an electric field.

In addition, when a wavepacket is excited to a different band, another interesting connection emerges between the observed anomalous drift and the shift vector, see Eq. (4.20). During the band switching, the wavepacket experiences an anomalous drift which consists of the difference of the Berry connections of the two bands, and a $\mathbf{q}$ space derivative of the argument of the interband matrix element of the drive. And hence, we demonstrated that shift vector expression is more general than the one encountered in the light-induced transitions [317, 393, 187, 19, 188, 101, 152, 398, 344, 172, 240, 239], and explored it in two types of drive.

Indeed, the anomalous drift from the electric field analog should be thought of as a powerful element in the arsenal for controlling a wavepacket in synthetic systems such as optical lattices. Some recent works have discussed how particle transport can be affected by the changes in the geometric flux [264, 363]. Such effects often average out in solid state systems, since all transport effects are averaged over a Fermi sea. Furthermore, changing the lattice geometry in materials on transport-relevant time scales is quite difficult. Atomic and optical systems, in contrast, allow the observation of the motion of tight wavepackets [26], and can realize a variety of time-dependent protocols which can explore the effects from time-dependent band geometry. In solid state setups, such as graphene, the band geometry can be changed by using a circularly polarized drive [254], and the changes could be made adiabatic by applying a smooth envelope to the pulse onset. In principle, one could create a compact wavepacket by creating optical excitations in the sample, and then collimating the beam with barrier structures similar to the methods used for wave vector filtering as described in Ref. [222].

In our manuscript, we provide an example for what the combination of the anomalous velocity effects from the time varying band geometry and interband transition could achieve. We construct a protocol which controllably 'pumps' a wavepacket perpendicular to its group velocity. The observed transverse drift could be amplified without any significant change in the wavepacket size.

Anomalous drifts from time-dependent Berry connection could be at the basis of a rich set of control protocols. It would be interesting to study the effects of time-dependent geometric properties for the degenerate Bloch bands or multi-band systems. Furthermore, geometric effects due to interband excitations could be made richer by considering a momentum shift $\mathbf{q}$. Time-dependent band geometry could even have an effect in solid state system, perhaps when the Fermi sea is shifted due to a constant external field, or a thermal gradient. Beyond wavepacket dynamics, Berry curvature can also modify the energy spectrum of excitons, and can give rise to orbital Zeeman shift analog [329, 406]. It would be interesting to explore stark shift analogs arising from time-dependent Berry connection. Additionally, higher order moments of Berry curvature can also affect the magneto-optical properties of the materials [203, 402]. Using the recent proposals to control and tune the band geometry in monolayer materials [311, 182], one can look up for the effects of time-dependent band geometry in many non linear optical responses as well. We expect that these effects will be the subject of future investigation, as well as the focus of experimental efforts.

Appendix A

APPENDIX

A.1 Electric field analog in equation of motion – adiabatic case

Consider a quantum system described by a Hamiltonian H which depends on quasi momentum $\mathbf{q}$, and on a set of parameters given by $\mathbf{G}$. The eigenstates of this H are denoted by $|u_n(\mathbf{q},\mathbf{G})\rangle$, such that,

$$H(\mathbf{q},\mathbf{G})\,|u_n(\mathbf{q},\mathbf{G})\rangle = E_n(\mathbf{q},\mathbf{G})\,|u_n(\mathbf{q},\mathbf{G})\rangle\,. \tag{A.1}$$

Now, consider the adiabatic evolution of this system as $\mathbf{q}(t)$ and $\mathbf{G}(t)$ changes slowly with time. According to the quantum adiabatic theorem, a system initially in one of its eigenstates $|u_n(\mathbf{q}(0),\mathbf{G}(0)\rangle$ will remain in the instantaneous eigenstate of the Hamiltonian $H(\mathbf{q}(t),\mathbf{G}(t))$ throughout the process. The additional (geometric) phase picked by the state, when $\mathbf{R}$ is varied slowly along the contour C is given by:

$$\gamma_n = \oint_C d\mathbf{R}\cdot\mathbf{A}^n(\mathbf{R}), \tag{A.2}$$

where $\mathbf{R} = (\mathbf{q},\mathbf{G})$, and $\mathbf{A}^n(\mathbf{R})$ is given by:

$$\mathbf{A}^n(\mathbf{R}) = i\,\langle u_n(\mathbf{R})|\,\frac{\partial}{\partial\mathbf{R}}\,|u_n(\mathbf{R})\rangle\,. \tag{A.3}$$

In this case $\mathbf{q}(t)$ is a 3D vector, and we can take the dimension of $\mathbf{G}$ as m, i.e, $\mathbf{G} = (G_1, G_2, ...G_m)$. We can define a gauge field tensor derived from the Berry vector potential:

$$\mathbf{\Omega}^{\mathbf{n}}_{\mu\nu} = \frac{\partial}{\partial R_\mu}A^n_{R_\nu} - \frac{\partial}{\partial R_\nu}A^n_{R_\mu}, \tag{A.4}$$

known as the Berry curvature. In this case $\mathbf{R} = (q_1, q_2, q_3, G_1, G_2, ...G_m)$, and thus we can recast the Eq. (A.4) into a vector form for $\mu,\nu \,\epsilon\, (1,2,3)$

$$\mathbf{\Omega}^n(\mathbf{q}) = \nabla_{\mathbf{q}}\times\mathbf{A}^n(\mathbf{q}), \tag{A.5}$$

where the vector $\mathbf{\Omega}^n$ is related to the Berry curvature tensor by $\Omega^n_{ij} = \epsilon_{ijk}(\mathbf{\Omega}^n)_k$. The main point to be noted here is that this vector form is not generalized here for all μ,ν, but only for the $\mathbf{q}$ part.

We are interested in studying the motion of particle as different parameters are varied slowly with time. For adiabatic evolution, the wave function changes slowly, and apart from a phase factor to the first order in the rate of change of the Hamiltonian, the wave function is given by:

$$|\psi(n)\rangle = |u_n\rangle - i\hbar \sum_{n'\neq n} \frac{|u_{n'}\rangle \left\langle u_{n'}|\frac{\partial u_{n'}}{\partial t}\right\rangle}{(\varepsilon_n - \varepsilon_{n'})}. \tag{A.6}$$

Now the velocity operator in the q-representation has the form $\mathbf{v}(q,t) = \frac{1}{\hbar}\nabla_q H(q,t)$, so the average velocity in a state of given q to the first order is given by

$$\begin{aligned} \mathbf{v}_n(\mathbf{q}) &= \frac{1}{\hbar}\nabla_{\mathbf{q}}\varepsilon_n(\mathbf{q}) \\ &- i\sum_{n'\neq n}\left\{\frac{\langle u_n|\,\nabla_{\mathbf{q}}H(\mathbf{q})\,|u_{n'}\rangle \left\langle u_{n'}|\frac{\partial u_n}{\partial t}\right\rangle}{\varepsilon_n - \varepsilon_n'} - c.c\right\}, \end{aligned} \tag{A.7}$$

where c.c denotes the complex conjugate. Using the fact that when $n \neq n'$, $\langle u_n|\,\nabla_{\mathbf{q}}H(\mathbf{q})\,|u_{n'}\rangle = (\varepsilon_n - \varepsilon_{n'})\left\langle \nabla_{\mathbf{q}}u_n|u_{n'}\right\rangle$, and the identity $\sum |u_{n'}\rangle\langle u_{n'}| = 1$, we find,

$$\mathbf{v}_n(\mathbf{q}) = \frac{1}{\hbar}\nabla_{\mathbf{q}}\varepsilon_n(\mathbf{q}) - i\left[\left\langle \nabla_{\mathbf{q}}u_n|\frac{\partial u_n}{\partial t}\right\rangle - \left\langle \frac{\partial u_n}{\partial t}|\nabla_{\mathbf{q}}u_n\right\rangle\right]. \tag{A.8}$$

The t dependence is coming through $\mathbf{R}$, and thus we can write

$$\left|\frac{\partial u_n}{\partial t}\right\rangle = \dot{\mathbf{q}}\cdot\nabla_{\mathbf{q}}\,|u_n\rangle + \dot{J}_\mu\left|\frac{\partial u_n}{\partial J_\mu}\right\rangle, \tag{A.9}$$

where summation over μ is implied. Substituting this expression in Eq. (A.8), we get the ith component of velocity as:

$$v_i(\mathbf{q}) = \frac{\partial\varepsilon_n}{\hbar\partial q_i} - i\dot{q}_j\left[\left\langle\frac{\partial u_n}{\partial q_i}|\frac{\partial u_n}{\partial q_j}\right\rangle - \left\langle\frac{\partial u_n}{\partial q_j}|\frac{\partial u_n}{\partial q_i}\right\rangle\right] - i\dot{J}_\mu\left[\left\langle\frac{\partial u_n}{\partial q_i}|\frac{\partial u_n}{\partial J_\mu}\right\rangle - \left\langle\frac{\partial u_n}{\partial J_\mu}|\frac{\partial u_n}{\partial q_i}\right\rangle\right]. \tag{A.10}$$

Using Eqs. (A.3), (A.4) and (A.5), we get:

$$v_i(\mathbf{q}) = \frac{\partial\varepsilon_n(\mathbf{q})}{\hbar\partial q_i} - \epsilon_{ijk}\dot{q}_j\mathbf{\Omega}_k^n - i\dot{J}_\mu\left[\left\langle\frac{\partial u_n}{\partial q_i}|\frac{\partial u_n}{\partial J_\mu}\right\rangle - \left\langle\frac{\partial u_n}{\partial J_\mu}|\frac{\partial u_n}{\partial q_i}\right\rangle\right]. \tag{A.11}$$

The last term in Eq. (A.11) above can be expanded as:

$$\begin{aligned} &i\left[\left\langle\frac{\partial u_n}{\partial q_i}|\frac{\partial u_n}{\partial J_\mu}\right\rangle - \left\langle\frac{\partial u_n}{\partial J_\mu}|\frac{\partial u_n}{\partial q_i}\right\rangle\right] \\ &= -i\frac{\partial}{\partial J_\mu}\left\langle u_n|\frac{\partial}{\partial q_i}|u_n\right\rangle + i\left\langle\frac{\partial u_n}{\partial q_i}|\frac{\partial u_n}{\partial J_\mu}\right\rangle + i\left\langle u_n|\frac{\partial}{\partial q_i}\frac{\partial}{\partial J_\mu}|u_n\right\rangle \\ &= -\frac{\partial A_{q_i}^n}{\partial J_\mu} + i\frac{\partial}{\partial q_i}\left\langle u_n|\frac{\partial}{\partial J_\mu}|u_n\right\rangle, \end{aligned} \tag{A.12}$$

and thus the Eq. (A.11) becomes:

$$\begin{aligned} v_i(\mathbf{q}) =& \frac{\partial \varepsilon_n(\mathbf{q})}{\hbar \partial q_i} - (\dot{\mathbf{q}} \times (\nabla \times \mathbf{A}^n))_i + \dot{J}_\mu \frac{\partial \mathbf{A}_i^n}{\partial J_\mu} \\ & - i\dot{J}_\mu \frac{\partial}{\partial q_i} \left\langle u_n \right| \frac{\partial}{\partial J_\mu} \left| u_n \right\rangle . \end{aligned} \tag{A.13}$$

It can be written more concisely as:

$$\dot{r}_i(\mathbf{q}) = \frac{\partial \varepsilon_n(\mathbf{q})}{\hbar \partial q_i} - (\dot{\mathbf{q}} \times (\nabla \times \mathbf{A}^n))_i + \left(\frac{\partial \mathbf{A}_i^n}{\partial t} \right)_{\mathbf{q}} - \nabla_{\mathbf{q}} \chi_n(t), \tag{A.14}$$

where

$$\chi_n(t) = i \left\langle u_n \right| \frac{\partial}{\partial t} \left| u_n \right\rangle . \tag{A.15}$$

This equation has a striking similarity with the equation of motion of a charged particle in the presence of an electric and magnetic field as given by:

$$\hbar \dot{\mathbf{k}} = Q \nabla_{\mathbf{r}} \Phi + Q \dot{\mathbf{r}} \times (\nabla_{\mathbf{r}} \times \mathbf{A}) - Q \left(\frac{\partial \mathbf{A}}{\partial t} \right)_{\mathbf{r}}, \tag{A.16}$$

where Q is the electric charge, Φ the scalar potential, and $\mathbf{A}$ is the electromagnetic vector potential. This allows us to define analogs of electric and magnetic field from the geometric quantities in Eq. (A.14) as follows:

$$\mathbf{B} \quad \rightarrow \quad \mathbf{\Omega}^n, \tag{A.17}$$

$$\mathbf{E} \quad \rightarrow \quad \left(\frac{\partial \mathbf{A}^n}{\partial t} - \nabla_{\mathbf{q}} \chi_n \right). \tag{A.18}$$

These quantities are gauge invariant as shown below.

Gauge invariance of the electric field analog

From electrodynamics, we know that $\mathbf{E} = -\nabla_{\mathbf{r}}(\Phi) - \frac{\partial \mathbf{A}}{\partial t}$, and $\mathbf{B} = \nabla \times \mathbf{A}$ are gauge invariant quantities. So in this section, we prove that a similar gauge invariance is satisfied by their analogs. If we make a gauge transformation

$$\left| u_n(\mathbf{R}) \right\rangle \rightarrow e^{i\zeta(\mathbf{R})} \left| u_n(\mathbf{R}) \right\rangle , \tag{A.19}$$

where $\zeta(\mathbf{R})$ is an arbitrary smooth function, then $\mathbf{A}^n$ transforms as follows:

$$\mathbf{A}^n \rightarrow \mathbf{A}^n - \nabla_{\mathbf{q}} \zeta(\mathbf{q}, \mathbf{G}). \tag{A.20}$$

In analogy to the EM vector potential, we want to show that in Eq. (A.14), $\left(\frac{\partial \mathbf{A}^n}{\partial t} \right)_{\mathbf{q}} - \nabla_{\mathbf{q}} \chi_n$ is a gauge invariant quantity. Let $\left| u_n'(\mathbf{R}) \right\rangle = e^{i\zeta(\mathbf{R})} \left| u_n(\mathbf{R}) \right\rangle$, then the term $\nabla_{\mathbf{q}} \chi$ transforms as :

$$\nabla_{\mathbf{q}} \chi' = i \nabla_{\mathbf{q}} \left\langle u_n' \right| \frac{\partial}{\partial t} \left| u_n' \right\rangle = i \nabla_{\mathbf{q}} \left[\left\langle u_n \right| \frac{\partial}{\partial t} \left| u_n \right\rangle + i \frac{\partial \zeta}{\partial t} \right],$$

$$\nabla_{\mathbf{q}}\chi' = \nabla_{\mathbf{q}}\chi - \nabla_{\mathbf{q}}\frac{\partial \zeta}{\partial t}, \tag{A.21}$$

and the other term $\left(\frac{\partial \mathbf{A}'^{n}}{\partial t}\right)_{\mathbf{q}}$ transforms as follows

$$\left(\frac{\partial \mathbf{A}'^{n}}{\partial t}\right)_{\mathbf{q}} = \left(\frac{\partial \mathbf{A}^{n}}{\partial t}\right)_{\mathbf{q}} - \nabla_{\mathbf{q}}\left(\frac{\partial \zeta}{\partial t}\right)_{\mathbf{q}}. \tag{A.22}$$

So, the expression $\left(\frac{\partial \mathbf{A}^{n}}{\partial t}\right)_{\mathbf{q}} - \nabla_{\mathbf{q}}\chi_n$ is gauge invariant, and hence the equation of motion is not modified under the gauge transformation. This term $\left(\frac{\partial \mathbf{A}^{n}}{\partial t}\right)_{\mathbf{q}} - \nabla_{\mathbf{q}}\chi_n$ is analogous to the electric field **E** in the real space.

A.2 Derivation for equation of motion for a Bloch wavepacket undergoing Rabi oscillations

Consider a wavepacket with support on two Bloch bands. We want to study its evolution under the Hamiltonian $H - \mathbf{F}(t)\cdot\hat{\mathbf{r}}$, where H is translationally invariant, and $\mathbf{F}(t)$ is the force applied on the wavepacket. The wavefunction describing the system is given by Schrodinger equation:

$$i\frac{\partial}{\partial t}\left|\Psi(\mathbf{r},t)\right\rangle = \left(H(t) - \mathbf{F}(t)\cdot\hat{\mathbf{r}}\right)\left|\Psi(\mathbf{r},t)\right\rangle. \tag{A.23}$$

Here, we can express $|\Psi(\mathbf{r},t)\rangle$ as a superposition of Bloch wavefunctions. For a two-band model we can write:

$$\left|\Psi(\mathbf{r},t)\right\rangle = \sum_{n=1,2}\int_{BZ} d^2\mathbf{k}\phi_n(\mathbf{k},t)e^{i\mathbf{k}\cdot\mathbf{r}}\left|u_n(\mathbf{k})\right\rangle, \tag{A.24}$$

where $|u_n(\mathbf{k})\rangle$ is the cell-periodic part of n^{th} Bloch wavefunction. Substituting in Eq. (A.23) above, we get:

$$\begin{aligned} &i\frac{\partial}{\partial t}(\phi_n(\mathbf{k},t)) = \\ &\sum_{m=1,2}\int_{BZ} d^2\mathbf{k}(\phi_m(\mathbf{k},t)\left\langle u_n(\mathbf{k},t)\right| H \left|u_m(\mathbf{k},t)\right\rangle \\ &\qquad - i\left\langle u_n(\mathbf{k},t)\right| \mathbf{F}\cdot\nabla_{\mathbf{k}}(\phi_m(\mathbf{k},t)\left|u_m(\mathbf{k})\right\rangle)). \end{aligned} \tag{A.25}$$

Now, since H is translationally invariant, and there is no mixing between different **k** components, so we can use the ansatz:

$$\left|\Psi(\mathbf{r},t)\right\rangle = \sum_{n=1,2}\int_{BZ} d^2\mathbf{k}\phi_n(\mathbf{k}(t),t)e^{i\mathbf{k}(t)\cdot\mathbf{r}}\left|u_n(\mathbf{k}(t))\right\rangle, \tag{A.26}$$

where $\mathbf{k}(t) = \mathbf{k} + \int_0^t \mathbf{F}(t')dt'$ and defining :

$$\psi_n(\mathbf{k}, t) \equiv \phi_n(\mathbf{k}(t), t), \tag{A.27}$$

we get the following equation for $\psi_n(\mathbf{k}, t)$

$$i\frac{\partial}{\partial t}\psi_n(\mathbf{k}, t) = \sum_m \left(H^{n,m}(t) - \mathbf{F} \cdot \mathbf{A}^{n,m}(\mathbf{k}(t))\right)\psi_m(\mathbf{k}, t), \tag{A.28}$$

where $\mathbf{A}^{n,m}(\mathbf{k}) = i\left\langle u_n(\mathbf{k})\right| \nabla_{\mathbf{k}} \left|u_m(\mathbf{k})\right\rangle$. This ansatz was used mainly to consider the fact that probability distribution in **k** moves in time in the presence of a force, and the coefficients at $\mathbf{k} + \int_0^t \mathbf{F}(t)dt$ are decided by the initial conditions at **k**. In the absence of an external force, we can write :

$$\left|\Psi(\mathbf{r}, t)\right\rangle = \sum_{n=1,2} \int_{BZ} d^2\mathbf{k} e^{i\mathbf{k}\cdot\mathbf{r}}\psi_n(\mathbf{k}, t)\left|u_n(\mathbf{k})\right\rangle. \tag{A.29}$$

For translationally invariant H, there is no mixing between different **k** and at each **k**, we have:

$$i\frac{\partial}{\partial t}\psi_n(\mathbf{k}, t) = \sum_{m=1,2} H(\mathbf{k}, t)^{n,m}\psi_m(\mathbf{k}), \tag{A.30}$$

and $|\psi_1(\mathbf{k}, t)|^2 + |\psi_2(\mathbf{k}, t)|^2$ is a function of **k** only. This allows us to express:

$$\left|\Psi(\mathbf{r}, t)\right\rangle = \int d^2\mathbf{k} e^{i\mathbf{k}\cdot\mathbf{r}}\phi(\mathbf{k})\left|\Phi(\mathbf{k}, t)\right\rangle, \tag{A.31}$$

where $\phi(\mathbf{k}) = \sqrt{|\psi_1(\mathbf{k}, t)|^2 + |\psi_2(\mathbf{k}, t)|^2}$ and $\left|\Phi(\mathbf{k}, t)\right\rangle$ is a superposition of $\left|u_n(\mathbf{k})\right\rangle$ with time-dependent coefficients such that

$$i\frac{\partial}{\partial t}\left|\Phi(\mathbf{k}, t)\right\rangle = H(\mathbf{k}, t)\left|\Phi(\mathbf{k}, t)\right\rangle, \tag{A.32}$$

and $\left\langle\Phi(\mathbf{k}, t)\right| \left|\Phi(\mathbf{k}, t)\right\rangle = 1$.

Now, we can do something similar in the presence of an external force by defining

$$\left|\Psi(\mathbf{r}, t)\right\rangle = \int d^2\mathbf{k} e^{i\mathbf{k}(t)\cdot\mathbf{r}}\phi(\mathbf{k})\left|\Phi(\mathbf{k}(t), t)\right\rangle, \tag{A.33}$$

where $\phi(\mathbf{k}) = \sqrt{\phi_1(\mathbf{k}, 0)^2 + \phi_2(\mathbf{k}, 0)^2}$, $\mathbf{k}(t) = \mathbf{k} + \int_0^t \mathbf{F}(t')dt'$, and $\left|\Phi(\mathbf{k}(t), t)\right\rangle$ is governed by $H - \mathbf{F} \cdot \mathbf{A}$. For the special case of sinusoidal force $\mathbf{F}(t) = \mathbf{F}_0 \sin(\omega t)$, we notice that $\mathbf{k}(t = nT) = \mathbf{k}$, and hence at any time t which is integer multiple of time period T, we can write:

$$\left|\Psi(\mathbf{r}, t)\right\rangle = \int d^2\mathbf{k} e^{i\mathbf{k}.\mathbf{r}}\phi(\mathbf{k})\left|\Phi(\mathbf{k}, t)\right\rangle, \tag{A.34}$$

where $\left|\Phi(\mathbf{k}, t)\right\rangle$ is governed by:

$$i\frac{\partial}{\partial t}\left|\Phi(\mathbf{k}, t)\right\rangle = \left(H_0 - \mathbf{F}(t) \cdot \mathbf{A}(\mathbf{k})\right)\left|\Phi(\mathbf{k}, t)\right\rangle. \tag{A.35}$$

C.O.M velocity for near resonant periodic drive

For a two-level system, consider the full Hamiltonian

$$H = H_0 + H' = \begin{bmatrix} E_1 & 0 \\ 0 & E_2 \end{bmatrix} + \begin{bmatrix} 0 & \frac{V}{2}e^{i\theta}e^{i\omega t} \\ \frac{V}{2}e^{-i\theta}e^{-i\omega t} & 0 \end{bmatrix}, \tag{A.36}$$

where V is taken as real. This gives

$$|\Phi(\mathbf{q},t)\rangle = a(t)e^{i\omega t/2}\,|u_1(\mathbf{q},t)\rangle + b(t)e^{-i\omega t/2}\,|u_2(\mathbf{q},t)\rangle\,, \tag{A.37}$$

and substituting in Eq. (4.15), and neglecting the terms oscillating at frequency ω, we get

$$\begin{aligned}\langle\mathbf{r}\rangle &= \int d^2\mathbf{q}|\phi(\mathbf{q},\mathbf{q}_0)|^2\,\langle\Phi(\mathbf{q},t)|\,\nabla_{\mathbf{q}}\,|\Phi(\mathbf{q},t)\rangle \\ &= \langle\mathbf{A}_{nn}\rangle\,|_{\mathbf{q}_0} + a^*(t)\nabla_{\mathbf{q}}a(t) + b^*(t)\nabla_{\mathbf{q}}b(t).\end{aligned} \tag{A.38}$$

Now, subsituting Eq. (A.37) in Eq. (A.36), we get

$$\frac{\partial}{\partial t}a(t) = -i\left((E_1 + \frac{\omega}{2})a(t) + \frac{V}{2}e^{i\theta}b(t)\right) \tag{A.39}$$

and

$$\frac{\partial}{\partial t}(b(t)) = -i\left(\left(E_2 - \frac{\omega}{2}\right)b(t) + \frac{V}{2}e^{-i\theta}a(t)\right). \tag{A.40}$$

If the wavepacket starts in one of the eigen states, we get the following expression for velocity:

$$\begin{aligned}\mathbf{v} =& |(a(t)|^2\nabla_{\mathbf{q}}E_1 + |b(t)|^2\nabla_{\mathbf{q}}E_2 \\ &+ \frac{\partial}{\partial t}\langle\mathbf{A}_{nn}\rangle + \frac{\partial}{\partial t}\left(|a(t)|^2\nabla_{\mathbf{q}}(\theta)\right).\end{aligned} \tag{A.41}$$

Given the fact that

$$\frac{\partial}{\partial t}|a(t)|^2 = -\frac{\partial}{\partial t}|b(t)|^2, \tag{A.42}$$

we can write

$$\mathbf{v} = \left\langle\nabla_{\mathbf{q}}E_n\right\rangle + \frac{\partial}{\partial t}\langle\mathbf{A}_{nn}\rangle + \frac{\partial}{\partial t}\langle\phi_n\rangle\,, \tag{A.43}$$

where

$$\phi_1 = -\phi_2 = \frac{\theta}{2} = \frac{1}{2}\mathrm{Arg}\,\langle u_1|\,H'\,|u_2\rangle\,. \tag{A.44}$$

It is worth mentioning again that the above equation does not take into account the fast oscillatory motion at frequency ω. Now, if we include such terms, then Eq. (A.38) is modified as follows:

$$\langle\mathbf{r}\rangle = \langle\mathbf{A}_{nn}\rangle\,|_{\mathbf{q}_0} + a^*(t)\nabla_{\mathbf{q}}(a(t)) + b^*(t)\nabla_{\mathbf{q}}b(t) + a^*(t)b(t)e^{-i\omega t}\mathbf{A}_{ge} + a(t)b^*(t)e^{i\omega t}\mathbf{A}_{eg}. \tag{A.45}$$

A.3 Results for different sizes of wavepacket

Here, we consider the effects of increasing the size of wavepacket in quasi-momentum space. Since, the resonance condition is satisfied only at the center of wavepacket, so a larger wavepacket would have significant detuning. This detuning would decrease the transition probability after a Rabi cycle, and would also decrease the transverse drift observed during the process of band switching. We plot the resulting transverse drift and excitation probabilities for three different wavepacket sizes in Fig. A.1, and the other parameters are same as that for Fig. 4.3 in the main text. These detuning effects would become more prominent when band switching process is repeated more than once and can result in a significant change in the transverse drift as shown in Fig. A.2.

A.4 Pump from non-adiabatic processes only

In Sec. 4.5, we showed how one can combine adiabatic and non-adiabatic steps to amplify the anomalous drift obtained from the electric field analog. We mainly exploited the fact that shift vector was vanishingly small when transition was achieved using a time-periodic force, and the transverse drift was same during two adiabatic steps of the cycle. In Sec. 4.4, we also showed that the shift vector is significantly large when band transition is achieved using the sublattice offset-energy modulation. Now, one can in fact combine these two different kinds of non-adiabatic processes to amplify the transverse drift arising purely from the changes in the Berry connection. Here, we simulate the motion of a wavepacket undergoing Rabi oscillations such that transition from lower to upper band is achieved by modulating offset energy, and use sinusoidal force for the opposite step. The wavepacket is shifted significantly during the sublattice offset-energy modulation step only, and its direction depends only on the bands involved in transition as shown in Fig. A.3.

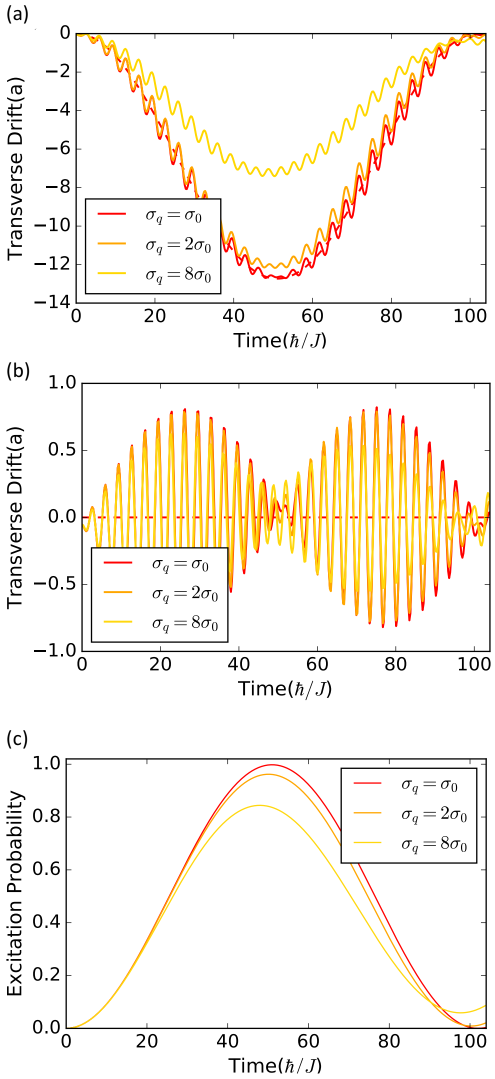

Figure A.1: Transverse drift for different wavepacket sizes for (a)$\Theta = 0.0$, (b) $\Theta = \phi$. Transition probability is the same for all of the above cases and its dependence on wavepacket size is shown in (c). Here σ_0 is the size of wavepacket considered in the main text (Fig. 4.3).

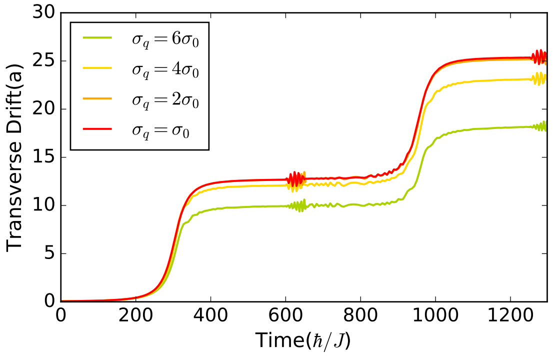

Figure A.2: This figures shows the effect of the wavepacket size on one full cycle of the scheme discussed in Sec. 4.5. For a large wavepacket, the anomalous drift after one cycle would decrease significantly with its size.

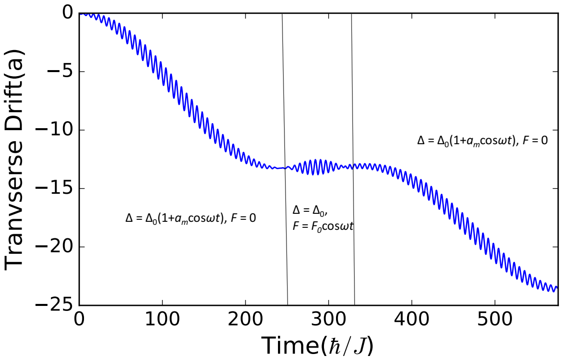

Figure A.3: Transverse drift during three different band switching steps. For the first and third steps, we modulate the sublattice offset-energy Δ, and the wavepacket moves from lower to upper band which results in a significant transverse drift. During the second step, we keep Δ constant, and apply a sinusoidal force which results in a negligible drift.

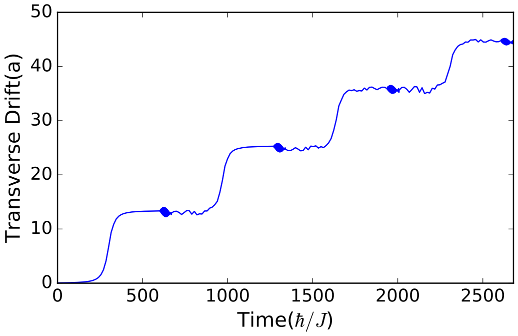

Figure A.4: Transverse drift after two cycles of the scheme discussed in Sec. 4.5.

Chapter 5

INTERACTION-ENHANCED SHIFT CURRENT IN TWISTED BILAYER GRAPHENE

5.1 Motivation

In the previous chapter, we came across an interesting quantity known as shift-vector. It represents the shift in the center of the Bloch wavepacket upon excitation between bands. It can give rise to a very strong non-linear optical response (NLOR) known as shift-current in materials with non-zero Berry curvature profile. This shift-current response is finding many applications in photovoltaics. The magnitude of shift-vector quantity is often dictated by the size of the unit cell in real space. The non-trivial topology along with large unit size of moiré materials renders them a perfect platform to study such responses. Moiré materials, in particular twisted bilayer graphene (TBG), exhibit a range of fascinating phenomena, the root of which can be traced back to the interplay of small kinetic energies, topologically non-trivial wavefunctions, and strong interactions. In this work, we analyze the non-linear second-order photoresponse of TBG as a function of various experimentally accessible parameters, specifically twist angle and doping. We find that, in the absence of interactions, the response of the system has a generic form near vicinity of the magic angle and, in general, is dictated by two energy scales: mean energy difference between same momentum states located in the hole and electron flat bands; and the direct gap between flat and dispersive bands. We then study how electron-electron interactions affect this photoconductivity, and find many additional features arising from the change in band structure and quantum geometry tensor. Our results highlight the connection between non-trivial geometric properties of TBG and its optical response, as well as provide a roadmap for optical probe experiments intended to study the role of interactions in moiŕe materials.

5.2 Introduction

The underlying quantum geometry (QG) of Bloch wavefunctions is playing an increasingly important role in predicting physical properties of quantum materials. Many interesting signatures of QG are revealed in transport properties and optical responses of these systems [240, 217, 259, 6, 355]. The quantized anomalous linear Hall effect in the absence of magnetic field in time-reversal symmetric setups is one very well-known example of band topology influence on transport properties [377]. Recently, it has been shown that such QG related phenomena are not limited to linear response to external electric fields, but can manifest themselves in nonlinear optical responses (NLOR) as well [238, 240, 217, 259, 6, 355, 157, 365, 323, 374]. Furthermore, such NLOR *do not require breaking of time-reversal symmetry* (TRS) but can occur in TRS preserving systems with non-zero Berry curvature profile [238, 157, 365, 323, 374]. These non-linear effects can manifest in various ways, such as non-linear response to DC fields (induced by Berry curvature dipole [238, 323, 383]), second-harmonic generation (SHG), and bulk-photovoltaic effects like shift-current (SC) [393, 342, 253, 285], and circular photogalvanic effects (CPGE)[140, 57, 158]. Especially, the band topology-induced non-linear response to AC fields have garnered significant attention in recent years [374, 57, 158].

The shift-current response [317] one example of a NLOR, has been of prime interest as it offers a possibility to generate a giant DC response from a weak linearly polarized electromagnetic fields, and can have immense potential in photovoltaic applications [285, 79, 393, 285]. Most interestingly, the origins of this effect can be traced back to the geometric properties of the system [365] and microscopically arises due to change in properties of the Bloch wavefunction upon excitation between bands. Specifically, the magnitude of such band transition-dependent QG effects is often dictated by the change in average position of Bloch wavefunctions within the unit cell. Many previous works have studied shift-current response in bilayer graphene and TMDs [382, 303, 7], and have found these 2D systems a promising platform to observe band topology-induced NLOR. Furthermore, QG-induced processes become more important for flat bands [355, 380] due to their featureless dispersion. Thus, a large unit cell along with very small electronic bandwidths of moiré materials renders them the perfect avenue to explore these QG-dependent non-linear optical responses. A few recent works have explored this possibility in twisted bilayer graphene (TBG) [166, 209], highlighting the unprecedented magnitude of the response at the magic angle. Here, we complement these studies by systematically studying dependence of photoresponse on system parameters and its robustness to electron-electron interactions that are known to drastically alter the non-interacting bandstructure profiles [73]. From the technological perspective, these moiré materials can find important applications in low THz optoelectronics due to their characteristic electron energy scales of the order of few meV's and highly tunable small bands gaps.

Many properties of TBG are tunable experimentally either by changing the twist angle, the encapsulation enviroment, or by varying doping of the sample. Varying twist angle allows to access regime where electronic bandwidth is minimal and small compared to the characteristic energy scale of electronic interaction. In this regime precisely, interactions are responsible for TBG exhibiting a plethora of complex phenomena such as correlated insulating and superconducting behavior [47, 49, 391], orbital magnetism [216, 308], and emergent ferromagnetism[310]. In this work, we present a detailed analysis of shift current response in TBG investigating its dependence on twist angle, encapsulation environment. Specifically, we identify the role of band structure, relevant quantum tensor elements, and the role of system's symmetries in determining the shift-current response. Inspired by recent experimental results [73] we consider specific types of electron-electron renormalizations of the electron bandstructure, see Fig.5.1a-b, [126, 284, 118] to demonstrate that these interactions can change both the magnitude and frequency response of the second-order conductivity. These changes can be understood as stemming from the interaction-induced band flattening modifying the quantum geometric tensor [69, 199], $\chi^n_{\mu\nu}$, which depends on the structure of Bloch wavefunctions:

$$\chi^n_{\alpha\beta}(\boldsymbol{k}) = \left\langle \frac{\partial u(\boldsymbol{k})}{\partial k_\alpha} \middle| \frac{\partial u(\boldsymbol{k})}{\partial k_\beta} \right\rangle - \left\langle \frac{\partial u(\boldsymbol{k})}{\partial k_\alpha} \middle| u(\boldsymbol{k}) \right\rangle \left\langle u(\boldsymbol{k}) \middle| \frac{\partial u(\boldsymbol{k})}{\partial k_\beta} \right\rangle \tag{5.1}$$

where $|u(\boldsymbol{k}\rangle$ is the cell-periodic part of the wavefunction. The imaginary part of the geometric tensor is the Berry curvature that is typically linked to the NLOR, whilst the real part is the Fubini-Study metric which quantifies minimal Wannier function spread and gives an enhancement to superconducting behavior [159, 380].

The paper is organized as follows: in Sec.II, we present a brief summary of our main results; in Sec.III, we present the model used in our simulations, the mean-field treatment of Coulomb interactions and the methods employed to evaluate the shift-current response. We also compare different approaches used in literature and comment on their numerical amenability; in Sec.IV, we proceed to study the shift-current response in a non-interacting twisted bilayer model and investigate the role of twist angle, sublattice offset, and symmetry properties. Additionally, we also analyze the contribution arising from different types of band transitions, e.g. flat to flat (FF) and flat to dispersive (FD) bands. We then try to understand the connection between observed shift-current response and the real space profile of Bloch wavefunctions involved in transitions; in Sec.V, we discuss how these results are modified by interactions; finally, we conclude by providing a summary of our analysis and specific experimental predictions.

5.3 Summary of results

We study the role of twist angle, encapsulation environment, and electron-electron interactions on shift-current response in twisted bilayer graphene. We find that interactions can significantly alter the shift-current response in both qualitative and quantitative ways as shown in Fig. 5.1c-f. The shift-current response has a contribution from transitions between flat bands whose gap can be controlled by the tuning the substrate properties. This contribution increases sharply in magnitude and narrows in the corresponding frequency window when Hartree corrections are taken into account. The key contribution to shift-current comes from the transition between flat and dispersive bands. We notice that incorporating interactions not only significantly enhances the shift-current response, but also gives rise to an additional peak. We explain these features on the basis of electron-electron interaction-driven changes to the band dispersion and quantum geometry. Also, we notice that since the position of dispersive bands is not affected much by the substrate-induced sublattice offset, Δ, but the flat bands are pushed away with increasing Δ, which can significantly change the frequency response of the flat-to-dispersive contribution. Our work demonstrates how second-order optical responses can serve as a probe for electron-electron interaction driven changes in twisted bilayer graphene. We also notice that its frequency range and magnitude can be tuned significantly by varying the twist angle or the substrate properties. We observe a second-order conductivity of the order of $1000\mu A.nm/V^2$ in frequency range of 10-100meV. This is roughly of the same order of magnitude as calculated in Ref. [166] and [382] for TBG and gapped bilayer graphene respectively. However, Ref. [166] studies the frequency response in range 1-10meV and Ref. [382] considers a frequency of 100meV.

5.4 Model and methods

TBG single-particle Hamiltonian

The single-particle energy spectrum of twisted bilayer graphene near the magic angle can be described with help of a continuum model [183, 35, 212]. Here, we follow the notation and model considered in Ref. [183] which gives a Hamiltonian:

$$\mathcal{H}_0 = \sum_{\gamma=\{\zeta,\sigma\}} \int_\Omega d^2\vec{r}\, \psi^\dagger_\gamma(\vec{r}) \hat{H}^{(\zeta,\sigma)} \psi_\gamma(\vec{r}), \tag{5.2}$$

$$\hat{H}^{(\zeta,\sigma)} = \begin{pmatrix} H_{\zeta 1}(\vec{r}) & U^\dagger_\zeta(\vec{r}) \\ U_\zeta(\vec{r}) & H_{\zeta 2}(\vec{r}) \end{pmatrix} \tag{5.3}$$

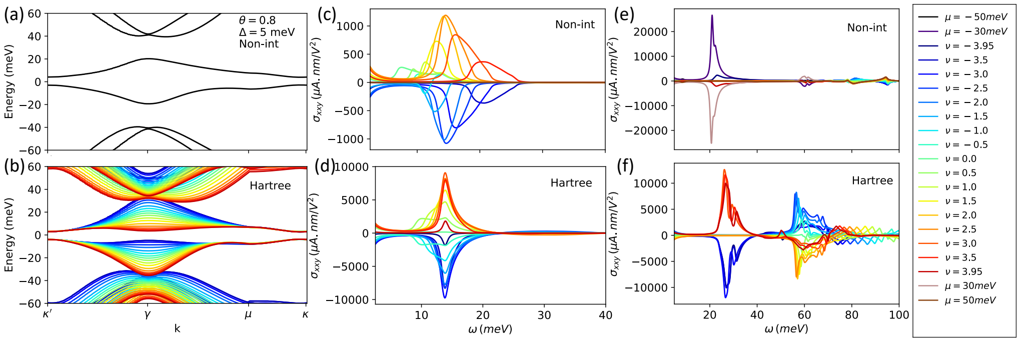

Figure 5.1: Main results: (a) Band structure for the non-interacting case, (b) Band structure for the interacting case with Hartree corrections at different fillings, (c,d) contributions to second-order conductivity $\sigma_{xxy}(0,\omega,-\omega)$ from flat-flat band transitions for non-interacting case and for the interacting case with Hartree corrections , and (e-f) contributions to second-order conductivity $\sigma_{xxy}(0,\omega,-\omega)$ from flat-dispersive band transitions for non-interacting case and for the interacting case with Hartree corrections. These Hartree corrections increase the band flattening significantly for both flat and dispersive bands as the filling is increased. This results in an enhanced second-order response and also gives rise to a second peak in flat-dispersive contribution.

where Ω represents the moiré unit cell, $H_{\zeta,l}$ represents the intralayer Hamiltonian of layer $l = 1, 2$, and $U_\zeta(\vec{r})$ encodes the moiré interlayer hopping. The Hamiltonian is written in the basis of (A_1, B_1, A_2, B_2) sites of the two layers, and we use the shorthand notation, $\gamma \equiv \{\zeta(=\pm1), \sigma(=\pm1)\}$, for the valley/spin degrees of freedom. In the rest of the chapter, we refer to this Hamiltonian as the "non-interacting model."

The intralayer Hamiltonian $H_{\zeta,l}$ is given by the two-dimensional Dirac equation expanded about the $\mathbf{K}_\zeta^l$ point of the original graphene layer,

$$H_l = -\hbar v \left[R(\pm\theta/2)(\mathbf{k} - \mathbf{K}_\zeta^l) \right] \cdot (\zeta\sigma_x, \sigma_y) + \Delta_l \sigma_z \,, \tag{5.4}$$

where $\vec{k}$ is a momentum in the BZ of the original graphene layers, $R\,(\pm\theta/2)$ is the 2×2 two-dimensional matrix accounting for the rotation of layer $l = 1(2)$ by an angle $+(-)\theta/2$ about z-axis with respect to the initial AA stacked bilayer. We set $\hbar v/a = 2.1354$ eV as the kinetic energy scale for the Hamiltonians $H_{\xi l}$ with $a = 0.246$ nm being the original graphene's lattice constant. We also introduce a layer dependent sublattice offset term, $\Delta_l \sigma_z$ that leads to a gap opening at the Dirac points.

The moiré intralayer potenial in Eq.(5.3) $U_\zeta(\vec{r})$ can be approximated as:

$$U = \begin{pmatrix} u & u' \\ u' & u \end{pmatrix} + \begin{pmatrix} u & u' e^{-i2\pi\zeta/3} \\ u' e^{i2\pi\zeta/3} & u \end{pmatrix} e^{i\zeta \vec{G}_1^M \cdot \vec{r}} + \begin{pmatrix} u & u' e^{i2\pi\zeta/3} \\ u' e^{-i2\pi\zeta/3} & u \end{pmatrix} e^{i\zeta\left(\vec{G}_1^M + \vec{G}_2^M\right)\cdot\vec{r}} \tag{5.5}$$

We treat the interlayer couplings u and u' as fitting parameters for the band structure according to the procedure introduced in Ref. [73] and summarized in App. **??**. To diagonalize the Hamiltonian Eq.(5.3) in $\vec{k}$-space, we can account for this interlayer potential by introducing a coupling between Bloch wave ansatzs at momentum $\mathbf{k}$ and $\mathbf{k} + \mathbf{G}$. Here, $\mathbf{G} = n_1 \vec{G}_1^M + n_2 \vec{G}_2^M$ is a linear combination of moiré reciprocal vectors $\vec{G}_1^M$ and $\vec{G}_2^M$ where n_1 and n_2 are integers. These reciprocal lattice vectors are given by $\vec{G}_i^M = R(-\theta/2)\vec{G}_i - R(\theta/2)\vec{G}_i$ with $\vec{G}_1 = (2\pi/a)\left(1, -1/\sqrt{3}\right)$ and $\vec{G}_1 = (2\pi/a)\left(0, 2/\sqrt{3}\right)$ being the reciprocal lattice vectors of graphene monolayer.

Mean-field interacting Hamiltonian

We consider electron-electron interactions given by the Coulomb term:

$$\mathcal{H}_c = \frac{1}{2}\int_\Omega d^2\vec{r}\, d^2\vec{r}'\ \delta\rho(\vec{r})\ _{\mathrm{c}}(\vec{r} - \vec{r}')\ \delta\rho(\vec{r}'), \delta\rho(\vec{r}) = \sum_{\gamma=\{\zeta,\sigma\}} \psi_\gamma^\dagger(\vec{r})\psi_\gamma(\vec{r}) - \rho_{\mathrm{CN}}(\vec{r}), \tag{5.6}$$

where $\delta\rho(\vec{r})$ is the density relative to that at charge neutrality, $\rho_{\mathrm{CN}}(\vec{r})$, and $_{\mathrm{c}}(\vec{r} - \vec{r}')$ is the Coulomb potential with a Fourier transform, $_{\mathrm{c}}(\vec{q}) = 2\pi e^2/\epsilon q$. The dielectric constant ϵ depends on the substrate, and is treated as a free parameter (reasons to be made clear below). We approximate the above interaction term using a self-consistent Hartree approximation $\mathcal{H}_c \approx \mathcal{H}_H$ where

$$\mathcal{H}_H = \sum_{\gamma=\{\zeta,\sigma\}} \int_\Omega d^2\mathbf{r} V_H(\mathbf{r})\psi_\gamma^\dagger(\mathbf{r})\psi_\gamma(\mathbf{r}) \tag{5.7}$$

with the Hartree potential

$$V_H(\mathbf{r}) = \int_\Omega d^2\mathbf{r}'_C(\mathbf{r} - \mathbf{r}') \sum_\gamma \left\langle \psi_\gamma^\dagger(\mathbf{r}')\psi_\gamma(\mathbf{r}')\right\rangle_H \tag{5.8}$$

In the above expression $\langle \ldots \rangle_H$ denotes a summation over occupied states measured from CNP ($\nu = 0$) [127]. When doping is increased with respect to the charge neutrality point, there is a preferential buildup of charge at AA sites in real space [127], corresponding to electronic states near κ points of the mini-Brillouin zone. The non-uniform spatial charge distribution generates an electrostatic potential that prefers an even redistribution of the electron density. In contrast, the real space charge distribution corresponding to electronic states near γ point is more uniform in the unit cell. The effect of the electrostatic Hartree potential and the associated charge redistribution thus leads to an increase in energy of the electronic states near the κ and μ points compared to to the energy of states near the γ points [126, 117, 284].

The effect of the Hartree potential becomes increasingly pronounced as a function of decreasing twist-angle, especially near the magic-angle where the non-interacting bandwidth is minimal. There is an increasing tendency towards band-inversion near the γ point [56, 117], a feature that has not been observed in experiments till date [74]. However, it is important to note that other mechanisms, for example strain or a Fock term, can act against this tendency towards band-inversion by increasing the overall bandwidth (both strain and Fock), or by contributing an opposing correction to the self-energy as compared to the Hartree term, Eq. (5.8) (Fock only). In our analysis we focus only on a Hartree correction for all θ and we take results for $0.96^\circ < \theta < 1.04^\circ$, where we anticipate Hartree term to produce band inversions not seen experimentally, with the understanding that another mechanism such a Fock would counteract these extreme band inversions.

The bandstructure is obtained by employing the fitting procedure detailed in Ref. [74]. The microscopic parameters of the Hamiltonian are determined by matching the theoretical energy spectrum of the system to the experimental STM results sufficiently far away from the magic-angle where no correlated effects are present. As explained in Ref. [74] for general agreement with the experimental results, it is necessary to use a dielectric constant ϵ larger than that set by the substrate. Similar procedures were employed in earlier studies [381, 127, 56] and their origins theoretically can be justified by arguing that dispersive bands renormalize the dielectric constant for the Coulomb interaction projected to the flat-bands. The final renormalized bandstructures at fixed angle of $\theta = 0.8^\circ$ is shown as a function of filling in Fig. 5.1(b). The most notable manifestation of the electron-electron interactions induced effects is the band-flattening around the γ and μ points beyond a certain filling.

We note that contribution of band-flattening effects on TBG properties were studied in recent works [179, 199, 55]. Qualitatively the role of band-flattening was to either enhance the density of states at the Fermi level or to decrease overall bandwidth and as a result corresponding twist angle range over which correlated effects were expected increased. We stress however that no papers that studied NLOR in TBG[166, 209] has considered the role interactions can play in the photo response.

Before proceeding with the discussion of the shift-currents in TBG, we pause to clarify key assumptions of our modelling. Firstly we intentionally do not include the effects associated with the "cascade transitions" at integer fillings near magic-angle [407, 370], and the correlated effects such as superconductivity[50] or insulating states[48]. Physically this approximation is justified as optical NLOR experiments are typically performed at temperaturesexceeding the characteristic temperatures ($T < 10K$) associated with these phenomena[48, 50, 407]. In principle however these effects, as well as more complex scenarios like the K-IVC state, could provide interesting constrains on and signatures in the photoresponse. The Hartree corrections we expect to persist to higher temperatures as they are a reflection of charge inhomogenity of the system. Secondly we also neglect the possibility of varying interlayer hopping parameters (u, u') in Eq.(5.5). We argue that this approximation is justified since our choice of $u\prime = 90$ meV is comparable to typical literature values and the ratio of $\eta = u/u' = 0.4$ is not too far from values quoted in literature that are typically in the range $\eta = 0.3$ to 0.7. Most crucially, however, even if η were to be varied as twist angle is changed, the location of the van Hove singularity remains fixed near filling of ±1.9 (or not drastically different energies) (see also Ref. [280]) until very high η's of 0.8 that are typically not used in modelling. As such we thus expect that although quantiative changes (such as precise frequency locations of peaks can vary) overall behavior of the system will remain qualitatively similar.

Shift current

The shift-current response is determined by a rank three tensor

$$J^{\mu}_{\alpha\alpha} = 2\sigma^{\mu}_{\alpha\alpha}(0, \omega, -\omega)\mathcal{E}^{\alpha}(\omega)\mathcal{E}^{\alpha}(-\omega) \tag{5.9}$$

where $\boldsymbol{\mathcal{E}}(t) = \boldsymbol{\mathcal{E}}(\omega)e^{i\omega t} + \boldsymbol{\mathcal{E}}(-\omega)e^{-i\omega t}$ is the electric field. The second-order conductivity tensor element, $\sigma^{\mu}_{\alpha\alpha}(0, \omega, -\omega)$ is given by (see Appendix B.2 and Ref. [100])

$$\sigma^{\mu}_{\alpha\alpha}(0, \omega, -\omega) = \frac{\pi e^3}{\hbar^2} \sum_{m,n} \int [d\mathbf{k}] f_{mn} |\mathbf{A}^{\alpha}_{mn}|^2 \mathbf{S}^{\mu\alpha}_{mn} \delta(\omega - \epsilon_{mn}) \tag{5.10}$$

where $\epsilon_{mn} = \epsilon_m - \epsilon_n$ is the energy difference, and $f_{mn} = f_m - f_n$ is the difference in occupancy of energy level a and b, and $\mathbf{S}^{\mu\alpha}_{mn} = \mathbf{A}^{\mu}_{mm} - \mathbf{A}^{\mu}_{mn} - \partial_{\mu}(\mathrm{Arg}\mathbf{A}^{\alpha}_{mn})$ is the shift-vector and $\mathbf{A}_{mn}$ is the interband Berry connection defined by $\frac{1}{i}\langle u_m|\nabla_{\mathbf{k}}|u_n\rangle$ for Bloch wavefunctions $|u_m\rangle$ and $|u_m\rangle$. This interband Berry connection comes into picture as the EM field couples through dipole matrix element. The shift-vector represents the shift experienced by the Bloch wavepacket upon excitation from m^{th} to n^{th} band [25, 100, 333]. The integrand $R^{\alpha\alpha\mu}_{mn} = |\mathbf{A}^{\alpha}_{mn}|^2 \mathbf{S}^{\mu\alpha}_{mn}$ and if $h^{\mu\alpha}_{ba} = 0$, it can also be expressed as

$$R^{\alpha\alpha\mu}_{ab} = \frac{1}{\epsilon^2_{ab}}\mathrm{Im}\left[\frac{h^{\alpha}_{ab}h^{\mu}_{ba}\Delta^{\alpha}_{ab}}{\epsilon_{ab}}\right] + \frac{1}{\epsilon^2_{ab}}\mathrm{Im}\left[\sum_{d\neq a,b}\left(\frac{h^{\alpha}_{ba}h^{\mu}_{ad}h^{\alpha}_{db}}{\epsilon_{ad}} - \frac{h^{\alpha}_{ba}h^{\mu}_{db}h^{\alpha}_{ad}}{\epsilon_{db}}\right)\right] \tag{5.11}$$

where $h^{\alpha}_{ab} = \langle a|\nabla_{k_\alpha}H|b\rangle$, $h^{\alpha\beta}_{ab} = \langle a|\nabla_{k_\alpha}\nabla_{k_\beta}H|b\rangle$ are the derivatives of Hmiltonian. This expression for shift-current integrand is equivalent to the sum rule commonly used to calculate the shift vector. If the time-reversal symmetry is broken intrinsically or by the light, there can be an additional contribution to the current density which is linear in time and is known as the injection current.

There are many different methods to calculate the second-order conductivity [317, 266, 79, 403], and in some previous works it is presented in a slightly different form without any reference to the shift-vector. For example, one of the most common expressions which we encountered in different works like Ref. [403, 209] is

$$\sigma^{mu}_{\alpha\beta} = -\frac{e^3}{\hbar^2\omega^2}\mathrm{Re}\left(\sum_{\Omega=\pm\omega,m,n,l}\int d^2\mathbf{k}\frac{h^{\alpha}_{nl}h^{\beta}_{lm}h^{\mu}_{mn}}{(\varepsilon_{mn}-i\eta)(\varepsilon_{nl}+\Omega-i\eta)}\right) \tag{5.12}$$

which we show in the Appendix B.2 is equivalent to Eq. 5.10 except for the injection current term which arises for $m = n$ in the above summation. This term vanishes if $\alpha = \beta$ case or if the TRS is preserved. On the other hand, some other works simply provide the shift vector expression without any intuition about the origin of this term. We highlight the connection between different expressions. This shift vector can be calculated directly from the Berry connection matrix in theory. However, in practice the direct numerical approach is plagued by the gauge fixing issues and hence is not reliable. We instead consider the approach used by Ref. [266, 79] to calculate the shift vector using the sum rule described in Eq. 5.11 which is equivalent to the three velocity expression in Ref. [266]. This approach is more amenable for numerical simulations and also puts different expressions considered above on an equal footing. We provide a detailed derivation of the shift-current conductivity in Appendix B.2, and elucidate the connection between different expressions encountered in the literature.

Symmetry constraints on second-order conductivity

It is a very well-known fact that the second optical processes are observed only in non-centrosymmetric materials. The number of non-vanishing and independent elements of the second-order conductivity tensor can be deduced directly from the symmetry groups of the crystal via a simple application of group theory. The

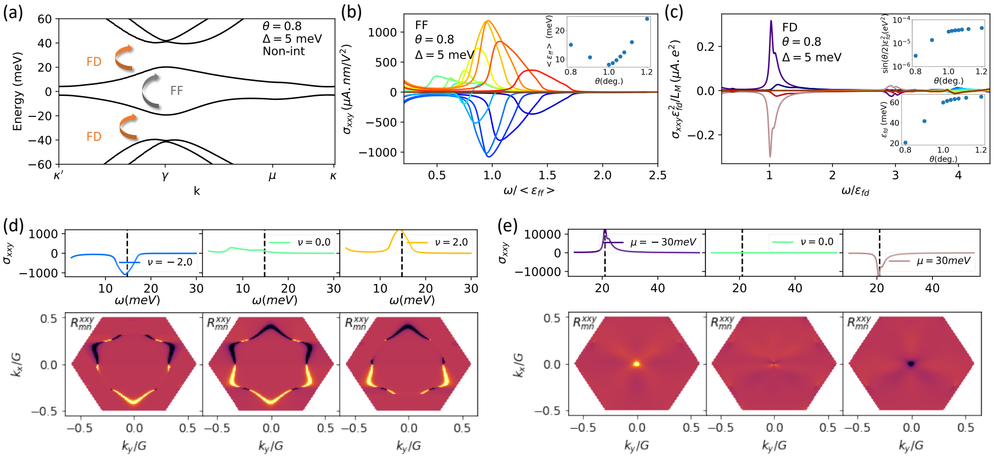

Figure 5.2: Band structure and shift current response for non-interacting case: (a) Bandstructure for non-interacting twisted bilayer graphene for twist angle $\theta = 0.8^\circ$ and sublattice offset $\Delta = 5meV$ on both layers. Here, FF and FD represent the transitions between two flat bands and between flat and dispersive bands, respectively. (b) FF contribution to second-order conductivity as a function of frequency shown in units of average gap between two flat bands. (c) FD contribution to shift current conductivity scaled by $\varepsilon_{fd}^2 \sin\theta/2$ as a function of frequency in units of the band gap between flat and dispersive bands. captions for d,e; In c can you instead write scaled by ε_{fd}^2/L_M, in (b) similarly to make sure there is a consistency, more points in the inset of (b) same for the inset of (c)

TBG model considered here has D_3 symmetry generated by a C_{3z} and C_{2y} when the sublattice offset term is the same on both layers. However, when $\Delta_1 \neq \Delta_2$, the symmetry group reduces to C_{3z}. As a result of these symmetry properties, as derived in Appendix B.1, we expect

$$\begin{aligned} \sigma^y_{xx} &= -\sigma^y_{yy} = \sigma^y_{xy} = \sigma^x_{yx} \neq 0 \\ \sigma^x_{yy} &= -\sigma^x_{xx} = \sigma^y_{yx} = \sigma^y_{xy} = 0 \end{aligned} \tag{5.13}$$

when $\Delta_1 = \Delta_2$. On the other hand, for $\Delta_1 \neq \Delta_2$, we have

$$\begin{aligned} \sigma^y_{xx} &= -\sigma^y_{yy} = \sigma^y_{xy} = \sigma^x_{yx} \neq 0 \\ \sigma^x_{yy} &= -\sigma^x_{xx} = \sigma^y_{yx} = \sigma^y_{xy} \neq 0. \end{aligned} \tag{5.14}$$

5.5 Shift current in non-interacting case

In this section, we investigate how this shift current changes with different parameters of the system. We identify two different contributions to this photocurrent in presence of linearly polarized light: (1) originating from transitions from a flat band to another flat band which is referred as FF, and (2) arising due to transitions between a flat band and a dispersive band which is referred as FD contribution in Fig. 5.2 (a).

In the first case, as expected, the frequency response is decided by the average gap of two flat bands as shown in Fig. 5.2 (b) and the obtained looks almost identical for all twist angles away from the magic angle ($|\theta - 1.0^{\text{deg}}| > 0.02$). Another important point to notice is the k profile of shift vector integrand R^{xxy} which peaks around Dirac points and has equal regions of positive and negative values. However, the energy contours for a given valley are not symmetric about $k_x = 0$ which results in a large net contribution whenever the filling is non-zero as shown in Fig. 5.2 (d). Similarly, the shift vector from negative valley is opposite of the positive valley but at the same time energy contours are also reversed which results in the same contribution to second-order conductivity. We can apply similar arguments to conclude that the contribution from shift vector R^{yyx} would vanish as the energy contours are symmetric about $k_y = 0$ but $R^{yyx}(k_x, k_y) = -R^{yyx}(k_x, -k_y)$. As also mentioned earlier, the frequency response is mainly decided by the gap which can be tuned by changing the distance between hBN layers and tBLG sample. We considered a sublattice offset, $\Delta = 5meV$ for both layers which results in a gap of about $10meV$ and thus the contribution from flat-flat bands peak around $10meV$. We also present our results for other sublattice offset values as presented in the appendix and as expected we notice that the frequency response can be tuned by varying the sublattice offset. Although this contribution is coming from transitions between two flat-bands but the shift vector between two flat-bands depends on dispersive bands as it involves virtual transitions to and from dispersive bands. We have included ten dispersive bands while evaluating this shift vector using the expression Eq. 5.11 where virtual transitions are captured by the second term.

Another contribution to second-order conductivity comes from real transitions between a flat band and a dispersive band depicted by orange arrows in Fig 5.2 (a). In this case, the shift vector is concentrated around γ point in k space (Fig. 5.2 (e)), and thus we observe a significant non-zero contribution only when the Fermi level lies between a flat band and a dispersive band. Now, as expected from Eq 5.11, the integrand R^{xxy}_{mn} decreases as $1/\varepsilon^2_{fd}$ where ε_{fd} is the gap between the flat band and the dispersive band. This quantity shows a very strong dependence on twist angle θ as it increases sharply with the increase in mini BZ size. Hence, we have presented the results for this contribution in a θ-independent manner in Fig. 5.2 (c). Although, the main plot shown in this figure was obtained for twist angle $\theta = 0.8$, but it looks almost identical for all other twist angles away from the magic angle. As evident from the behavior of scaling factor $\epsilon_{fd}^2 \sin(\theta/2)$, the second order quantity is orders of magnitude larger for $\theta = 0.8$.

When the sublattice offset, Δ is increased from 5mev to 10meV, we notice that the FD signal is shifted to a lower frequency and the peak becomes more pronounced. This can be explained on the basis of the shift in band energies. An increased Δ increases the gap between flat bands but does not affect the dispersive bands much and as a result the gap between flat and dispersive bands start to decrease. A smaller value of gap, ε_{fd} shifts the peak to lower frequency and also increases the value of integrand which scales as $1/\varepsilon_{fd}$ as mentioned earlier. However, if we increase the sublattice offset further, it suppresses the quantum geometric features of the bands and the shift-current signal is suppressed as shown in Fig. B.1. This shows that the sublattice offset can serve as an important knob to tune the optical response. Additionally, the direction of current density and its relation to the polarization of EM field can also be modified by changing the sublattice offset independently in two-layers. As discussed in Sec. 5.4, the constraints on second-order conductivity tensor are different for $\Delta_1 = \Delta_2$ case and $\Delta_1 \neq \Delta_2$ case. Here, in Figs. 5.2-5.4, we have considered $\Delta_1 = \Delta_2$, and thus the only non-zero components are $\sigma_{xx}^{y}, \sigma_{yy}^{y}, \sigma_{xy}^{y}, \sigma_{yx}^{x} \neq 0$ which can all be expressed in terms of σ_{xx}^{y} plotted in these figures. We also verified the relation between different elements as shown in Fig. B.2. However, for $\Delta_1 \neq \Delta_2$, there are two independent non-zero elements which are shown in the lower panel of the same figure.

5.6 Interaction induced in shift-current response

Next, we proceed to discuss how the shift current response is modified by electron-electron interactions which we incorporate by using mean-field methods described above. As shown in Fig. 5.1 (b), one of the most prominent effect of interactions is the band-flattening of the flat bands near the γ point causing a large enhancement of density of states. Additionally, these interactions also affect the structure of the Bloch wavefunction in real-space.

For the flat-flat contribution shown in non-interacting case, we noticed that the σ_{xx}^{y} peak was significantly larger for fillings, $\nu \approx 2$ Fig. 5.2(b). We explained this behavior on the basis of a significant contribution from the extreme flat regions around μ points, corresponding to the van Hove singularities, as depicted in Fig. 5.2(b) and Fig. 5.5 (a). On increasing the filling further beyond these flat-regions, the transitions to these states was Pauli blocked and they no longer contributed to the optical response in non-interacting case. However, when electron-electron interactions are included in the analysis, we notice that these flat-regions around μ point expand further in k space as shown in Fig. 5.3(a) until they span the whole mini-BZ (when the γ point is locally flat). Now, these extremely flat regions can participate in band transitions even at much larger fillings. It consequently affects the peaks at larger fillings, e.g $|\nu| > 3$, which not only increase in strength but also shift in frequency and coincide with the peaks at fillings $|\nu| = 1.5, 2$. This behavior clearly arises due to the increased density of states coming from Hartree band-flattening that shifts van Hove singularity to higher fillings. Additionally, we also notice a change in the profile of flat-dispersive contribution of the integrand $\sum_{mn} R^{xxy}_{mn}\delta(\omega - \varepsilon_{mn})$ along $\gamma - \mu$ line which leads to an increased asymmetry in positive and negative regions of the mini-BZ with increasing $|\nu|$ as depicted in the third column of Fig. 5.3(c), and hence an enhanced response.

These interaction induced changes in band structure also affect the contribution coming from transitions between flat and dispersive bands. One obvious modification arises from the changes in band structure which are quite prominent around γ point. This region was the hotspot for FD contribution in non-interacting case as shown in Fig. 5.2(e). The Hartree corrections to the non-interacting Hamiltonian increases the gap at γ points. It also results in an increased band flattening of dispersive bands, which in turn decreases the gap significantly in a large region of mini BZ around μ points as shown in Fig 5.4 (a).

Hartree corrections to the band structure and Bloch wavefunctions result in modifying also the shift current integrand, R^{xxy}. Its momentum profile exhibits a significant increase at regions away from γ point as shown in Fig. 5.4 (d-g) and Fig. 5.6 (b). These factors give rise to some unexpected features in the second-order conductivity response. We can now observe a reasonably large contribution at fillings less than $|\nu| = 4$, which arises due to spreading of R^{xxy}_{mn} in miniBZ as shown in the bottom panel of Fig.5.6(b).

Arguably however, the most important role (at least experimentally) of these filling-dependent corrections is the appearance of new features in the second-order shift current conductivity. Specifically, there is also a second peak, in Fig.5.4(c) at $\omega \approx 60$ meV, which has the opposite sign, to the peak at $\omega \approx 25$ meV. We attribute this second-peak to transitions that involve van-Hove singularity points of the flat-band as their frequency is quite close to the energy gap around those k points. This is further substantiated by the fact that the integrand in these regions is opposite to the that of the contribution from γ point as shown in Fig. 5.6(b) and the third column of Fig 5.4 (e,f).We argue that this enhanced response and the appearance of the second peak can act as a probe of interactions induced changes to both the band structure and quantum geometry. Most crucially however this additional peak occurs at frequencies that far exceed those characteristic of flat bands (few meV's), placing it more firmly in the characteristic range of optical experiments (tens of meV's).

5.7 Discussion

In this work, we have focused on the shift-current response, but CPGE and injection currents are another very important photo-responses observed in materials with Dirac cone dispersions. The injection current is the response which comes into picture because of the difference in group velocity of two bands involved in the transition process. This term is proportional to the relaxation time and is usually the dominant contribution [157, 57] in the second-order photoresponse. However, this term is non-zero only for circularly polarized light or for systems with tilted Dirac cones illuminated by linearly polarized light. As a result, we can safely ignore the injection current contribution in our calculations where we focused on linear polarization only. A similar analysis of interaction induced effects can be done for the injection current would be investigated in future [5].

Clearly, we have considered a time-dependent perturbation arising from the EM field only. Another very interesting but somewhat underappreciated aspect of the shift-vector is that it also depends on the nature of the perturbation [61]. For the case of EM field, the interband transition is induced due to the coupling between E field and the dipole matrix element between two bands. In minimal coupling approach, this dipole matrix term is same as the interband Berry connection and hence we get a contribution of the form $\partial_\mu(\text{Arg}\mathbf{A}^{\alpha}_{mn})$ in the shift-vector. However, it can be generalized to other drives such as orbital-mixing or phonon-drive where this interband term might look different. Thus, it would be interesting to explore shift-current generated from perturbation different than an EM field.

Furthermore in the manuscript, we mainly focused on the photoresponse originating from interband processes. However, if the symmetry of the system is lowered further, we can also get a second-order contribution from intraband processes which are captured by Berry curvature dipole [323]. Such processes can be made to contribute in twisted bilayer graphene photoresponse by applying a strain as discussed in Ref. [166]. However, the additional contribution is typically of the same order of magnitude and should not alter our results drastically. add references

It can be shown that the shift-current expression considered in Eq. 5.10 has equal contribution from both valleys if the Dirac cones of underlying graphene layers are not tilted. However, in addition to the shift-current contribution which comes with a Dirac-delta function, the second-order conductivity also has a contribution from the principal part as presented in Eq. B.24 of Appendix B.2. This contribution is equal and opposite from two valleys and hence can affect the shift-current response for a valley-polarized setup. On the other hand, the injection current response here would be more susceptible to valley polarization.

Although not demonstrated explicitly in the text, shift current is directly related to quantum geometric objects as it involves Berry connection as its building block. In future work it will be worthwhile to explore this connection further, in particular how it interplays with different physical ingredients of the TBG system such as the changes in Bloch wavefunction structure upon excitation. Specifically, as argued in the Sec. 5.4, different momentum states lead to a different spatial distribution of charge, e.g. for flat-bands κ points states give rise to charge buildup near AA sites whilst γ point states cause a buildup of charge in a ring surrounding AA sites. For the first dispersive bands however, the relation flips - κ points states give rise to charge buildup in a ring surrounding AA sites whilst γ point states lead to a charge buildup at the AA sites. We find that qualitatively sharp resonances seen in Fig.5.4 correspond precisely to the transitions for AA charge profile to that of a ring surrounding the AA sites or vice versa. It is therefore inviting to consider this additional possible details about shift current origins and further explore how it can be further modified to increase second-order response even further.

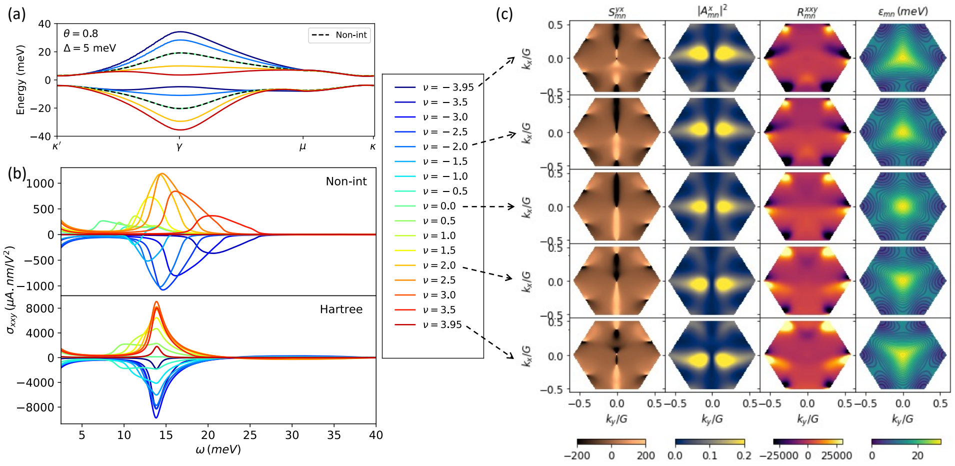

Figure 5.3: Band structure and FF contribution to shift current quantities with Hartree corrections: (a) Band structure with Hartree corrections, (b) FF contribution to shift-current conductivity for the non-interacting case and the interacting case, and (c) k space profiles of Shiftvector ($S_m^{yx} n$), Interband Berry connection magnitude square, $|A_{mn}^x|^2$, the integrand R_{mn}^{xxy} and energy contours for ε_{fd} in k space for the transition between two flat-flat bands at four different fillings.

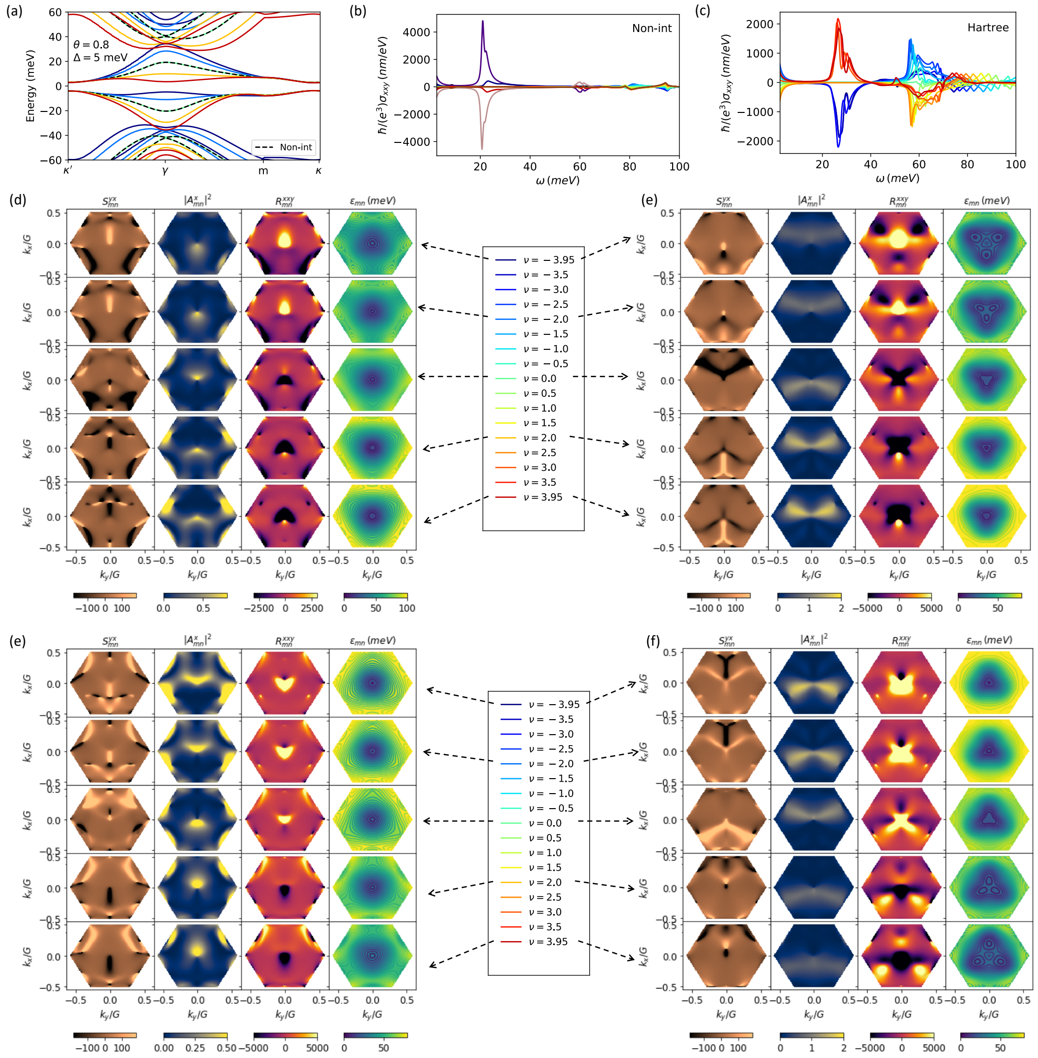

Figure 5.4: Band structure and FD contribution to shift current quantities with Hartree corrections: (a) Band structure with Hartree corrections, (b) FD contribution to shift-current conductivity for the non-interacting case, (c) FD contribution when Hartree corrections are included, and (d-f) Shift vector ($S^{yx}_m n$), Interband Berry connection magnitude square, $|A^x_{mn}|^2$, the integrand R^{xxy}_{mn} and energy contours for ε_{fd} in k space for the four FD transitions where (d-e) represents transitions between the hole flat band and hole dispersive bands, and (e-f) represents transitions between the electron flat band and the electron dispersive bands.

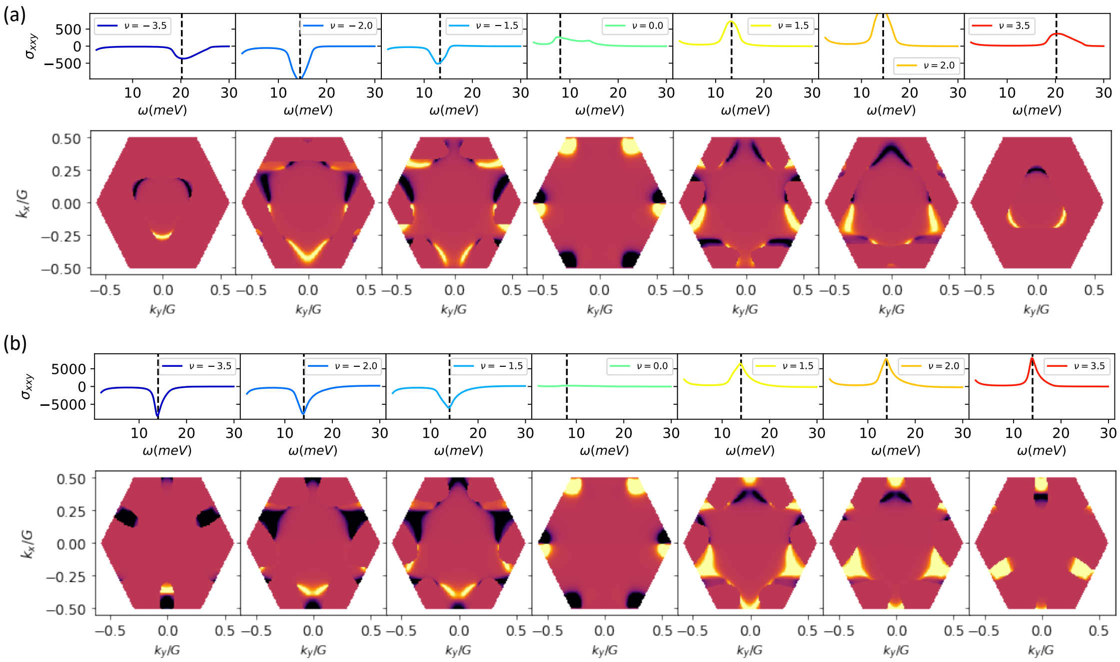

Figure 5.5: The flat-flat band transition contribution to the peak of second-order conductivity from different k points within the mBZ at different fillings for (a) non-interacting model and (b) interacting model with Hartree corrections. We notice a significant increase in the contribution from the regions near the *mu* point which mainly arises from the band-flattening effect of interactions.

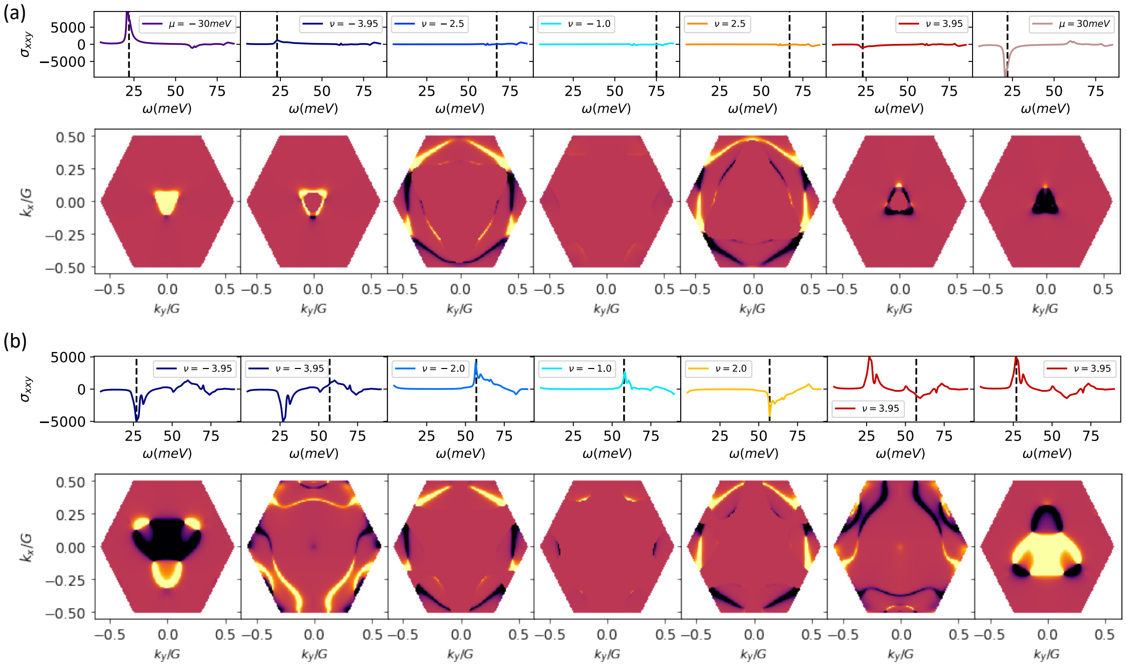

Figure 5.6: The flat-dispersive band transition contribution to the peak of second-order conductivity from different k points within the mBZ at different fillings for (a) non-interacting model and (b) interacting model with Hartree corrections. We notice a significant increase in the contribution from the regions near the μ point which mainly arises from the band-flattening effect of interactions.

Appendix B

APPENDIX

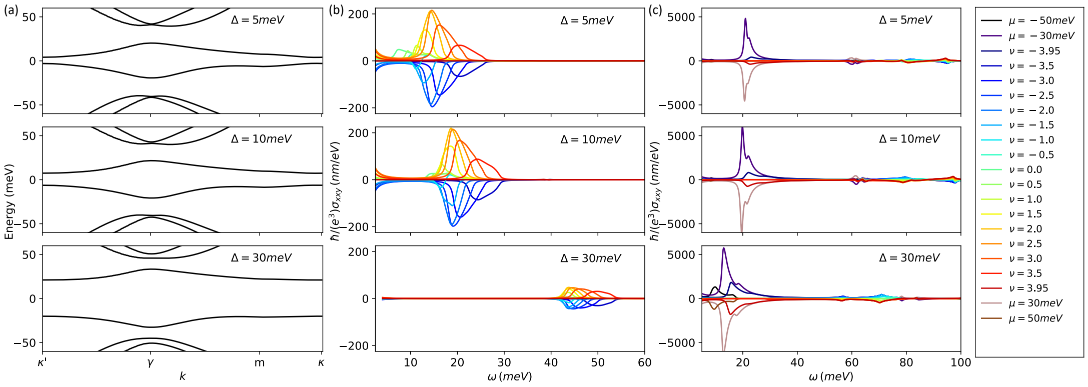

Figure B.1: Bandstructure and second-order conductivity for different sublattice offset energies: (a) Energy spectrum around flat-bands, (b) FF contribution to seconf-order conductivity, and (c) FD contribution to second-order conductivity for three different sublattice offset energies. As Δ increases, the gap between flat bands increases but they come closer to the dispersive bands and this results in an opposite frequency shift for the peak value in FF and FD case.

B.1 Symmetry analysis

If we consider a TBLG encapsulated with hBN from both sides such that the sublattice symmetry breaking effect is same on both layers, we have $\Delta_1 = \Delta_2$. In this case, the symmetry group of TBLG is D_3 generated by C_{3z} and C_{2y}. In our simulations, we found that there is only one independent component of $\sigma^{\mu}_{\alpha\beta}$ tensor when $\Delta_1 = \Delta_2$. It can be directly read from the character table of D_3 in Tab. B.1.

Irreps	E	$2C_{3z}$	$3C_{2y}$	Cubic functions
A_1	1	1	1	$y(y^2 - 3x^2)$
A_2	1	1	-1	$z^3, x(3y^2 - x^2), z(x^2 + y^2)$
E	2	-1	0	(xz^2, yz^2) $\left[xyz, z(y^2 - x^2)\right]$ $\left[y(x^2 + y^2), x(x^2 + y^2)\right]$

Table B.1: Character table for point group D_3.

As we can see, the trivial irrep of D_3 has only one cubic function which indicates

Irreps	e	c	c^2	Cubic functions
A_1	1	1	1	z^3,$y(y^2-3x^2)$,$y(y^2-3x^2)$,$z(x^2+y^2)$
E	1 1	$e^{i\frac{2\pi}{3}}$ $e^{-i\frac{2\pi}{3}}$	$e^{-i\frac{2\pi}{3}}$ $e^{i\frac{2\pi}{3}}$	(xz^2, yz^2) $\left[xyz, z(x^2-y^2)\right]$ $\left[x(x^2+y^2), y(x^2+y^2)\right]$

Table B.2: Character table for point group C_3.

that the second order tensor $\sigma^{\mu}_{\alpha\beta}$ has only one independent element and thus

$$\begin{aligned} \sigma^{y}_{xx} &= -\sigma^{y}_{yy} = \sigma^{y}_{xy} = \sigma^{x}_{yx} \neq 0 \\ \sigma^{x}_{yy} &= -\sigma^{x}_{xx} = \sigma^{y}_{yx} = \sigma^{y}_{xy} = 0. \end{aligned} \tag{B.1}$$

On the other hand, the trivial irrep for C_{3z} has two cubic functions (ignoring the ones involving z as our system is two-dimensional only) indicating that a rank three tensor can have two independent components under C_3. As a result of this, for $\Delta_1 \neq \Delta_2$, we have

$$\begin{aligned} \sigma^{y}_{xx} &= -\sigma^{y}_{yy} = \sigma^{y}_{xy} = \sigma^{x}_{yx} \neq 0 \\ \sigma^{x}_{yy} &= -\sigma^{x}_{xx} = \sigma^{y}_{yx} = \sigma^{y}_{xy} \neq 0 \end{aligned} \tag{B.2}$$

which is consistent with our observation in Fig. B.2.

B.2 Shift-current expressions

Within the independent particle approximation and using minimal coupling approach, the second-order conductivity for a perturbation arising from a linearly polarized EM field can be obtained using formula Eq. 43 of Ref. [266]

$$\begin{aligned} \sigma^{\mu}_{\alpha\beta}(\omega_Z, \omega_1, \omega_2) = -\frac{e^3}{\hbar^2\omega_1\omega_2}\sum_{a,b,c}\int d\mathbf{k}\, & \frac{1}{2} f_a h^{\mu\alpha\beta}_{aa} + \frac{1}{2} f_a h^{\mu\beta\alpha}_{aa} + f_{ab}\frac{h^{\alpha}_{ab}h^{\mu\beta}_{ba}}{\omega_1 - \epsilon_{ab}} \\ & + f_{ab}\frac{h^{\beta}_{ab}h^{\mu\alpha}_{ba}}{\omega_2 - \epsilon_{ab}} + \frac{1}{2} f_{ab}\frac{h^{\alpha\beta}_{ab}h^{\mu}_{ba}}{\omega_Z - \epsilon_{ab}} + \frac{1}{2} f_{ab}\frac{h^{\beta\alpha}_{ab}h^{\mu}_{ba}}{\omega_Z - \epsilon_{ab}} \\ & + \frac{h^{\alpha}_{ab}h^{\beta}_{bc}h^{\mu}_{ca}}{\omega_Z - \epsilon_{ca}}\left[\frac{f_{ab}}{\omega_1 - \epsilon_{ba}} + \frac{f_{cb}}{\omega_2 - \epsilon_{cb}}\right] \\ & + \frac{h^{\beta}_{ab}h^{\alpha}_{bc}h^{\mu}_{ca}}{\omega_Z - \epsilon_{ca}}\left[\frac{f_{ab}}{\omega_2 - \epsilon_{ba}} + \frac{f_{cb}}{\omega_1 - \epsilon_{cb}}\right] \end{aligned} \tag{B.3}$$

where $\omega_Z = \omega_1 + \omega_2$, $h^{\alpha}_{ab} = \langle a|\nabla_{k_\alpha} H|b\rangle$, $h^{\alpha\beta}_{ab} = \langle a|\nabla_{k_\alpha}\nabla_{k_\beta} H|b\rangle$ are derivatives of Hamiltonian, $\epsilon_{ab} = \epsilon_a - \epsilon_b$ is the energy difference, and $f_{ab} = f_a - f_b$ is the difference in occupancy of energy level a and b. This formula many different contributions

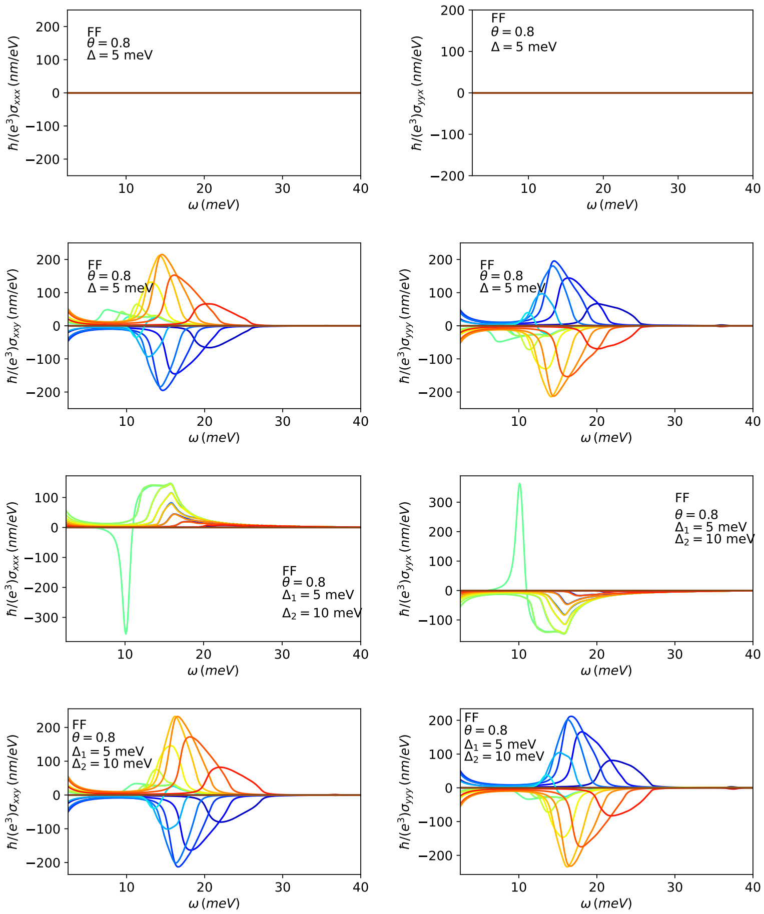

Figure B.2: Different second order conductivity tensor elements for $\Delta_1 = \Delta_2 = \Delta$ case (upper row) and for $\Delta_1 \neq \Delta_2$ (lower row).

like injection current, shift current, etc. It can be recast in a slightly different form by shifting all frequencies by $\omega \longrightarrow \omega + i\eta$ and the above equation reduces to

$$
\begin{aligned}
\sigma^{\mu}_{\alpha\beta}(\omega_Z, \omega_1, \omega_2) = -\frac{e^3}{\hbar^2\omega_1\omega_2} \sum_{a,b,c} \int d\mathbf{k}\, & \frac{1}{2} f_a h^{\mu\alpha\beta}_{aa} + \frac{1}{2} f_a h^{\mu\beta\alpha}_{aa} + f_{ab} \frac{h^{\alpha}_{ab} h^{\mu\beta}_{ba}}{\omega_1 + i\eta - \epsilon_{ab}} \\
& + f_{ab} \frac{h^{\beta}_{ab} h^{\mu\alpha}_{ba}}{\omega_2 + i\eta - \epsilon_{ab}} + \frac{1}{2} f_{ab} \frac{h^{\alpha\beta}_{ab} h^{\mu}_{ba}}{\omega_Z + i\eta - \epsilon_{ab}} + \frac{1}{2} f_{ab} \frac{h^{\beta\alpha}_{ab} h^{\mu}_{ba}}{\omega_Z + i\eta - \epsilon_{ab}} \\
& + \frac{h^{\alpha}_{ab} h^{\beta}_{bc} h^{\mu}_{ca}}{\omega_Z + i\eta - \epsilon_{ca}} \left[\frac{f_{ab}}{\omega_1 + i\eta - \epsilon_{ba}} + \frac{f_{cb}}{\omega_2 + i\eta - \epsilon_{cb}} \right] \\
& + \frac{h^{\beta}_{ab} h^{\alpha}_{bc} h^{\mu}_{ca}}{\omega_Z + i\eta - \epsilon_{ca}} \left[\frac{f_{ab}}{\omega_2 + i\eta - \epsilon_{ba}} + \frac{f_{cb}}{\omega_1 + i\eta - \epsilon_{cb}} \right].
\end{aligned}
\tag{B.4}
$$

The DC response to an AC field of frequency ω is given by $\sigma^{\mu}_{\alpha\beta}(0,\omega,-\omega)$. which can be obtained from Eq. B.4 by substituting $\omega_1 = -\omega_2 = \omega$ and for our prime case of interest ($\alpha = \beta$), we get

$$\begin{aligned}\sigma^{\mu}_{\alpha\alpha}(0,\omega,-\omega) = \frac{e^3}{\hbar^2\omega^2}\sum_{a,b,c}\int & d\mathbf{k}\, f_a h^{\mu\alpha\alpha}_{aa} + f_{ab}\frac{h^{\alpha}_{ab}h^{\mu\alpha}_{ba}}{\omega + i\eta - \epsilon_{ab}} \\ & + f_{ab}\frac{h^{\alpha}_{ab}h^{\mu\alpha}_{ba}}{-\omega + i\eta - \epsilon_{ab}} + f_{ab}\frac{h^{\alpha\alpha}_{ab}h^{\mu}_{ba}}{\epsilon_{ba}} \\ & + \frac{h^{\alpha}_{ab}h^{\alpha}_{bc}h^{\mu}_{ca}}{\epsilon_{ac}}\left[\frac{f_{ab}}{\omega + i\eta - \epsilon_{ba}} + \frac{f_{cb}}{-\omega + i\eta - \epsilon_{cb}}\right] \\ & + \frac{h^{\alpha}_{ab}h^{\alpha}_{bc}h^{\mu}_{ca}}{\epsilon_{ac}}\left[\frac{f_{ab}}{-\omega + i\eta - \epsilon_{ba}} + \frac{f_{cb}}{\omega + i\eta - \epsilon_{cb}}\right].\end{aligned} \tag{B.5}$$

Connections with shift-current expression

In order to understand the connections between the shift-current expression we encountered in the main text and the form of the second-order conductivity considered above, we can first split this equation into two different kinds of contributions

$$\begin{aligned}\sigma^{\mu}_{\alpha\alpha}(0,\omega,-\omega) = \frac{e^2}{\hbar^2\omega^2}\sum_{a,b,c}\int & d\mathbf{k}\, f_a h^{\mu\alpha\alpha}_{aa} + f_{ab}\frac{h^{\alpha\alpha}_{ab}h^{\mu}_{ba}}{\epsilon_{ba}} \\ & \underbrace{+ f_{ab}\frac{h^{\alpha}_{ab}h^{\mu\alpha}_{ba}}{\omega + i\eta - \epsilon_{ab}} + f_{ab}\frac{h^{\alpha}_{ab}h^{\mu\alpha}_{ba}}{-\omega + i\eta - \epsilon_{ab}}}_{\sigma^{23}} + \\ \underbrace{\frac{h^{\alpha}_{ab}h^{\alpha}_{bc}h^{\mu}_{ca}}{\epsilon_{ac}}\left[\frac{f_{ab}}{\omega + i\eta - \epsilon_{ba}} + \frac{f_{cb}}{-\omega + i\eta - \epsilon_{cb}}\right] + \frac{h^{\alpha}_{ab}h^{\alpha}_{bc}h^{\mu}_{ca}}{\epsilon_{ac}}\left[\frac{f_{ab}}{-\omega + i\eta - \epsilon_{ba}} + \frac{f_{cb}}{\omega + i\eta - \epsilon_{cb}}\right]}_{\sigma^{56}} &\end{aligned} \tag{B.6}$$

Let us first focus on the 2nd and 3rd term of Eq. B.6, σ^{23}, where the integrand can be expressed as

$$\begin{aligned}f_{ab}\frac{h^{\alpha}_{ab}h^{\mu\alpha}_{ba}}{\omega + i\eta - \epsilon_{ab}} + f_{ab}\frac{h^{\alpha}_{ab}h^{\mu\alpha}_{ba}}{-\omega + i\eta - \epsilon_{ab}} &= f_{ab}\frac{h^{\alpha}_{ab}h^{\mu\alpha}_{ba}}{\omega + i\eta - \epsilon_{ab}} - f_{ba}\frac{h^{\alpha}_{ba}h^{\mu\alpha}_{ab}}{\omega - i\eta + \epsilon_{ba}} \\ &= f_{ab}\frac{h^{\alpha}_{ab}h^{\mu\alpha}_{ba}}{\omega + i\eta - \epsilon_{ab}} + f_{ab}\frac{h^{\alpha}_{ba}h^{\mu\alpha}_{ab}}{\omega - i\eta - \epsilon_{ab}} \\ = f_{ab}P\left(\frac{1}{\omega - \epsilon_{ab}}\right)\left[h^{\alpha}_{ab}h^{\mu\alpha}_{ba} + h^{\alpha}_{ba}h^{\mu\alpha}_{ab}\right] + f_{ab}i\pi & \left[h^{\alpha}_{ab}h^{\mu\alpha}_{ba} - h^{\alpha}_{ba}h^{\mu\alpha}_{ab}\right]\delta(\omega - \epsilon_{ab}).\end{aligned} \tag{B.7}$$

For our purpose, the most interesting term is the one involving $\delta(\omega - \epsilon_{ab})$. We can write

$$h^{\alpha}_{ab} h^{\mu\alpha}_{ba} - h^{\alpha}_{ba} h^{\mu\alpha}_{ab} = h^{\alpha}_{ab} h^{\mu\alpha}_{ba} - [a \leftrightarrow b]. \tag{B.8}$$

Now, first we derive an expression for $h^{\alpha\beta}_{mn}$. According to the notation used in Ref. [266],

$$h^{\alpha\beta}_{mn} = \left[D^{\alpha} D^{\beta}[H_0]\right]_{mn} \equiv \left\langle m|\nabla_{\alpha}\nabla_{\beta}(H_0)|n\right\rangle \tag{B.9}$$

where H_0 is the unperturbed Hamiltonian and for a given operator O

$$D[O]_{ab} = [D, O]_{ab} = \nabla_k(O_{ab}) - i[\mathbf{A}, O]_{ab} \tag{B.10}$$

where $\mathbf{A}$ is the Berry-connection matrix with $\mathbf{A}^{\mu}_{mn} = i\langle u_m|\partial_{k^{\mu}}|u_n\rangle$. We can thus write

$$h^{\alpha\beta}_{mn} = \left[D^{\alpha} D^{\beta}[H_0]\right]_{mn} = \partial_{\alpha}\left(\left[D^{\beta}[H_0]\right]_{mn}\right) - i\left[\mathbf{A}^{\alpha}, D^{\beta}[H_0]\right]_{mn}. \tag{B.11}$$

We have

$$h^{\beta}_{mn} = \left(D^{\beta}[H_0]\right)_{mn} = \partial_{\beta}((H_0)_{mn}) - i\left[\mathbf{A}^{\beta}, H_0\right]_{mn} = \underbrace{\delta_{mn} v^{\beta}_{nn} - i(\epsilon_n - \epsilon_m)\mathbf{A}^{\beta}_{mn}}_{v^{\beta}_{mn}} \tag{B.12}$$

where we have used the fact that $\langle m|H_0|n\rangle = \delta_{mn}\epsilon_n$ and $v^{\beta}_{nn} = \partial_{\beta}\epsilon_n$. We can express

$$\left[\mathbf{A}^{\alpha}, D^{\beta}[H_0]\right]_{mn} = \left[\mathbf{A}^{\alpha} h^{\beta} - h^{\beta}\mathbf{A}^{\alpha}\right]_{mn} = \mathbf{A}^{\alpha}_{md} h^{\beta}_{dn} - \mathbf{A}^{\alpha}_{dn} h^{\beta}_{md}. \tag{B.13}$$

For the first term in Eq. B.11, we can use Eq. B.12 to write

$$\partial_{\alpha}\left(\left[D^{\beta}[H_0]\right]_{mn}\right) = \delta_{mn}\partial_{\alpha}\epsilon_n - i(v^{\alpha}_{nn} - v^{\alpha}_{mm})\mathbf{A}^{\beta}_{mn} - i\epsilon_{nm}\partial_{\alpha}\mathbf{A}^{\beta}_{mn} \tag{B.14}$$

and the second part can be fully extended using Eq. B.12 and Eq. B.13

$$-i\left[\mathbf{A}^{\alpha}, D^{\beta}[H_0]\right]_{mn} = -i\mathbf{A}^{\alpha}_{md}\left(\delta_{dn} v^{\beta}_{nn} - i\epsilon_{nd}\mathbf{A}^{\beta}_{db}\right) + i\mathbf{A}^{\alpha}_{dn}\left(\delta_{md} v^{\beta}_{mm} - i\epsilon_{dm}\mathbf{A}^{\beta}_{md}\right). \tag{B.15}$$

Now, combining these two equations we get:

$$\begin{aligned} h^{\alpha\beta}_{mn} = \partial_{\alpha}\left(\left[D^{\beta}[H_0]\right]_{mn}\right) - i\left[\mathbf{A}^{\alpha}, D^{\beta}[H_0]\right]_{mn} &= \delta_{mn}\partial_{\alpha}\epsilon_n - i(v^{\alpha}_{nn} - v^{\alpha}_{mm})\mathbf{A}^{\beta}_{mn} \\ -i\epsilon_{nm}\partial_{\alpha}\mathbf{A}^{\beta}_{mn} - i\mathbf{A}^{\alpha}_{md}\delta_{dn} v^{\beta}_{nn} + i\mathbf{A}^{\alpha}_{dn}\delta_{md} v^{\beta}_{mm} &- \epsilon_{nd}\mathbf{A}^{\alpha}_{md}\mathbf{A}^{\beta}_{dn} + \epsilon_{dm}\mathbf{A}^{\alpha}_{dn}\mathbf{A}^{\beta}_{md}. \end{aligned} \tag{B.16}$$

$$\begin{aligned} \implies h^{\alpha\beta}_{mn} = \partial_{\alpha}\left(\left[D^{\beta}[H_0]\right]_{mn}\right) - i\left[\mathbf{A}^{\alpha}, D^{\beta}[H_0]\right]_{mn} &= \delta_{mn}\partial_{\alpha}\epsilon_n - i(v^{\alpha}_{nn} - v^{\alpha}_{mm})\mathbf{A}^{\beta}_{mn} \\ -i\epsilon_{nm}\partial_{\alpha}\mathbf{A}^{\beta}_{mn} - i\mathbf{A}^{\alpha}_{mn} v^{\beta}_{nn} + i\mathbf{A}^{\alpha}_{mn} v^{\beta}_{mm} &- \epsilon_{nd}\mathbf{A}^{\alpha}_{md}\mathbf{A}^{\beta}_{dn} + \epsilon_{dm}\mathbf{A}^{\alpha}_{dn}\mathbf{A}^{\beta}_{md}. \end{aligned} \tag{B.17}$$

Our goal was to evaluate $h^{\alpha}_{ab}h^{\mu\alpha}_{ba}$ in Eq. B.8. For now, we are going to focus on case $a \neq b$ For $a \neq b$, $h^{\alpha}_{ab} = -i\epsilon_{ba}\mathbf{A}^{\alpha}_{ab}$ from Eq. B.12 and similarly

$$h^{\alpha}_{ab}h^{\mu\alpha}_{ba} = -i\epsilon_{ba}\mathbf{A}^{\alpha}_{ab}\left(-i\Delta^{\mu}_{ab}\mathbf{A}^{\alpha}_{ba} - i\epsilon_{ab}\partial_{\mu}\mathbf{A}^{\alpha}_{ba} - i\mathbf{A}^{\mu}_{ba}\Delta^{\alpha}_{ab} - \epsilon_{ad}\mathbf{A}^{\mu}_{bd}\mathbf{A}^{\alpha}_{da} + \epsilon_{db}\mathbf{A}^{\mu}_{da}\mathbf{A}^{\alpha}_{bd}\right). \tag{B.18}$$

where $\Delta^{\mu}_{ab} = v^{\mu}_{aa} - v^{\mu}_{bb}$. This gives

$$\begin{aligned} h^{\alpha}_{ab}h^{\mu\alpha}_{ba} - h^{\alpha}_{ba}h^{\mu\alpha}_{ab} &= \epsilon^{2}_{ab}\left(\mathbf{A}^{\alpha}_{ab}\partial_{\mu}\mathbf{A}^{\alpha}_{ba} - \mathbf{A}^{\alpha}_{ba}\partial_{\mu}\mathbf{A}^{\alpha}_{ab}\right) - \epsilon_{ba}\Delta^{\alpha}_{ab}\left(\mathbf{A}^{\alpha}_{ab}\mathbf{A}^{\mu}_{ba} - \mathbf{A}^{\alpha}_{ba}\mathbf{A}^{\mu}_{ab}\right) \\ -i\epsilon_{ba}\left(-\epsilon_{ad}\mathbf{A}^{\alpha}_{ab}\mathbf{A}^{\mu}_{bd}\mathbf{A}^{\alpha}_{da} - \epsilon_{bd}\mathbf{A}^{\alpha}_{ba}\mathbf{A}^{\mu}_{ad}\mathbf{A}^{\alpha}_{db}\right) &- i\epsilon_{ba}\left(\epsilon_{db}\mathbf{A}^{\alpha}_{ab}\mathbf{A}^{\mu}_{da}\mathbf{A}^{\alpha}_{bd} + \epsilon_{da}\mathbf{A}^{\alpha}_{ba}\mathbf{A}^{\mu}_{db}\mathbf{A}^{\alpha}_{ad}\right). \end{aligned} \tag{B.19}$$

It can be written as

$$\begin{aligned} h^{\alpha}_{ab}h^{\mu\alpha}_{ba} - h^{\alpha}_{ba}h^{\mu\alpha}_{ab} &= 2i\epsilon^{2}_{ab}\left(|\mathbf{A}^{\alpha}_{ab}|^{2}\partial_{\mu}\phi^{\alpha}_{ba}\right) - \epsilon_{ba}\Delta^{\alpha}_{ab}\left(\mathbf{A}^{\alpha}_{ab}\mathbf{A}^{\mu}_{ba} - \mathbf{A}^{\alpha}_{ba}\mathbf{A}^{\mu}_{ab}\right) \\ -i\epsilon_{ba}\left(-\epsilon_{ab}\mathbf{A}^{\alpha}_{ab}\mathbf{A}^{\mu}_{bb}\mathbf{A}^{\alpha}_{ba} - \epsilon_{ba}\mathbf{A}^{\alpha}_{ba}\mathbf{A}^{\mu}_{aa}\mathbf{A}^{\alpha}_{ab}\right) &- i\epsilon_{ba}\left(\epsilon_{ab}\mathbf{A}^{\alpha}_{ab}\mathbf{A}^{\mu}_{aa}\mathbf{A}^{\alpha}_{ba} + \epsilon_{ba}\mathbf{A}^{\alpha}_{ba}\mathbf{A}^{\mu}_{bb}\mathbf{A}^{\alpha}_{ab}\right) \\ \sum_{d\neq a,b} -i\epsilon_{ba}\left(-\epsilon_{ad}\mathbf{A}^{\alpha}_{ab}\mathbf{A}^{\mu}_{bd}\mathbf{A}^{\alpha}_{da} - \epsilon_{bd}\mathbf{A}^{\alpha}_{ba}\mathbf{A}^{\mu}_{ad}\mathbf{A}^{\alpha}_{db}\right) &- i\epsilon_{ba}\left(\epsilon_{db}\mathbf{A}^{\alpha}_{ab}\mathbf{A}^{\mu}_{da}\mathbf{A}^{\alpha}_{bd} + \epsilon_{da}\mathbf{A}^{\alpha}_{ba}\mathbf{A}^{\mu}_{db}\mathbf{A}^{\alpha}_{ad}\right) \end{aligned} \tag{B.20}$$

where $\phi^{\mu}_{ba} = \mathrm{Arg}[\mathbf{A}^{\mu}_{ba}]$, and simplifying it further we get

$$\begin{aligned} h^{\alpha}_{ab}h^{\mu\alpha}_{ba} - h^{\alpha}_{ba}h^{\mu\alpha}_{ab} = 2i\epsilon^{2}_{ab}\left(|\mathbf{A}^{\alpha}_{ab}|^{2}\partial_{\mu}\phi^{\alpha}_{ba}\right) - 2i\epsilon^{2}_{ba}\left|\mathbf{A}^{\alpha}_{ab}\right|^{2}\left(\mathbf{A}^{\mu}_{bb} - \mathbf{A}^{\mu}_{aa}\right) - \epsilon_{ba}\Delta^{\alpha}_{ab}\left(\mathbf{A}^{\alpha}_{ab}\mathbf{A}^{\mu}_{ba} - \mathbf{A}^{\alpha}_{ba}\mathbf{A}^{\mu}_{ab}\right) \\ + \sum_{d\neq a,b} -i\epsilon_{ba}\left(-\epsilon_{ad}\mathbf{A}^{\alpha}_{ab}\mathbf{A}^{\mu}_{bd}\mathbf{A}^{\alpha}_{da} - \epsilon_{bd}\mathbf{A}^{\alpha}_{ba}\mathbf{A}^{\mu}_{ad}\mathbf{A}^{\alpha}_{db}\right) - i\epsilon_{ba}\left(\epsilon_{db}\mathbf{A}^{\alpha}_{ab}\mathbf{A}^{\mu}_{da}\mathbf{A}^{\alpha}_{bd} + \epsilon_{da}\mathbf{A}^{\alpha}_{ba}\mathbf{A}^{\mu}_{db}\mathbf{A}^{\alpha}_{ad}\right). \end{aligned} \tag{B.21}$$

Now, we can further simplify it by using $h^{\gamma}_{mn} = i\epsilon_{nm}\mathbf{A}^{\gamma}_{mn}$ for $m \neq n$,

$$\begin{aligned} h^{\alpha}_{ab}h^{\mu\alpha}_{ba} - h^{\alpha}_{ba}h^{\mu\alpha}_{ab} = -2i\epsilon^{2}_{ab}|\mathbf{A}^{\alpha}_{ab}|^{2}\underbrace{\left(\mathbf{A}^{\mu}_{bb} - \mathbf{A}^{\mu}_{aa} - \partial_{\mu}\phi^{\alpha}_{ba}\right)}_{\text{Shift vector, }\mathbf{S}^{\mu}_{ba}} - \epsilon_{ba}\Delta^{\alpha}_{ab}\left(\mathbf{A}^{\alpha}_{ab}\mathbf{A}^{\mu}_{ba} - \mathbf{A}^{\alpha}_{ba}\mathbf{A}^{\mu}_{ab}\right) \\ \sum_{d\neq a,b}\left(-\epsilon_{ad}h^{\alpha}_{ab}\mathbf{A}^{\mu}_{bd}\mathbf{A}^{\alpha}_{da} + \epsilon_{bd}h^{\alpha}_{ba}\mathbf{A}^{\mu}_{ad}\mathbf{A}^{\alpha}_{db}\right) + \left(\epsilon_{db}h^{\alpha}_{ab}\mathbf{A}^{\mu}_{da}\mathbf{A}^{\alpha}_{bd} - \epsilon_{da}h^{\alpha}_{ba}\mathbf{A}^{\mu}_{db}\mathbf{A}^{\alpha}_{ad}\right). \end{aligned} \tag{B.22}$$

It can be simplified further

$$\begin{aligned} h^{\alpha}_{ab}h^{\mu\alpha}_{ba} - h^{\alpha}_{ba}h^{\mu\alpha}_{ab} &= -2i\epsilon^{2}_{ab}|\mathbf{A}^{\alpha}_{ab}|^{2}\mathbf{S}^{\mu}_{ba} + \Delta^{\alpha}_{ab}\left(\frac{1}{\epsilon_{ab}}h^{\alpha}_{ab}h^{\mu}_{ba} + \frac{1}{\epsilon_{ba}}h^{\alpha}_{ba}h^{\mu}_{ab}\right) \\ \sum_{d\neq a,b}\left(-\frac{1}{\epsilon_{bd}}h^{\alpha}_{ab}h^{\mu}_{bd}h^{\alpha}_{da} + \frac{1}{\epsilon_{ad}}h^{\alpha}_{ba}h^{\mu}_{ad}h^{\alpha}_{db}\right) &+ \left(\frac{1}{\epsilon_{da}}h^{\alpha}_{ab}h^{\mu}_{da}h^{\alpha}_{bd} - \frac{1}{\epsilon_{db}}h^{\alpha}_{ba}h^{\mu}_{db}h^{\alpha}_{ad}\right). \end{aligned} \tag{B.23}$$

Now substituting it back in $\delta(\omega-\epsilon_{ab})$ part of Eq. B.7, we get the contribution of 2nd and 3rd terms of Eq. B.6

$$\begin{aligned}
\sigma^{23}_{\delta(\omega-\epsilon_{ab})} &= \frac{2\pi e^3}{\hbar^2}\int [d\mathbf{k}] f_{ab}|\mathbf{A}^{\alpha}_{ab}|^2\mathbf{S}^{\mu}_{ba}\delta(\omega-\epsilon_{ab})\\
&+\boxed{\frac{2\pi e^3}{\hbar^2\omega^2}\int [d\mathbf{k}] f_{ab}\Delta^{\alpha}_{ab}\left(\frac{1}{\epsilon_{ab}}h^{\alpha}_{ab}h^{\mu}_{ba}+\frac{1}{\epsilon_{ba}}h^{\alpha}_{ba}h^{\mu}_{ab}\right)i\delta(\omega-\epsilon_{ab})}\\
&\boxed{+\frac{2\pi e^3}{\hbar^2\omega^2}\sum_{d\neq a,b}\int [d\mathbf{k}] f_{ab}\left[\left(-\frac{1}{\epsilon_{bd}}h^{\alpha}_{ab}h^{\mu}_{bd}h^{\alpha}_{da}+\frac{1}{\epsilon_{ad}}h^{\alpha}_{ba}h^{\mu}_{ad}h^{\alpha}_{db}\right)\right]i\delta(\omega-\epsilon_{ab})}\\
&\boxed{+\frac{2\pi e^3}{\hbar^2\omega^2}\sum_{d\neq a,b}\int [d\mathbf{k}] f_{ab}\left[\left(\frac{1}{\epsilon_{da}}h^{\alpha}_{ab}h^{\mu}_{da}h^{\alpha}_{bd}-\frac{1}{\epsilon_{db}}h^{\alpha}_{ba}h^{\mu}_{db}h^{\alpha}_{ad}\right)\right]i\delta(\omega-\epsilon_{ab})}
\end{aligned}\tag{B.24}$$

It is worth mentioning that the quantity $\Delta^{\alpha}_{ab}\left(\frac{1}{\epsilon_{ab}}h^{\alpha}_{ab}h^{\mu}_{ba}+\frac{1}{\epsilon_{ba}}h^{\alpha}_{ba}h^{\mu}_{ab}\right)$ and $\left[\left(-\frac{1}{\epsilon_{bd}}h^{\alpha}_{ab}h^{\mu}_{bd}h^{\alpha}_{da}+\frac{1}{\epsilon_{ad}}h^{\alpha}_{ba}h^{\mu}_{ad}h^{\alpha}_{db}\right)+\left(\frac{1}{\epsilon_{da}}h^{\alpha}_{ab}h^{\mu}_{da}h^{\alpha}_{bd}-\frac{1}{\epsilon_{db}}h^{\alpha}_{ba}h^{\mu}_{db}h^{\alpha}_{ad}\right)\right]$ are imaginary by default. This shows that the second and third terms of Eq. B.6 contains not only the shift vector term but also a few extra terms which include three velocity elements. Next, we would like to check if these extra terms shown in the box above cancel out σ^{56} (5th and 6th terms) of Eq. B.6. We have

$$\begin{aligned}
\sigma^{56} &= \frac{2\pi e^3}{\hbar^2\omega^2}\int [d\mathbf{k}]\frac{h^{\alpha}_{ab}h^{\alpha}_{bc}h^{\mu}_{ca}}{\epsilon_{ac}}\left[\frac{f_{ab}}{\omega+i\eta-\epsilon_{ba}}+\frac{f_{cb}}{-\omega+i\eta-\epsilon_{cb}}\right]\\
&+\frac{2\pi e^3}{\hbar^2\omega^2}\int [d\mathbf{k}]\frac{h^{\alpha}_{ab}h^{\alpha}_{bc}h^{\mu}_{ca}}{\epsilon_{ac}}\left[\frac{f_{ab}}{-\omega+i\eta-\epsilon_{ba}}+\frac{f_{cb}}{\omega+i\eta-\epsilon_{cb}}\right]
\end{aligned}\tag{B.25}$$

and after switching $a \leftrightarrow c$ in 3rd and 4th terms, it can be written as

$$\begin{aligned}
\sigma^{56} &= \frac{2\pi e^3}{\hbar^2\omega^2}\int [d\mathbf{k}]\left[\frac{f_{ab}}{\epsilon_{ac}}\frac{h^{\alpha}_{ab}h^{\alpha}_{bc}h^{\mu}_{ca}}{\omega+i\eta-\epsilon_{ba}}+\frac{f_{ab}}{\epsilon_{ca}}\frac{h^{\alpha}_{cb}h^{\alpha}_{ba}h^{\mu}_{ac}}{-\omega+i\eta-\epsilon_{ab}}\right]\\
&+\frac{2\pi e^3}{\hbar^2\omega^2}\int [d\mathbf{k}]\left[\frac{f_{ab}}{\epsilon_{ac}}\frac{h^{\alpha}_{ab}h^{\alpha}_{bc}h^{\mu}_{ca}}{-\omega+i\eta-\epsilon_{ba}}+\frac{f_{ab}}{\epsilon_{ca}}\frac{h^{\alpha}_{cb}h^{\alpha}_{ba}h^{\mu}_{ac}}{\omega+i\eta-\epsilon_{ab}}\right]
\end{aligned}\tag{B.26}$$

$$\begin{aligned}
\implies \sigma^{56} = {} & \frac{2\pi e^3}{\hbar^2\omega^2}\int [d\mathbf{k}] f_{ba}\left[\frac{h^{\alpha}_{ba}h^{\alpha}_{ac}h^{\mu}_{cb}}{\epsilon_{bc}} - \frac{h^{\alpha}_{ca}h^{\alpha}_{ab}h^{\mu}_{bc}}{\epsilon_{cb}}\right] P\left(\frac{1}{\omega-\epsilon_{ab}}\right) \\
& + \frac{2\pi e^3}{\hbar^2\omega^2}\int [d\mathbf{k}] f_{ba}\left[\frac{h^{\alpha}_{ab}h^{\alpha}_{bc}h^{\mu}_{ca}}{\epsilon_{ac}} - \frac{h^{\alpha}_{cb}h^{\alpha}_{ba}h^{\mu}_{ac}}{\epsilon_{ca}}\right] P\left(\frac{1}{\omega-\epsilon_{ab}}\right) \\
& + \frac{2\pi e^3}{\hbar^2\omega^2}\int [d\mathbf{k}] f_{ba}\left[\frac{h^{\alpha}_{ba}h^{\alpha}_{ac}h^{\mu}_{cb}}{\epsilon_{bc}} + \frac{h^{\alpha}_{ca}h^{\alpha}_{ab}h^{\mu}_{bc}}{\epsilon_{cb}}\right] i\pi\delta(\omega-\epsilon_{ab}) \\
& + \frac{2\pi e^3}{\hbar^2\omega^2}\int [d\mathbf{k}] f_{ba}\left[-\frac{h^{\alpha}_{ab}h^{\alpha}_{bc}h^{\mu}_{ca}}{\epsilon_{ac}} - \frac{h^{\alpha}_{cb}h^{\alpha}_{ba}h^{\mu}_{ac}}{\epsilon_{ca}}\right] i\pi\delta(\omega-\epsilon_{ab}).
\end{aligned} \tag{B.27}$$

Now, the term involving $\delta(\omega-\epsilon_{ab})$ can be written as

$$\begin{aligned}
\sigma^{56}_{\delta(\omega-\epsilon_{ab})} = {} & \frac{2\pi e^3}{\hbar^2\omega^2}\int [d\mathbf{k}] f_{ba}\left[\frac{h^{\alpha}_{ba}h^{\alpha}_{ad}h^{\mu}_{db}}{\epsilon_{bd}} + \frac{h^{\alpha}_{da}h^{\alpha}_{ab}h^{\mu}_{bd}}{\epsilon_{db}}\right] i\pi\delta(\omega-\epsilon_{ab}) \\
& + \frac{2\pi e^3}{\hbar^2\omega^2}\int [d\mathbf{k}] f_{ba}\left[-\frac{h^{\alpha}_{ab}h^{\alpha}_{bd}h^{\mu}_{da}}{\epsilon_{ad}} - \frac{h^{\alpha}_{db}h^{\alpha}_{ba}h^{\mu}_{ad}}{\epsilon_{da}}\right] i\pi\delta(\omega-\epsilon_{ab}).
\end{aligned} \tag{B.28}$$

After rearranging these terms and using $\Delta^{\alpha}_{ab} = h^{\alpha}_{aa} - h^{\alpha}_{bb}$, we get

$$\begin{aligned}
\sigma^{56}_{\delta(\omega-\epsilon_{ab})} = {} & \boxed{(-1)\frac{2\pi e^3}{\hbar^2\omega^2}\int [d\mathbf{k}] f_{ab}\Delta^{\alpha}_{ab}\left[\frac{h^{\alpha}_{ab}h^{\mu}_{ba}}{\epsilon_{ab}} + \frac{h^{\alpha}_{ba}h^{\mu}_{ab}}{\epsilon_{ba}}\right] i\pi\delta(\omega-\epsilon_{ab})} \\
& - \boxed{\frac{2\pi e^3}{\hbar^2\omega^2}\int [d\mathbf{k}] f_{ab}\sum_{d\neq a,b}\left[-\frac{h^{\alpha}_{da}h^{\alpha}_{ab}h^{\mu}_{bd}}{\epsilon_{bd}} + \frac{h^{\alpha}_{db}h^{\alpha}_{ba}h^{\mu}_{ad}}{\epsilon_{ad}}\right] i\pi\delta(\omega-\epsilon_{ab})} \\
& - \boxed{\frac{2\pi e^3}{\hbar^2\omega^2}\int [d\mathbf{k}] f_{ab}\sum_{d\neq a,b}\left[\frac{h^{\alpha}_{ab}h^{\alpha}_{bd}h^{\mu}_{da}}{\epsilon_{da}} - \frac{h^{\alpha}_{ba}h^{\alpha}_{ad}h^{\mu}_{db}}{\epsilon_{db}}\right] i\pi\delta(\omega-\epsilon_{ab})}.
\end{aligned} \tag{B.29}$$

Now, we can see that the above expression $\sigma^{56}_{\delta(\omega-\epsilon_{ab})}$ is equal and opposite to the boxed part (three velocity terms) of Eq. B.24. In other words:

$$\sigma^{23}_{\delta(\omega-\epsilon_{ab})} + \sigma^{56}_{\delta(\omega-\epsilon_{ab})} = \frac{2\pi e^3}{\hbar^2}\int [d\mathbf{k}] f_{ab}|\mathbf{A}^{\alpha}_{ab}|^2\mathbf{S}^{\mu\alpha}_{ba}\delta(\omega-\epsilon_{ab}) \tag{B.30}$$

which is the shift-current expression used in the main text.

Chapter 6

ANOMALOUS EXCITON DRIFT IN RESPONSE TO A UNIFORM, IN-PLANE ELECTRIC FIELD

"Science is the cognition of necessity; freedom is the recognition of necessity." – D.D. Kosambi

In above two chapters, we described the effects of quantum geometry within single-particle picture. In addition to single-particle behavior, many QG signatures also manifest in collective excitations. In this chapter, we explore the consequences of Berry curvature on exciton transport.

Excitons are neutral objects, that, naively, should have no response to a uniform, electric field. Could the Berry curvature of the underlying electronic bands alter this conclusion? In this work, we show that Berry curvature can indeed lead to anomalous transport for excitons in 2D materials subject to a uniform, in-plane electric field. By considering the constituent electron and hole dynamics, we demonstrate that there exists a regime for which the corresponding anomalous velocities are in the same direction. We establish the resulting center of mass motion of the exciton through both a semiclassical and fully quantum mechanical analysis, and elucidate the critical role of Bloch oscillations in achieving this effect. We identify transition metal dichalcogenide heterobilayers as candidate materials to observe the effect.

This chapter is based on the following reference:

Swati Chaudhary, Christina Knapp, and Gil Refael. "Anomalous exciton transport in response to a uniform in-plane electric field." In: Phys. Rev. B **103**, 165119 (2019)

6.1 Introduction

Berry curvature of electronic bands plays an important role in the transport phenomena and optical responses of a system [378]. Among the myriad consequences of a finite Berry curvature is the anomalous velocity, in which an electron experiencing a force perpendicular to the Berry curvature of the band acquires a contribution to the velocity perpendicular to both. The anomalous velocity can be well understood from a single particle and semi-classical treatment, and leads to a variety of interesting features including the quantum anomalous Hall effect. In this work, we consider the role played by the anomalous velocity for exciton transport.

Excitons have attracted renewed interest for their dominant role in the optical response of van der Waals materials [106, 99, 289, 66, 246, 364, 360, 192, 231, 233]. An exciton is a neutral boson consisting of an electron-hole pair bound by Coulomb interactions. In van der Waals materials, such as transition metal dichalcogenides (TMDs) [106], excitons exhibit a variety of interesting behaviors intimately tied to Berry curvature, including valley selective optical response [392, 46, 219, 220, 281, 401, 154, 45], topological bands in the presence of a moiré potential [315, 372, 373, 195], and non-hydrogenic spectra [329, 406, 10, 138]. In particular, anomalous exciton transport in response to electric and magnetic fields has garnered significant interest [184, 151, 186, 258, 108]. Typically, such transport requires a net force acting on the exciton center of mass, e.g. by utilizing the exciton dipole moment. In contrast, here we consider excitons confined to a two-dimensional system in the presence of a uniform in-plane electric field[1]. Given the absence of a net force on the exciton center of mass, anomalous transport can only arise by considering the internal structure of the exciton.

Heuristically, one might anticipate that in response to a uniform, in-plane electric field the electron and hole composing the exciton would initially move apart until they reach an equilibrium point at which the force from the electric field is balanced by the Coulomb interaction. If the electronic bands have some out-of-plane Berry curvature component, both constituent particles will move with an anomalous velocity while they experience a net force [378]. In the case of intervalley excitons, the electron and hole bands can experience the same Berry curvature. As a result, the anomalous velocity will point in the same direction for the electron and hole, thereby resulting in exciton center of mass motion. However, this anomalous motion will only happen for the short period of time that it takes the electron and hole to reach their equilibrium separation, after which the exciton will once again remain stationary.

In this work, we show that when the electron and hole undergo Bloch oscillations, the anomalous velocity persists over an extended period of time resulting in a measurable anomalous exciton drift. While the effect is predicted to be stronger for topological bands, it does not require them. Essentially, Bloch oscillations bound the relative

---

[1] For our purposes, we only consider an electron and hole pair to constitute an exciton if the electric field is below the ionization field, such that they remain bound together when we turn off the electric field. This definition requires the electric field to only mix the initial exciton ground state with other bound exciton levels and not with the continuum.

separation of the electron and hole by the bandwidth so that the electron and hole can never reach their equilibrium separation. The exciton center of mass moves as a result of the sustained anomalous velocity, resulting in anomalous transport in response to a uniform in-plane electric field. A semiclassical analysis predicts Bloch oscillations when the electric field is sufficiently large compared to the Coulomb interaction. Surprisingly, we find that Bloch oscillations can also occur when the interaction strength is large compared to the electric field. This additional region of parameter space supporting anomalous exciton transport only manifests when evolving the exciton quantum mechanically. Our main goal is to identify a proof-of-principle of this anomalous exciton transport through toy models. Although we roughly choose the toy model parameters on the basis of exciting materials, we avoid a material specific calculation and overlook some of the complications present in such materials.

The remainder of this work is organized as follows. In Section 6.2, we identify the necessary ingredients for anomalous exciton transport. We first consider a semiclassical analysis and derive a lower bound on the electric field for the electron and hole to experience Bloch oscillations. We then motivate why the small-field, strong-interaction limit also supports Bloch oscillations, with insight from a simple 1D toy model. In Section 6.3, we present numerically simulated phase diagrams of the anomalous exciton drift when the underlying electronic bands are both topological and trivial. We plot the semiclassical equations of motion for both harmonic and Coulombic potentials. We further simulate exciton dynamics quantum mechanically for a toy model of the electron and hole, again with both harmonic and Coulombic potentials. Section 6.4 identifies additional complications beyond the models considered in the previous sections and argues that TMD heterobilayers are an attractive candidate system to observe anomalous exciton transport. Finally, in Section 6.5 we discuss the relation to previous works and identify future directions. Details of the analytical and numerical analyses are relegated to the appendices.

6.2 Anomalous exciton drift: Theory

In this section, we introduce the toy models used to study anomalous exciton transport. We begin with a semiclassical analysis highlighting the critical role of Bloch oscillations. We then motivate how a quantum mechanical treatment indicates an additional region supporting the effect that is not predicted by semiclassics.

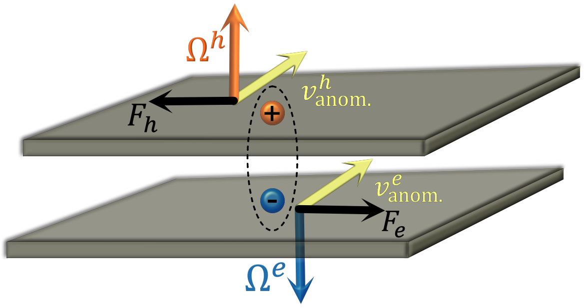

Figure 6.1: Schematic of an interlayer exciton with electron and hole bound to opposite layers. When the valence and conduction bands have the same Berry curvature, the anomalous velocity of the electron and hole $v^{e/h}_{\text{anom}}$ points in the same direction, resulting in a net transverse drift of the exciton.

Semiclassical exciton dynamics

We model the exciton as an electron-hole pair subject to an interaction potential $U(\mathbf{r}_e - \mathbf{r}_h)$ with the electron in the conduction band and the hole in the valence band. We assume both bands have finite Berry curvature $\mathbf{\Omega}^{c/v}_{e/h}$. In the presence of a uniform in-plane electric field, the semiclassical equations of motion are

$$\dot{\mathbf{k}}_{e/h} = -\nabla_{\mathbf{r}_{e/h}} U(\mathbf{r}_e - \mathbf{r}_h) \mp e\mathbf{E} \tag{6.1}$$

$$\dot{\mathbf{r}}_{e/h} = \partial_{\mathbf{k}_{e/h}} \varepsilon_{e/h}(\mathbf{k}_{e/h}) - \dot{\mathbf{k}}_{e/h} \times \mathbf{\Omega}^{c/v}_{e/h} \tag{6.2}$$

where we have set $\hbar = 1$ and $\varepsilon_{e/h}(\mathbf{k}_{e/h})$ denotes the electron/hole band dispersion. In Eq. (6.2), the first term corresponds to the group velocity resulting from the band dispersion, while the second term is the anomalous velocity resulting from finite Berry curvature.

The force experienced by the electron and hole are precisely opposite for uniform $\mathbf{E}$. As such, the force on the exciton center of mass is strictly vanishing,

$$\dot{\mathbf{K}} = \dot{\mathbf{k}}_e + \dot{\mathbf{k}}_h = 0. \tag{6.3}$$

The relative and center of mass (COM) position coordinates evolve according to

$$\dot{\mathbf{r}} = \partial_{\mathbf{k}_e} \varepsilon_e(\mathbf{k}_e) - \partial_{\mathbf{k}_h} \varepsilon_h(\mathbf{k}_h) - \dot{\mathbf{k}}_e \times \left(\mathbf{\Omega}^c_e(\mathbf{k}_e) + \mathbf{\Omega}^v_h(\mathbf{k}_h)\right) \tag{6.4}$$

$$\dot{\mathbf{R}} = \frac{\partial_{\mathbf{k}_e} \varepsilon_e(\mathbf{k}_e) + \partial_{\mathbf{k}_h} \varepsilon_h(\mathbf{k}_h)}{2} - \dot{\mathbf{k}}_e \times \frac{\mathbf{\Omega}^c_e(\mathbf{k}_e) - \mathbf{\Omega}^v_h(\mathbf{k}_h)}{2} \tag{6.5}$$

when $m_e = m_h$. Note that for a given band α, $\mathbf{\Omega}^\alpha_h(\mathbf{k}_h) = -\mathbf{\Omega}^\alpha_e(-\mathbf{k}_h)$, see Appendix C.1 for a derivation.

In a particle-hole symmetric two-band model, $\varepsilon_e(\mathbf{k}_e) = \varepsilon_h(-\mathbf{k}_h)$ and $\mathbf{\Omega}_e^c(\mathbf{k}) = \mathbf{\Omega}_h^v(\mathbf{k})$. Therefore, a direct momentum exciton $\mathbf{k}_e = -\mathbf{k}_h$ has no center of mass motion, $\dot{\mathbf{R}} = 0$. In this case, the Berry curvature can only affect the relative motion of the electron and hole. These internal dynamics can affect the exciton spectra [329, 406], but do not result in anomalous transport.

In contrast, any deviation from the two-band, direct-momentum, particle-hole symmetric system can result in Berry curvature effects on COM motion. Motivated by intervalley excitons in TMD bilayers, we consider a direct momentum exciton $\mathbf{k}_e = -\mathbf{k}_h$ with opposite Berry curvatures for the conduction and valence bands[2]. The corresponding relative and COM equations are

$$\dot{\mathbf{r}} = 2\partial_{\mathbf{k}_e}\varepsilon_e(\mathbf{k}_e), \qquad \dot{\mathbf{R}} = -2\dot{\mathbf{k}}_e \times \mathbf{\Omega}_e^c(\mathbf{k}_e). \tag{6.6}$$

In the absence of interactions, the relative and center of mass motions decouple, and an electric field $\mathbf{E}$ results in a net transverse drift of the exciton if the line integral of Berry curvature along the direction of $\mathbf{E}$ is non-zero.

Interactions complicate the story by coupling the relative and center of mass motion. The relative strength of interactions, bandwidth, and electric field result in two limiting regimes:

1. Harmonic oscillator regime: The restoring force is able to overcome the applied electric field and the relative momentum $\mathbf{k}$ of the exciton is not able to reach the Brillouin zone boundaries. As a result, $\dot{\mathbf{k}}$ changes sign and the exciton oscillates perpendicular to the direction of $\mathbf{E}$.
2. Bloch oscillation regime: The electric field is sufficiently large that $\dot{\mathbf{k}}$ has the same sign as $\mathbf{E}$ at all times. The relative momentum of the exciton crosses the Brillouin zone momentum-space boundary. The cooperative anomalous velocity results in a non-vanishing transverse drift in center of mass position whenever the line-integral of Berry curvature along the direction of $\mathbf{E}$ is non-zero.

The restoring force is provided by the attraction between the electron and hole; as such, it depends on both the strength of interactions (e.g. dielectric constant) and the displacement from the equilibrium position. The nature of the electron-hole

---

[2] We take momentum measured from the Dirac point to consider intervalley excitons and $\mathbf{k}_e = -\mathbf{k}_h$ simultaneously.

interaction depends on the type of exciton (intralayer or interlayer), as well as material specific parameters. In TMD monolayers, the interaction is often approximated by the Keldysh potential [60, 167, 81], while for TMD bilayers it takes a somewhat different form discussed in Ref. [360] that depends on the polarizability of both layers and the surrounding environment. However, in both cases the interaction is approximated by a simple harmonic potential near the equilibrium point. Below, we gain intuition by first considering toy models with a harmonic interaction to identify the necessary conditions for excitons to undergo anomalous transport. We then turn to a Coulombic interaction, thereby demonstrating a parameter regime for which the effect survives away from the harmonic limit. While these two toy models are sufficient for establishing proof-of-concept, a quantitative analysis of the anomalous exciton transport in a specific material would need to account for these more realistic models of the interaction.

Harmonic potential

When the attraction between the electron and hole is modeled as a harmonic potential

$$U(\mathbf{r}) = -V_0 + \frac{1}{2}\kappa r^2, \tag{6.7}$$

the non-vanishing equations of motion in the presence of a uniform electric field $\mathbf{E} = E\hat{\mathbf{x}}$ are

$$\begin{aligned} \dot{\mathbf{r}}(t) &= 2Ja\sin\left(k_x(t)a\right)\,\hat{\mathbf{x}} + 2Ja\sin\left(k_y a\right)\,\hat{\mathbf{y}} && (6.8)\\ \dot{\mathbf{k}}(t) &= -\left(\kappa x(t) + eE\right)\,\hat{\mathbf{x}} - \kappa y(t)\,\hat{\mathbf{y}} && (6.9)\\ \dot{\mathbf{R}}(t) &= 2\dot{k}_x\Omega_e^c(\mathbf{k}(t))\,\hat{\mathbf{y}} - 2\dot{k}_y\Omega_e^c(\mathbf{k}(t))\hat{\mathbf{x}} && (6.10) \end{aligned}$$

where $\mathbf{r} = \mathbf{r}_e - \mathbf{r}_h$ and $\mathbf{k} = (\mathbf{k}_e - \mathbf{k}_h)/2$. If there is no interaction, we expect Bloch oscillations in relative space with amplitude and period

$$x_{\text{Bloch}} = \frac{2J}{eE}, \qquad \tau_{\text{Bloch}} = \frac{2\pi}{eEa}. \tag{6.11}$$

The exciton COM experiences a net transverse drift provided $\oint \Omega_e^c(\mathbf{k})dk_x \neq 0$.

Interactions reduce the magnitude of $\mathbf{k}(t)$, and thus slow down the anomalous velocity. If at any point $x(t)$ exceeds the equilibrium position $x_{\text{eq}} = eE/\kappa$, the electron/hole does not reach the Brillouin zone boundary and $\mathbf{k}(t)$ changes sign. In this case, both relative and COM motion oscillate, corresponding to the harmonic oscillator regime.

The value of E for which $x_{\text{eq}} > x_{\text{Bloch}}$ sets a lower bound on E to achieve Bloch oscillations; in the absence of interactions, this bound is given by

$$eE > \sqrt{2J\kappa}. \tag{6.12}$$

Interactions modify the above, but do not change the fact that semiclassics only predicts anomalous exciton transport when the electric field is sufficiently large compared to J and κ.

Thus far, we have focused on the simple limit $\mathbf{\Omega}_e^c(\mathbf{k}) = \mathbf{\Omega}_e^v(\mathbf{k})$ for which the relative and COM motion decouple, with Berry curvature affecting only the latter. In the opposite limit $\mathbf{\Omega}_e^c(\mathbf{k}) = -\mathbf{\Omega}_e^v(\mathbf{k})$, relative and COM motion again decouple, with Berry curvature affecting only the former. More generally, both the relative and COM motion will be coupled by the Berry curvature terms. We discuss this intermediate case in Appendix C.2.

Coulombic potential

The harmonic potential considered above is a limiting case for which there exists a bound state for all values of electron and hole separation. To go beyond this limit, we consider the Coulomb interaction for interlayer excitons, where the electron and hole are confined to layers separated by a distance D,

$$U(\mathbf{r}) = -\frac{ke^2}{\epsilon}\frac{1}{\sqrt{D^2+r^2}} = -\frac{\kappa D^2}{\sqrt{1+r^2/D^2}}. \tag{6.13}$$

In the above, $\kappa \equiv ke^2/(\epsilon D^3)$. When $r \ll D$, $U(\mathbf{r})$ is well approximated by Eq. (6.7) with $V_0 = \kappa D^2$. For a system with anisotropic dielectric response, the interlayer separation D should be rescaled by a factor of $\sqrt{\epsilon_\perp/\epsilon_\parallel}$ and ϵ should be replaced by $\sqrt{\epsilon_\perp\epsilon_\parallel}$, where $\epsilon_\perp (\epsilon_\parallel)$ is the out-of plane (in-plane) dielectric constant. For TMD monolayers separated by layers of hBN, $\epsilon_\perp/\epsilon_\parallel$ is of the order of unity [198], and thus does not qualitatively affect our results.

The corresponding equations of motion for relative and COM position are again given by Eqs. (6.8) and (6.10), but $U(\mathbf{r})$ modifies Eq. (6.9) to

$$\dot{\mathbf{k}}(t) = -\nabla_{\mathbf{r}}U(\mathbf{r}) - eE\,\hat{\mathbf{x}}. \tag{6.14}$$

We again expect a net transverse drift in exciton COM motion for sufficiently large E. When $\langle x\rangle \ll D$, the transition between Bloch and harmonic oscillator regimes should agree with the bound derived for a harmonic potential. When $\langle x\rangle \sim D$, the restoring force is weaker than for the harmonic potential case. We expect this to result in the anomalous drift persisting for a larger region of E versus κ space.

Our semiclassical analysis considers separate wavepackets for the electron and hole. Alternatively, the single particle semiclassical formalism can be extended for an exciton, as was done recently by Ref. [44]. We compare these approaches in Appendix C.3.

Small field limit: Intuition from 1D toy model

The semiclassical analysis predicts anomalous exciton transport only when the electric field E is sufficiently large compared to the interaction strength κ. Our numerics, however, indicate that there is also anomalous drift in the small field regime. We can gain insight into this regime by considering a 1D toy model

$$\begin{aligned} H_{1\mathrm{D}} = -\sum_n \left[J \left(|n\rangle \langle n+1| + \mathrm{h.c} \right) + \frac{1}{2}\kappa a^2 \, \hat{n}^2 \, |n\rangle \langle n| \right] \\ + eEa \sum_n \hat{n} \, |n\rangle \langle n| \, , \end{aligned} \tag{6.15}$$

where $|n\rangle$ corresponds to the position eigenstate on the nth lattice site and $\hat{n}\,|n\rangle = n\,|n\rangle$. The position n represents the relative coordinate of the electron and hole in the exciton discussion.

In the previous section, we argued that for appropriate Berry curvature profiles, the exciton experiences an anomalous drift when the electron and hole cannot reach their equilibrium separation. The analogous consideration for the 1D toy model in Eq. (6.15) is to consider when the position expectation value $\langle a\hat{n}\rangle$ is less than the equilibrium separation $x_{\mathrm{eq}} \sim eE/\kappa$. If we begin in the ground state of $H_{1\mathrm{D}}$ for $E = 0$ and evolve for finite E, we find two regimes. When $\kappa a^2/J \lesssim 1$, the ground state resembles a wavepacket in both position and momentum space, resulting in good agreement with the semiclassical dynamics. In contrast, when $\kappa a^2/J \gg 1$, the ground state wavefunction $\psi_0(x)$ is confined to a single site and is therefore spread over the full Brillouin zone. The wavefunction experiences an averaged group velocity, resulting in a much smaller restoring force compared to the semiclassical regime. The position expectation value $\langle a\hat{n}\rangle$ oscillates with amplitude $\sim \left(J^2/(\kappa^2 a^4)\right) x_{\mathrm{eq}} \ll x_{\mathrm{eq}}$, see Appendix C.4, allowing Bloch oscillations even in the small E field limit. Extrapolating to exciton dynamics, we should therefore expect anomalous drift in both the semiclassical Bloch oscillation regime and in the small field-large interaction limit. We emphasize that the latter required taking into

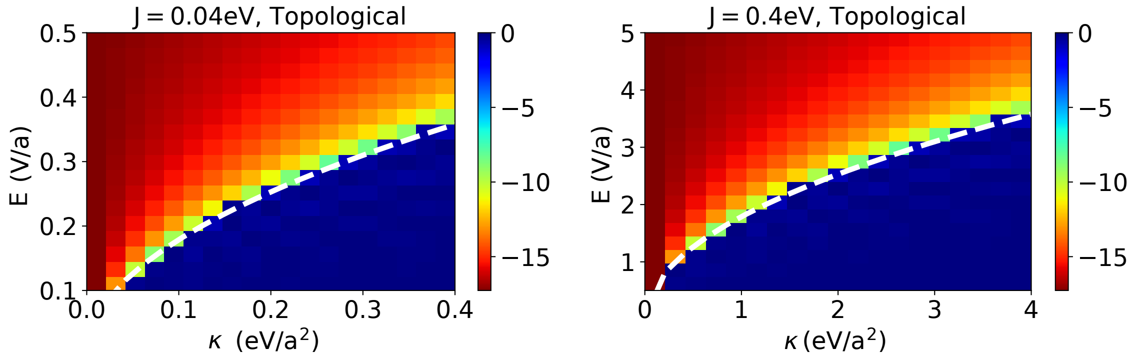

Figure 6.2: Semiclassical dynamics for harmonic potential. Average Y per Bloch cycle in units of the lattice constant a plotted against E and κ for $J = 0.04\,\mathrm{eV}$ (top) and $J = 0.4\,\mathrm{eV}$ (bottom) for topological bands ($m_0 = 1.4$ eV). The white dashed curve shows $2\sqrt{2J\kappa}$ separating the harmonic oscillator regime (dark blue) from the Bloch oscillator regime (red) in the case of topological bands. Note that the x-axis is in units of eV/a^2 and y-axis is in units of V/a, where a is the lattice constant. For $E = 0.25\,\mathrm{V/a}$, $a = 8\,\mathrm{nm}$, a transverse displacement of $5a$ indicates an anomalous velocity, $v^y_{\mathrm{anom.}} \approx 3 \times 10^6$ m/s.

account the finite spread of the wavefunction in position and momentum space, and thus only emerges in a quantum mechanical treatment of the dynamics.

6.3 Anomalous exciton drift: Numerics

We now numerically simulate a toy model of an exciton whose electron and hole occupy bands with the same Berry curvature profile. We consider both a semiclassical and a quantum mechanical model with similar band dispersion and Berry curvature profiles. For each case, we consider both harmonic and Coulombic potentials.

Semiclassical numerics

We simulate the center of mass motion according to the semiclassical equation of motion Eq. (6.5) with a simple cosine dispersion and with the Berry curvature profile set by the BHZ Hamiltonian [32]. More explicitly, we take the electron and hole to evolve according to the upper band of the band-flattened Hamiltonian

$$H^{\mathrm{FB}}_{\mathrm{BHZ}}(\mathbf{k}) = \varepsilon(\mathbf{k}) \frac{H_{\mathrm{BHZ}}(\mathbf{k})}{\mathcal{E}_{\mathrm{BHZ}}(\mathbf{k})}. \tag{6.16}$$

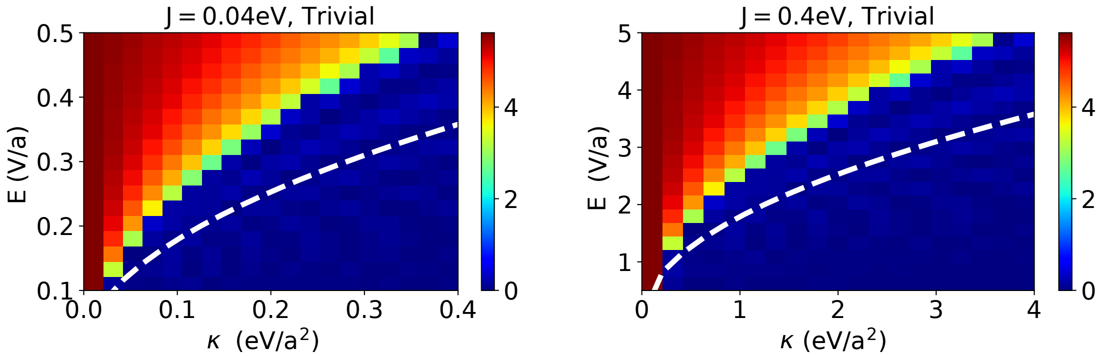

Figure 6.3: Semiclassical dynamics for harmonic potential. Average Y per Bloch cycle in units of the lattice constant a plotted against E and κ for $J = 0.04\,\text{eV}$ (top) and $J = 0.4\,\text{eV}$ (bottom) for trivial bands ($m_0 = 2.4\,\text{eV}$). The white dashed curve shows $2\sqrt{2J\kappa}$ separating the harmonic oscillator regime (dark blue) from the Bloch oscillator regime (red) in the case of topological bands. The Bloch oscillator regime is reduced, comparatively, for trivial bands.

In the above, H_{BHZ} and $\mathcal{E}_{\text{BHZ}}$ are the BHZ Hamiltonian and energy spectrum,

$$H_{\text{BHZ}}(\mathbf{k}) = \sum_{j\in\{x,y,z\}} c_j(\mathbf{k})\sigma_j \tag{6.17}$$

$$\mathcal{E}_{\text{BHZ}}(\mathbf{k}) = \sqrt{c_x(\mathbf{k})^2 + c_y(\mathbf{k})^2 + c_z(\mathbf{k})^2}, \tag{6.18}$$

for $c_z = m_0 - b[\cos(k_x a) + \cos(k_y a)]$, $c_{x/y} = v_{x/y}\sin(k_{x/y}a)$. We take the dispersion ε to be

$$\varepsilon(\mathbf{k}) = -J\left(\cos\left(k_x a\right) + \cos\left(k_y a\right)\right). \tag{6.19}$$

Figures 6.2 and 6.3 plots the average transverse COM motion per Bloch cycle in units of the lattice constant a for topological ($m_0 = 1.4\,\text{eV}$) and trivial ($m_0 = 2.4\,\text{eV}$) bands, respectively. We see that in the presence of harmonic interactions, the semiclassical Bloch oscillation regime for topological bands is bounded by

$$eE > 2\sqrt{2J\kappa}. \tag{6.20}$$

Above this bound, the exciton experiences an anomalous drift; below it, the exciton's center of mass displacement averages to zero. The top and bottom panels correspond to different values of the bandwidth J; as expected, the phase diagram is unchanged by scaling J, κ, and E by the same factor. We take parameters $b = 1\,\text{eV}$, $v_x = \pm v_y^{e/h} = 0.9\,\text{eV}$, and set $e = 1$. With these parameters and $E = 0.25\,\text{V}/a$, $a = 8\,\text{nm}$, a transverse displacement of $5a$ indicates an anomalous velocity $v^y_{\text{anom}} \approx 3 \times 10^6$ m/s.

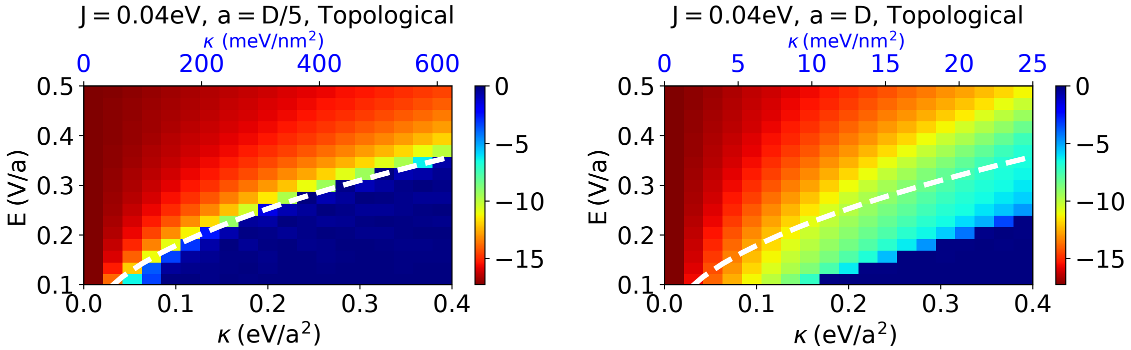

Figure 6.4: Semiclassical dynamics for Coulombic potential. Same phase diagram as in Fig. 6.2 for Coulombic interaction with $J = 0.04$ eV. For $a \ll D$ (top) the phase diagram is similar to that in Fig. 6.2. For $a = D$ (bottom), there is an increased Bloch oscillation regime compared to the harmonic potential case. The top x-axis in blue indicates the absolute scale of κ in meV/nm^2. The Berry curvature profile is again similar to that of Eq. (6.17) with the same parameters as in Fig. 6.2.

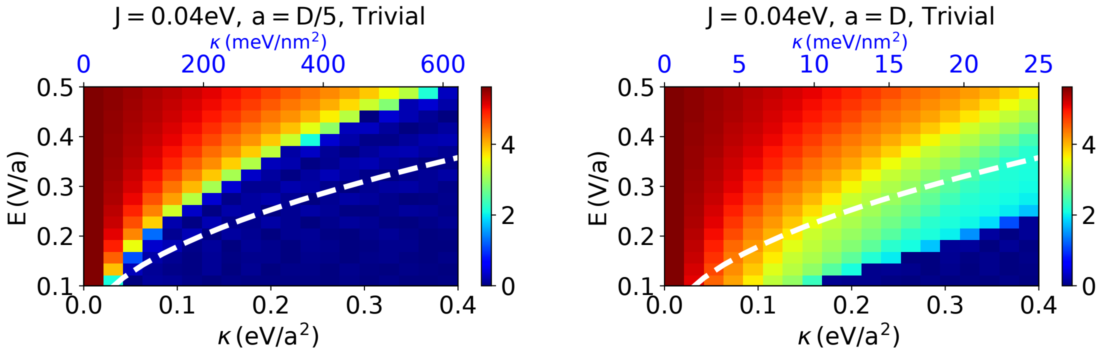

Figure 6.5: Semiclassical dynamics for Coulombic potential. Same phase diagram as in Fig. 6.3 for Coulombic interaction with $J = 0.04$ eV. For $a \ll D$ (top) the phase diagram is similar to that in Fig. 6.2. For $a = D$ (bottom), there is an increased Bloch oscillation regime compared to the harmonic potential case. The top x-axis in blue indicates the absolute scale of κ in meV/nm^2. The Berry curvature profile is again similar to that of Eq. (6.17) with the same parameters as in Fig. 6.2.

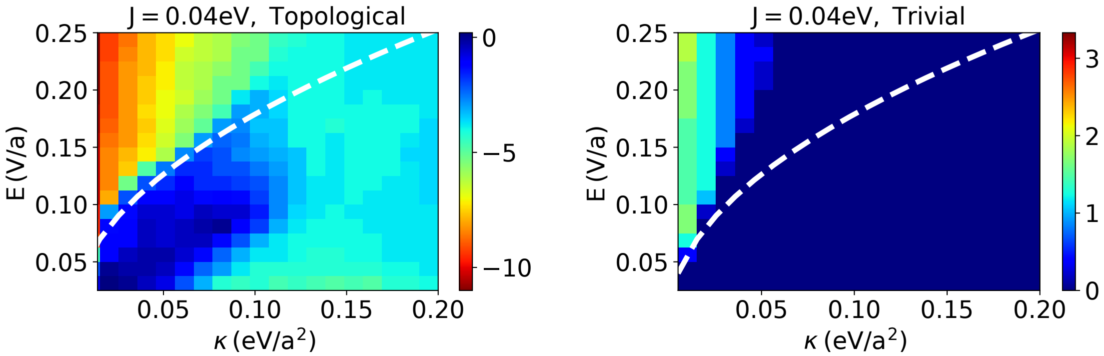

Figure 6.6: Exact dynamics for harmonic potential. Same phase diagram as in Fig. 6.2 simulated for exact dynamics with $J = 0.04\,\mathrm{eV}$ and harmonic potential. Changing m_0 tunes the system between topological bands (top, $m_0 = 1.4\,\mathrm{eV}$) and trivial bands (bottom, $m_0 = 2.4\,\mathrm{eV}$). The exciton ground state corresponds to the electron and hole both occupying the upper band of their respective copies of $H^{\mathrm{FB}}_{\mathrm{BHZ}}$, with the remaining parameters the same as in Fig. 6.2. The white dashed curve again corresponds to the semiclassical boundary between the harmonic (dark blue) and Bloch (red) oscillation regimes. Large κ corresponds to the exciton ground state being a wide wavepacket in relative momentum space. As a result, the group velocity is close to zero which suppresses the effect of the restoring force. When the band is topological, there is still a net transverse drift from average Berry curvature in this regime, in contrast to the semiclassical case in Fig. 6.2.

We plot the same phase diagrams for Coulombic potential in Figs. 6.4 and 6.5. The white dashed curve again plots the bound in Eq. (6.20). We see that for large D (top), the plot agrees with the phase diagram for the harmonic potential. As anticipated, for small D the Bloch oscillation regime extends beyond this bound. We take the same parameters as for Fig. 6.2.

Exact dynamics simulation

We simulate the exact dynamics of the exciton for a four band model with the same Berry curvature profiles and electron and hole dispersion as for the semiclassical numerics. We consider the Hamiltonian

$$\begin{aligned} H_{\mathbf{K}} =& H^{\mathrm{FB}}_{\mathrm{BHZ},\mathbf{K}} \otimes 1_h + 1_e \otimes H^{\mathrm{FB}}_{\mathrm{BHZ},\mathbf{K}} \\ &+ \sum_{\mathbf{r}} V(\mathbf{r}) 1_e \otimes 1_h \otimes |\mathbf{r}\rangle\langle\mathbf{r}| \end{aligned} \tag{6.21}$$

where $H^{\mathrm{FB}}_{\mathrm{BHZ},\mathbf{K}}$ is a tight-binding Hamiltonian obtained from the partial Fourier transform (performed in k space) of the band-flattened BHZ Hamiltonian in Eq. (6.16), $1_{e/h}$ is the identity matrix for the electron/hole Hilbert space, and $V(\mathbf{r})$ is the potential modeling the interaction (either harmonic or Coulombic). Note that as the interaction only depends on the relative coordinate, the Hamiltonian decouples into different $\mathbf{K}$ sectors. We initialize the system in the state

$$|\psi_0\rangle = \sum_{\mathbf{K}} \omega(\mathbf{K}) \, |\Phi_0(\mathbf{K})\rangle \tag{6.22}$$

where $\omega(\mathbf{K})$ is a narrow Gaussian envelope and $|\Phi_0(\mathbf{K})\rangle$ is the ground state of the Hamiltonian projected into the exciton Hilbert space

$$H_K^{\text{ex.}} = \hat{P}_e \, \hat{P}_h \, H_{\mathbf{K}} \, \hat{P}_h \, \hat{P}_e . \tag{6.23}$$

The operators $\hat{P}_{e/h}$ project onto the upper band of $H_{\text{BHZ}}^{\text{FB}}$, thereby ensuring the electron remains in the conduction band and the hole in the valence band. Our simulations use a real-space tight-binding approximation. Further details of the numerics are given in Appendix C.5.

For a harmonic potential, Fig. 6.6 plots the average COM motion of the exciton over a Bloch cycle when the BHZ parameters are chosen such that the bands are topological (top panel) and trivial (bottom panel). The former corresponds to $m_0 = 1.4\,\text{eV}$ while the latter corresponds to $m_0 = 2.4\,\text{eV}$. The remaining parameters are the same as in Fig. 6.2. The dashed curves again indicate the semiclassical boundary in Eq. (6.20). Just as was seen for semiclassical simulations of the harmonic potential, the plots remain the same when J, E, and κ are scaled by the same factor.

For non-trivial Chern number, we observe a large transverse drift in the COM position throughout the semiclassical Bloch oscillation regime. Additionally, we also observe the large κ regime discussed in the previous section. The latter has a smaller anomalous drift compared to the semiclassical regime. There is no transverse drift when we choose our band projection such that the electron and hole bands have opposite Berry curvature.

The bottom panel of Fig. 6.6 demonstrates that trivial electronic bands can still support an anomalous exciton drift, albeit of reduced magnitude. We see the effect only exists for the semiclassical Bloch oscillation regime corresponding to small κ and large E. This can be understood as a consequence of large κ binding the ground state wavefunction more tightly in relative real space: as a result, the wavefunction spreads in relative momentum space, and thus experiences an averaged Berry curvature. The averaged Berry curvature approaches the Chern number C over the area of the Brillouin zone, and thus becomes vanishingly small when $C = 0$.

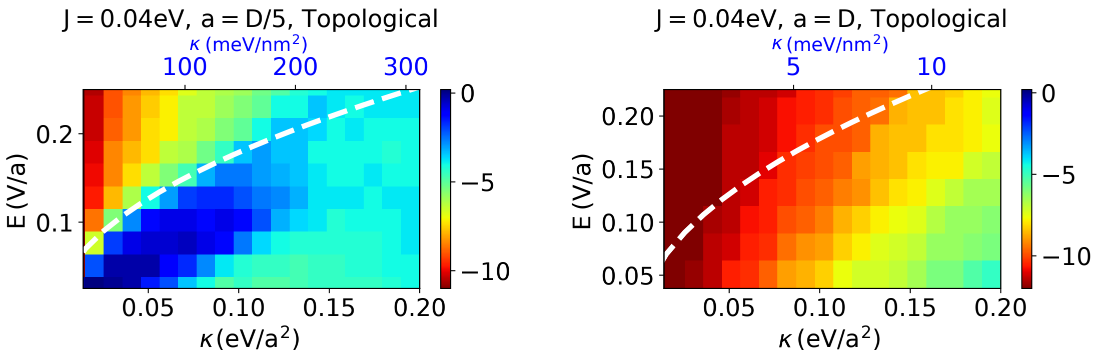

Figure 6.7: Exact dynamics for Coulombic potential: topological bands. Same phase diagram as in Fig. 6.2 simulated for exact dynamics with $J = 0.04\,\mathrm{eV}$ and Coulombic potential for $a = D/5$ (top) and $a = D$ (bottom). The exciton ground state corresponds to both electron and hole occupying the upper band of Eq. (6.17) with the same parameters as in Fig. 6.2.

Correspondingly, trivial bands do not support a large κ regime of anomalous exciton transport.

Figures 6.7 and 6.8 plot the anomalous exciton drift for the case of Coulomb interaction with topological and trivial bands, respectively. We take the same parameters as for Fig. 6.6. As expected, when $a \ll D$ (top panels), we see good agreement with Fig. 6.6, including the 'large κ' Bloch oscillation regime for the case of topological bands. When $a = D$, we again see an increased Bloch oscillation regime. The bottom panel of Fig. 6.7 can be understood analogously to the semiclassical simulation with Coulomb interactions in Fig. 6.4. Note that for fixed D, the bottom panel corresponds to a smaller range of E and κ compared to the top panel (see top axis in blue).

6.4 Candidate physical systems

In the previous sections, we demonstrated regimes of anomalous exciton transport in response to a uniform in-plane electric field. We now discuss additional complications beyond the scope of the models considered. We posit that transition metal dichalcogenide (TMD) heterobilayers are potential platforms for hosting this effect due to their ability to support intervalley, interlayer excitons with large binding energies and long lifetimes. Moiré TMDs are especially intriguing given the presence of flat, topological bands. However, the large moiré lattice period compared to the exciton Bohr radius, as well as the presence of additional bands, add complications beyond the scope of the current analysis. At the end of this section, we describe

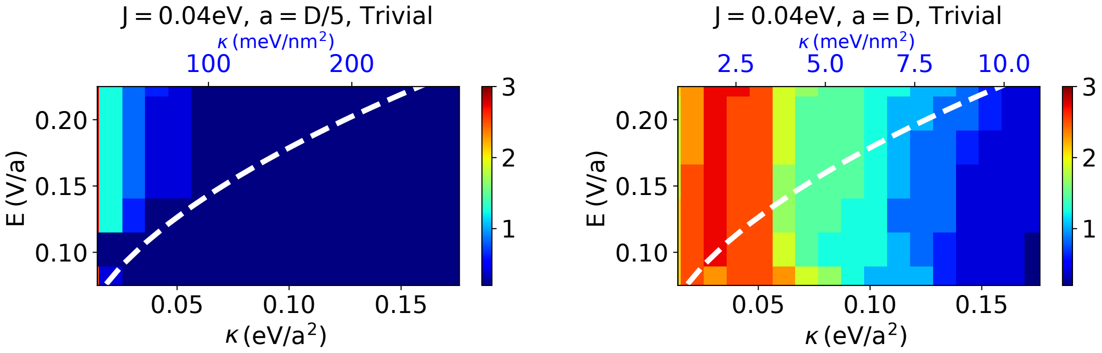

Figure 6.8: Exact dynamics for Coulombic potential: trivial bands. Same phase diagram as in Fig. 6.2 simulated for exact dynamics with $J = 0.04$ eV and Coulombic potential for $a = D/5$ (top) and $a = D$ (bottom). The exciton ground state corresponds to both electron and hole occupying the upper band of Eq. (6.17) with the same parameters as in Fig. 6.2 except for $m_0 = 2.4$ eV, corresponding to the trivial regime.

potential measurement schemes for observing anomalous exciton transport.

Physical constraints

The toy models considered earlier demonstrate that in principle an exciton can move in response to a uniform in-plane electric field when the constituent electron and hole undergo Bloch oscillations. We now discuss additional physical constraints not captured by these models. We reinsert factors of $\hbar$ throughout this section for ease of conversion to physical units.

First, if the electric field is sufficiently large, the gain in potential energy from spatially separating the electron and hole can overcome the binding energy ε_B. When this occurs, the electron and hole dissociate into two freely moving particles and there is no well-defined exciton. For the effect considered here, the electron and hole undergo Bloch oscillations and thus their maximum spatial separation is bounded by the Bloch amplitude x_{Bloch} in Eq. (6.11). Therefore, provided the bandwidth does not exceed the binding energy, the exciton remains well-defined throughout the Bloch oscillation regime, i.e. we require

$$\varepsilon_B > eE\, x_{\text{Bloch}} \sim 2J. \tag{6.24}$$

When a system has multiple electronic bands, we also need to consider the possibility of Landau-Zener transitions. For instance, an electron transitioning to a higher band effectively increases the bandwidth, potentially allowing the electron and hole to reach their equilibrium position, thereby transitioning to the harmonic oscillator regime (no anomalous COM drift). For a Landau-Zener Hamiltonian $H_{\mathrm{LZ}} = ct\sigma_z + \lambda\sigma_x$, the transition probability is given by $p = \exp\left\{-\pi\lambda^2/\hbar c\right\}$. Minimizing these transitions thus amounts to finding a regime where the sweep rate c satisfies $\hbar c \ll \pi\lambda^2$. In the case of an electron transitioning out of the conduction band, λ corresponds to the minigap at the Brillouin zone boundary. We can roughly approximate the sweep rate c as the linearized slope of the band $J/(\pi/a)$ multiplied by $\hbar\dot{k}_e = eE$ (neglecting interactions), so that $\hbar c = (JaeE)/\pi$. Landau-Zener transitions can then be neglected, provided that

$$E \ll E_{\max} = \frac{\pi^2\lambda^2}{Jae}. \tag{6.25}$$

As such, flatter bands and larger minigaps can sustain a larger electric field, and thus a stronger effect. Note that Eq. (6.25) competes with the lower bound of the semiclassical regime given in Eq. (6.20), but not with the large κ regime identified in our simulations.

Additionally, when evaluating the attractiveness of any candidate physical system, we must further consider the time scales of the exciton. Clearly, the exciton lifetime must be sufficiently long that the anomalous drift can be observed. At a minimum, this requires the exciton lifetime exceeding the Bloch oscillation period. Moreover, if the exciton relaxes to its equilibrium position, e.g. through phonon scattering, the anomalous velocity will vanish. Provided the energy separation between the excited exciton (undergoing anomalous drift) and the (stationary) exciton ground state is less than the optical phonon band gap, we only need to consider acoustic phonon scattering. Assuming the bands are flat enough that the electron and hole group velocities are slower than the speed of sound, such scattering only occurs when the exciton hits an impurity and should therefore be negligible for sufficiently clean systems.

Finally, the anomalous velocity grows linearly with $\mathbf{\Omega}_e^c(\mathbf{k}_e) - \mathbf{\Omega}_h^v(\mathbf{k}_h)$, thus a system that hosts intervalley excitons and topological bands will have a stronger response. We emphasize that topological bands are not a prerequisite (see Fig. 6.6 and 6.8), but will make the effect more visible.

TMD heterobilayers

TMDs are an excellent platform to study Berry curvature effects on excitonic properties: excitons in these materials have large binding energies and dominate the optical responses of the system. In particular, we posit that TMD heterobilayers are an attractive platform to observe the anomalous excitonic drift studied in this paper.

One of the key requirements of the anomalous excitonic drift is the formation of intervalley excitons so that the electron and hole bands have opposite Berry curvature. In a TMD monolayer, such an exciton requires a large COM momentum and thus is optically dark. However, a TMD heterobilayer with a type-II band alignment (e.g., $\mathrm{MoX_2/WX_2}$) supports excitons whose electron and hole are localized in different layers. When the two layers are twisted by an angle $\theta \approx 60^\circ$ (Fig. 3(g) in Ref.[394]), the system can support an intervalley exciton with close to zero COM momentum. There are two distinct benefits: (1) such an exciton can be optically bright and as such can be easily excited and detected, and (2) the spatial separation of the electron and hole enhances the exciton lifetime to anywhere from hundreds of nanoseconds to a few microseconds [288, 287].

TMD heterobilayers have a slight lattice mismatch. When the layers are closely aligned, a moiré potential forms with amplitude up to $\sim 150\,\mathrm{meV}$ [287] and lattice period up to $\sim 20\,\mathrm{nm}$ [373]. As a result, the electronic bands flatten to a bandwidth $\sim 10-50\,\mathrm{meV}$ [299], which can be adjusted further by changing the twist angle. The resulting interlayer excitons [66, 197, 185, 371, 109, 357, 75, 107, 161] retain a large binding energy $\sim 100-200\,\mathrm{meV}$ and a Bohr radius $\sim 2\,\mathrm{nm}$ [299]. At first glance, moiré TMDs seem especially promising for observing anomalous excitonic drift due to the flatter bands and similar binding energy making the Bloch oscillation regime more accessible. We might further hope that the possibility of topological moiré bands [315, 372, 373, 195] and the larger moiré lattice period would result in a more pronounced exciton anomalous velocity. We note there are two features that complicate interpretation of our numerics for moiré TMDs. First, the exciton's Bohr radius is significantly smaller than the moiré lattice period; in our simulations this corresponds to the large κ region of phase space only (for which the ground state wavefunction extent is less than a lattice constant). Second, our assumption that electron and hole occupy a single band may not apply given the reduced size of the moiré Brillouin zone. Survival of the anomalous excitonic drift in moiré TMDs remains an interesting open question we plan to investigate in a future work.

A back of the envelope estimate suggests the parameters of TMD heterobilayers are compatible with the bounds identified in the previous section. The binding energy $\sim 100-200\,\mathrm{meV}$ easily exceeds the typical bandwidth $\sim 10-50\,\mathrm{meV}$, satisfying the necessary condition in Eq. (6.24) to avoid exciton ionization. The upper bound on the electric field in Eq. (6.25) from Landau Zener transitions is compatible with the lower bound in Eq. (6.20) from the semiclassical Bloch oscillation regime. For instance, the anti-parallel configuration of $\mathrm{MoSe_2/WS_2}$ has a bandwidth $J \sim 5\,\mathrm{meV}$, energy gap between lowest flat band to next moiré band $\lambda \sim 20\,\mathrm{meV}$, and a lattice constant $a \sim 8\,\mathrm{nm}$ [299, 298], corresponding to $E_{\max} \sim \pi^2\lambda^2/(Jae) \sim 60\,\mathrm{mV/nm}$. Taking interlayer separation $D \approx 3\,\mathrm{nm}$, dielectric constant $\epsilon \approx 4$, and interaction parameter $\kappa \approx 20\,\mathrm{meV/nm^2}$ [30], $E_{\max} > E_{\min} \sim 2\sqrt{2J\kappa} \approx 30\,\mathrm{mV/nm}$. We further note that optical phonons in most TMDs have energies greater than 30 meV [261, 237]; given that the energy gained by the exciton is on the order of the bandwidth J, the exciton cannot relax to its ground state by emitting a phonon. As noted previously, relaxation from acoustic phonon scattering can be neglected for sufficiently clean systems.

Measurement

Lastly, we discuss possible measurements to observe the anomalous exciton drift in TMD heterobilayers. As noted in the previous section, several TMD heterobilayers naturally support optically bright intervalley, interlayer excitons [287]. Thus, we consider a situation where excitons are excited by illuminating one side of the sample, a uniform in-plane electric field $\mathbf{E} = E\hat{\mathbf{x}}$ is turned on, and we look for signatures of the excitons in the transverse direction.

The exciton trajectories can be directly observed using photoluminescence [289, 295, 151]. Polarization-resolved photoluminescence has been proposed [392, 201, 189] and used [258] to observe the excitonic Hall effect on the micron scale. A similar approach could be used here, provided the anomalous drift survives sufficiently many Bloch cycles. A photoluminescence measurement in the transverse direction from where the excitons are initially excited should have a stronger response than the same measurement performed in the direction parallel to the electric field.

An alternative approach is to separately contact and measure the current in the TMD layers. For a TMD heterobilayer with type-II band alignment, all interlayer excitons have electrons localized to one layer, and holes to the other. As such, the anomalous exciton drift should manifest as a current in the transverse direction (positive for one layer, negative for the other. Separately contacting the layers requires an insulating layer inserted between the TMDs so as not to short-circuit the sample. Interlayer excitons have been predicted and observed in TMD monolayers separated by hBN [96, 104, 197, 287, 42, 109, 395]. This approach is analogous to a Coulomb drag measurement, in which a voltage is applied in one layer and the current is measured in the other. Coulomb drag has previously been used to measure spatially indirect exciton transport in bilayer 2DEGs [249].

Other potential measurement schemes could utilize the out-of-plane dipole moment of the interlayer excitons participating in the effect, or the thermal gradient resulting from exciton transport across the system. The former would require measuring the dipole density to detect that excitons excited on one edge of the sample had traveled in the transverse direction. Both such measurements would likely require a high density of excitons to be observable, as could be provided by an exciton condensate.

6.5 Discussion and outlook

In this work, we have studied anomalous exciton drift in response to a uniform in-plane electric field. We have demonstrated this effect semiclassically for intervalley excitons when the electron and hole bands have finite Berry curvature. We have further simulated a toy model exhibiting this effect for a range of electric field and interaction strengths. Our numerics indicate a Bloch oscillation regime not predicted by semiclassics, which we can analytically understand through a simple 1D model. We have postulated that TMD heterobilayers are an attractive candidate system for observing anomalous exciton transport.

Previous works have also considered anomalous exciton transport resulting from finite Berry curvature when the exciton center of mass experiences a net force [392, 184, 195, 44]. As we were completing this manuscript, Ref. [44] by Cao, Fertig, and Brey was posted. Cao et al. propose that a similar anomalous effect can arise from a COM momentum-dependent dipole curvature of the exciton ground state, originating from the geometry of the exciton ground state. They primarily consider excitons in a magnetic field, with the exception of excitons in bilayer graphene (Sec. IV ibid.), where an asymmetry of the two layers is required for a non-vanishing effect. In contrast, the anomalous exciton transport established here is a dynamical effect at zero magnetic field, that cannot be accounted for without considering the internal exciton dynamics and binding interaction. Nonetheless, the underlying origin of both proposals is related, particularly in the small field limit. We leave a detailed comparison of our results with Ref. [44] to future work.

Lastly, we note that moiré TMDs remain an interesting potential platform for the anomalous exciton drift due to the flat bands, enhanced Berry curvature, and large lattice spacing. We emphasize that additional care is needed to apply our results to these systems given our assumption that electron and hole each occupy a single band. Potentially, more complicated TMD heterostructures might also provide a platform for observing the effect, for instance a pair of moiré TMD bilayers separated by insulating hBN layers.

APPENDIX

C.1 Relation between Berry curvature of electron and hole in a given band

The Berry curvature $\mathbf{\Omega}_\alpha$ and Berry connection $\mathbf{A}_\alpha$ for a band α can be defined as

$$\Omega_\alpha(\mathbf{k}) = \nabla_\mathbf{k} \times \mathbf{A}_\alpha(\mathbf{k}) \tag{C.1}$$

$$\mathbf{A}_\alpha(\mathbf{k}) = \langle u_\alpha | \, i\nabla_\mathbf{k} \, | u_\alpha \rangle , \tag{C.2}$$

where $|u_\alpha\rangle$ is the Bloch state for band α. We can write the Berry connection in terms of the Bloch wavefunctions using

$$\begin{aligned} \mathbf{A}_\alpha(\mathbf{k}) &= \int d\mathbf{r} \, \langle u_\alpha | \, \mathbf{r}\rangle i\nabla_\mathbf{k} \, \langle \mathbf{r} | \, u_\alpha \rangle \\ &= i \int d\mathbf{r} \, (u_{\alpha,\mathbf{k}}(\mathbf{r}))^* \, \nabla_\mathbf{k} u_{\alpha,\mathbf{k}}(\mathbf{r}). \end{aligned} \tag{C.3}$$

In order to understand the connection between the Berry curvature for a hole in band α compared to the Berry curvature for an electron in the same band, we can assume that the creation operator for a hole in band α at momentum $\mathbf{k}$ is equal to the annihilation operator for an electron in band α at momentum $-\mathbf{k}$:

$$d^\dagger_{\mathbf{k},\alpha} = c_{-\mathbf{k},\alpha}, \tag{C.4}$$

where d is for the hole and c is for the electron. In real space, we have

$$c^\dagger_\alpha(\mathbf{r}) = d_\alpha(\mathbf{r}). \tag{C.5}$$

Therefore, we see

$$c^\dagger_{\mathbf{k},\alpha} = \int d\mathbf{r} e^{i\mathbf{k}\cdot\mathbf{r}} u^e_{\alpha,\mathbf{k}}(\mathbf{r}) c^\dagger_\alpha(\mathbf{r}) \tag{C.6}$$

$$d_{-\mathbf{k},\alpha} = \int d\mathbf{r} e^{i\mathbf{k}\cdot\mathbf{r}} \left(u^h_{\alpha,-\mathbf{k}}(\mathbf{r}) \right)^* d_\alpha(\mathbf{r}) \tag{C.7}$$

$$\Rightarrow u^e_{\alpha,\mathbf{k}}(\mathbf{r}) = \left(u^h_{\alpha,\mathbf{k}}(\mathbf{r}) \right)^* . \tag{C.8}$$

Using the above equations, the Berry connection for the hole can be related to the Berry connection of the electron by

$$\begin{aligned}
\mathbf{A}_\alpha^h(\mathbf{k}) &= i\int d\mathbf{r}\left(u_{\alpha,\mathbf{k}}^h(\mathbf{r})\right)^*\nabla_\mathbf{k}u_{\alpha,\mathbf{k}}^h(\mathbf{r}) && \text{(C.9)}\\
&= i\int d\mathbf{r}u_{\alpha,-\mathbf{k}}^e(\mathbf{r})\nabla_\mathbf{k}\left(u_{\alpha,-\mathbf{k}}^e(\mathbf{r})\right)^* && \text{(C.10)}\\
&= -i\int d\mathbf{r}\left(u_{\alpha,-\mathbf{k}}^e(\mathbf{r})\right)^*\nabla_\mathbf{k}u_{\alpha,-\mathbf{k}}^e(\mathbf{r}) && \text{(C.11)}\\
&= i\int d\mathbf{r}\left(u_{\alpha,-\mathbf{k}}^e(\mathbf{r})\right)^*\nabla_{-\mathbf{k}}u_{\alpha,-\mathbf{k}}^e(\mathbf{r}) && \text{(C.12)}\\
&= \mathbf{A}_\alpha^e(-\mathbf{k}). && \text{(C.13)}
\end{aligned}$$

It follows that the Berry curvatures are related by

$$\begin{aligned}
\mathbf{\Omega}_\alpha^h(\mathbf{k}) &= \nabla_\mathbf{k}\times\mathbf{A}_\alpha^h(\mathbf{k}) = \nabla_\mathbf{k}\times\mathbf{A}_\alpha^e(-\mathbf{k})\\
&= -\nabla_{-\mathbf{k}}\times\mathbf{A}_\alpha^e(-\mathbf{k}) = -\mathbf{\Omega}_\alpha^e(-\mathbf{k}).
\end{aligned} \tag{C.14}$$

Now, if the momentum of the created hole is $\mathbf{k}_h$, then the momentum of the electron that was removed is $\mathbf{k}_e = -\mathbf{k}_h$ and

$$\mathbf{\Omega}_\alpha^h(\mathbf{k}_h) = -\mathbf{\Omega}_\alpha^e(\mathbf{k}_e). \tag{C.15}$$

C.2 Intermediate semiclassical case

In the main text, we considered the fine-tuned limit of equal Berry curvature for electron and hole, $\mathbf{\Omega}_e^c(\mathbf{k}) = \mathbf{\Omega}_e^v(\mathbf{k})$, equivalently $\mathbf{\Omega}_e^c(\mathbf{k}) = -\mathbf{\Omega}_h^v(-\mathbf{k})$ from Eq. (C.15). In this particular case, Berry curvature effects appear only in COM motion. Similarly, for $\mathbf{\Omega}_e^c(\mathbf{k}) = \mathbf{\Omega}_e^v(-\mathbf{k})$, Berry curvature only affects the relative motion. However, in type-II heterobilayers none of these conditions are satisfied exactly, and Berry curvature effects couple the COM and relative space equations of motion. For a direct momentum exciton, the relative and COM position evolve according to

$$\begin{aligned}
\dot{\mathbf{r}} &= \left(2Ja\sin(k_xa) - \dot{k}_y\Delta\Omega_e^{vc}(\mathbf{k})\right)\hat{\mathbf{x}}\\
&\quad + \left(2Ja\sin\left(k_ya\right) + \dot{k}_x\Delta\Omega_e^{vc}(\mathbf{k})\right) && \text{(C.16)}\\
\dot{\mathbf{R}} &= 2\dot{k}_x\Omega_e^{\text{avg}}(\mathbf{k})\,\hat{\mathbf{y}} - 2\dot{k}_y\Omega_e^{\text{avg}}(\mathbf{k})\,\hat{\mathbf{x}} && \text{(C.17)}
\end{aligned}$$

where the difference and average Berry curvatures are defined by

$$\begin{aligned}
\Delta\Omega_e^{vc}(\mathbf{k}) &= \Omega_e^c(\mathbf{k}) - \Omega_e^v(\mathbf{k}) && \text{(C.18)}\\
\Omega_e^{\text{Avg}}(\mathbf{k}) &= \frac{1}{2}\left(\Omega_e^c(\mathbf{k}) + \Omega_e^v(\mathbf{k})\right). && \text{(C.19)}
\end{aligned}$$

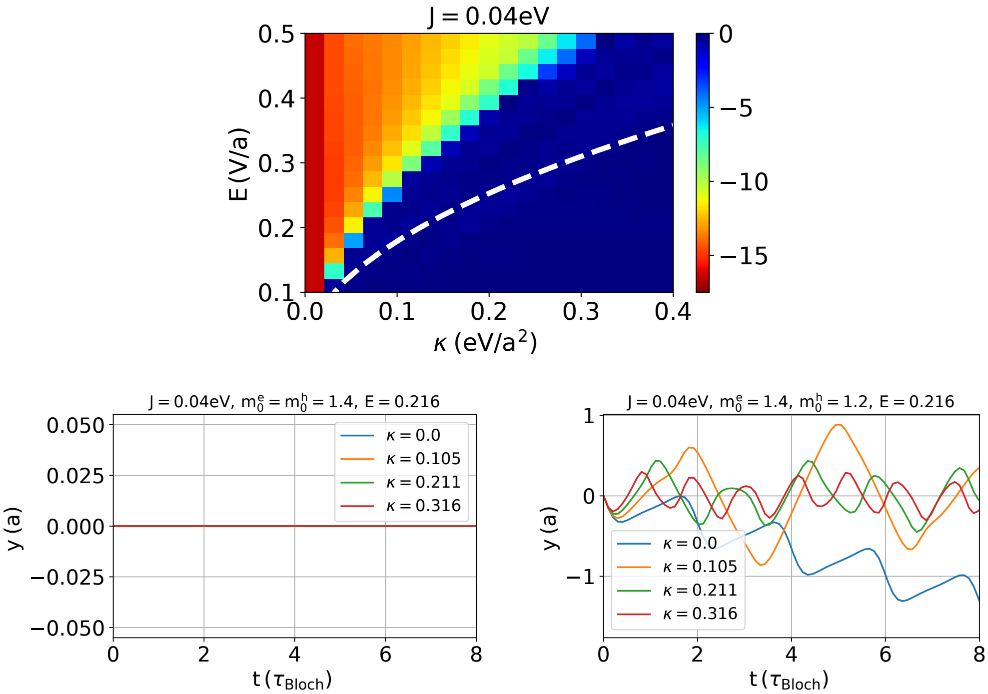

Figure C.1: Intermediate semiclassical dynamics. The top panel plots average Y per Bloch cycle when $\Delta\Omega_e^{vc}(\mathbf{k}) \neq 0$. To give the electron and hole bands slightly different Berry curvature we use $m_0^e = 1.4\,\text{eV}$ and $m_0^h = 1.2\,\text{eV}$. The other parameters are the same as in Fig. 6.2. The dashed white curve is again the semiclassical boundary $E = 2\sqrt{2J\kappa}$ shown in Figs. 6.2-6.7; Berry curvature couples Y and y, thereby reducing the Bloch oscillation regime compared to the symmetric case considered in Fig. 6.2. In the bottom panel, we compare transverse drift in y as a function of time for equal (middle) and different (bottom) electron and hole Berry curvatures.

Bloch oscillations are obfuscated in the relative motion when $\mathbf{R}$ and $\mathbf{r}$ are coupled. We continue to define the Bloch period as $\tau_{\text{Bloch}} = 2\pi/(aeE)$.

We plot the effect of $\Delta\Omega_e^{vc}(\mathbf{k}) \neq 0$ in Fig. C.1. The top panel shows the average transverse COM drift per Bloch cycle in E versus κ space. The magnitude of the transverse drift is less than when the Berry curvatures of the electron and hole bands are equal (Fig. 6.2), thus a system that approaches particle-hole symmetry should have a stronger anomalous exciton response. We note the transition between harmonic and Bloch oscillation regimes is affected by the fact that relative and COM motion are now coupled. The bottom panel plots the relative transverse motion when $\Delta\Omega_e^{vc}(\mathbf{k}) = 0$ (right) and $\Delta\Omega_e^{vc}(\mathbf{k}) \neq 0$ (left). As predicted by Eqs. (C.16) and (C.17), the former corresponds to no Berry curvature effects on y, while the latter corresponds to y and Y being coupled.

C.3 Comparison of semiclassical approaches

We review different semiclassical approaches used to study the dynamics of electrons and excitons in Bloch bands. We contrast them with the semiclassical and exact dynamics approach used in the main text.

Semiclassical description for non-interacting electron wavepacket in a Bloch band

In this subsection, we review the semiclassical dynamics of a non-interacting electron wavepacket in a Bloch band. We closely follow the approach presented in Ref. [338]. Consider a wavepacket in k-space described by the wavefunction

$$|\Psi(t)\rangle = \int d\mathbf{k}\, a(\mathbf{k}, t)\, |\psi_n(\mathbf{k})\rangle\,, \tag{C.20}$$

where $|\psi_n(\mathbf{k})\rangle = \sum_{\mathbf{r}} e^{i\mathbf{k}\cdot\mathbf{r}}\, |u_n(\mathbf{k})\rangle \otimes |\mathbf{r}\rangle$ are Bloch wavefunctions of n^{th} eigenstates and $|a(\mathbf{k}, t)|^2$ is centered around the point

$$\mathbf{k}_c = \int d\mathbf{k}(\mathbf{k}|a(\mathbf{k}, t)|^2). \tag{C.21}$$

We express

$$a(\mathbf{k}, t) = |a(\mathbf{k}, t)|e^{-i\gamma(\mathbf{k},t)}. \tag{C.22}$$

The center of wavepacket in real space is

$$\begin{aligned}
\mathbf{r}_c &= \langle\Psi|\, \mathbf{r}\, |\Psi\rangle && \text{(C.23)}\\
&= \nabla_{\mathbf{k}}\gamma(\mathbf{k}, t)|_{\mathbf{k}=\mathbf{k}_c} + \langle u(\mathbf{k})|i\nabla_{\mathbf{k}}|u(\mathbf{k})\rangle\, |_{\mathbf{k}=\mathbf{k}_c} && \text{(C.24)}\\
&= \nabla_{\mathbf{k}_c}\gamma(\mathbf{k}_c, t) + \left\langle u(\mathbf{k}_c)|i\nabla_{\mathbf{k}_c}|u(\mathbf{k}_c)\right\rangle . && \text{(C.25)}
\end{aligned}$$

The dynamics of the mean position $\mathbf{r}_c$ and momentum $\mathbf{k}_c$ can be obtained using a time-dependent variational principle with the Lagrangian

$$L = \langle\Psi|\, i\frac{d}{dt} - H\, |\Psi\rangle\,, \tag{C.26}$$

where $H = H_{\text{Bloch}} - e\mathbf{E}\cdot\mathbf{r}$. We have

$$\begin{aligned}
\left\langle\Psi|i\frac{d\Psi}{dt}\right\rangle &= \int d\mathbf{k}|a(\mathbf{k}, t)|^2 \\
&\quad\times \langle u(\mathbf{k}, t)|\, e^{i\gamma(\mathbf{k},t)}\frac{d}{dt}(e^{-i\gamma(\mathbf{k},t)}\, |u(\mathbf{k}, t)\rangle) && \text{(C.27)}\\
&= \frac{\partial\gamma(\mathbf{k}_c, t)}{\partial t} + \left\langle u(\mathbf{k}_c, t)|i\frac{\partial}{\partial t}u(\mathbf{k}_c, t)\right\rangle . && \text{(C.28)}
\end{aligned}$$

We can write

$$\frac{\partial \gamma(\mathbf{k}_c, t)}{\partial t} = \frac{d\gamma(\mathbf{k}_c)}{dt} - \dot{\mathbf{k}}_c \cdot \frac{\partial \gamma(\mathbf{k}_c)}{\partial \mathbf{k}_c} \tag{C.29}$$

and

$$\langle \Psi | H | \Psi \rangle = \langle \Psi | H_{\text{Bloch}} | \Psi \rangle - e\mathbf{E} \cdot \mathbf{r}_c = \mathcal{E}_{\text{Bloch}} - e\mathbf{E} \cdot \mathbf{r}_c. \tag{C.30}$$

Now, the Lagrangian is

$$L = -\mathcal{E}(\mathbf{r}_c, \mathbf{k}_c) + \mathbf{k}_c \cdot \dot{\mathbf{r}}_c + \dot{\mathbf{k}}_c \cdot \left\langle u | i \frac{\partial u}{\partial \mathbf{k}_c} \right\rangle + \left\langle u | i \frac{\partial u}{\partial t} \right\rangle + \frac{d\gamma(\mathbf{k}_c, t)}{dt}. \tag{C.31}$$

In the above, $\mathcal{E}(\mathbf{r}_c, \mathbf{k}_c) = \langle \Psi | H_{\text{Bloch}} | \Psi \rangle - \mathbf{E} \cdot \mathbf{r}_c$, and we used $\nabla_{\mathbf{k}_c} \gamma(\mathbf{k}_c, t) = \mathbf{r}_c - \langle u(\mathbf{k}_c) | \, i\nabla_{\mathbf{k}_c} \, | u(\mathbf{k}_c) \rangle$.

This Lagrangian is a function of $\mathbf{r}_c$, $\dot{\mathbf{r}}_c$, $\mathbf{k}_c$, $\dot{\mathbf{k}}_c$, and t. If we assume $\left\langle u | i \frac{\partial u}{\partial t} \right\rangle = 0$ (as is usually the case for adiabatic evolution and a translationally invariant system), the equations of motion for the wavepacket center are

$$\frac{d}{dt}\left(\frac{\partial L}{\partial \dot{\mathbf{r}}_c}\right) - \frac{\partial L}{\partial \mathbf{r}_c} = 0, \quad \frac{d}{dt}\left(\frac{\partial L}{\partial \dot{\mathbf{k}}_c}\right) - \frac{\partial L}{\partial \mathbf{k}_c} = 0 \tag{C.32}$$

which implies

$$\frac{d\mathbf{k}_c}{dt} = -\frac{\partial \mathcal{E}(\mathbf{r}_c, \mathbf{k}_c)}{\partial \mathbf{r}_c}, \tag{C.33}$$

$$\dot{x}_c = \frac{\partial \mathcal{E}}{\partial k_{xc}} + \frac{d}{dt}\left(\left\langle u | i \frac{\partial u}{\partial k_{xc}} \right\rangle\right) - \dot{k}_{xc} \frac{\partial}{\partial k_{xc}} \left\langle u | i \frac{\partial u}{\partial k_{xc}} \right\rangle - \dot{k}_{yc} \frac{\partial}{\partial k_{xc}} \left\langle u | i \frac{\partial u}{\partial k_{yc}} \right\rangle \tag{C.34}$$

$$\begin{aligned} \dot{x}_c =& \frac{\partial \mathcal{E}}{\partial k_{xc}} + \dot{k}_{yc} \frac{\partial}{\partial k_{yc}} \left(\left\langle u | i \frac{\partial u}{\partial k_{xc}} \right\rangle\right) - \dot{k}_{yc} \frac{\partial}{\partial k_{xc}} \left(\left\langle u | i \frac{\partial u}{\partial k_{yc}} \right\rangle\right) \\ =& \frac{\partial \mathcal{E}}{\partial k_{xc}} + \dot{k}_{yc} \left(\frac{\partial A_x}{\partial k_{yc}} - \frac{\partial A_y}{\partial k_{xc}}\right). \end{aligned} \tag{C.35}$$

In the above, $\mathbf{A}$ is the Berry-connection, and we use the fact that

$$\frac{d}{dt}\left(\left\langle u | i \frac{\partial u}{\partial k_{xc}} \right\rangle\right) = \dot{k}_{yc} \frac{\partial}{\partial k_{yc}} \left(\left\langle u | i \frac{\partial u}{\partial k_{xc}} \right\rangle\right) + \dot{k}_{xc} \frac{\partial}{\partial k_{xc}} \left(\left\langle u | i \frac{\partial u}{\partial k_{xc}} \right\rangle\right) \tag{C.36}$$

as we already assumed $\langle u | \left| i \frac{\partial u}{\partial t} \right\rangle = 0$. Similarly,

$$\begin{aligned} \dot{y}_c =& \frac{\partial \mathcal{E}}{\partial k_{yc}} + \dot{k}_{xc} \frac{\partial}{\partial k_{xc}} \left(\left\langle u | i \frac{\partial u}{\partial k_{yc}} \right\rangle\right) - \dot{k}_{xc} \frac{\partial}{\partial k_{yc}} \left(\left\langle u | i \frac{\partial u}{\partial k_{xc}} \right\rangle\right) \\ =& \frac{\partial \mathcal{E}}{\partial k_{xc}} + \dot{k}_{xc} \left(\frac{\partial A_y}{\partial k_{xc}} - \frac{\partial A_x}{\partial k_{yc}}\right). \end{aligned} \tag{C.37}$$

Combining Eqs. (C.33), (C.35), and (C.37), we get the more familiar expressions

$$\dot{\mathbf{k}}_c = eE \tag{C.38}$$

$$\dot{\mathbf{r}} = \frac{\partial \mathcal{E}}{\partial \mathbf{k}_c} + \dot{\mathbf{k}}_c \times (\nabla \times \mathbf{A})\,. \tag{C.39}$$

Comparison to Ref. [44]

We have employed a simple semiclassical description of the exciton that considers separate wavepackets for the electron and hole. Reference [44] instead extended the single particle formalism for semiclassical dynamics to an exciton. In this case, the initial state is given by

$$|\Psi(t=0)\rangle = \int d\mathbf{K}\, a(\mathbf{K})\, |\Phi_0(\mathbf{K})\rangle \tag{C.40}$$

where $\mathbf{K}$ is the COM momentum, $a(\mathbf{K}) = |a(\mathbf{K})|e^{-i\gamma(\mathbf{K},t)}$ and $|a(\mathbf{K})|$ centered at $\mathbf{K} = \mathbf{K}_c$. The exciton ground state $|\Phi_0(\mathbf{K})\rangle$ for a given COM momentum is

$$|\Phi_0(\mathbf{K})\rangle = \sum_{\mathbf{k}} C_{\mathbf{k}}(\mathbf{K}) \left|\phi^{e,\uparrow}_{\mathbf{K},\mathbf{k}}\right\rangle \otimes \left|\phi^{h,\uparrow}_{\mathbf{K},-\mathbf{k}}\right\rangle . \tag{C.41}$$

At a later time t, this system is described by

$$|\Psi(t)\rangle = \int d\mathbf{K} a(\mathbf{K},t)\, |\Phi(\mathbf{K},t)\rangle \tag{C.42}$$

where $|\Phi(\mathbf{K},t)\rangle = \sum_{\mathbf{k}} C_{\mathbf{k}}(\mathbf{K},t) \left|\phi^{e,\uparrow}_{\mathbf{K},\mathbf{k}}\right\rangle \otimes \left|\phi^{h,\uparrow}_{\mathbf{K},-\mathbf{k}}\right\rangle$. In order to study the dynamics of this system, we can again employ time-dependent variational principle with the Lagrangian of Eq. (C.26) for $H = H_0 + \mathbf{E}\cdot(\mathbf{r}_e - \mathbf{r}_h)$ and $H_0 = H^e \otimes 1^h + 1^e \otimes H^h + V(\mathbf{r}_e - \mathbf{r}_h)$. Here, we can calculate the expectation value $\langle\Psi|\mathbf{r}_e - \mathbf{r}_h|\Psi\rangle$ using

$$\begin{aligned}\langle \mathbf{r}_e, \mathbf{r}_h|\Phi(\mathbf{K},t)\rangle = e^{-i\frac{\mathbf{K}}{2}\cdot(\mathbf{r}_e+\mathbf{r}_h)} &\sum_{\mathbf{k}} C_{\mathbf{k}}(\mathbf{K},t) e^{-i\mathbf{k}\cdot(\mathbf{r}_e-\mathbf{r}_h)} \\ &\times \left|u^{e,\uparrow}_{\mathbf{K},\mathbf{k}}\right\rangle \otimes \left|u^{h,\uparrow}_{\mathbf{K},-\mathbf{k}}\right\rangle\end{aligned} \tag{C.43}$$

where $\left|u^{e/h,\uparrow}_{\mathbf{K},\mathbf{k}}\right\rangle$ is cell-periodic part of Bloch wavefunctions of $H^{e/h}$ with momentum $\mathbf{k}_{e/h} = \frac{\mathbf{K}}{2} + \mathbf{k}$. Similar to the technique employed in Ref. [44], we can express

$$\langle\Phi(\mathbf{K},t)|\mathbf{r}_e - \mathbf{r}_h|\Phi(\mathbf{K},t)\rangle = \mathbf{A}^1(\mathbf{K},t) - \mathbf{A}^0(\mathbf{K},t) \tag{C.44}$$

where $\mathbf{A}^\alpha(\mathbf{K},t) = i\,\langle\Phi(\mathbf{K},t,\alpha)|\nabla_{\mathbf{K}}|\Phi(\mathbf{K},t,\alpha)\rangle$ and $|\Phi(\mathbf{K},t,\alpha)\rangle = e^{-i(\alpha-\frac{1}{2})\mathbf{K}\cdot(\mathbf{r}_e-\mathbf{r}_h)}\,|\Phi(\mathbf{K},t)\rangle$.

If we assume the adiabaticity condition, E does not change the exciton eigenstate for a given $\mathbf{K}$. As a result $|\Phi(\mathbf{K},t)\rangle = |\Phi_0(\mathbf{K})\rangle$ and thus

$$\langle\Psi(t)|H_0 + \mathbf{E}\cdot(\mathbf{r}_e - \mathbf{r}_h)\,|\Psi(t)\rangle = E_0(\mathbf{K}_c) + \mathbf{E}\cdot\mathbf{D}(\mathbf{K}_c) \tag{C.45}$$

where $\mathbf{D}((\mathbf{K}_c) = \mathbf{A}^1(\mathbf{K}_c) - \mathbf{A}^0(\mathbf{K}_c)$ is referred to as dipole curvature and $\mathbf{K}_c = \mathbf{K}_c(t) = \int d\mathbf{K}|a(\mathbf{K},t)|^2\mathbf{K}$ is the mean of distribution at time t and $E_0(\mathbf{K}_c)$ is the ground state energy of the exciton with COM momentum $\mathbf{K}_c$. Following the same steps as the single-particle case, it can be shown

$$\begin{aligned}\dot{\mathbf{R}}_c &= -\nabla_{\mathbf{K}_c}E_0(\mathbf{K}_c) - \nabla_{\mathbf{K}_c}\left(\mathbf{E}\cdot\mathbf{D}(\mathbf{K}_c)\right)\\ &\quad + \dot{\mathbf{K}}_c \times \left(\nabla_{\mathbf{K}_c} \times \mathbf{A}(\mathbf{K}_c)\right)\\ \dot{\mathbf{K}}_c &= 0\end{aligned} \tag{C.46}$$

where $\mathbf{A}(\mathbf{K}_c) = i\langle\Phi_0(\mathbf{K}_c)|\nabla_{\mathbf{K}}|\Phi_0(\mathbf{K}_c)\rangle$ is the Berry connection of exciton. Reference [44] found that the dipole curvature $\nabla_{\mathbf{K}_c}\left(\mathbf{E}\cdot\mathbf{D}(\mathbf{K}_c)\right)$ usually points in the direction $\hat{z} \times \mathbf{K}_c$ for a simple 2D system with finite Berry curvature. Hence, in addition to the exciton Berry curvature, the dipole curvature term $\nabla_{\mathbf{K}_c}\left(\mathbf{E}\cdot\mathbf{D}(\mathbf{K}_c)\right)$ also gives rise to an anomalous transverse drift.

Comparison to exact dynamics simulation

A key assumption of the above derivation is adiabaticity, so that for a given COM momentum $\mathbf{K}$, the exciton always remains in its ground state

$$|\Phi(\mathbf{K},t)\rangle = |\Phi_0(\mathbf{K})\rangle = \sum_{\mathbf{k}} C_{\mathbf{k}}(\mathbf{K})\left|\phi^{e,\uparrow}_{\mathbf{K},\mathbf{k}}\right\rangle \otimes \left|\phi^{h,\uparrow}_{\mathbf{K},-\mathbf{k}}\right\rangle. \tag{C.47}$$

As a result, the expectation values of relative momentum $\mathbf{k}$ and relative position $\mathbf{r}_e - \mathbf{r}_h$ remain fixed during the evolution if $\dot{\mathbf{K}}_c = 0$. This condition does not allow the difference in Berry curvature of electron and hole band to affect the COM motion and corresponds to the deep harmonic regime where the exciton is stuck at its equilibrium position both in k and r space.

In our exact dynamics, we start with a wavepacket in COM space similar to the one described in Eq. (C.40) and then we evolve it numerically. Hence, in our case we are not imposing this adiabaticity condition. Accordingly, the only way k and r can change in the absence of a net COM force is if the applied electric field mixes the ground state with other exciton states or other continuum states. The exciton remains bounded as long as as all states involved in the mixture are bounded. Mixing with continuum states would dissociate the exciton before it can traverse the full Brillouin zone.

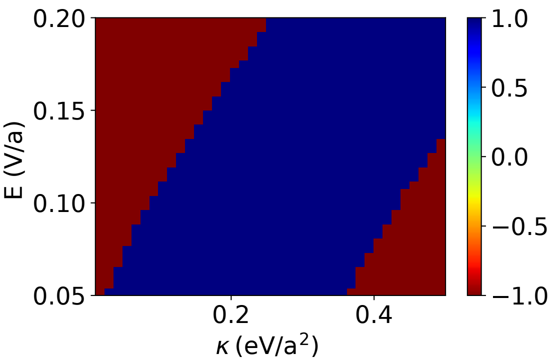

Figure C.2: Phase diagram for 1D model: Sign$(x_{\max} - x_{\text{eq}})$ for different values of E and κ as obtained from Eq. (C.63) for $J_{1D} = 0.08eV$. When $x_{\max} - x_{\text{eq}}$ is negative, the particle cannot reach its equilibrium position. We see that this occurs even at large κ, contrary to semiclassical predictions.

C.4 1D model

Perturbation theory in $J_{\mathbf{1D}}/(\kappa a^2)$

Consider the following one-band tight binding model with nearest neighbor hopping and a harmonic potential trap:

$$H_{\text{1D}} = \sum_n \frac{J_{\text{1D}}}{2} \left(|n\rangle \langle n+1| + |n\rangle \langle n-1| \right) + \sum_n \left(\frac{1}{2}\kappa a^2\, \hat{n}^2 + eEa\, \hat{n} \right) |n\rangle \langle n|$$

$$= \begin{pmatrix} 2\kappa a^2 - 2eEa & \frac{J_{\text{1D}}}{2} & 0 & 0 & 0 \\ \frac{J_{\text{1D}}}{2} & \frac{1}{2}\kappa a^2 - eEa & \frac{J_{\text{1D}}}{2} & 0 & 0 \\ 0 & \frac{J_{\text{1D}}}{2} & 0 & \frac{J_{\text{1D}}}{2} & 0 \\ 0 & 0 & \frac{J_{\text{1D}}}{2} & \frac{1}{2}\kappa a^2 + eEa & \frac{J_{\text{1D}}}{2} \\ 0 & 0 & 0 & \frac{J_{\text{1D}}}{2} & 2\kappa a^2 + 2eEa \end{pmatrix}. \tag{C.48}$$

In the second line, we truncate the Hamiltonian at states $|n = \pm 2\rangle$. To second order in $J_{\text{1D}}/(\kappa a^2)$, the eigenvalues and eigenstates are

$$E_n = \frac{1}{2}\kappa a^2 n^2 + eEan + \left(\frac{J_{\text{1D}}}{2}\right)^2 \left(\frac{1}{\kappa a^2 n + eEa - \frac{1}{2}\kappa a^2} - \frac{1}{\kappa a^2 n + eEa + \frac{1}{2}\kappa a^2} \right) \tag{C.49}$$

$$= \frac{1}{2}\kappa a^2 n^2 + eEan + \left(\frac{J_{\text{1D}}}{2}\right)^2 \frac{4\kappa a^2}{4(\kappa a^2 n + eEa)^2 - \kappa^2 a^4} \tag{C.50}$$

and

$$\begin{aligned}\left|\tilde{n}\right\rangle = \left|n\right\rangle & \left(1 - \frac{1}{2}\left(\frac{J_{1\mathrm{D}}}{2}\right)^2 \sum_{\sigma=\pm1} \frac{1}{\left(\frac{1}{2}\kappa a^2 + \sigma(n\kappa a^2 + eEa)\right)^2}\right) \\ - \quad & \frac{J_{1\mathrm{D}}}{2} \sum_{\sigma=\pm1} \left|n+\sigma\right\rangle \left(\frac{1}{\frac{1}{2}\kappa a^2 + \sigma(n\kappa a^2 + eEa)}\right) \\ + \quad & \frac{1}{2}\left(\frac{J_{1\mathrm{D}}}{2}\right)^2 \sum_{\sigma=\pm1} \left|n+2\sigma\right\rangle \left(\frac{1}{\frac{1}{2}\kappa a^2 + \sigma(n\kappa a^2 + eEa)} \cdot \frac{1}{\kappa a^2 + \sigma(n\kappa a^2 + eEa)}\right).\end{aligned} \tag{C.51}$$

We initialize the system at $t = 0$ in the ground state for $E = 0$,

$$\left|\psi(t=0)\right\rangle = \left(1 - \frac{J_{1\mathrm{D}}^2}{\kappa^2 a^4}\right)\left|0\right\rangle - \frac{J_{1\mathrm{D}}}{\kappa a^2}\left|1\right\rangle - \frac{J_{1\mathrm{D}}}{\kappa a^2}\left|-1\right\rangle + \frac{J_{1\mathrm{D}}^2}{4\kappa^2 a^4}\left|2\right\rangle + \frac{J_{1\mathrm{D}}^2}{4\kappa^2 a^4}\left|-2\right\rangle. \tag{C.52}$$

Rewriting the position eigenstates in terms of energy eigenstates $\left|\tilde{n}\right\rangle$, such that $H\left|\tilde{n}\right\rangle = E_n\left|\tilde{n}\right\rangle$, we have

$$\begin{aligned}\left|0\right\rangle = & \left(1 - \left(\frac{J_{1\mathrm{D}}}{2}\right)^2\left[\frac{2}{(\kappa a^2 + 2eEa)^2} + \frac{2}{(\kappa a^2 - 2eEa)^2}\right]\right)\left|\tilde{0}\right\rangle \\ & + \frac{J_{1\mathrm{D}}}{\kappa a^2 + 2eEa}\left|\tilde{1}\right\rangle + \frac{J_{1\mathrm{D}}}{\kappa a^2 - 2eEa}\left|-\tilde{1}\right\rangle\end{aligned} \tag{C.53}$$

$$\left|+1\right\rangle = \left|\tilde{1}\right\rangle - \frac{J_{1\mathrm{D}}}{\kappa a^2 + 2eEa}\left|\tilde{0}\right\rangle + \frac{J_{1\mathrm{D}}}{3\kappa a^2 + 2eEa}\left|\tilde{2}\right\rangle + O(J_{1\mathrm{D}}^2) \tag{C.54}$$

$$\left|-1\right\rangle = \left|-\tilde{1}\right\rangle - \frac{J_{1\mathrm{D}}}{\kappa a^2 - 2eEa}\left|\tilde{0}\right\rangle + \frac{J_{1\mathrm{D}}}{3\kappa a^2 + 2eEa}\left|-\tilde{2}\right\rangle + O(J_{1\mathrm{D}}^2) \tag{C.55}$$

$$\left|+2\right\rangle = \left|\tilde{2}\right\rangle + O(J_{1\mathrm{D}}) \tag{C.56}$$

$$\left|-2\right\rangle = \left|-\tilde{2}\right\rangle + O(J_{1\mathrm{D}}). \tag{C.57}$$

In addition to $J_{1\mathrm{D}} \ll \kappa$, we have also assumed that $J_{1\mathrm{D}} \ll |n\kappa \pm 2E|$ for all n. Ignoring $O(J_{1\mathrm{D}}^2)$ terms, we find

$$\left|\psi(t=0)\right\rangle \approx \left|\tilde{0}\right\rangle - \frac{2J_{1\mathrm{D}}eEa}{\kappa a^2(\kappa a^2 + 2eEa)}\left|\tilde{1}\right\rangle + \frac{2J_{1\mathrm{D}}eEa}{\kappa a^2(\kappa a^2 - 2eEa)}\left|-\tilde{1}\right\rangle. \tag{C.58}$$

Evolving $\left|\psi\right\rangle$ according to H with $E \neq 0$, we find

$$\left|\psi(t)\right\rangle \approx e^{-iE_0 t}\left(\left|\tilde{0}\right\rangle - e^{-i(E_1 - E_0)t}\frac{2J_{1\mathrm{D}}eEa}{\kappa a^2(\kappa a^2 + 2eEa)}\left|\tilde{1}\right\rangle + e^{-i(E_{-1} - E_0)t}\frac{2J_{1\mathrm{D}}eEa}{\kappa a^2(\kappa a^2 - 2eEa)}\left|-\tilde{1}\right\rangle\right) \tag{C.59}$$

with position expectation value

$$\begin{aligned}\langle\psi(t)|\,a\hat{n}\,|\psi(t)\rangle =& a\left\langle\tilde{0}\right|\hat{n}\left|\tilde{0}\right\rangle + a\left(\frac{2J_{1\mathrm{D}}eEa}{\kappa a^2(\kappa a^2+2eEa)}\right)^2\left\langle\tilde{1}\right|\hat{n}\left|\tilde{1}\right\rangle\\ &+ a\left(\frac{2J_{1\mathrm{D}}eEa}{\kappa a^2(\kappa a^2-2eEa)}\right)^2\left\langle-\tilde{1}\right|\hat{n}\left|-\tilde{1}\right\rangle\\ &- 2a\cos\left((E_1-E_0)t\right)\frac{2J_{1\mathrm{D}}eEa}{\kappa a^2(\kappa a^2+2eEa)}\left\langle\tilde{0}\right|\hat{n}\left|\tilde{1}\right\rangle\\ &+ 2a\cos\left((E_{-1}-E_0)t\right)\frac{2J_{1\mathrm{D}}eEa}{\kappa a^2(\kappa a^2-2eEa)}\left\langle\tilde{0}\right|\hat{n}\left|-\tilde{1}\right\rangle .\end{aligned} \tag{C.60}$$

Plugging in the position expectation values of the energy eigenstates

$$\begin{aligned}\langle\psi(t)|\,a\hat{n}\,|\psi(t)\rangle =& \frac{J_{1\mathrm{D}}^2}{\kappa^2a^4}a\left(\frac{1+4n_{\mathrm{eq}}^2+4n_{\mathrm{eq}}\cos\left(\left[n_{\mathrm{eq}}+\frac{1}{2}\right]\kappa a^2t\right)}{\left(1+2n_{\mathrm{eq}}\right)^2}\right)\\ &- \frac{J_{1\mathrm{D}}^2}{\kappa^2a^4}a\left(\frac{1+4n_{\mathrm{eq}}^2-4n_{\mathrm{eq}}\cos\left(\left[n_{\mathrm{eq}}-\frac{1}{2}\right]\kappa a^2t\right)}{\left(1-2n_{\mathrm{eq}}\right)^2}\right)\end{aligned} \tag{C.61}$$

where we have defined $n_{\mathrm{eq}} = x_{\mathrm{eq}}/a = eE/\kappa a$. The above can be rewritten as

$$\langle\psi(t)|\,a\hat{n}\,|\psi(t)\rangle = 4\frac{J_{1\mathrm{D}}^2}{\kappa^2a^4}x_{\mathrm{eq}}\left(\frac{\cos\left(\left[n_{\mathrm{eq}}+\frac{1}{2}\right]\kappa a^2t\right)-1}{(1+2n_{\mathrm{eq}})^2}+\frac{\cos\left(\left[n_{\mathrm{eq}}-\frac{1}{2}\right]\kappa a^2t\right)-1}{(1-2n_{\mathrm{eq}})^2}\right). \tag{C.62}$$

The maximum amplitude $|\langle a\hat{n}\rangle| = x_{\mathrm{max}}$ corresponds to both cosines taking value -1 (note that it is not always possible to simultaneously maximize both cosines):

$$x_{\mathrm{max}} = \frac{J_{1\mathrm{D}}^2}{\kappa^2a^4}a\frac{16n_{\mathrm{eq}}}{(1+2n_{\mathrm{eq}})^2(1-2n_{\mathrm{eq}})^2}. \tag{C.63}$$

When $x_{\mathrm{max}} < x_{\mathrm{eq}}$, the system never reaches its equilibrium value and always experiences a net force. In the context of excitons, this implies that there is a regime of large κ for which the electron and hole never reach their equilibrium separation and therefore undergo Bloch oscillations. Fig. C.2 plots $\mathrm{Sign}(x_{\mathrm{max}} - x_{\mathrm{eq}})$ for $J_{1D} = 0.08eV$. The analysis in this appendix relies on perturbation theory; it does not apply to regions of the phase diagram for which $J_{1\mathrm{D}}/\kappa a^2$ and $J_{1\mathrm{D}}/|n\kappa a^2 \pm 2Ea|$ are not small.

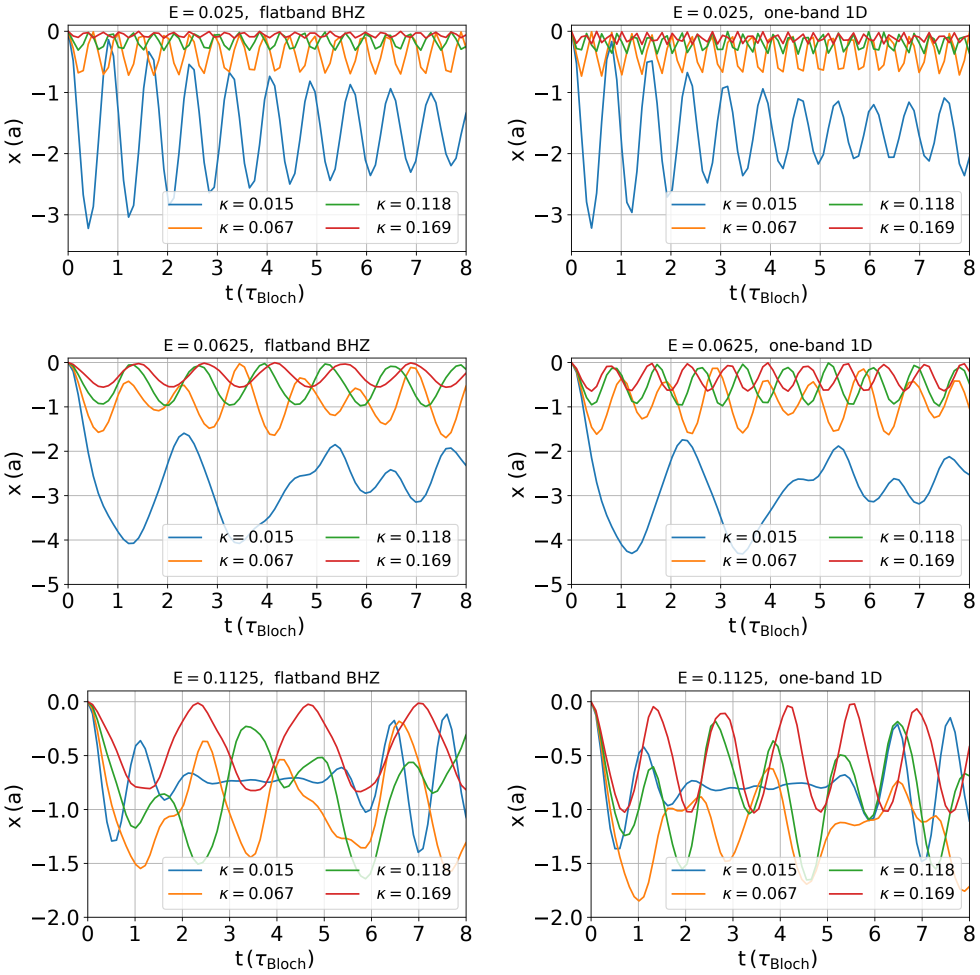

Figure C.3: Relative position x as a function of t obtained from exact dynamics for the 1D version of Eq. (6.21) with COM momentum $K = 0$ (left) and for H_{1D} (right).

Comparison between one-band model and $H^{\mathbf{FB}}_{\mathbf{BHZ}}(k_y = 0)$

In order to verify that the above 1D model can capture the dynamics of the exciton Hamiltonian used in our numerical simulations, we compare the evolution of relative coordinate x for the two cases. We compare dynamics according to H_{1D} presented above and the 1D form of Eq. (6.21) with a harmonic potential and $\mathbf{K} = 0$. More specifically, the latter replaces each copy of $H^{\text{FB}}_{\text{BHZ}}(\mathbf{K}, \mathbf{r})$ with the real-space version of $H^{\text{FB}}_{\text{BHZ}}(\mathbf{K} = 0, k_y = 0)$.

Figure C.3 shows qualitative agreement between the two cases. We note that large κ suppresses the Bloch oscillations in both cases.

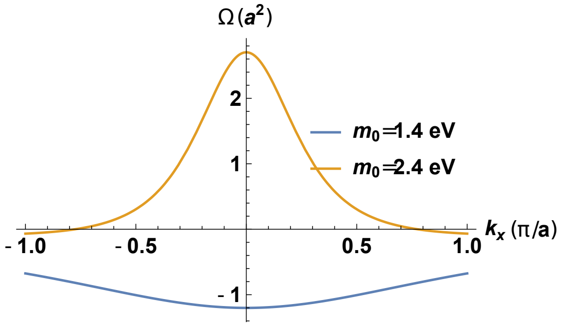

Figure C.4: Berry curvature profile of $H_{\text{BHZ}}(k_y = 0)$. The Berry curvature profile of the upper band is plotted for the topological and trivial cases discussed in the main text, with $v_x = v_y = 0.93\,\text{m/s}$, $b = 1\,\text{eV}$.

C.5 Exact dynamics simulation details

In this appendix, we provide details of our numerical simulations. We first explain our non-interacting Hamiltonian composed of two copies of the BHZ Hamiltonian [32], one for the electron and one for the hole, written in relative real space and COM momentum space. We then explain our band flattening method. Next, we describe our projection into the exciton Hilbert space and incorporating electron-hole interactions. Finally, we describe the ground state preparation and its times evolution.

Non-interacting Hamiltonian

We consider two copies of the BHZ Hamiltonian

$$H^{\alpha}_{\text{BHZ}}(\mathbf{k}_\alpha) = \Big(m_0 - b\cos(k^\alpha_x a) - b\cos(k^\alpha_y a)\Big)\sigma_z + v^\alpha_x \sin(k^\alpha_x a)\sigma_x + v^\alpha_y \sin(k^\alpha_y a)\sigma_y \tag{C.64}$$

for $\alpha = e/h$ for the electron and hole, respectively. In Fig. C.4, we plot the Berry curvature profile for the two values of m_0 used in the figures in the main text; $m_0 = 1.4\,\text{eV}$ (blue curve) corresponds to topological bands with Chern number $C = -1$, while $m_0 = 2.4\,\text{eV}$ (yellow curve) corresponds to trivial bands with Chern number $C = 0$. We introduce COM and relative coordinates:

$$\mathbf{K} = \mathbf{k}_h + \mathbf{k}_e, \qquad \mathbf{k} = (\mathbf{k}_e - \mathbf{k}_h)/2 \tag{C.65}$$

in terms of which the electron and hole momenta can be written

$$\mathbf{k}_{e/h} = \frac{\mathbf{K}}{2} \pm \mathbf{k}. \tag{C.66}$$

In our simulations, $\mathbf{K}$ is conserved and thus different $\mathbf{K}$ sectors are completely decoupled. For a given $\mathbf{K}$,

$$\begin{aligned} H^{\alpha}_{\text{BHZ}}(\mathbf{K},\mathbf{k}) &= \left(m_0 - \sum_i b\cos\left([\frac{K_i}{2}+k_i]a\right)\right)\sigma_z + \sum_i v_i^{\alpha}\sin\left([\frac{K_i}{2}+k_i]a\right)\sigma_i \\ &= \left[m_0 - \sum_i b\cos\left(\frac{K_i a}{2}\right)\cos(k_i a) \mp \sin\left(\frac{K_i a}{2}\right)\sin(k_i a)\right]\sigma_z \\ &\quad + \sum_i v_i^{\alpha}\left[\sin\left(\frac{K_i a}{2}\right)\cos(k_i a) \pm \cos\left(\frac{K_i a}{2}\right)\sin(k_i a)\right]\sigma_i. \end{aligned} \tag{C.67}$$

We do a partial Fourier transform on $\mathbf{k}$ to write $H^{\alpha}_{\text{BHZ},\mathbf{K}}$ which is a tight-binding Hamiltonian in relative position basis with nearest neighbor hopping only. Now, the Hilbert space is $\mathcal{H}_e \otimes \mathcal{H}_h \otimes \mathcal{H}_{\mathbf{r}}$ where $\mathcal{H}_{e/h}$ is the two-dimensional Hilbert space associated with electron/hole degrees of freedom and $\mathcal{H}_{\mathbf{r}}$ is the $N_x \times N_y$-dimensional Hilbert space spanned by the relative position eigenstates $|\mathbf{r}\rangle$. We can express any state in the full Hilbert space as

$$|\psi\rangle = \sum_{i,j=1,2}\sum_{\mathbf{r}} \alpha_{i,j}(\mathbf{r})\left|e^i\right\rangle \otimes \left|h^j\right\rangle \otimes |\mathbf{r}\rangle \tag{C.68}$$

where $\sum_{i,j=1,2}\sum_{\mathbf{r}}|\alpha_{i,j}(\mathbf{r})|^2 = 1$. Here, $\mathbf{r} = m\mathbf{a}_1 + n\mathbf{a}_2$ where $\mathbf{a}_i$ are the lattice vectors of the underlying lattice. The full non-interacting tight-binding Hamiltonian at a fixed $\mathbf{K}$ is given by

$$H^{(0)}_{\mathbf{K}} = H^{e}_{\text{BHZ},\mathbf{K}} \otimes 1_h + 1_e \otimes H^{h}_{\text{BHZ},\mathbf{K}} \tag{C.69}$$

where $H^{\alpha}_{\text{BHZ},\mathbf{K}}$ is a tight-binding model with nearest-neighbor interactions in relative space obtained by performing a partial Fourier transform in k space.

Band flattening method

We now detail our band flattening procedure. We modify each band so that the eigenstates (and Berry curvatures) are unchanged, but the bandwidth is significantly reduced. We then add back in a finite, cosine dispersion. This scheme only applies to a gapped Hamiltonian.

We first flatten each single particle band completely by replacing all positive eigenvalues $\varepsilon_\alpha > 0$ by the same number E_0, and all negative eigenvalues by the opposite constant $-E_0$. In the eigenstate basis, $H_{\text{BHZ}}|\phi_\alpha\rangle = \varepsilon_\alpha|\phi_\alpha\rangle$, the transformation takes

$$H_{\text{BHZ}} = \sum_{\alpha;\,\varepsilon_\alpha>0}\varepsilon_\alpha|\phi_\alpha\rangle\langle\phi_\alpha| - \sum_{\alpha;\,\varepsilon_\alpha<0}\varepsilon_\alpha|\phi_\alpha\rangle\langle\phi_\alpha| \tag{C.70}$$

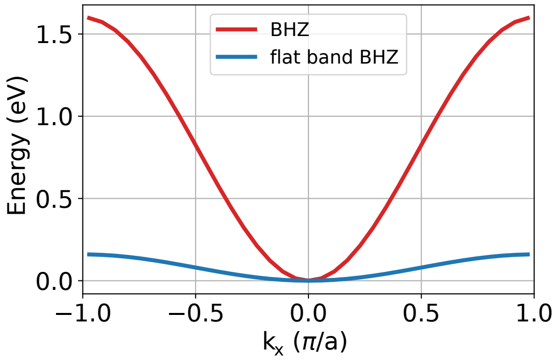

Figure C.5: Band dispersion of the single-particle H_{BHZ} before and after the band flattening process. This flat band BHZ Hamiltonian has a bandwidth determined by the extra nearest-neighbor hopping added to $\tilde{H}_{\text{BHZ}}$.

to the completely flattened

$$\tilde{H}_{\text{BHZ}} = E_0 \sum_{\alpha;\varepsilon_\alpha>0} |\phi_\alpha\rangle\langle\phi_\alpha| - E_0 \sum_{\alpha,\varepsilon_\alpha<0} |\phi_\alpha\rangle\langle\phi_\alpha| . \tag{C.71}$$

We can then perform a basis change to write $\tilde{H}_{\text{BHZ}}$ in relative position space. More explicitly, the algorithm implements the following steps:

1. Express $E_k = a_0 + \sum_{m,n\neq 0} a_{mn} \cos([mk_x + nk_y]a)$.
2. Extract a_{mn} and introduce them as hopping between $\mathbf{r}_{mn}$ neighbors. The resulting Hamiltonian should give completely flat bands but with the same spinor structure at each k point.

This scheme provides completely flat bands at the cost of non-local hopping. In order to get a finite bandwidth, we scale $\tilde{H}_{\mathbf{BHZ}}$ by a matrix containing only nearest-neighbor hopping so that the bandwidth is directly proportional to these nearest neighbor terms, as shown in Fig. C.5.

Projection and interactions

After band flattening, our new Hamiltonian is given by:

$$\tilde{H}^{(0)}_{\mathbf{K}} = \tilde{H}^{e}_{\text{BHZ},\mathbf{K}} \otimes 1_h + 1_e \otimes \tilde{H}^{h}_{\text{BHZ},\mathbf{K}}. \tag{C.72}$$

We want to project to the intervalley exciton Hilbert space, formed by both the electron and hole occupying the upper band of H_{BHZ}. This is accomplished using

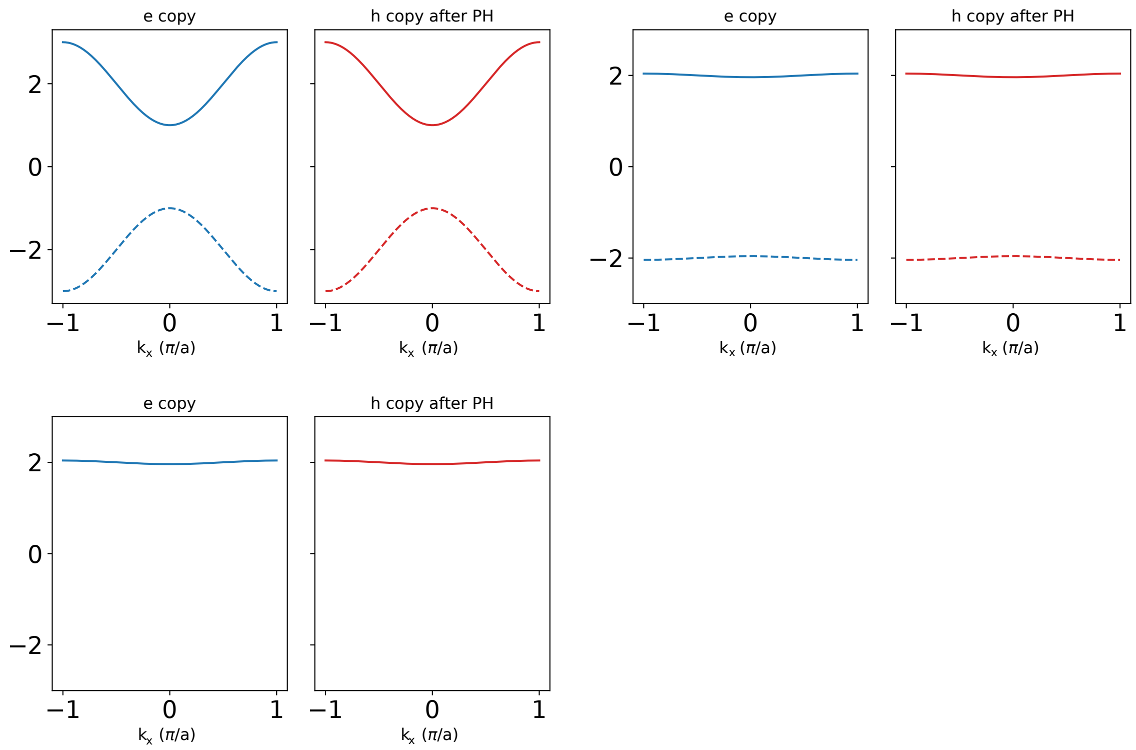

Figure C.6: Schematic of simulation procedure. Top: We start with two copies of a two-band Hamiltonian. Bands shown in dashed line are fully occupied. An exciton is supposed to form between upper bands of electron and hole. Center: Same bands after band flattening procedure. Bottom: We project into the exciton Hilbert space.

the projectors $\hat{P}_{e/h}$

$$\hat{P}_{e/h} = \sum_{\alpha, \mathcal{E}_\alpha > 0} \left|\phi^{\alpha}_{e/h}\right\rangle \left\langle \phi^{\alpha}_{e/h}\right| \tag{C.73}$$

where $\left|\phi^{\alpha}_{e/h}\right\rangle$ are eigenstates of $H^{e/h}_{\text{BHZ}}$. After projection, both valence and conduction bands (equivalently, hole and electron bands in our model) will have the same Berry curvature. Figure C.6 illustrates the projection procedure.

We incorporate interactions using

$$H_{\text{int}} = \hat{P}_e \hat{P}_h \left(\sum_{\mathbf{r}} V(\mathbf{r}) 1_e \otimes 1_h \otimes |\mathbf{r}\rangle \langle \mathbf{r}| \right) \hat{P}_h \hat{P}_e. \tag{C.74}$$

Note that including the projectors ensures that we only consider interactions between electrons and holes within the exciton Hilbert space.

Ground state preparation and time-evolution

For each K, our full Hamiltonian in absence of E is given by:

$$H^{\mathrm{ex}}_{\mathbf{K}} = \hat{P}_e \hat{P}_h \tilde{H}^{(0)}_{\mathbf{K}} \hat{P}_h \hat{P}_e + H_{\mathrm{int}} \tag{C.75}$$

where $\tilde{H}^{(0)}_{\mathbf{K}}(\mathbf{r})$ and $H_{\mathrm{int}}(\mathbf{r})$ are defined in Eqs. (C.72) and (C.74). Denote the ground state of this Hamiltonian by $|\Phi_0(\mathbf{K})\rangle$. Beginning from $|\Phi_0(\mathbf{K})\rangle$, we evolve according to $H_{\mathrm{exciton}} + H_E$ where

$$H_E = \hat{P}_e \hat{P}_h \left(\sum_{\mathbf{r}} (e\mathbf{E} \cdot \mathbf{r}) 1_e \otimes 1_h \otimes |\mathbf{r}\rangle \langle \mathbf{r}| \right) \hat{P}_h \hat{P}_e. \tag{C.76}$$

We repeat the same process for each K on a grid of 27×81 points. At an arbitrary time, the full state of the system is given by:

$$|\psi(t)\rangle = \sum_{\mathbf{K}} w(\mathbf{K}) |\Phi_t(\mathbf{K})\rangle \tag{C.77}$$

where $w(\mathbf{K}) = e^{-K^2\sigma_k^2}$, $|\Phi_t(\mathbf{K})\rangle = e^{-i\left(H^{\mathrm{ex}}_{\mathbf{K}} + H_E\right)t} |\Phi_0(\mathbf{K})\rangle$. We choose a narrow wavepacket with $\sigma_K = \pi/15$ and a numerically smooth gauge such that the initial wavepacket is a coherent wavepacket in both R and K space. We then extract the COM position by performing a Fourier transform in COM space. The observed Y does not change qualitatively as we vary the wavepacket width σ_K from $\pi/10$ to $\pi/20$.

Part III

Ultrafast Control of Quantum Matter

Chapter 7

PHONON-INDUCED FLOQUET TOPOLOGICAL PHASES PROTECTED BY SPACE-TIME SYMMETRIES

In this chapter, we present a toy model for space-time symmetry protected Floquet topological phases induced by symmetry-promotion action of the periodic drive. For systems with spatial and non-spatial symmetries, the topological classification depends not only on these symmetries but also on the commutation/ anti-commutation relations between spatial and non-spatial symmetries. The co-existence of spatial and non-spatial symmetries together with appropriate commutation/ anticommutation relations between them can give rise to crystalline and higher-order topological phases, which host gapless boundary modes. Alternatively, space-time symmetries in a Floquet system can take the role of spatial symmetries in deciding the topological classification. Promoting a spatial symmetry to a space-time symmetry can alter the commutation relations which in turn can modify the topological properties of the system. We show how a coherently excited phonon mode can be used to promote a spatial symmetry with which the static system is always trivial, to a space-time symmetry which supports non-trivial Floquet topological phase. We demonstrate this effect by considering two systems, the first is a second-order topological superconductor and the second is a first-order crystalline topological insulator. In both these cases, a coherently excited phonon mode is responsible for promoting the reflection symmetry to a time-glide symmetry. This newly introduced symmetry allows the previously trivial system to host gapless modes. In first cases, these are protected corner modes while in second case, these are gapless edge modes.

This chapter is based on the following reference:

Swati Chaudhary, Arbel Haim, Yang Peng, and Gil Refael. “Phonon-induced Floquet topological phases protected by space-time symmetries”. Phys. Rev. Research **2**, 043431 (2020)

7.1 Introduction

The topology of electronic band structures of crystals is largely restricted by the existing symmetries [307, 177, 300, 359, 142, 102, 71, 312], and its nontriviality is reflected in the presence of gapless modes located at the crystal boundaries [346, 72, 168, 169, 358]. For example, in topological insulators [132, 279, 31], where the band topology respects only nonspatial symmetries, such as the time-reversal, particle-hole, and chiral symmetries, the boundary modes are of codimension one (the codimension is the difference between the bulk dimension and the dimension along which the gapless modes propagate).

The presence of spatial symmetries can enrich the existing topological classification further and can also modify the conventional bulk-boundary correspondence. For example, recently, systems [28, 270, 196, 27, 328, 304, 105, 386, 36] were theoretically proposed to support gapless modes of higher codimensions, because of the additional spatial symmetries coexisting with the nonspatial ones. The order of such higher-order topological insulators is given by the codimension of the boundary modes. On the experimental side, codimension-two boundary modes are observed mostly in metamaterials, such as electric circuits [145], photonic [273] and phononic [309, 384, 251] systems. The electronic second-order topological insulator is only realized in Bismuth [305].

If a spatial symmetry coexists with nonspatial symmetries, the symmetry operator of the former can either commute or anticommute with the ones of the latter [71, 312]. Therefore, the coexistence of a certain spatial symmetry alone is not enough to guarantee the possibility of having a nontrivial band topology, but with appropriate commutation or anticommutation relations between the spatial and nonspatial symmetry operators.

Very recently, it was demonstrated that in a periodically driven system, a new space-time symmetry, such as time-glide or time-screw can emerge, if the system is invariant under reflection or two-fold rotation, together with a half-period time translation [241]. As far as topological classification is concerned, such a space-time symmetry can lead to a nontrivial Floquet band topology, in the same way as its spatial counterpart does in a static system, except for a possible alternation of the commutation/anticommutation relations with respect to the non-spatial symmetries [271, 269].

This result leads to the following interesting question. When the commutation/anticommutation relation alternation does occur, is it able to periodically drive an initially topological trivial system, whose spatial symmetry does not have appropriate relations with respect to the non-spatial symmetries, into a nontrivial Floquet topological phase?

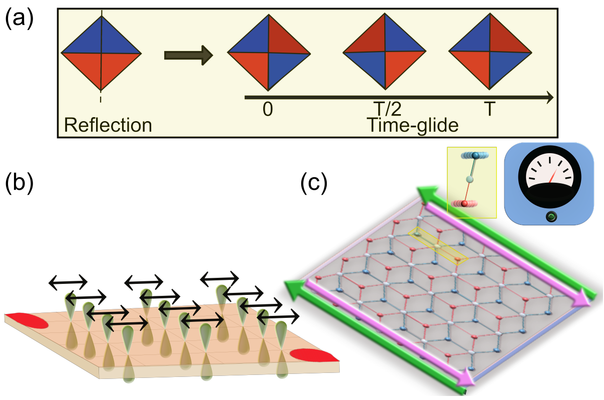

Figure 7.1: Phonon-assisted space-time engineering: (a) Promotion of mirror symmetry to a time-glide symmetry (b) A schematic of our proposal for class D where a phonon mode shown by black arrows can give rise to Floquet corner modes shown by red dots. (c) Similarly, in class AIII, a phonon mode shown in yellow inset can give rise to Floquet edge modes which result in a quantized conductance in a sample of bilayer graphene.

In this work, we answer this question by considering phonon-assisted space-time engineering, which promotes the spatial symmetry (such as reflection) of a static system into a space-time symmetry (such as time-glide), without changing the symmetry operator. In this way, the relations with respect to the non-spatial symmetries that are inappropriate for the spatial symmetry, would become otherwise appropriate for the space-time symmetry.

7.2 Phonon-assisted space-time engineering

One assumption in the electronic band structure of a crystal is that the lattice is rigid, with ions fixed to their equilibrium positions. The success of this assumption in characterizing lots of properties of materials is that the energy due to lattice vibrations or phonons is much smaller compared to the electronic energy at the equilibrium lattice configuration.

However, it is known that a coherently excited and macroscopically occupied phonon mode can result in ions moving collectively [194]. When the material is in such a state, the electrons will experience a periodically oscillating ionic potential which can no longer be neglected. Indeed, it has been proposed in some recent works [141, 43] that a phonon drive can be used to tune the topological features of graphene.

It is known that the symmetries of a crystal in equilibrium with a rigid lattice configuration are described by the space group of the lattice. The normal modes of the lattice vibrations, namely, the phonons, form the irreducible representations of this group. To be more specific, consider an order-two point group operation $\hat{g}$ which squares to identity; the phonon modes must have a definite parity under this operation. Whereas the oscillating potential generated by the even-parity phonon is invariant under such a point group operation at arbitrary times, the one generated by an odd-parity phonon breaks this point group symmetry. Nevertheless, the time-dependent potential $V(\boldsymbol{r}, t)$ generated by the latter acquires the space-time symmetry, given by $V(\hat{g}\boldsymbol{r}, t) = V(\boldsymbol{r}, t + T/2)$, where $\boldsymbol{r}$ and t are the spatial and temporal coordinates, and T is the oscillation period for the phonon. Hence, we have managed to promote a spatial order-two symmetry described by $\hat{g}$, to a space-time symmetry described by the same operator, by coherently exciting a phonon mode that is odd under $\hat{g}$. This is an example of phonon-assisted space-time engineering.

In this manuscript, we provide two examples in which by promoting a spatial symmetry with operator $\hat{g}$ to a space-time symmetry, the commutation relations between $\hat{g}$ and nonspatial symmetries become appropriate for supporting a nontrivial (Floquet) topological phase, whereas only a trivial phase exists in a $\hat{g}$-symmetric static system. In the first case, adding a phonon drive gives rise to corner Majorana modes and in second case, it results in a quantized conductance as shown in Fig. 7.1. In Appendix D, we list all possibilities of realizing a topological nontrivial Floquet phase from a static trivial system by such phonon-assisted space-time engineering.

7.3 2D system in class D/BDI

It is known that in the presence of reflection symmetry, class D or BDI exhibit topological behavior characterized by a mirror topological invariant whenever the reflection operator (described by M) commutes with the particle-hole operator (C) (Table I in Appendix D). We demonstrate how a phonon drive can turn a trivial static system with $\{C, M\} = 0$ into non-trivial Floquet topological phase.

Consider a tight-binding model with nearest-neighbor hopping, t_0, on a two-dimensional square lattice placed in the proximity to a s-wave superconductor described by the Bloch Hamiltonian

$$H_0(\mathbf{k}) = (m_0 - 2t_0 \cos k_x - 2t_0 \cos k_y)\tau_z + \Delta\tau_x + b\sigma_x, \tag{7.1}$$

where σ and τ are Pauli matrices acting on spin and particle-hole degree of freedom respectively. Here, we have expressed BdG Hamiltonian using Nambu spinor basis $(c_\uparrow^\dagger, c_\downarrow^\dagger, c_\downarrow, -c_\uparrow)$. In this basis, the last term $b\sigma_x$ arises from a magnetic field in x

direction and particle-hole symmetry is given by $C = \tau_y \sigma_y$. This Hamiltonian has a reflection given by $M = \sigma_x$ flipping the coordinates in the y direction. This also has a time-reversal symmetry given by $T = \mathbb{I}$, but it is not relevant for our purpose as the commutation relation with the time-reversal operator cannot be altered. Let us consider the effect of a reflection-symmetry breaking phonon which produces a time-dependent Rashba SOC given by:

$$H(\mathbf{k}, t) = 2\alpha_0 \cos \omega t (\sin k_x \sigma_y - \sin k_y \sigma_x) \tau_z. \tag{7.2}$$

An example for a phonon mode generating such a term is described in the next section.

The full Hamiltonian $H_0(\mathbf{k}) + H(\mathbf{k}, t)$ has a time-glide symmetry with reflection $M = \sigma_x$, promoted from the static reflection symmetry. The role of this periodic drive on topological behavior can be understood better by considering the frequency-domain formulation of the Floquet problem restricted to two Floquet zones [271, 269]. This two-by-two enlarged Hamiltonian reads

$$\mathscr{H}(\mathbf{k}) = \begin{pmatrix} H_0(\mathbf{k}) + \frac{\omega}{2} & H_1 \\ H_{\bar{1}} & H_0(\mathbf{k}) - \frac{\omega}{2} \end{pmatrix} \tag{7.3}$$

where $H_n = \frac{1}{T} \int_0^T H(t) e^{-in\omega t} dt$ and H_0 is described in Eq. 7.1.

This Hamiltonian has particle-hole symmetry given by $\mathscr{C} = \sigma_y \tau_y \rho_x$ and reflection $\mathscr{R} = \sigma_x \rho_z$ where we have introduced a set of Pauli matrices $\rho_{x,y,z}$ for the new spinor degree of freedom in the extended Floquet basis. It belongs to class D and has appropriate commutation relations. Its topological behavior can thus be understood in terms of mirror topological invariant $\mathbb{Z}_2$ (see Appendix D). The resulting band structure is shown in Fig. 7.2 with periodic boundary conditions in one direction. It features gapless modes around quasienergy $\omega/2$ for periodic BC in y direction whenever $\mathbb{Z}_2$ is non-trivial. Now, if we modify the boundary such that the reflection-symmetry is broken every where except at corners, then the edge modes are gapped out with opposite mass terms on two sides of the corner. However, at reflection-symmetric corners, this mass-term is zero and hence the edge modes are replaced by the hinge modes as shown in Fig. 7.3. We would like to emphasize that in our scheme gapless modes appear only around quasienergy $\omega/2$ while in certain Floquet schemes [37, 290] this kind of corner modes can appear at both quasienergy zero and $\omega/2$.

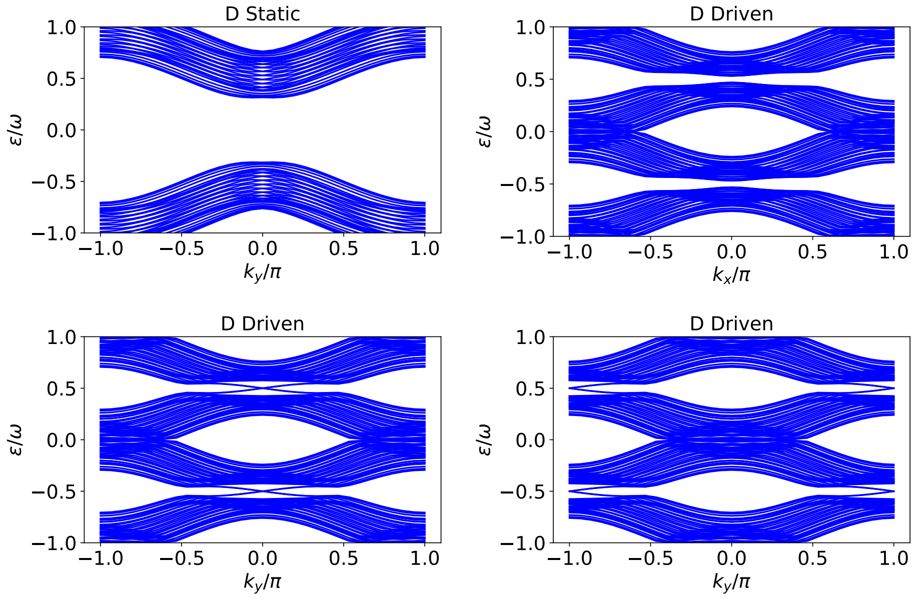

Figure 7.2: Band structure for $m_0 = \omega/2 + 1$, $\Delta = 0.9$, $\omega = 4.8$, $L = 15$, $b = 0.15$, and $\alpha_0 = 0.5$ with periodic boundary conditions in y direction for static Hamiltonian (Top Left), in x direction (Top Right), and in y direction (Bottom) for Floquet Hamiltonian. In the last plot $m_0 = -\omega/2 - 1$, and this change of sign results in a shift in the position of gapless mode from $k_y = 0$ to $k_y = \pi$ ($\Delta = 0.5$, $\alpha_0 = 1.0$ is shown in Supplemental material). (All energies are in units of t_0.)

These corner modes are very robust to disorder and other perturbations. We study the effect of disorder by modifying each nearest neighbor interaction $t \longrightarrow t(1+h)$ where h is a random number in the range of $[-\frac{d}{2}, \frac{d}{2}]$. When $d \ll 1$, we observe that the corner modes persist although there degeneracy is slightly lifted as shown in Fig. D.7. These corner modes start to mix with bulk states only when the disorder becomes comparable to hopping amplitudes. However, this splitting becomes exponentially small for large-enough system size as shown in Fig. D.9. In addition to disorder, these corner modes are very robust to other perturbations in hopping and sample boundaries (see Appendix D).

A toy model for phonon-induced Rashba SOC

The main ingredients needed for a Rashba SOC are the on-site π-σ spin-dependent interactions and the nearest-neighbor π-σ hopping between same parity orbitals. The spin-dependent on-site π-σ interaction occurs naturally because of an $\mathbf{L} \cdot \mathbf{S}$ term, and the nearest neighbor hopping between π-σ orbitals of same parity can be facilitated by the opposite parity orbitals or by ligands. For example, in graphene

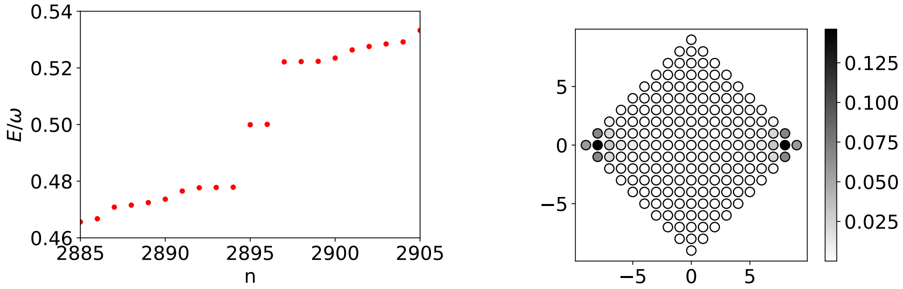

Figure 7.3: Energy spectrum of the Floquet Hamiltonian with H_1 of Eq. 7.2 around quasienergy $\omega/2$ for open boundary conditions in both directions with reflection-symmetry broken edges (left panel). Support of the hinge mode for these boundary conditions corresponding to quasienergy $\omega/2$ (right panel).

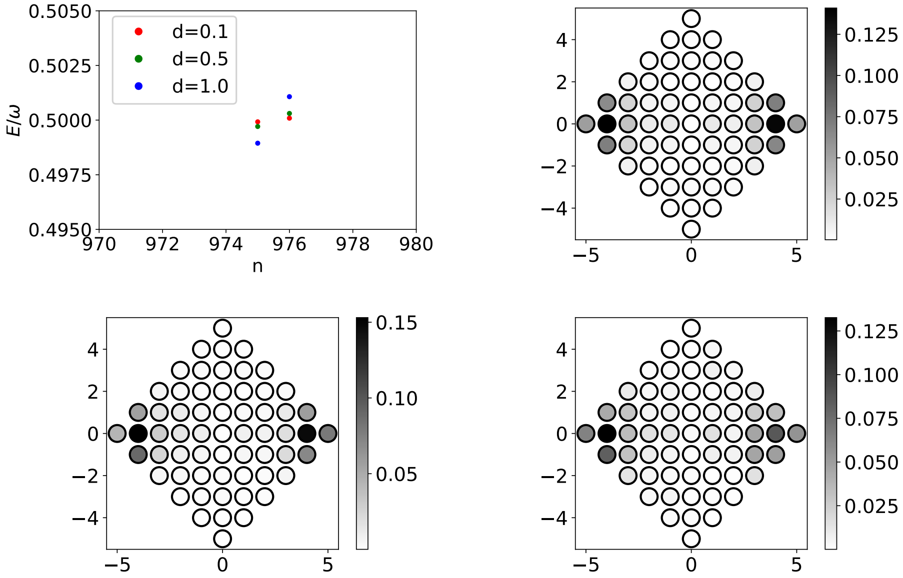

Figure 7.4: Spectra around $\omega/2$ for three different values of disorder strength d and corner modes associated with these states for system size $L = 6$. As d increases, the corner start to smear out into the bulk.

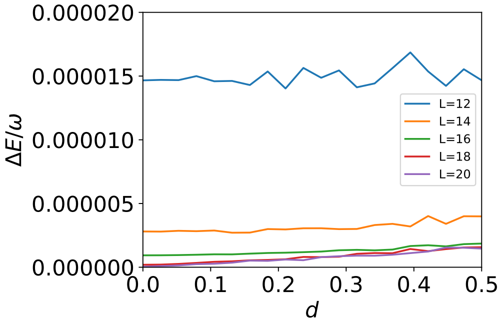

Figure 7.5: Splitting of Majorana corner modes at quasi-energy $\omega/2$ as a function of disorder strength for different sample size obtained by averaging over 50 disorder realizations. These corner modes are obtained for open boundary conditions on a square shaped sample of length L.

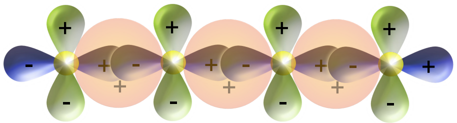

Figure 7.6: This figure shows the p_z (green) and p_x (blue) orbitals of the two-dimensional square lattice along the x direction with s orbitals of the ligands shown in orange color. When the ligand ion is displaced in z direction, it induces a hopping between p_x and p_z orbitals.

the intrinsic Rashba SOC occurs because of nearest-neighbor hopping between p and s/d orbitals [181, 235]. Furthermore, the ligands can mediate a nearest-neighbor π-σ hopping which depends on their position, and thus can give rise to a time-dependent Rashba SOC when they oscillate. Consider that each site of our square lattice model considered above has three non-degenerate p orbitals where neighboring p_z orbitals hybridize to form π bands and rest of the orbitals form σ bands. These π and σ orbitals interact via $\mathbf{L}\cdot\mathbf{S}$ coupling (Table 7.1). Furthermore, assume that an additional atom (which we call ligand) with active s orbitals is located between two lattice sites as shown in Fig. 7.6. This arrangement essentially forms a Lieb lattice. When the ligand is displaced in z direction, it induces a hopping between π and σ orbitals. When combined with on-site interaction $\mathbf{L}\cdot\mathbf{S}$ between π and σ orbitals, it produces an effective spin-dependent hopping between π orbitals given by:

$$\begin{aligned}\left\langle p_{z,i,j}|H_{\text{eff}}|p_{z,i+1,j}\right\rangle &= t_{zz} + \frac{1}{\epsilon_{zx}} t^{z,x}_{i,i+1} \left\langle p_{x,i+1}|\mathbf{L}\cdot\mathbf{S}|p_{z,i+1}\right\rangle \\ &= t_{zz} + i\frac{t_u\zeta}{\epsilon_{zx}}\sigma_y,\end{aligned} \tag{7.4}$$

where $t_{zz} = t_0$ is the direct-hopping between two p_z orbitals, ϵ_{zx} is the energy gap between p_z and p_x orbitals, ζ is SOC strength, and t_u is ligand-induced hopping between $p_{z,i}$ and $p_{x,i+1}$ Similarly, we can get a σ_x dependent hopping in y direction. For a small lattice displacement, this ligand-induced hopping $t_u \approx \left(\frac{u(t)}{L} t_{sp\sigma}\right) t_{sp\sigma}/\epsilon_{sp}$ where $t_{sp\sigma}$ is the hopping between $p_{x/y}$ orbital and the s orbital of the ligand, ϵ_{sp} is the energy separation between s and p orbitals, L is the distance of the ligand from the neighboring lattice site, and $t_{sp\sigma}u(t)/L$ is the hopping between the π orbital and s orbital of the ligand which comes into picture only when the lattice displacement $u(t)$ is non-zero [320]. It gives rise to a time-dependent Rashba SOC which can be controlled by the lattice vibrations associated with the ligand motion. For a coherent phonon, $u(t) \approx u_0 \cos \omega t$ where the ratio u_0/L can be as large as 0.1 in certain cases [334, 123]. The ligand-induced hopping t_u depends on a lot of factors like the phonon amplitude, energy separation ϵ_{sp}, and the hopping $t_{sp\sigma}$ which can be much larger than the π hopping t_{zz}. Depending on the ligand species, $\epsilon_{sp} \approx$ 1-10eV, and thus the effective hopping $t^2_{sp\sigma}/\epsilon_{sp}$ can be anywhere between $0.1t_{zz}$ and $5t_{zz}$ since the ratio $t_{sp\sigma}/t_{zz} \approx$ 1-10 usually. This rough estimate indicates that the ligand-induced hopping t_u can be anywhere between $0.1t_{zz}$ and t_{zz}, and thus the drive strength $\alpha_0 \approx (0.1-1)t_{zz}\zeta/\epsilon_{zx}$ can be of the same order as t_{zz} if SOC ζ is comparable to the energy separation between π and σ orbitals.

Orbital	p_x	p_y	p_z
p_x	0	$-i\zeta s_z$	$i\zeta s_y$
p_y	$i\zeta s_z$	0	$-i\zeta s_x$
p_z	$-i\zeta s_y$	$i\zeta s_x$	0

Table 7.1: Matrix element of $\mathbf{L}\cdot\mathbf{S}$ operator for p orbitals.

7.4 2D system in class AIII

It is known that insulators in class AIII respecting the chiral symmetry (described by S) alone have only the trivial band topology. When a unitary reflection symmetry (described by M, with $M^2 = 1$) exists, a $\mathbb{Z}$ topological classification is possible if $[S, M] = 0$ [71, 312].

Consider a tight-binding model for Bernal-stacked bilayer graphene-like lattice with nearest-neighbor intra-layer hopping for all sites and nearest-neighbor inter-layer hopping between non-dimer sites as shown in Fig. 7.7. For periodic boundary conditions, the corresponding Bloch Hamiltonian reads

$$\begin{aligned} H_0(\mathbf{k}) &= t_a\tau_x + t_3(\tau_x\sigma_x + \sigma_y\tau_y) \\ &+ 2t_b\left(\cos\frac{k_x}{2}\cos\frac{\sqrt{3}k_y}{2}\tau_x + \cos\frac{k_x}{2}\sin\frac{\sqrt{3}k_y}{2}\tau_y\right) \\ &+ \left(t_w\cos\frac{k_x}{2}\cos\frac{\sqrt{3}k_y}{2} + \frac{t_{w2}}{2}\cos\sqrt{3}k_y\right)(\sigma_x\tau_x - \sigma_y\tau_y) \\ &+ \left(t_w\cos\frac{k_x}{2}\sin\frac{\sqrt{3}k_y}{2} + \frac{t_{w2}}{2}\sin\sqrt{3}k_y\right)(\tau_x\sigma_y + \tau_y\sigma_x) \end{aligned} \tag{7.5}$$

where τ and σ now operate on sublattice and layer degrees of freedom, respectively. It has chiral symmetry $S = \tau_z$ and mirror-symmetry $M = \sigma_x\tau_x$ flipping the coordinates in the y direction.

When a phonon mode is coherently excited such that the atoms A_1 and B_2 oscillate out of phase along the x direction, the hopping for the nearest neighbors in $\mathbf{a}_1$ and $\mathbf{a}_2$ direction as shown in Fig. 7.7 acquires an additional contribution

$$\begin{aligned} H(t) =&\beta(t)\sum_{\mathbf{r}_i,\alpha=1,2}\left(a^\dagger_{\alpha,\mathbf{r}_i}b_{\alpha,\mathbf{r}_i+\mathbf{a}_1} - a^\dagger_{\alpha,\mathbf{r}_i}b_{\alpha,\mathbf{r}_i+\mathbf{a}_2} + h.c\right) \\ &+ \gamma(t)\sum_{\mathbf{r}_i}\left(a^\dagger_{1,\mathbf{r}_i}b_{2,\mathbf{r}_i+\mathbf{a}_1} - a^\dagger_{1,\mathbf{r}_i}b_{2,\mathbf{r}_i+\mathbf{a}_2} + h.c\right), \end{aligned} \tag{7.6}$$

and thus adds

$$\begin{aligned} H(\mathbf{k},t) =&\beta(t)\left(-\sin\frac{k_x}{2}\cos\frac{\sqrt{3}k_y}{2}\tau_y + \sin\frac{k_x}{2}\sin\frac{\sqrt{3}k_y}{2}\tau_x\right) \\ &+ \gamma(t)\sin\frac{k_x}{2}\cos\frac{\sqrt{3}k_y}{2}(\sigma_x\tau_y + \sigma_y\tau_x) \\ &+ \gamma(t)\sin\frac{k_x}{2}\sin\frac{\sqrt{3}k_y}{2}(\sigma_x\tau_x - \sigma_y\tau_y) \end{aligned} \tag{7.7}$$

to $H_0(\mathbf{k})$ where a/b refers to A and B sublattice sites, α indicates the layer index, and $\beta(t)$ and $\gamma(t)$ are proportional to the lattice displacement $u(t)$ for small phonon amplitudes. Their magnitude can be estimated as $\beta(t) \approx \eta u(t)t_0/d_0$, where $\eta \approx$ 1-4, t_0 is the static hopping between two sites, and d_0 is the equilibrium separation between two sites, as the hopping in a tight binding model usually changes by a factor of $\left(\frac{d_0}{d_0+u}\right)^\eta$ [150]. For a coherent phonon, the lattice displacement $u(t) \approx u_0\cos\omega t$ which gives $\beta(t) = \beta_0\cos\omega t$, and thus $H(\mathbf{k},t) = H_1(\mathbf{k})\cos\omega t$. For a lattice displacement of 5-10%, the drive strength β_0 and γ_0 can be anywhere between 5-40% of the static hopping amplitude t_0.

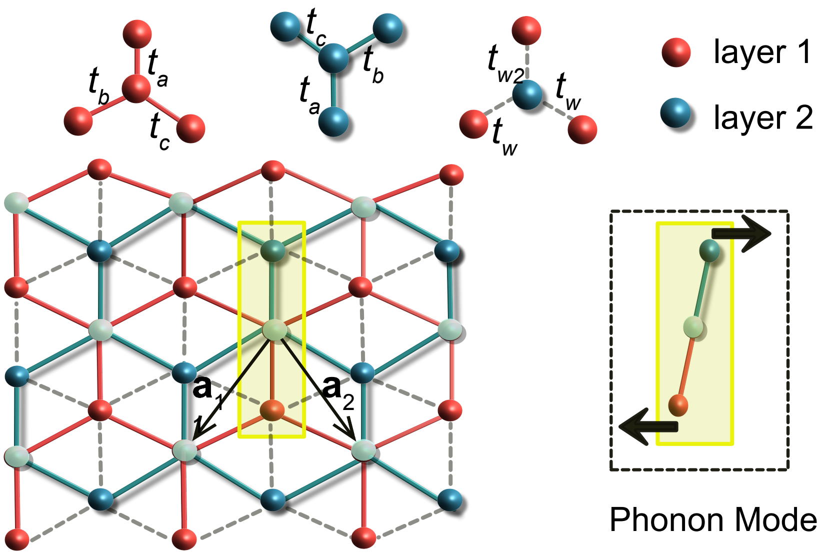

Figure 7.7: A schematic for A-B stacked bilayer honeycomb lattice with nearest-neighbor intra-layer (solid lines) and inter-layer(dashed lines) hopping. The unit cell of the triangular lattice is shown in a yellow box. The dimer sites (shown in light blue color) do not participate in any nearest-neighbor inter-layer hopping. The right inset shows the phonon mode which affects the hopping parameters t_b,t_c, and t_w.

Now, the two-by-two enlarged Hamiltonian (Eq.7.3) has a chiral symmetry, $\mathscr{S} = S\rho_x$ and a reflection symmetry realized by $\mathscr{R} = M\rho_z$. Since $[\mathscr{S}, \mathscr{R}] = 0$, we can have a nontrivial classification with a mirror $\mathbb{Z}$ topological invariant. As shown in Fig.7.8, in non-trivial regime, it hosts gapless edge modes along y boundaries for the driven system which are protected by reflection-symmetry. These gapless edge modes at $k_y = 0$ co-exist with some gapless bulk modes at arbitrary $\pm k_y$ which are not protected by the reflection-symmetry. These points arise due to bulk-band gap closings which can be gapped out by a charge-density wave (CDW) of wavelength q . This perturbation is implemented by adding a term of the form of $\cos(qp)$ to all nearest-neighbor hoppings in the static and the drive parts for each site $\mathbf{R} = n\mathbf{a}_1 + p\mathbf{a}_2$ on the underlying triangular lattice of bilayer graphene (see appendix D for more details). This kind of perturbation results in a quantized conductance as shown in Fig. 7.8 where we have calculated the DC conductance numerically by using Floquet scattering matrix approach [242]. We obtain this S matrix using Kwant [120] for two leads by accounting for the photon degree of freedom using the Floquet representation of the Hamiltonian. In order to calculate the transmission coefficient, we sum up over incoming modes in zeroth Floquet sector which accounts for the

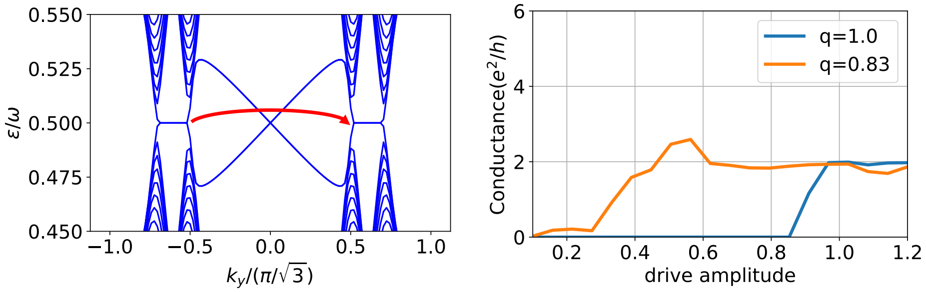

Figure 7.8: Band structure around $\omega/2$ for Floquet Hamiltonian (up to two Floquet sectors) of Eq.D.23. At $k_y = 0$ for $t_a = 2.4$, $t_b = 1.2$, $t_3 = 0.5$, $\beta_0 = 0.1$, $t_w = 0.5$, $\gamma_0 = 0.5$, $\omega = 4.4$, $t_{w_2} = 0.1$. Here, time-glide symmetry gives rise to two gapless edge modes which co-exist with other gapless modes (left panel). Conductance of a sample of width, $W = 51$ and length, $L = 61$ as a function of drive amplitude in the presence of a cdw perturbation which suppresses the contribution of bulk modes, but the edge modes contribution survives. In this case, cdw $q \approx 0.8$ connects the two bulk gap closings as shown by red arrow in left figure (right panel).

absence of drive in leads. For the outgoing modes, we keep non-zero photon sectors to account for photon-assisted transport which gives the transmission at energy E:

$$T(E) = \sum_{\alpha,\beta,n} |S_{\alpha,n;\beta,0}(E)|^2 \tag{7.8}$$

where α, β represents the outgoing and incoming modes, respectively, and n is the photon degree of freedom. Alternatively, the gapless bulk modes can also be removed by a drive-induced interlayer imaginary hopping between dimers which makes it a Floquet higher-order topological phase (see SM).

This establishes that the symmetry-promotion action of phonon drive can have much broader implications as it offers a possibility to produce a quantized conductance with a phonon-drive in a previously trivial system.

7.5 Conclusions

We discussed how the symmetry-promotion action of a phonon-drive can allow a previously trivial system to exhibit a topological classification. We presented two schemes where this can occur involving systems in class D and class AIII. These schemes require a phonon drive with a lattice displacement of the order of 0.1. This can be achieved, for example, by exciting a particular phonon mode using ultrafast light pulses (see for example Ref. [352]). Usually, these phonons have a life-time greater than 10ps and which can allow a conductivity measurement with ultrafast devices based on THz operated photoconductive switches and STM tips [78, 226], or even time-resolved ARPES [223, 306, 322, 324, 314].

Both of these schemes need phonon frequencies to be of the same order as hopping parameter. In most materials, electronic bandwidths are usually much greater than phonon frequencies. These frequencies are decided by the bond strength while the hopping parameter in graphene-like lattices depend on overlap between neighboring π orbitals. This kind of parameter regime can be realized by suppressing the hopping parameter without affecting the bond strengths between neighboring atoms, as the latter determine the phonon frequencies. Alternatively, one can consider placing the system on a substrate which binds to different sites such that the phonon frequencies are increased. These lattice models can be possibly realized using covalent organic framework [80, 153] where molecular orbitals play the same role as atomic orbitals in our model and hopping parameters are of the order of 100meV and some of these materials can have phonon frequencies of the same order [174]. Similarly, twisted bilayer materials can provide another platform to realize the Class AIII model where hopping parameters can be made comparable to certain phonon frequencies [213, 77].

Appendix D

APPENDIX

D.1 Effective Symmetry Operators and modified commutation relations in extended Floquet basis

In this section, we briefly review the effective symmetry operations for the frequency-domain representation of the time-periodic Hamiltonian when the system has a time-glide symmetry.

In this case, we show that the original time-glide symmetry of a time-periodic Hamiltonian is mapped to the reflection symmetry for the effective Hamiltonian [271]. The time-periodic Hamiltonian here follows:

$$MH(\mathbf{k},t)M^{-1} = H(-k_x,\mathbf{k}_{\parallel},t+T/2). \tag{D.1}$$

Here, we are interested in studying these systems in Fourier basis and thus consider the above Hamiltonian in extended Floquet basis given by:

$$H_{\text{full}}(\mathbf{k}) = \begin{pmatrix} . & & & & & & & \\ H_0+2\omega & H_1 & H_2 & . & . & & & \\ H_{\bar{1}} & H_0+\omega & H_1 & H_2 & & & & \\ H_{\bar{2}} & H_{\bar{1}} & H_0 & H_1 & H_2 & . & & \\ . & H_{\bar{2}} & H_{\bar{1}} & H_0-\omega & H_1 & H_2 & . & \\ & & H_{\bar{2}} & H_{\bar{1}} & H_0-2\omega & H_1 & H_2 & . \\ & & & & & . & & \\ & & & & & & . & \end{pmatrix}, \tag{D.2}$$

and

$$H_n(\mathbf{k}) = \frac{1}{T}\int_0^T H(\mathbf{k},t)e^{-in\omega t}. \tag{D.3}$$

In this basis, the time-glide symmetry is given by effective reflection

$$\mathcal{R}_{\text{eff}} = \begin{pmatrix} \ddots &&&&& \\ & M &&&& \\ && -M &&& \\ &&& M && \\ &&&& -M & \\ &&&&& \ddots \end{pmatrix}, \tag{D.4}$$

and other symmetry operators are also modified, for example the new (effective) operators for time-reversal, charge-conjugation, and chiral symmetry are now given by:

$$\mathscr{T} = \begin{pmatrix} \ddots &&&&& \\ & \mathcal{T} &&&& \\ && \mathcal{T} &&& \\ &&& \mathcal{T} && \\ &&&& \mathcal{T} & \\ &&&&& \mathcal{T} \end{pmatrix}, \mathscr{C} = \begin{pmatrix} &&& \\ &&& C \\ && C & \\ & C && \\ &&& \end{pmatrix}, \mathscr{S} = \begin{pmatrix} &&& \\ &&& S \\ && \mathcal{S} & \\ & \mathcal{S} && \\ &&& \end{pmatrix}. \tag{D.5}$$

Now, the commutation relation between effective different symmetry operators is different from the commutation relation for the static case. This indicates that the effective Hamiltonian, although belongs to the same AZ class as the static Hamiltonian, it can allow the existence of a non trivial topological phase (For e.g $\{M, S\} = 0 \implies [\mathcal{R}, \mathscr{S}] = 0$) in the presence of this time-glide symmetry. We are going to exploit this feature in realizing non-topological phase by altering the modified commutation relations which results in a change in topological classification as shown in Table. D.1. Although, in this work we use a periodic drive to promote reflection symmetry to a time-glide symmetry in two dimensions, the same ideas can be applied to two-fold rotations and inversion symmetry in two and three dimensions and the consequences of such promotions are discussed in table D.1 and table D.2.

When the drive is monochromatic, $H_n = 0$ for $|n| > 1$, and thus the above symmetries can be best described in terms of constraints on H_0 and H_1. In this case, the chiral symmetric Hamiltonians satisfy:

$$SH_0(\mathbf{k}, \mathbf{r})S^{-1} = -H_0(\mathbf{k}, \mathbf{r}), \quad SH_1(\mathbf{k}, \mathbf{r})S^{-1} = -H_1^{\dagger}(\mathbf{k}, \mathbf{r}). \tag{D.6}$$

Class	2D		3D	
	Symmetry Promotion	Classification	Symmetry Promotion	Classification
AIII	R_-	$\mathbb{Z}$	R_+	$\mathbb{Z}^2$
BDI	R_{+-}	$\mathbb{Z}$	R_{--}	$\mathbb{Z}$
D	R_-	$\mathbb{Z}_2$	R_-	$\mathbb{Z}$
DIII	R_{+-}	$\mathbb{Z}_2$	R_{--}	$\mathbb{Z}^2$
CII	R_{+-}	$2\mathbb{Z}$	R_{++}	$\mathbb{Z}_2^2$
CI	R_{-+}	$2\mathbb{Z}$	R_{++}	$\mathbb{Z}$
AIII	C_{2+}	$\mathbb{Z}$	C_{2-}	$\mathbb{Z}^2$
BDI	C_{2++}	$\mathbb{Z}$	C_{2+-}	$\mathbb{Z}$
DIII	C_{2++}	$\mathbb{Z}$	C_{2+-}	$\mathbb{Z}$
CII	C_{2++}	$2\mathbb{Z}$	C_{2+-}	$\mathbb{Z}$
CI	C_{2++}	$2\mathbb{Z}$	C_{2+-}, C_{2-+}	$\mathbb{Z}$, $(2\mathbb{Z})^2$

Table D.1: Symmetry promotion from reflection R and two-fold rotation C.

Class	3D	
	Symmetry Promotion	Classification
AIII	I_+	$\mathbb{Z}^2$
BDI	I_{++}	$\mathbb{Z}$
D	I_+	$\mathbb{Z}$
DIII	I_{++}	$\mathbb{Z}^2$
CII	I_{--}	$\mathbb{Z}_2^2$
CI	I_{--}, I_{++}	$\mathbb{Z}$, $(2\mathbb{Z})^2$

Table D.2: Symmetry promotion from inversion I.

Similarly particle-hole symmetry is given by:

$$CH_0^*(\mathbf{k},\mathbf{r})C^{-1} = -H_0(-\mathbf{k},\mathbf{r}), \quad CH_1^*(\mathbf{k},\mathbf{r})C^{-1} = -H_1^+(-\mathbf{k},\mathbf{r}) \tag{D.7}$$

and time-glide by:

$$MH_0(k_x,k_y)M^{-1} = H_0(-k_x,k_y), \quad MH_1(k_x,k_y)M^{-1} = -H_1(-k_x,k_y). \tag{D.8}$$

D.2 Mirror topological invariant $M\mathbb{Z}_2$ for class D, R_+ in two dimensions

For class D, when the particle-hole and reflection symmetry operator commute, the different topological phases can be distinguished on the basis of mirror topological invariant $M\mathbb{Z}_2$. This invariant can be calculated at reflection symmetric hyperplanes by first block diagonalizing the Hamiltonian in $\mathscr{R}$ basis, and then calculating the $\mathbb{Z}_2$ invariant for one block. When the reflection operator commutes with the effective particle-hole operator $\mathscr{C}$, these two blocks do not mix and hence a classification can be made on the basis of this topological invariant for one block. In the main text we considered the undriven model:

$$H_0(k_x, k_y) = m_1\tau_z + \Delta\tau_x + b\sigma_x \tag{D.9}$$

where $m_1 = m - 2t_0 \cos k_x - 2t_0 \cos k_y$ with a drive of the form:

$$H(t) = 2\alpha_0 \cos \omega t(\sin k_x\sigma_y - \sin k_y\sigma_x)\tau_z = H_1 e^{i\omega t} + H_1^\dagger e^{-i\omega t}. \tag{D.10}$$

This Hamiltonian has a particle-hole symmetry given by $C = \tau_y\sigma_y$ and time-glide with reflection $M = \sigma_x$ about y axis ($y \longrightarrow -y$). We can cast it into a more familiar form if we use the eigenstate basis of $m(\mathbf{k})\tau_z + \Delta\tau_x$ which corresponds to a transformation $\tau_z \longrightarrow \cos\theta\tau_z - \sin\theta\tau_x$ where $\cos\theta = \frac{m(\mathbf{k})}{\sqrt{m(\mathbf{k})+\Delta^2}}$. In this basis:

$$H_0 = \sqrt{m(\mathbf{k})^2 + \Delta^2}\tau_z + b\sigma_x, \tag{D.11}$$

and

$$H_1 = 2\alpha_0(\sin k_x\sigma_y - \sin k_y\sigma_x)\left(\frac{m(\mathbf{k})}{E_k}\tau_z - \frac{\Delta}{E_k}\tau_x\right) \tag{D.12}$$

where $E_k = \sqrt{m(\mathbf{k})^2 + \Delta^2}$. In this basis, the particle-hole operator $C = \tau_y\sigma_y$ and time-glide $M = \sigma_x$ remains the same. Now the Floquet Hamiltonian for photon sectors n and $n + 1$ can be written as:

$$H_F(\mathbf{k}) = \begin{pmatrix} E_k\tau_z + \frac{\omega}{2}\mathbb{I} + b\sigma_x & \alpha_0(\sin k_x\sigma_y - \sin k_y\sigma_x)\left(\frac{m(\mathbf{k})}{E_k}\tau_z - \frac{\Delta}{E_k}\tau_x\right) \\ \alpha_0(\sin k_x\sigma_y - \sin k_y\sigma_x)\left(\frac{m(\mathbf{k})}{E_k}\tau_z - \frac{\Delta}{E_k}\tau_x\right) & E_k\tau_z - \frac{\omega}{2}\mathbb{I} + b\sigma_x \end{pmatrix}. \tag{D.13}$$

The topological behavior of this Hamiltonian can also be understood by focusing on its inner 4×4 block given by:

$$\begin{aligned} \mathscr{H}(\mathbf{k}) &= \begin{pmatrix} (-E_k + \frac{\omega}{2})\mathbb{I} + b\sigma_x & \alpha_0(\sin k_x\sigma_y - \sin k_y\sigma_x)\frac{\Delta}{E_k} \\ \alpha_0(\sin k_x\sigma_y - \sin k_y\sigma_x)\frac{\Delta}{E_k} & (E_k - \frac{\omega}{2})\mathbb{I} + b\sigma_x \end{pmatrix} \\ &= (-E_k + \frac{\omega}{2})\rho_z + b\sigma_x + \alpha_0(\sin k_x\sigma_y - \sin k_y\sigma_x)\frac{\Delta}{E_k}\rho_x \end{aligned} \tag{D.14}$$

where ρ indicates the photon degree of freedom. In this case, the particle-hole symmetry $\mathscr{C} = \sigma_y p_y$, and it has a reflection symmetry $\mathscr{R} = \sigma_x\rho_z$ which commutes with $\mathscr{C}$, and hence it can be characterized by a mirror $\mathbb{Z}_2$ invariant. In order to calculate this topological invariant, we go to reflection symmetric hyperplanes

$(k_y = 0, \pi)$ and express this Hamiltonian in the basis of M arranged such that the first block has eigenvalue +1. The above Hamiltonian of Eq. D.14 takes the following form:

$$\mathscr{H}(k_x) = \begin{pmatrix} H_+ & \\ & H_- \end{pmatrix} = \begin{pmatrix} -E_k + \frac{\omega}{2} + b & -i\alpha_0 \sin k_x \frac{\Delta}{E_k} & 0 & 0 \\ i\alpha_0 \sin k_x \frac{\Delta}{E_k} & E_k - \frac{\omega}{2} - b & 0 & 0 \\ 0 & 0 & E_k - \frac{\omega}{2} + b & -i\alpha_0 \sin k_x \frac{\Delta}{E_k} \\ 0 & 0 & i\alpha_0 \sin k_x \frac{\Delta}{E_k} & -E_k + \frac{\omega}{2} - b \end{pmatrix} \tag{D.15}$$

with

$$R = \begin{pmatrix} 1 & & & \\ & 1 & & \\ & & -1 & \\ & & & -1 \end{pmatrix} \text{ and } P = \begin{pmatrix} & -1 & & \\ -1 & & & \\ & & & 1 \\ & & 1 & \end{pmatrix} \tag{D.16}$$

in the new basis. Now, each block belongs to class D, and in order to calculate the mirror $\mathbb{Z}_2$ invariant, we can pick any block. For example, if we pick H_+, then the invariant can be calculated from Pffafin of H_+ at $k_x = 0, \pi$. At $k_y = 0$, the $\mathbb{Z}_2$ topological invariant is given by:

$$\eta_{k_y=0} = \text{Sign}[(E_k - \frac{\omega}{2} + b)_{(k_x=0,k_y=0)}(E_k - \frac{\omega}{2} + b)_{(k_x=\pi,k_y=0)}]. \tag{D.17}$$

Similarly, at $k_y = \pi$

$$\eta_{k_y=\pi} = \text{Sign}[(E_k - \frac{\omega}{2} + b)_{(k_x=0,k_y=\pi)}(E_k - \frac{\omega}{2} + b)_{(k_x=\pi,k_y=\pi)}], \tag{D.18}$$

and thus the mirror $\mathbb{Z}_2$ invariant is now given by :

$$\eta_{M\mathbb{Z}_2} = 1 - |\eta_{k_y=0} - \eta_{k_y=\pi}| = \text{Sign}[\eta_{k_y=0}\eta_{k_y=\pi}], \tag{D.19}$$

and its dependence on m_0 and Δ is shown in Fig. D.1. This indicates that if the system size is quite large, we can get a non-trivial phase for a very small value of superconducting gap Δ, but for small system sizes, we find the gapless edge modes only for $\Delta \approx 0.5$ as the bulk gap becomes very small for lower values of Δ. Although, the topological invariant is non-trivial for a large range of m and Δ, the system does not seem to exhibit corner modes for small values of Δ. In order to understand the regime for gapless boundary states we study an eightband model which captures the essential features of the above model. This model is given by Hamiltonian:

$$H_{\text{eff}} = \begin{pmatrix} H_0 + \frac{\omega}{2} & H_1 \\ H_1^\dagger & H_0 - \frac{\omega}{2} \end{pmatrix}. \tag{D.20}$$

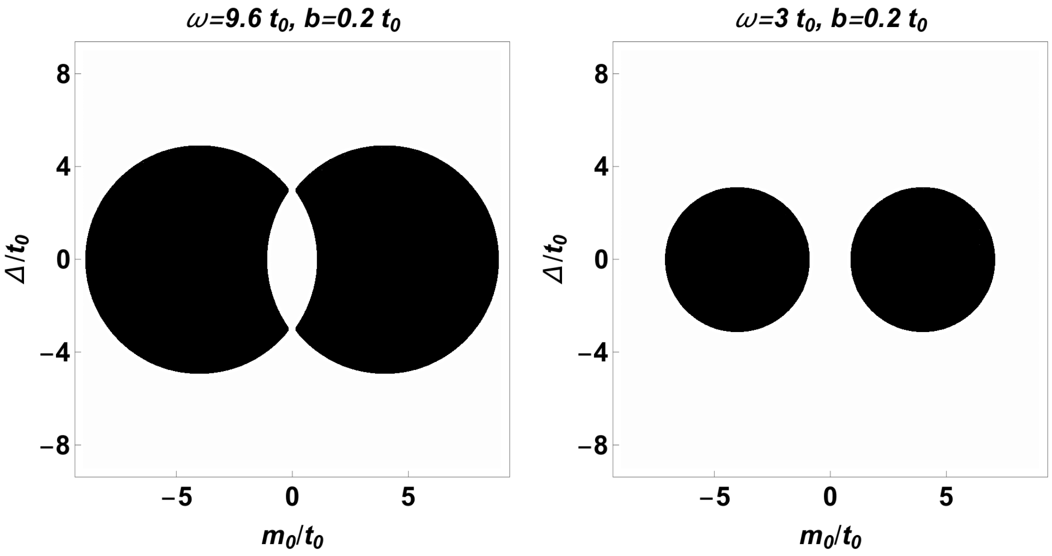

Figure D.1: Mirror topological invariant $\eta_{M\mathbb{Z}_2}$ on parameters m_0 and Δ for two different values of ω. All parameters are given in units of hopping amplitude t_0. Black regions indicate the non-trivial region.

The spectrum of this hamiltoninan is shown in Fig. D.2 for open boundary conditions. In certain cases, the bulk gap becomes very small and thus the gapless boundary modes or zero energy hinge modes can not be observed for a small system size.

D.3 Effect of a CDW perturbation and a phonon-induced complex hopping term in Class AIII example.

Effect of translation-symmetry breaking perturbations on gapless bulk modes at Floquet zone boundaries

We study the effect of a charge-density wave type perturbation in the bilayer graphene model considered above. For each site $\mathbf{R} = n\mathbf{a}_1 + p\mathbf{a}_2$ on the underlying triangular lattice of bilayer graphene,we add a term of the form of $A_0 \cos(qp)$ to all the nearest-neighbor hopping in the static and the drive part. We calculate the conductance in the y direction for different amplitudes A_0 and wavevector q of this extra term using Kwant [120]. Without this charge-density wave term, the observed conductance has a contribution from both edge and bulk modes at quasienergy $\omega/2$, but this term suppresses the bulk contribution as shown in Fig. D.4. In the presence of the charge-density wave perturbation, the conductance is quantized to two which indicates that it arises from the protected edge modes in the presence of a gapped bulk. It is further verified by the fact that modifying the geometry of the system from a strip to a cylindrical tube kills the contribution of edge modes and the conductance

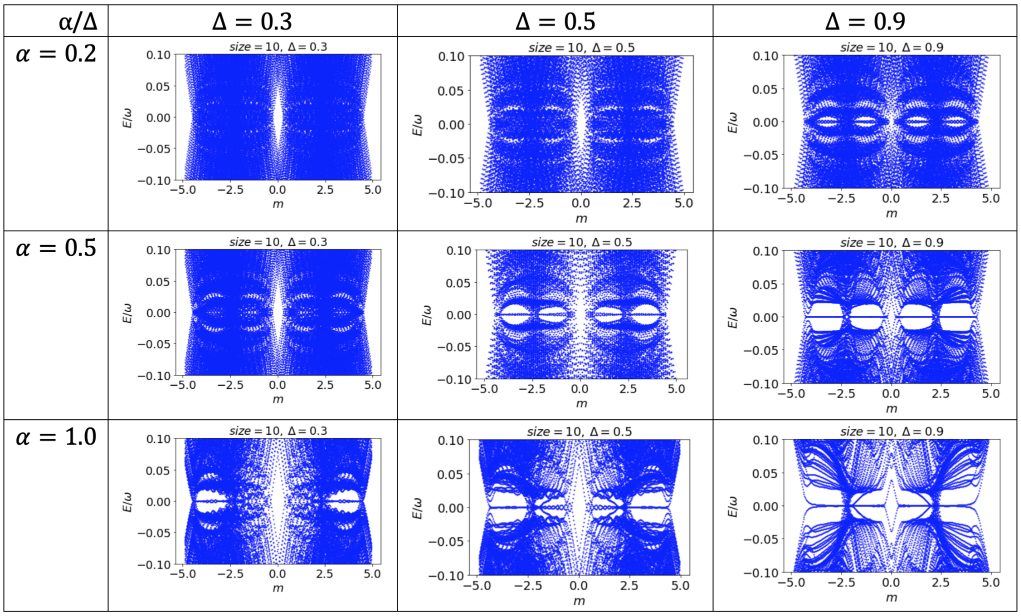

Figure D.2: Energy spectrum around zero energy as a function of m for an eight band model capturing the main features of the τ_z drive considered in Eq. D.20.

becomes zero as shown in Fig. D.3. In order to calculate the conductance of the Floquet Hamiltonian, we first get the S matrix using Kwant for two leads by treating the photon degree as a static degree of freedom, but since the lead is static, in order to calculate the transmission coefficient, we sum up over those incoming modes only which belong to zeroth Floquet sector. For the outgoing modes, we keep non-zero photon sectors to account for photon-assisted transport [242], and thus the transmission at energy E is given by

$$T(E) = \sum_{\alpha,\beta,n} |S_{\alpha,n;\beta,0}(E)|^2 \tag{D.21}$$

where α, β represents the outgoing and incoming modes, respectively, and n is photon degree of freedom.

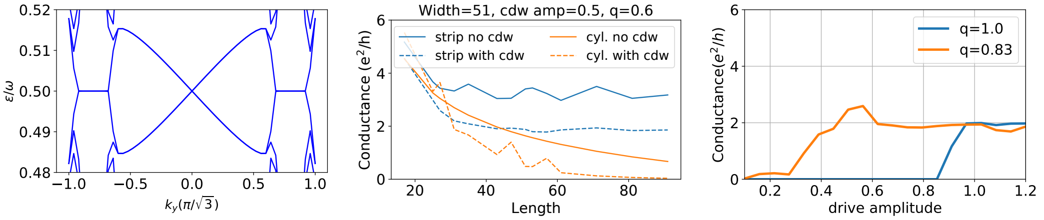

Figure D.3: Spectra and conductance in presence of a cdw perturbation. Left: Spectra for a system with periodic boundary condition in y direction. In this case, the translational vector is given by $\mathbf{a}_2 = \sqrt{3}\hat{y}$. Center: Conductance as a function of sample length for two different geometries with and without cdw. Right: Conductance as a function of drive strength for two different cdw q for a sample of length, $L = 81$ and width, $W = 51$.

Phonon-induced complex hopping: Second-order TI

For class AIII, static Hamiltonian

$$
\begin{aligned}
H_0(\mathbf{k}) = t_a\tau_x + 2t_b\left(\cos\frac{k_x}{2}\cos\frac{\sqrt{3}k_y}{2}\tau_x + \cos\frac{k_x}{2}\sin\frac{\sqrt{3}k_y}{2}\tau_y\right)\\
+\left(t_w\cos\frac{k_x}{2}\cos\frac{\sqrt{3}k_y}{2} + \frac{t_{w2}}{2}\cos\sqrt{3}k_y\right)(\sigma_x\tau_x - \sigma_y\tau_y)\\
+\left(t_w\cos\frac{k_x}{2}\sin\frac{\sqrt{3}k_y}{2} + \frac{t_{w2}}{2}\sin\sqrt{3}k_y\right)(\tau_x\sigma_y + \tau_y\sigma_x) + t_3(\tau_x\sigma_x + \sigma_y\tau_y)
\end{aligned}
\tag{D.22}
$$

and phonon-drive

$$
\begin{aligned}
H(\mathbf{k},t) =& \beta(t)\left(-\sin\frac{k_x}{2}\cos\frac{\sqrt{3}k_y}{2}\tau_y + \sin\frac{k_x}{2}\sin\frac{\sqrt{3}k_y}{2}\tau_x\right)\\
&+\gamma(t)\sin\frac{k_x}{2}\cos\frac{\sqrt{3}k_y}{2}(\sigma_x\tau_y + \sigma_y\tau_x)\\
&+\gamma(t)\sin\frac{k_x}{2}\sin\frac{\sqrt{3}k_y}{2}(\sigma_x\tau_x - \sigma_y\tau_y),
\end{aligned}
\tag{D.23}
$$

we obtained gapless edge modes which co-exist with some gapless bulk modes. In the main text, we presented cdw-based mechanism to remove these gapless points. Alternatively as shown in Fig. D.5, the gapless bulk modes can also be removed by a drive-induced interlayer imaginary hopping between dimers

$$
H_I(t) = \lambda(t)\sum\left(ia^{\dagger}_{1,\mathbf{r}_i}b_{2,\mathbf{r}_i+\mathbf{a}_1} + ia^{\dagger}_{1,\mathbf{r}_i}b_{2,\mathbf{r}_i+\mathbf{a}_2} + h.c\right)
\tag{D.24}
$$

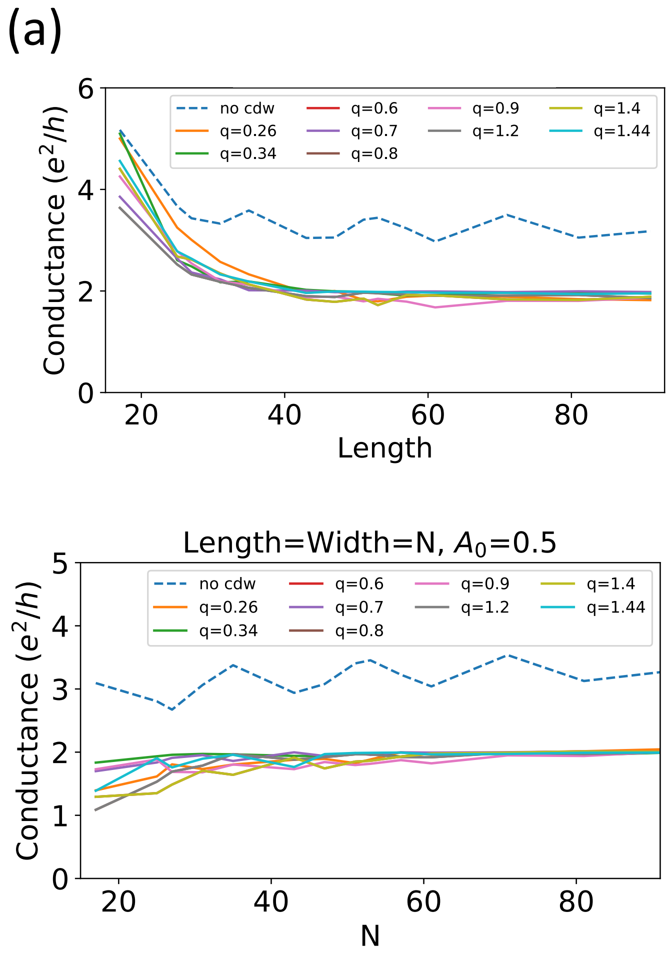

Figure D.4: Conductance at energy very close to $\omega/2$ as a function of system size for different values of charge-density wave perturbation. This perturbation suppresses the contribution of bulk gapless modes and thus only the quantized contribution from gapless edge modes survive.

which in k space becomes

$$H_I(\mathbf{k}) = \lambda(t)\cos\frac{k_x}{2}\sin\frac{\sqrt{3}k_y}{2}(\sigma_x\tau_x + \sigma_y\tau_y). \tag{D.25}$$

This kind of hopping might not be so easy to realize, but it verifies the fact that these gapless bulk modes are not protected by reflection-symmetry alone. In this case, if we modify the boundary such that it gives rise to an effective reflection symmetric-breaking mass term, the gapless edge modes are replaced by the hinge modes on reflection-symmetric corners as shown in Fig. D.5.

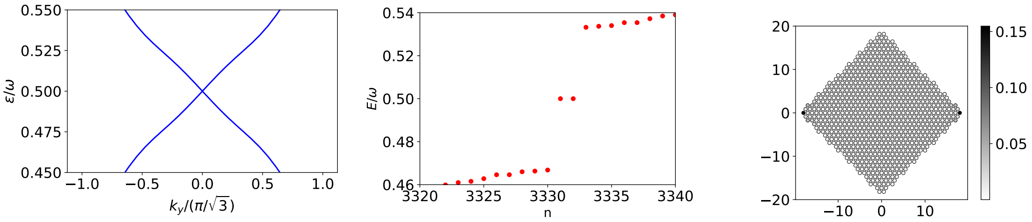

Figure D.5: Band structure and corner modes in presence of an imaginary hopping term. Left panel: Band structure around $\omega/2$ for Floquet Hamiltonian (up to two Floquet sectors) with imaginary hopping term of Eq. D.23 for PBC in y direction. Center panel: Energy spectrum of Floquet Hamiltonian with H_1 of Eq. D.24 around quasienergy $\omega/2$ for open boundary conditions with reflection-symmetry breaking term. Right panel: Support of the hinge mode for these boundary conditions corresponding to quasinergy $\omega/2$. The parameters for this figure are: $t_a = 2.4, t_b = 1.2, t_3 = 0.5, t_w = 0.1, \beta_0 = 0.1, \gamma_0 = 0.8, \lambda_0 = 0.8, t_{w_2} = 0.1$

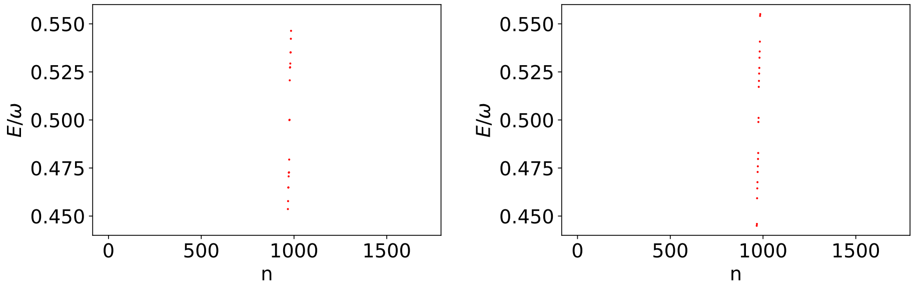

Figure D.6: Spectra around $\omega/2$ without disorder (left) and for a disorder with $d = 1.0$ (right) for sample size $L = 6$.

D.4 Effect of disorder and other perturbations on corner modes of Class D

We study the effect of three different kinds of perturbations on Floquet Majorana corner modes discussed in the main text. We obtained these corner modes for open boundary conditions on a square shaped sample of length L.

Disorder

We modify each nearest neighbor interaction $t \longrightarrow t(1+h)$ where h is a random number in the range of $[-\frac{d}{2}, \frac{d}{2}]$. When $d \ll 1$, we observe that the corner modes persist although there degeneracy is slightly lifted as shown in Fig. D.6 and D.7. For larger disorder these states start to mix with bulk states which results in energy splitting of zero modes. However, this splitting decreases significantly for a significantly large system size as shown in Fig. D.9.

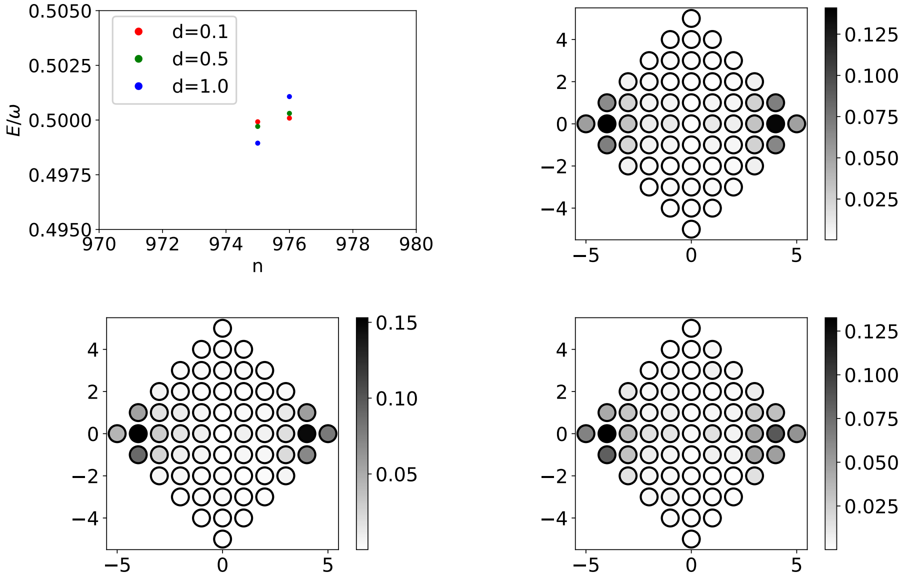

Figure D.7: Spectra around $\omega/2$ for three different values of d and corner modes associated with these states for sample size $L = 6$. As d increases, the corner mode starts to smear out into the bulk.

Perturbations to static Hamiltonian

We first consider a perturbation which modified the static term:

$$H_0(\mathbf{k}) \to H_0(\mathbf{k}) + d_1 \left(\sin k_x \sigma_x \tau_z + \sin k_y \sigma_y \tau_z\right). \tag{D.26}$$

In this case, the corner modes survive only for $d_1 < 0.5$ as shown in Fig. D.8.

Next, we consider a perturbation which modified the static term:

$$H_0(\mathbf{k}) \to H_0(\mathbf{k}) + d_1 \left(\sin k_x \sigma_y \tau_z - \sin k_y \sigma_x \tau_z\right). \tag{D.27}$$

We observe that the corner modes can persist for small values of d_1 as shown in Fig. D.10. As we increase d_1, we notice that the corner modes smear out and mix with bulk for large d_1.

Modified corner

We modify the corner by rotating the sample, and we notice that a small change in orientation can split up these modes as shown in Fig. D.12. We also tried to modify the corner conditions by changing the slope of lower edges but keeping the rotation angle $\theta = 0$. This kind of change results in corner angle different than $\pi/4$, and below we show how the splitting of Majorana corner modes is affected by this change.

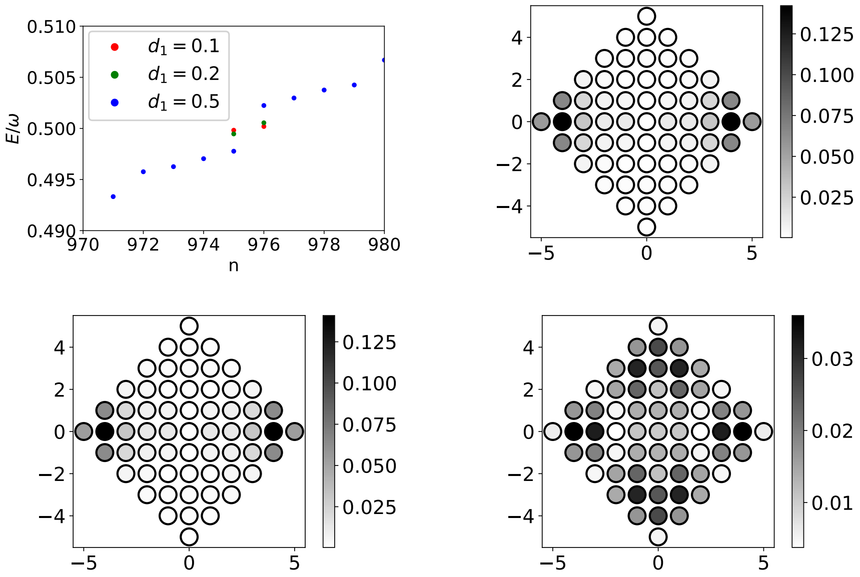

Figure D.8: Spectra around $\omega/2$ for three different values of d_1 and corner modes associated with these states for sample size L=6. As d_1 increases, the corner modes start to mix with the bulk states.

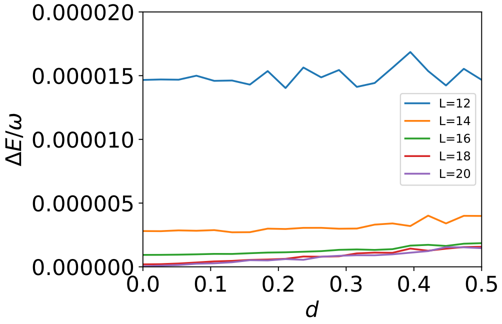

Figure D.9: Splitting of Majorana corner modes at quasi-energy $\omega/2$ as a function of disorder strength for different sample size obtained by averaging over 50 disorder realizations. Here, size (L) is the length of each side of square shaped system.

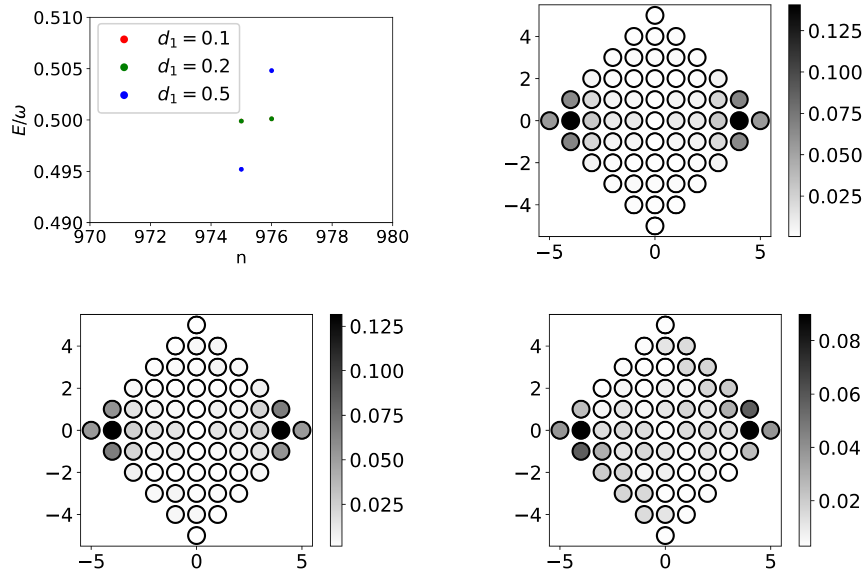

Figure D.10: Spectra around $\omega/2$ for three different values of d_1 and corner modes associated with these states for sample size, $L = 6$ As d_1 increases, the corner modes start to mix with the bulk states. It is worth noticing that this splitting is much smaller than the separation between zero modes and the bulk modes which is roughly equal to 0.02ω.

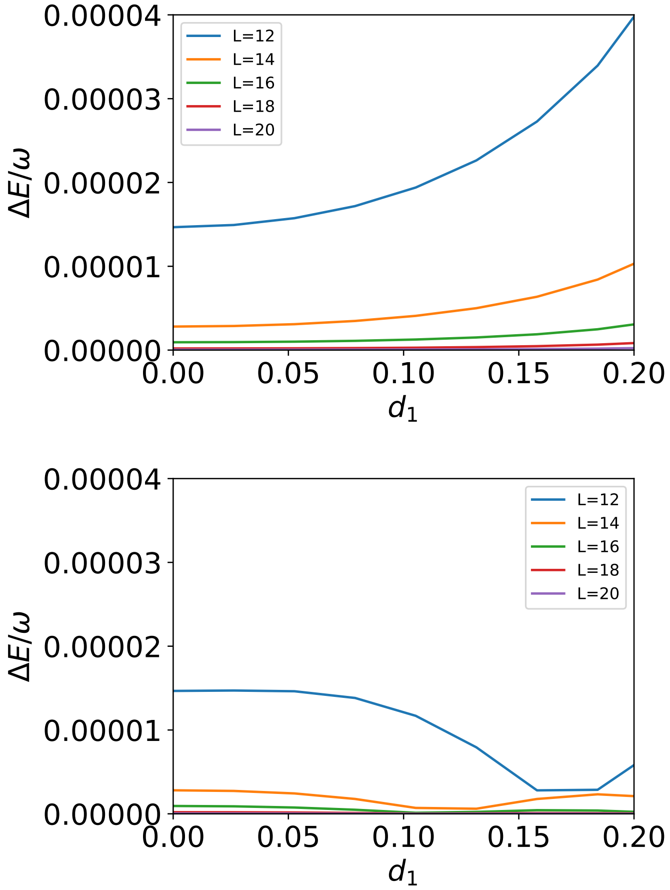

Figure D.11: Splitting of corner modes at quasi-energy $\omega/2$ as a function of perturbation strength d_1 for Hamiltonians in Eq. D.26 and Eq. D.27, respectively, for different lengths of sample.

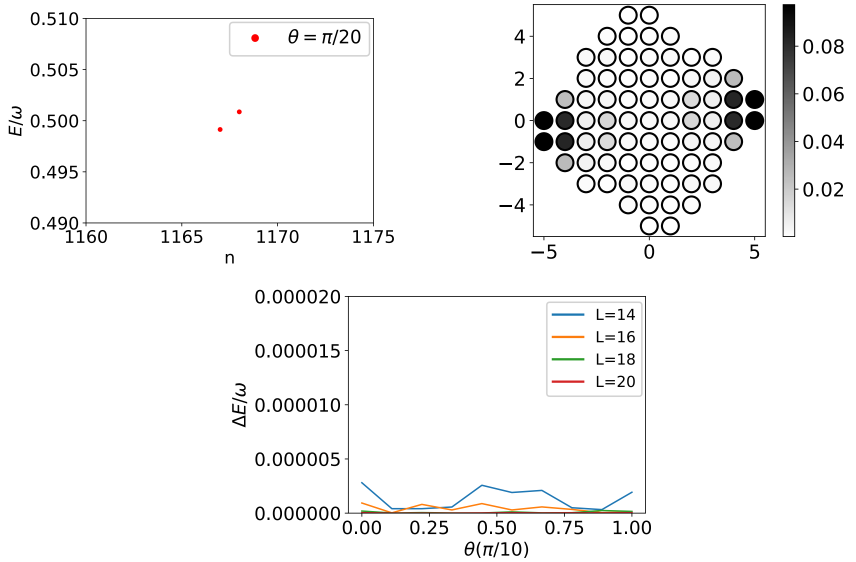

Figure D.12: Spectra around $\omega/2$ for a sample rotated by angle θ about y axis. We notice that a change in orientation results in splitting of corner modes, and the system can exhibit corner states for small values of θ. Last figure shows how the splitting of Majorana modes is affected by the rotation angle θ for different lengths of sample.

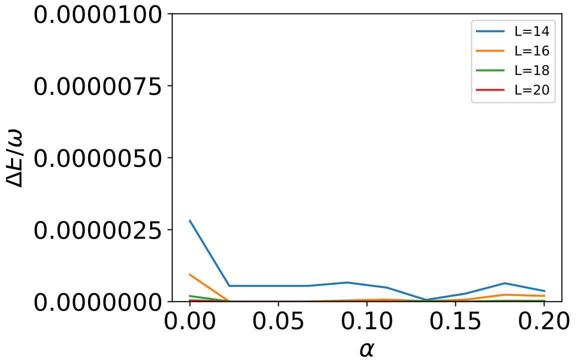

Figure D.13: Spectra around $\omega/2$ for a sample where the upper two edges have slope equal to unity but lower two edges have slope equal to $1-\alpha$. We notice that a change in slope for the lower edges results in splitting of corner modes, and the system can exhibit corner states for small values of θ. Last figure shows how the splitting of Majorana modes is affected by the rotation angle θ for different lengths of sample.

Chapter 8

ORBITAL FLOQUET ENGINEERING OF EXCHANGE INTERACTIONS IN MAGNETIC MATERIALS

“Perhaps there is more sense in our nonsense and more nonsense in our ‘sense’ than we would care to believe.” – David Bohm

In this chapter, we present a new scheme to control the spin exchange interactions by manipulating the orbital degrees of freedom using a periodic drive. We discuss two different protocols for orbital Floquet engineering. In one case, a periodic drive modifies the properties of the ligand orbitals which mediate magnetic interactions between transition metal ions. In the other case, we consider drive-induced mixing of d orbitals on each magnetic ion. We first find that AC Stark shift of orbitals induces a change comparable to that induced from photo-induced hopping schemes, but expands the applicable frequency ranges. Next, we find that radiatively induced coherent vibrations provide a realistic path for Floquet orbital engineering with short pulses of electric fields weaker than $0.5V/\text{Å}$ producing 5-10% changes in the magnetic coupling of Mott insulators such as the rare-earth titanates.

This chapter is based on following reference:

Swati Chaudhary, David Hsieh, and Gil Refael. “Orbital Floquet engineering of exchange interactions in magnetic materials.” Phys. Rev. B **100**, 220403 (2019).

8.1 Introduction

Periodic drive is emerging as an intriguing tool for controling and manipulating quantum many-body systems. Floquet engineering has been invoked in contexts ranging from the generation of artificial gauge fields to realization of many-body localization [90, 255, 178, 147, 208, 111, 351, 93, 16, 93, 97, 180, 122, 135, 131, 24, 112, 139, 148, 236, 366, 275, 291, 340, 347, 29, 202, 390, 301, 156, 85, 263, 133, 272, 350, 146, 339, 400, 58, 103, 252, 94, 387, 39, 83, 95, 388] with ultracold atoms in optical lattices. These methods can potentially provide an external control knob for material properties, and can be naturally applied to controlling quantum materials [21, 256].

Recent works [228, 230, 229, 40, 211, 137, 20, 92] discussed using Floquet engineering to manipulate magnetic exchange interactions. These schemes relied on properties of the photo-assisted hopping and become effective only for electric field well above $E \approx 1V/\text{Å}$. They feature a renormalized electronic hopping, and, therefore, a renormalized energy splittings in the effective Floquet Hamiltonian. These works assume direct hopping between two magnetic ions, and we refer to them as photo-modified direct hopping scheme henceforth.

In transition metal (TM) compounds, ligand ions are crucial for spin exchange processes. For example, in 2D transition metal trichalcogenides (TMTCs), the magnetic interactions are mainly mediated by ligand ions through multiple spin exchange channels. The orbitals of these ligand ions provide extra degrees of freedom that can be manipulated to modify the exchange interactions. The magnetic coupling induced via ligand ions depends on the electronic energy and the shape of the orbitals available for spin exchange on the ligands, as well as on the strong orbital-spin interplay of the TM ions [113, 171, 170, 353, 190, 331]. Many previous works have successfully manipulated some orbital properties using strain [268] and heterostructuring [274, 86].

In this work, we propose a novel scheme to modify the exchange interactions by manipulating the orbital degrees of freedom with a periodic drive. Particularly, we consider changes in the hybridization and energy of the levels involved in exchange processes. We use two toy models where a strong time-dependent electric field couples two orbitals, either of the ligand ion or of the TM ion. While these two approaches which concentrate on direct radiative effect serve to develop our ideas, we find that realizing the metal-orbital manipulation scheme with radiatively-induced phonons achieves significant improvements. It can be implemented by using an ultrashort mid infrared laser pulse, as opposed to a continuous wave in other schemes. Furthermore, this scheme extends the target frequency window to range from 100meV to 10eV, and in certain cases, a significant change can be observed at $E \approx 0.5V/\text{Å}$.

8.2 Floquet engineering with ligand orbitals

The spin-exchange interactions between two metal ions (M) are typically mediated by non-magnetic intermediary ligand ions (X) as shown in Fig. 8.1. This superexchange occurs due to virtual hopping of electrons within the cluster M-X-M. Therefore, the exchange interactions also depend on the properties of the non-magnetic ions' orbitals, and can be controlled by manipulating the properties of the relevant ligand orbitals.

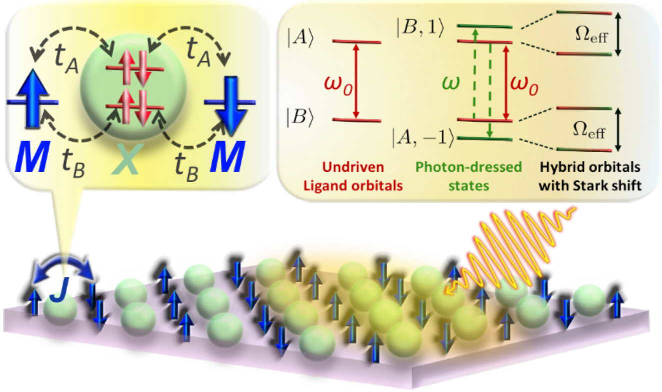

Figure 8.1: Floquet engineering of spin exchange interactions using ligand orbitals: Spin exchange interactions are typically mediated by non-magnetic ligand ions. Left Panel: Virtual hopping of electrons from one magnetic ion (M) to another via two orbitals (A and B) of the ligand ion (X). The magnetic coupling strength depends on the hopping parameter and the energy of the orbitals involved in this hopping process. Right Panel: In the presence of a periodic drive, these orbitals are replaced by hybridized photon-dressed orbitals ("Floquet replicas shown in green"). This splits the exchange channels and shifts the energies of virtual excitations, which modifies the exchange interactions.

The effect of dynamically-coupled ligand orbitals on the spin-exchange interactions follows from the Autler-Townes (AT) effect [14], where a periodic drive splits absorbtion peaks by changing the energy of the excited states. Similarly, ligand-orbitals-mixing changes the energy and hybridization of virtual excitations. These, in turn, alter the exchange interactions mediated by the ligand atoms. Consider a simple toy model with two metal ions, each with one spin, and a ligand ion with two filled orbitals, which give rise to AF interaction between metal-ions spins. Without drive, the Hamiltonian includes hopping between ligand orbitals (subscript α) and metal sites (subscript i), metal ion on-site spin interactions, and the energy of the ligand orbitals. It is given by:

$$H_1 = H_0 + H_t = \sum_{\alpha=A,B} \sum_{\sigma} E_\alpha n_{\alpha\sigma} + U \sum_i n_{i\uparrow} n_{i\downarrow} + H_t, \tag{8.1}$$

and H_t, the metal-sites to ligand orbitals hopping, is:

$$H_t = -\sum_i \sum_\alpha t_\alpha c^\dagger_{\alpha\sigma} c_{i\sigma} + \text{h.c} \tag{8.2}$$

with $|t_\alpha| \ll |E_\alpha|, U$. Assuming completely filled ligand orbitals, and a single spin per metal site on average, to find the exchange energy, we need fourth-order perturbation theory involving all possible exchange pathways (e.g., see Fig. (1) of the App. E). The magnetic coupling (J_{ex}) up to fourth-order is:

$$\begin{aligned} J_{\text{ex}} = 4 \sum_{\alpha=A,B} t_\alpha^4 \left(\frac{1}{\Delta_\alpha^2 U} + \frac{1}{\Delta_\alpha^3} \right) + \frac{8t_A^2 t_B^2}{\Delta_A \Delta_B U} \\ + 4t_A^2 t_B^2 \left(\frac{1}{\Delta_A \Delta_B \Delta_{AB}} + \frac{1}{\Delta_A^2 \Delta_{AB}} + \frac{1}{\Delta_B^2 \Delta_{AB}} \right), \end{aligned} \tag{8.3}$$

where, $\Delta_\alpha = U - E_\alpha$ is the charge transfer gap and $\Delta_{AB} = (\Delta_A + \Delta_B)/2$. In Mott insulators, $\Delta_\alpha \gg U$, and thus the exchange interactions reduces to:

$$J_{\text{ex}} \approx 4\frac{t_{\text{eff}}^2}{U}, \tag{8.4}$$

with $t_{\text{eff}} = \sum\limits_{\alpha} \frac{t_\alpha^2}{\Delta_\alpha}$ the effective metal-ion - ligand hopping.

Next, consider a drive coupling two ligand-ion orbitals:

$$H(t) = \Omega e^{-i\omega t} c_{A\sigma}^\dagger c_{B\sigma} + \Omega^* e^{i\omega t} c_{B\sigma}^\dagger c_{A\sigma}. \tag{8.5}$$

An oscillating electric field $\mathbf{E}(t)$, e.g., could couple orbitals A and B with strength $\Omega = \mathbf{E} \cdot \mathbf{P}/2$, where $\mathbf{P} = e \langle A|\mathbf{r}|B \rangle$. This would modify orbitals involved in the spin exchange (Fig. 8.1), and thus change the energies of virtual excitations, as well as increase their number (while their weights still sum up to the same value as the undriven case, see App. E).

The complete Hamiltonian, $H = H_0 + H_t + H(t)$, can be analyzed using an extended Floquet basis, i.e, the tensor product of the electronic states and the harmonic ('photon') number, n. We treat the hopping part, H_t, perturbatively, with eigenstates of the Floquet Hamiltonian describing $H_0 + H(t)$ as virtual excitations. We choose drive parameters such thateffective-spin Hamiltonian picture remains valid. The periodic drive in Eq. (E.13) mixes the ligand orbitals A and B, and the virtual excitations now involve:

$$\begin{aligned} |P, n\rangle &= \cos\frac{\theta}{2} |A, n\rangle + \sin\frac{\theta}{2} |B, n+1\rangle, \\ |M, n\rangle &= \sin\frac{\theta}{2} |A, n\rangle - \cos\frac{\theta}{2} |B, n+1\rangle, \end{aligned} \tag{8.6}$$

where $\cos\theta = \frac{\delta}{\sqrt{\delta^2+4\Omega^2}}$, $\sin\theta = -\frac{2\Omega}{\sqrt{\delta^2+4\Omega^2}}$, $\delta = \omega - \omega_0$ is the detuning, n denotes the photon index, and $\omega_0 = E_B$-E_A is the energy difference between two ligand orbitals. The drive-modified magnetic-coupling strength again emerges from fourth-order perturbation theory or numerical diagonalization of the Floquet Hamiltonian

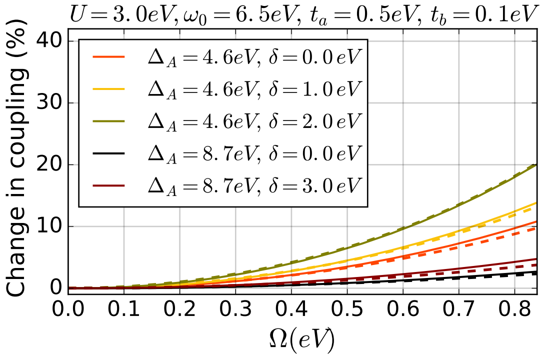

Figure 8.2: Change in magnetic coupling vs. drive strength Ω from numerics (solid lines) and theory (dashed lines) where the periodic drive mixes two orbitals of the ligand ion. The effect of the drive is large when the effective Rabi frequency is comparable to the charge transfer gap Δ_A. These parameters were chosen according to the typical values of interaction energy U and hopping parameter for TMTCs.

(truncated to include 4 Floquet zones). The expression for the new magnetic coupling J_{ex} is similar to that in Eq. (E.5), with orbitals A and B replaced by their hybrid counterparts $|P, n\rangle$ and $|M, n\rangle$ (see App. E. How much J_{ex} is modified is shown in Fig. 8.2. The exchange interactions depends mainly on Ω/Δ_{Ai} and δ/Δ_{Ai}. The energy and number of virtual excitations change due to the splitting os spin-exchange channels into different Floquet sectors (right panel of Fig. 8.1). Significant changes in the coupling strength require a Rabi splitting Ω_{eff} between two states in each Floquet sector of the same order as the charge transfer gap Δ_{Ai}. The hopping amplitudes and the energy of these virtual levels now depend on detuning δ. A large detuning brings some virtual excitation levels close to the d orbitals, which amplifies the effect (see App. E).

As shown in Fig. 8.2, significant magnetic-coupling changes occur only if the shift in energy of virtual-excitations levels is comparable to the charge-transfer gap. Usually, the charge transfer gap $\Delta_{Ai} \approx$ 5-10eV, and thus a change of 5-10%, requires $\Omega \approx$ 1eV. A common ligand is Sulphur, with accessible $3s$ and $3p$ orbitals. The energy difference between the two orbitals is $\omega_0 \approx$ 10eV [276], and the dipole moment matrix element is $|\mathbf{P}| \approx 0.6e$Å (see App. E), and thus we need $E \approx$ 2V/Å to get a $\Delta J/J \approx$ 10%. Materials with small charge transfer gap, large dipole moment matrix element, and small energy gap (ω_0) are ideal candidates for this scheme to work at lower electric field. This charge transfer gap is usually lower for heavier transition metal ions and decreases down the chalcogen group, which indicates that the materials with TM ion Mn, Ni, or Cu, and ligand S or Se would be the

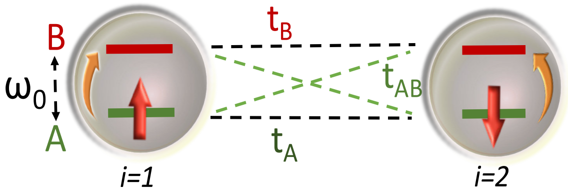

Figure 8.3: Metal orbital Floquet Engineering : A two-site Fermi-Hubbard model with two orbitals on each site at quarter filling. Two orbitals denoted by A and B with energy E_A, and $E_A + \omega_0$ are mixed using a periodic drive given in Eq. (8.11). For simplicity, we assume direct hopping between the metal ions.

best candidates. However, a very high frequency is necessary as the s-p energy separation is high, and for common ligands like O and S it is above $10eV$, which makes it somewhat impractical.

8.3 Floquet engineering with metal ion orbitals

. The high frequency requirement above goes away if we focus on metal orbitals. Above, we assumed only a single orbital for each TM ion. Magnetism in TM's, however, is significantly affected by the occupancy of other d orbitals, crystal field splitting, and the on-site interactions. The d-orbital energies are usually split by the crystal-field, yielding energy gaps from a few meVs to almost 1eV. A periodic drive can also modify these orbitals, and result in an AC Stark shift of both singly- and doubly-occupied sectors. Since the virtual excitations involve the Floquet orbitals, the magnetic coupling changes as long as the Stark shift is different for the low-energy and virtually excited states (see App. E). The effect of orbital mixing can be studied with a toy model where magnetic interactions arise from direct hopping between two TM ions. We consider a two-site Fermi-Hubbard model with two orbitals on each site and at quarter filling, and a periodic drive which couples the two levels on each site. Consider the Hamiltonian:

$$H = H_t + H_k + H_0, \tag{8.7}$$

where H_t is hopping term given by:

$$H_t = -\sum_{\sigma,\alpha=A,B} t_\alpha c^\dagger_{1\alpha\sigma} c_{2\alpha\sigma} - t_{AB} \sum_{\sigma,i\neq j} c^\dagger_{1A\sigma} c_{2B\sigma} + \text{h.c}, \tag{8.8}$$

H_k is the on-site Kanamori interaction [162],

$$H_k = U \sum_{i,\alpha} \hat{n}_{i\alpha\uparrow}\hat{n}_{i\alpha\downarrow} + U_1 \sum_{i,\alpha<\beta,\sigma,\sigma'} \hat{n}_{i\alpha\sigma}\hat{n}_{i\beta\sigma'} - J_H \sum_{i,\alpha<\beta,\sigma,\sigma'} c^\dagger_{i\alpha\sigma} c_{i\alpha\sigma'} c^\dagger_{i\beta\sigma'} c_{i\beta\sigma}, \tag{8.9}$$

and the on-site energy

$$H_0 = \sum_i E_A(\hat{n}_{iA} - 1) + (E_A + \omega_0)\hat{n}_{iB} \tag{8.10}$$

with U, $U_1 \gg t_\alpha$. At quarter filling, if $\omega_0 \gg \frac{t_\alpha^2}{U}$, then the low-energy subspace consists of states with one spin in each A orbital, and the magnetic coupling is approximately $J_{ex} = 4t_A^2/U$. On the other hand, if $\omega_0 = 0$ and $t_{ab} = 0$, the ground state is FM in spin but AFM in the orbital degree of freedom. We focus on the first scenario, which allows us to mix two orbitals by applying a periodic drive of the form:

$$H(t) = \sum_{i,\sigma}(\Omega e^{i\omega t} c^\dagger_{iA\sigma} c_{iB\sigma} + \Omega^* e^{-i\omega t} c^\dagger_{iB\sigma} c_{iA\sigma}). \tag{8.11}$$

Let us next focus on the Floquet eigenstates connected to the low energy subspace of the undriven Hamiltonian, and where the effective spin picture is valid. We then calculate the spin-exchange interactions from the singlet-triplet energy splitting (details in App. E). As in Fig. 8.4, the magnetic-coupling strength strongly depends on the drive's frequency and strength. It is mainly the hybridization between A and B orbitals which affects the change. This hybridization depends on $\frac{\Omega}{\delta}$ and allows virtual excitation to states at energy $U_1 + J$ in the doubly-occupied sector. This contribution decreases as the detuning δ increases. A large detuning also lowers the energy of the virtual excitation state at $U_1 + J_H$ in the doubly occupied sector, but this is negligible compared to hybridization effect as long as $|U_1 + J_H - U| \gg \delta$. The magnetic properties in this scheme are controlled by the ratios $\frac{\Omega}{\delta}$, $\frac{U_1+J_H}{U}$, and $\frac{t_b}{t_a}$.

This scheme requires magnetic materials where TM ions have d^1 configuration. In transition-metal compounds with octahedral or tetrahedral ligand cages, d orbitals split into e_g and t_{2g} levels with crystal-field splitting parameter in the range of 0.3 eV to 1.5 eV. The periodic drive can be realized with an AC electric field which couples these d orbitals. Therefore, the drive amplitude is $\Omega = e\langle\psi_A|\mathbf{E}\cdot\mathbf{r}|\psi_B\rangle/2$. Only d orbitals are involved in this transition, however, and dipole transitions between same-parity orbitals are forbidden. Nevertheless, the crystal field can induce d-p mixing in non-centrosymmetric compounds, which lends some p character to otherwise pure d orbitals, and allows weak dipole transitions. For some tetrahedral complexes, this mixing is 1-5% [18], and thus the matrix element $|\langle d_i|\mathbf{r}|d_j\rangle| \approx 0.05$eÅ which corresponds to a drive strength $\Omega \approx 0.02eV$ at $E = 1V/$Å. Although there are materials with tetrahedral ligand arrangement [12], currently we are not

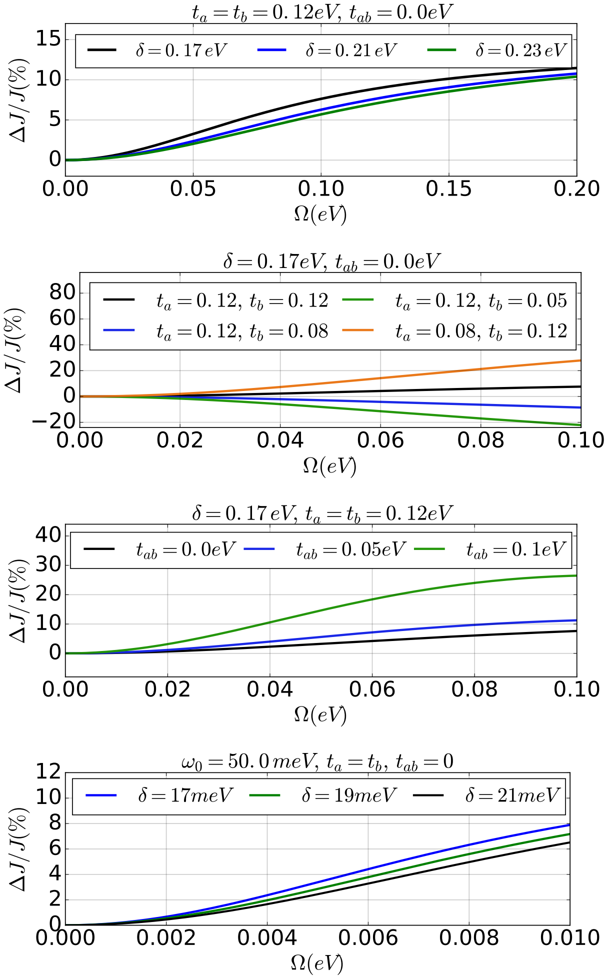

Figure 8.4: Effect of different parameters on the change in magnetic coupling strength as a function of drive amplitude Ω for $U = 4.0eV$, $J_H = 0.8eV$, $U_1 = U - 2J_H$, and $\omega_0 = 0.91eV$ when not specified. These changes are large when the detuning is decreased. The second panel shows that large imbalance between t_a and t_b makes these changes more prominent. Similarly, we also observe that large t_{ab} results in larger changes, and the change is proportional to Ω/δ when $t_a = t_b$. In the last panel, we show the changes for a very small ω_0 and small detuning where a significant change can be seen at extremely small drive amplitudes which is the case for a phonon drive.

aware of any such magnetic materials where the TM ion with d^1 configuration is surrounded by a tetrahedral cage of ligand ions. Nevertheless, in octahedral geometry, some mechanisms like coupling with vibrational modes, and mixing with ligand p orbitals [247, 204, 18, 17] allow these d-d transitions. This d-p mixing can be estimated from the oscillator strength of d-d transitions in octahedral complexes (Table I of Ref.[204]), and it is roughly 0.1%. This corresponds to a d-d electric dipole moment matrix element, $P = e\left|\left\langle d_{t_{2g}}\middle|\mathbf{r}\middle|d_{t_{e_g}}\right\rangle\right| \approx 0.01\text{eÅ}$, and thus the drive strength, $\Omega \approx 0.005\text{eV}$ for $E = 1V/\text{Å}$.

The metal-orbital-hybridization scheme requires mixing the relevant two d orbitals with light. In addition to the dipole transition, such mixing can also be achieved by employing two-photon processes. For a two-photon process between two $3d$ orbitals, the drive amplitude, $\Omega \approx e^2E^2P_{dd}$, where $P_{dd} \approx \frac{1}{2}\frac{|\langle 3d|\mathbf{r}|4p\rangle/2|^2}{E_{4p}-E_{3d}} \approx 10^{-3}\text{Å}^2/\text{eV}$, and thus $\Omega \approx 10^{-3}\text{eV}$ for electric field, $E \approx 1\text{V/Å}$.

The applicability of Floquet orbital engineering, however, becomes much broader by employing direct vibrational coupling between the metal-ions d levels. Contrary to the above hard-to-realize schemes, using coherent lattice vibrations to achieve a similar hybridization between two d orbitals appears experimentally accessible. In perfect octahedral symmetry, the direct vibrational coupling between some d orbitals can occur for those Raman active modes which involve metal-ligand bond rotation. With typical phonons frequency of such modes in the range 50-100meV, it might be applied to materials with d orbital energy splitting in the same range. This scheme can be used in some rare-earth titanates (RTiO$_3$), where even t_{2g} bands are non-degenerate with a crystal-field splitting $\Delta_{\text{CF}} \approx$ 30-400meV [325], and some phonon modes (e.g. $A_g(2), A_g(4), B_{1g}(3), B_{1g}(4), B_{2g}(4)$) which involve bond rotations have frequencies in the range 10-100meV [144, 143]. In this scheme, the drive strength is $\Omega \approx 0.25u_0\text{eV}$ (Sec. V of App. E) where u_0 is the phonon-induced lattice displacement in Å.

How lattice displacement, u_0 depends on the electric field amplitude, E, depends on different material properties and the details of the drive [160]. Here, we consider the indirect excitation of Raman modes in the impulsive limit which relies on large nonlinear coupling with some infrared (IR) active modes [335, 124]. In these schemes, a phonon amplitude of approximately 0.03Å can be achieved by using a few-femtosecond mid IR laser pulse with maximum electric field amplitude $E \approx 0.5\text{V/Å}$ if the non-linear coupling between two modes is sufficiently large as is the case for Raman mode $A_g(25)$ and IR mode $B_{1u}(54)$ in some Mott insulating titanates [335, 124] (more details in App. E Sec. VI). This corresponds to a change of magnetic coupling by 5-10%. For some materials like bismuth ferrites ($BiFeO_3$), the effect could even be more staggering, and combining Raman mode excitation schemes can lead to displacements of 0.05Å at $E < 0.1V/Å$ [160]. Such strong effects could arise in some $RTiO_3$, but finding appropriate materials would require first-principle calculations which are beyond our scope.

The coherent phonon scheme also offers the advantage of using ultrashort laser pulses. Short laser pulses (e.g., $50fs$) could produce lattice vibrations that persist for over $10ps$. This lowers the required fluence further as compared to other schemes where a laser with electric field amplitude $E \approx 1V/Å$ must be kept on for the entire duration of the measurement.

8.4 Conclusions

We proposed a new protocol for controlling the magnetic properties of materials through Floquet engineering of their orbital degrees of freedom. While previous works [228, 230, 229, 40, 211, 137], concentrated on spin-exchange interactions change due to photo-assisted hopping, we explore the effects of drive-induced modifications of the orbitals involved in the virtual processes involved in the exchange process.

We first developed our ideas by considering AC Stark shift of excited levels in ligand orbitals as well as in the magnetic metal ions. Disappointingly, the AC Stark schemes yield significant changes with electric field amplitudes similar to those needed for the photo-modified direct hopping schemes, $E \approx$ 1-5eV/Å and require a continuous laser input. The frequency ranges of these various methods, however, are different. The ligand scheme needs $\omega \approx$ 5-10eV while the photo-modified direct hopping works well for $\omega \approx$ 0.5-2eV.

Orbital Floquet engineering using phonons, however, emerges as a very promising magnetic control scheme. Using short light pulses to induce coherent lattice vibrations can modify the magnetic metal-ion orbitals, and thereby change magnetic couplings by 5-10% at much smaller frequencies ($\omega \approx$ 0.1eV), and fields $E \approx$ 0.5V/Å, an order of magnitude smaller than the amplitudes required for other schemes, and without the need for a continuous wave beam. Note that previous studies considered the phonon-induced magnetic coupling effects due to the shift in the atomic equilibrium position [124]. Also, Refs. [20, 92] studied the effect of orbital properties in photo-assisted hopping scheme. We expanded both of these perspectives by considering orbital hybridization, and showed that controlling the orbital degrees of freedom with light opens up new possibilities for the manipulation of correlated quantum materials, and brings the quest for drive-controlled magnetism much closer to experimental realization.

APPENDIX

E.1 Review : Toy model for AFM coupling renormalization due to photo-modified direct hopping

We briefly review the effect of a periodic drive on the exchange interactions using the periodically driven Fermi Hubbard model (FHM) in Mott regime at half-filling. In the presence of a time-dependent electric field, the full Hamiltonian of the Fermi-Hubbard model is given by:

$$H = -t \sum_{<i,j>} c^{\dagger}_{i\sigma} c_{j\sigma} + \text{h.c} + U \sum_{i} n_{i\uparrow} n_{i\downarrow} + \mathbf{E} \cdot \sum_{\mathbf{i},\sigma} n_{i\sigma} \mathbf{r_j} \cos(\omega \mathbf{t}). \tag{E.1}$$

After Peierls substitution, it becomes:

$$H' = -t \sum_{<i,j>} e^{i\left[\frac{\mathbf{E}\cdot(\mathbf{r_j}-\mathbf{r_i})}{\omega} \sin(\omega t)\right]} c^{\dagger}_{i\sigma} c_{j\sigma} + \text{h.c} + H_U = H'_t + H_U. \tag{E.2}$$

In the limit $U \gg t$, and for a non-resonant drive, the exchange coupling is given by:

$$J'_i = J_i U \sum_{n=-\infty}^{\infty} \frac{1}{U + n\omega} \mathcal{J}_n(\zeta_i)^2, \tag{E.3}$$

where, $J_i = \frac{4t^2}{U}$ is the magnetic coupling strength for the undriven case, $\mathcal{J}_n$ denotes n^{th} order Bessel function, and drive parameter

$$\zeta_i = \frac{\mathbf{E} \cdot (\mathbf{r}_j - \mathbf{r}_i)}{\omega}. \tag{E.4}$$

In the presence of this periodic drive, the spin exchange interactions are affected mainly due to two factors: (a) change in the hopping parameter due to photon-assisted tunneling, and (b) virtual excitations between different Floquet sectors as shown in Fig. 3 of Ref. [229]. As a result, the effective spin exchange interactions can be controlled by changing the frequency, polarization and intensity of the laser. Previous works [228, 230, 229, 40, 211, 137] have studied the periodically driven FHM extensively for both resonant and off-resonant cases. The above expression in Eq. (9.3) is valid only for a non-resonant drive where doublon sectors are well separated in energy from the single occupation sector. Resonant drive can be handled using a somewhat similar machinery of Floquet formalism as shown in Ref. [40]. For a near resonant drive, real doublon-holon pairs can significantly affect the exchange interactions and its effects are discussed in great details in Ref. [211].

E.2 AFM exchange via two orbitals of the same ligand ion in the presence of a periodic drive

When the hopping between two metal sites is allowed via two orbitals of the ligand ion, spin exchange energy for undriven case is given by :

$$\begin{aligned} J_{ex} = 4 \sum_{\alpha=A,B} t_\alpha^4 \left(\frac{1}{\Delta_{\alpha i}^2 U} + \frac{1}{\Delta_{\alpha i}^3} \right) + \frac{8 t_A^2 t_B^2}{\Delta_{Ai} \Delta_{Bi} U} \\ + 4 t_A^2 t_B^2 \left(\frac{1}{\Delta_{Ai} \Delta_{Bi} \Delta_{ABi}} + \frac{1}{\Delta_{Ai}^2 \Delta_{ABi}} + \frac{1}{\Delta_{Bi}^2 \Delta_{ABi}} \right), \end{aligned} \tag{E.5}$$

where, $\Delta_{\alpha i} = U - E_\alpha$ is the charge transfer gap, and $\Delta_{ABi} = (\Delta_{Ai} + \Delta_{Bi})/2$. This expression was obtained by applying fourth order perturbation theory to the following Hamiltonian:

$$\begin{aligned} H_1 = H_0 + H_t = \sum_{\alpha=A,B} \sum_\sigma E_\alpha n_{\alpha\sigma} + U \sum_{i=1,2} n_{i\uparrow} n_{i\downarrow} \\ - \sum_{i=1,2} \sum_\alpha t_\alpha c_{\alpha\sigma}^\dagger c_{i\sigma} + \text{h.c} \end{aligned} \tag{E.6}$$

where $\alpha = A, B$ are two orbitals of the ligand ion involved in the process of superexchange between the spins at two metal sites denoted by $i = 1, 2$ above, and the hopping parameter $t_{A/B} \ll U, |E_\alpha|$.

In this case, spin exchange energy is decided by the virtual excitations which lead to spin exchange between two sites, and thus depends on the number of orbitals available for the exchange process and the energy of these orbitals. There are multiple pathways available for these spin exchange processes. Two such exchange processes are shown in Fig. E.1, where we have shown the virtual excitations giving rise to the magnetic interactions between two metal ions. These virtual excitations involve the charge transfer from ligand orbitals to the magnetic ion. Their contribution to magnetic coupling depends on the energy difference between obitals and the on-site columbic repulsions. In the presence of a drive discussed in Sec. IV, these orbitals of the ligand ion are modified according to the drive amplitude and frequency. Now, we proceed in the same way as the undriven case, but the orbitals A and B are replaced by the hybrid orbitals:

$$\begin{aligned} P, n = \cos\frac{\theta}{2} A, n + \sin\frac{\theta}{2} B, n+1, \\ M, n = \sin\frac{\theta}{2} A, n - \cos\frac{\theta}{2} B, n+1, \end{aligned} \tag{E.7}$$

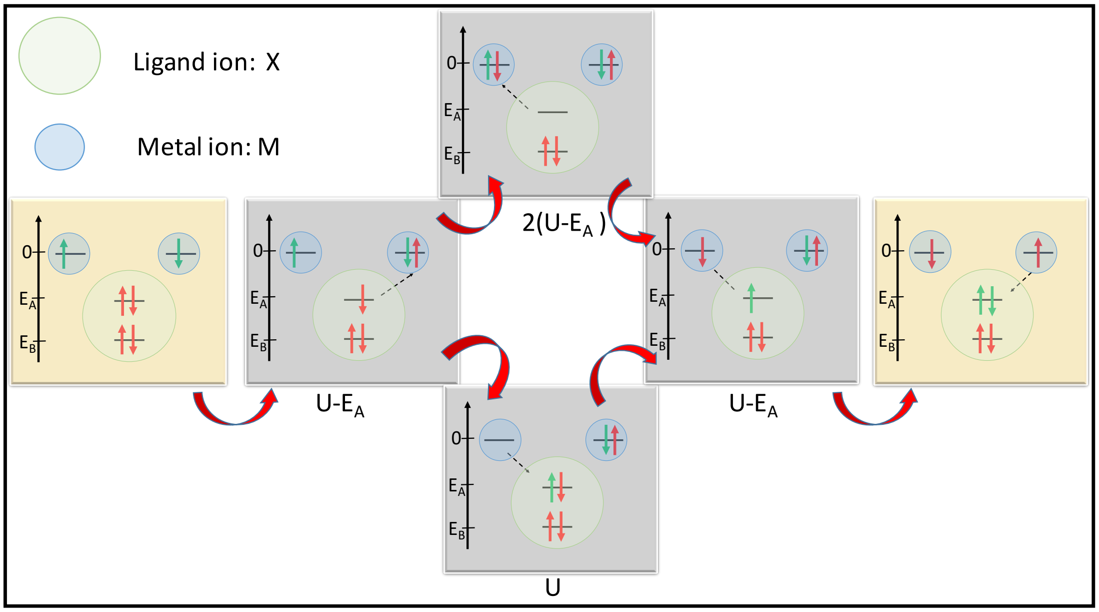

Figure E.1: Two possible spin exchange processes when the hopping between two metal sites is mediated via ligand orbitals. Gray panels show virtual intermediate states with their energies relative to the ground state with one spin on each metal site. Here, the ligand ion has two orbitals, and as a result there are many other channels available for spin exchange if the hopping between orbital B and metal sites is allowed.

where n denotes the Floquet index, $\cos\theta = \frac{\delta}{\sqrt{\delta^2+4\Omega^2}}$, $\sin\theta = -\frac{2\Omega}{\sqrt{\delta^2+4\Omega^2}}$, and $\delta = \omega - \omega_0$ is the detuning. If the parameter $eEa/\omega \ll 1$ (which is the case here, as $\omega \approx 10eV$ and $eEa \approx 1eV$), then the hopping is allowed between orbitals within the same photon sector only in the Floquet picture. Using this fact, we can calculate the hopping elements between metal sites, and the new orbitals can be expressed as:

$$t_P = \langle A, 0|P, 0\rangle\, t_A + \langle B, 0|P, 0\rangle\, t_B = \cos\frac{\theta}{2} t_A, \tag{E.8}$$

$$t_M = \langle A, 0|M, 0\rangle\, t_A + \langle B, 0|M, 0\rangle\, t_B = \sin\frac{\theta}{2} t_A. \tag{E.9}$$

Now, if $t_B \neq 0$, the hopping element between $|P/M, -1\rangle$ and metal sites can still be non-zero as:

$$\begin{aligned} P, -1 &= \cos\frac{\theta}{2} A, -1 + \sin\frac{\theta}{2} B, 0, \\ M, -1 &= \sin\frac{\theta}{2} A, -1 - \cos\frac{\theta}{2} B, 0, \end{aligned} \tag{E.10}$$

with

$$t_{P1} = \langle A, 0|P, -1\rangle\, t_A + \langle B, 0|P, -1\rangle\, t_B = \sin\frac{\theta}{2} t_B, \tag{E.11}$$

and

$$t_{M1} = \langle A, 0|M, -1\rangle\, t_A + \langle B, 0|M, -1\rangle\, t_B = -\cos\frac{\theta}{2} t_B. \tag{E.12}$$

As a result of the drive

$$H(t) = \Omega e^{-i\omega t} c^{\dagger}_{A\sigma} c_{B\sigma} + \Omega^* e^{i\omega t} c^{\dagger}_{B\sigma} c_{A\sigma}, \tag{E.13}$$

the magnetic coupling strength now has contributions from different exchange mechanisms which include virtual excitations via four states, i.e P, M, $P, -1$, $M, -1$ given by:

$$J_{ex} = E_0 + E_1 + E_2 \tag{E.14}$$

where

$$E_0 = \sum_{\alpha=P,M,P1,M1} \frac{4t_\alpha^4}{\Delta_\alpha^2}\left(\frac{1}{U} + \frac{1}{\Delta_\alpha}\right) \tag{E.15}$$

$$\begin{aligned} E_1 = \frac{1}{2}\sum_{\beta}\sum_{\alpha,\alpha\neq\beta} & \frac{8t_\alpha^2 t_\beta^2}{(\Delta_\alpha + \Delta_\beta)\Delta_\alpha\Delta_\beta} + \frac{4t_\alpha^2 t_\beta^2}{(\Delta_\alpha + \Delta_\beta)\Delta_\alpha^2} \\ & + \frac{4t_\alpha^2 t_\beta^2}{(\Delta_\alpha + \Delta_\beta)\Delta_\beta^2} + \frac{8t_\alpha^2 t_\beta^2}{U\Delta_\alpha\Delta_\beta}, \end{aligned} \tag{E.16}$$

and

$$\begin{aligned} E_2 = & \frac{8t_P t_{P1} t_M t_{M1}}{\Delta_{P1} U_{m1} \Delta_{M1}} + \frac{8t_P t_{P1} t_{M1} t_M}{\Delta_P U_1 \Delta_M} + \frac{4t_P t_{P1}^2 t_P}{\Delta_P U_1 \Delta_P} \\ & + \frac{4t_M t_{M1}^2 t_M}{\Delta_M U_1 \Delta_M} + \frac{4t_P^2 t_{P1}^2}{\Delta_{P1} U_{m1} \Delta_{P1}} + \frac{4t_M^2 t_{M1}^2}{\Delta_{M1} U_{m1} \Delta_{M1}}, \end{aligned} \tag{E.17}$$

where, $\Delta_\alpha = U - E_\alpha$, $U_1 = U + \omega$, $U_{m1} = U - \omega$ with

$$E_{P/M} = E_A + \frac{\delta}{2} \mp \sqrt{\left(\frac{\delta}{2}\right)^2 + \Omega^2}, \tag{E.18}$$

and

$$E_{P1/M1} = E_{P/M} - \omega \tag{E.19}$$

is the energy of Floquet states $|P/M, -1\rangle$. If we consider a very simple situation where $\Delta_A \gg U, \Delta_A >> \Delta_B, \delta = 0$, then in the undriven case, the magnetic coupling strength is $J_{ex} = 4\frac{t_A^4}{\Delta_A^2 U}$, and for the driven case, it is given by:

$$J_{ex} = \frac{4}{U}\left(\frac{t_P^2}{\Delta_A + \Omega} + \frac{t_M^2}{\Delta_A - \Omega}\right) \tag{E.20}$$

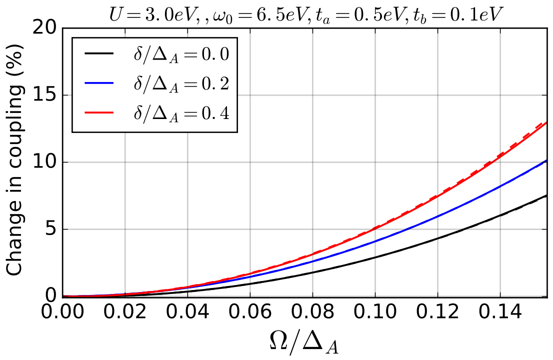

Figure E.2: Change in magnetic coupling as a function of Ω/Δ for ligand orbital scheme for different values of detuning δ. These changes occur mainly due to change in the virtual excitation energy which decreases as detuning increases. This decrease in virtual excitation energy enhances the exchange interactions and thus the change is larger for large detuning.

where now $t_P = t_M = t_A/\sqrt{2}$, and thus the change depends mainly on the ratio Ω/Δ_A. In order to understand the effect of detuning, let us consider a somewhat simple situation $t_b = 0$ and small drive strength. Now, the virtual excitation involves two states with energy $E_P \approx E_A + \delta + \frac{\Omega^2}{\delta}$ and $E_M \approx E_A - \frac{\Omega^2}{\delta}$ and the corresponding hopping amplitudes are $t_P = \frac{\Omega}{\delta}$ and $t_M = 1 - \frac{\Omega^2}{2\delta^2}$, respectively. In this case, large detuning δ brings the level E_P much closer to d orbitals in energy, and hence the virtual excitation energy is reduced as δ increases. Also, the detuning values are quite close to charge-transfer gap Δ, and thus the change in the magnetic coupling increases with large detuning. This picture was further verified by the numerical calculations as shown in Fig. E.2 where we plot the change in magnetic coupling strength as a function of Ω/Δ for different values of detuning δ.

E.3 Changes in AFM coupling due to orbital hybridization on each metal site

In the undriven model, the spin interactions arise due to virtual excitations between singly and doubly occupied sectors. For large U, the low energy subspace is described by an effective spin Hamiltonian. In the presence of a periodic drive which couples two orbital on each metal site, all the states in this subspaces undergo some changes. These changes are best studied using the Floquet formalism, where many singly occupied states now hybridize and the new levels are given by the eigenstates of Floquet Hamiltonian. Usually the hopping amplitudes are much smaller in comparison to other energy scales in the problem, and thus we treat the hopping part of the Hamiltonian as a perturbation to Floquet Hamiltonian obtained

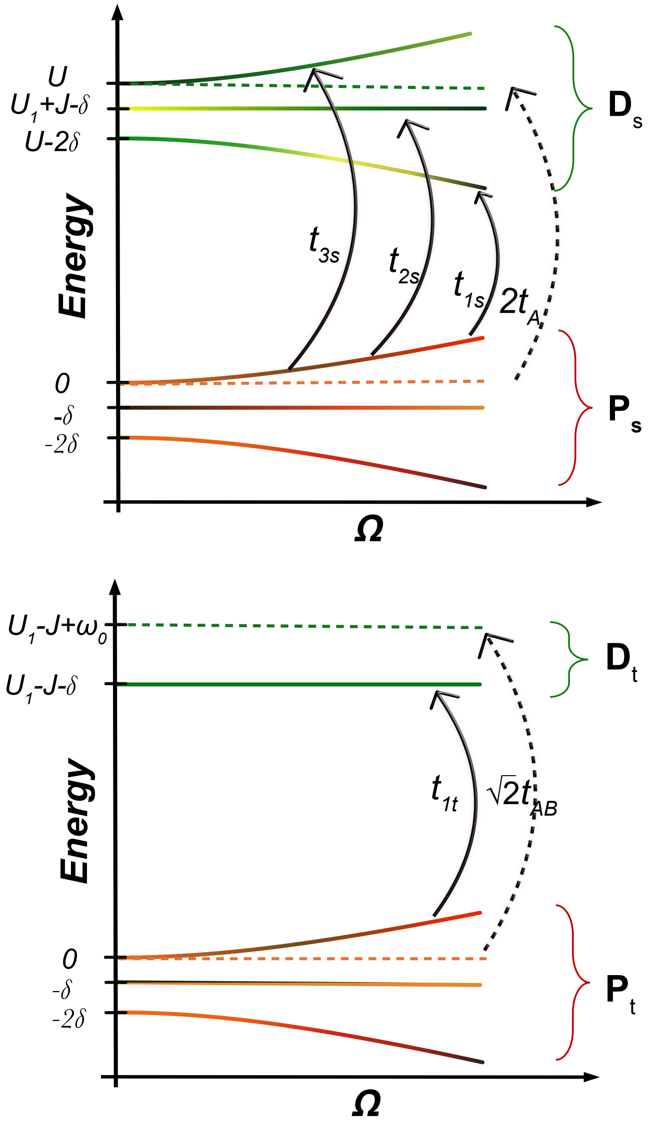

Figure E.3: This diagram shows the effect of the periodic drive on the energy levels of a two metal site and two orbital model discussed in Eq. E.21 and Eq. E.22. The lower levels shown in shades of red represent the states connected to the low energy subspace of the undriven model, and the lines in green show the states available for virtual excitations which belong to the doubly occupied sector. These excitations are shown by solid arrows for the driven model, and by the dashed arrow for the undriven case. For clarity, we show the excitations for the singlet (top) and triplet (bottom) sectors in different diagrams. Here the subspace P and D refers to the singly and doubly occupied states, respectively, and the subscript t/s denotes the singlet or triplet nature.

from $H_k + H_0 + H(t)$. The schematic of the changes in the energy levels of this Hamiltonian is shown in Fig. E.3 as a function of the drive amplitude for some of the eigenstates relevant for the exchange interactions.

For the undriven case, there is only one energy eigenstate available for virtual excitations to the doubly occupied sector as denoted by the dashed arrow in Fig. E.3. This virtual process lifts the degeneracy between singlet and triplet sectors resulting in a magnetic coupling strength $\frac{4t_A^2}{U}$. For the driven case, the low energy subspace is replaced by the eigenstates of the Rabi Hamiltonian:

$$H_{R_P} = \begin{bmatrix} 0 & \Omega\sqrt{2} & 0 \\ \Omega\sqrt{2} & -\delta & \Omega\sqrt{2} \\ 0 & \Omega\sqrt{2} & -2\delta \end{bmatrix} \tag{E.21}$$

with basis vectors given by $\left|P_{AA}^{s/t}, 0\right\rangle, \left|P_{AB}^{s/t}, -1\right\rangle, \left|P_{BB}^{s/t}, -2\right\rangle$ where P denotes the singly occupied sector with subscripts denoting the orbitals on each site, s/t refers to the singlet and triplet sectors, and the integers denote the photon number. For the singly occupied sector, the effects of drive are independent of the spin configuration. This drive also mixes the doubly occupied subspace for the singlet sector in a similar manner but in this case the energy levels are given by eigenstates of the following Hamiltonian:

$$H_{R_{D_s}} = \begin{bmatrix} U & \Omega\sqrt{2} & 0 \\ \Omega\sqrt{2} & U_1 + J - \delta & \Omega\sqrt{2} \\ 0 & \Omega\sqrt{2} & U - 2\delta \end{bmatrix} \tag{E.22}$$

which give rise to a different energy shift for the two sectors if $U_1 + J \neq U$. On the other hand, for the triplet sector, the doubly occupied subspace consists of is only one state at energy $U_1 - J - \delta$. In addition to the changes in the energy levels this drive also changes the eigenstates, and thus the hopping parameters are changed accordingly. The hopping processes in the presence of a periodic drive are shown by solid arrows in Fig. E.3.

In terms of these hopping amplitudes, the new magnetic coupling strength is given by:

$$E_s - E_t = \sum_{i=1}^{3} \frac{t_{is}^2}{E_{d_s}^i - E_{p_s}^1} - \sum_i \frac{t_{it}^2}{E_{d_t}^i - E_{p_t}^1} \tag{E.23}$$

where $E_{d_{s/t}}^i$ is the energy corresponding to the eigenstate $\left|D_{s/t}\right\rangle$ of Hamiltonian $H_{R_{D_{s/t}}}$ in Eq. E.22, and

$$t_{is/t} = \left\langle P_{s/t}^1 \middle| H_t \middle| D_{s/t}^i \right\rangle, \tag{E.24}$$

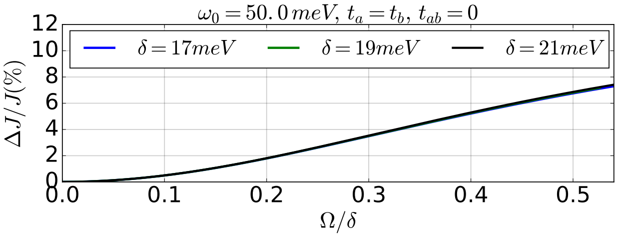

Figure E.4: Change in magnetic coupling as a function of Ω/δ for metal orbital scheme. For the special case where $t_{ab} = 0$, these changes depend on the hybridization between A and B orbitals which is a function of Ω/δ, and thus for a given drive strength Ω, the observed change is larger for small detuning.

where $\left|P^1_{s/t}\right\rangle$ is the eigenstate corresponding to the eigenvalue $\delta\left(1 - \sqrt{1 + 2\left(\frac{\Omega}{\delta}\right)^2}\right)$ of the Hamiltonian H_{R_P} for the singly occupied sector, and H_t is the hopping part given by:

$$H_t = -\sum_{\sigma,\alpha=A,B} t_\alpha c^\dagger_{1\alpha\sigma} c_{2\alpha\sigma} - t_{AB} \sum_{\sigma,i\neq j} c^\dagger_{1A\sigma} c_{2B\sigma} + \text{h.c.} \tag{E.25}$$

One of the most important contribution to exchange coupling comes from the virtual excitation to the eigenstate with energy $U_1 \pm J - \delta$. If we consider a simple scenario with $t_a = t_b$ and $t_{ab} = 0$, then the virtual hopping to $U_1 - J - \delta$ in the triplet sector, $t_{1t} = 0$, and for $U_1 + J - \delta$ in the singlet sector is given by $t_{2s} \approx \frac{\Omega}{\delta} t_b$ which decreases as the detuning δ increases. Although the detuning also affects the energy of the virtual excitation associated with $U_1 + J - \delta$, the change in exchange energy is dictated by $\frac{\Omega}{\delta}$ mainly as the change in δ is negligible in comparison to $U_1 + J = U - J$. This explains why the observed change decreases with increased detuning. It is also in good agreement with the numerical results shown in Fig. E.4 where we plotted the change in magnetic coupling as a function of Ω/δ. Furthermore, the presence of two orbitals can allow virtual processes even for the triplet sector which changes the energy of the FM state when $t_a \neq t_b$ or $t_{ab} \neq 0$.

E.4 Approximate values of dipole moment matrix element using Slater type orbitals

Dipole moment for ligand orbitals

The strength of the drive used in the orbital hybridization scheme depends on the value of the dipole moment operator between the two orbitals. Here, we have used Slater type orbitals [319] to calculate these dipole moments. The wavefunction of these orbitals is given by:

$$\left|\Psi_{n,l,m}(\mathbf{r})\right\rangle = R_n(r)Y_l^m(\mathbf{r}), \tag{E.26}$$

where

$$R_n(r) = (2\zeta)^n\sqrt{\frac{2\zeta}{(2n)!}}r^{n-1}e^{-\zeta r}, \tag{E.27}$$

with $\zeta = \frac{Z^*}{n}$ and Z^* is the effective charge which can be calculated using Slater's rules when distances are expressed in atomic units (1 unit $=a_0$). Using these Slater type orbitals, we approximate the expectation value of the position operator for different ligand and transition metal orbitals as shown in Table E.1.

Dipole moment for *d*-*d* transitions

In addition to the dipole transitions between different parity orbitals in the ligand ion, we also studied the effects of on-site *d*-*d* transitions. Although for pure *d* orbitals these kinds of transitions are forbidden, but there are many different *d*-*p* mixing mechanisms available in transition metal compounds which allow these dipole transitions. In most of the transition metal compounds, e_g and t_{2g} orbitals are not purely of *d* character but has some contribution from *p* orbitals. These *p* orbitals can either belong to the same magnetic ion or to the ligand ion. In the absence of a center of symmetry, the t_{2g} orbitals can mix with *p* orbitals of the same ion. These *d* orbitals can also mix with the *p* orbitals of the ligand ion due to covalency efffects. This kind of mixing is allowed for both tetrahedral and octahedral crystal fields and is one of the most prominent mechanism for *d*-*p* mixing as indicated by the studies of the intensities of *d*-*d* observed in many transition metal compounds [247, 204, 18, 17]. In transition metal compounds, the outermost electrons reside in *d* orbitals and the covalent bonding between the metal and the ligand ion can result in *d*-*p* mixing, and hence modifying the wavefunction of *d* orbitals as follows:

$$\left|\psi'_{d_i}\right\rangle = \frac{1}{\sqrt{1+\alpha^2}}\left(\left|\psi_{d_i}\right\rangle + \alpha\left|\chi_p\right\rangle\right), \tag{E.28}$$

where χ denotes the orbitals of ligand ions and $\alpha \ll 1$ (check Ref. [336] for more details of *d*-*p* mixing). As a result, the dipole moment operator $e\left|\left\langle\psi'_{t_{2g}}|\mathbf{r}|\psi_{e_g}\right\rangle\right| \approx e\left|\frac{\alpha}{\sqrt{1+\alpha^2}}\left\langle\psi_{3d_{z^2-r^2}}|\mathbf{r}|\chi_{p_z}\right\rangle\right|$ depends on the arrangement of ligand ions around the metal ion. This quantity can be estimated from Slater like orbitals if the mixing parameter is known which is usually difficult to determine. Since, this dipole moment is also proportional to the oscillator strength which can be calculated

Element	A	B	$\langle\psi_A\|\mathbf{r}\|\psi_B\rangle$
O	$2s$	$2p_z$	$0.6\, a_0\, \hat{z}$
S	$3s$	$3p_z$	$1.1\, a_0\, \hat{z}$
Sc	$3d_{z^2-r^2}$	$3p_z$	$0.3\, a_0\, \hat{z}$
Mn	$3d_{z^2-r^2}$	$4p_z$	$1.0\, a_0\, \hat{z}$

Table E.1: Position operator matrix elements between different orbitals calculated using Slater type orbitals.

directly from the absorption spectra of these complexes. In some tetrahedral complex salts [18], the dipole moment between two different d orbitals belonging to t_{2g} and e_g sets can be as high as 0.5 Debye= $0.1e$Å. This kind of d-d transition also occur in some transition metal trichalcogenides like NiPS$_3$ [173] but the associated dipole moment would be much smaller as indicated by the extremely weak absorption for this peak.

E.5 Vibronic coupling estimate

In this section, we calculate the matrix element between two d orbitals for a phonon drive. We assume that the transition metal ion is surrounded by an octahedral arrangement of ligand ions, and the phonon mode involves the symmetric motion of ligand ions perpendicular to the metal ligand bond. For the geometry shown in Fig. E.5, the potential around TM ion due to ligand ions is given by

$$V(\mathbf{r},t) = \sum_{L=1}^{8} \frac{q_L e^2}{4\pi\epsilon_0 |\mathbf{a}_L(t) - \mathbf{r}|} \tag{E.29}$$

where q_L is the charge on ligand ion (in units of e), $\mathbf{a}_L$ is the position vector of ligand L from the center of the TM ion, and

$$\mathbf{a}_L(t) = \mathbf{a}_L^0 + \mathbf{u}_L(t) \tag{E.30}$$

where $\mathbf{a}_L^0$ is the equilibrium distance of M-L bond, and $\mathbf{u}_L$ is the phonon amplitude. For small $\mathbf{u}_L$, we can expand V around its equilibrium value as follows:

$$V(\mathbf{r},t) = \frac{q_L e^2}{4\pi\epsilon_0} \sum_{L=1}^{8} \left(\frac{1}{|\mathbf{a}_L^0 - \mathbf{r}|} - \frac{(\mathbf{a}_L^0 - \mathbf{r}) \cdot \mathbf{u}_L(t)}{|\mathbf{a}_L^0 - \mathbf{r}|^3} + \ldots \right), \tag{E.31}$$

and thus up to first-order, the perturbation is given by:

$$H' \approx -\frac{q_L e^2}{4\pi\epsilon_0} \sum_{j}^{8} \frac{(\mathbf{a}_L^0 - \mathbf{r}) \cdot \mathbf{u}_L(t)}{|(a_L^0)^2 + r^2|^{\frac{3}{2}}} \left(1 + 3\frac{\mathbf{a}_L^0 \cdot \mathbf{r}}{|(a_L^0)^2 + r^2|} + \ldots \right). \tag{E.32}$$

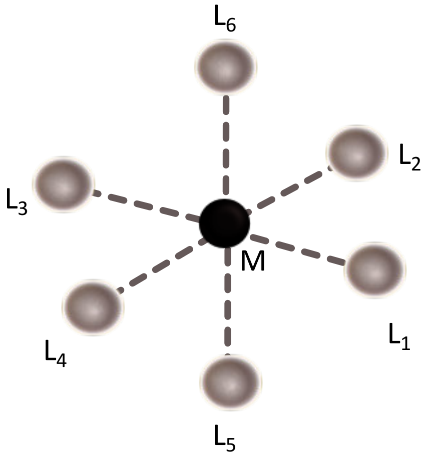

Figure E.5: Arrangement of ligand ions around a transition metal ion in octahedral geometry.

Now, the only terms which can couple two d orbitals are:

$$\left\langle d_\alpha | H' | d_\beta \right\rangle = \frac{3 q_L e^2}{4\pi\epsilon_0} \sum_{L=1}^{8} \left\langle d_\alpha \left| \frac{(\mathbf{r}\cdot\mathbf{u}_L(t))(\mathbf{a}_L^0\cdot\mathbf{r})}{|(a_L^0)^2 + r^2|^{\frac{5}{2}}} \right| d_\beta \right\rangle . \tag{E.33}$$

Furthermore, the matrix element $\left\langle d_\alpha | \mathbf{r}_k \mathbf{r}_l | d_\beta \right\rangle$ is non-zero for the cases shown in Table E.2. In RTiO$_3$, the ligand-metal distance, $|a_L^0| \approx 2$Å, and thus the matrix element coupling two d orbitals becomes:

$$| \left\langle d_\alpha \, | H' | \, d_\beta \right\rangle | \approx 0.5 u(t) \text{eV} = 0.25 (e^{i\omega t} + e^{-i\omega t}) u_0 \text{eV} \tag{E.34}$$

for a g symmetry phonon mode, where u_0 is the displacement (in units of Å) of the ligand ion perpendicular to the M-L bond.

E.6 Excitation mechanism for the Raman mode coupled to IR mode

In Mott insulating titanates YTiO$_3$ and LaTiO$_3$, some of the Raman modes can be excited by making use of non-linear phonon coupling between different phonons. In the presence of an oscillating E field which excites the IR mode, the time-evolution of different phonon modes is governed by the following equations:

$$\ddot{Q}_{IR} = -\omega_{IR}^2 Q_{IR} + F(t) - 2g Q_R Q_{IR} - b_4 Q_{IR}^3 \tag{E.35}$$

$$\ddot{Q}_R = -\omega_R^2 Q_R - g Q_{IR}^2 - a_3 Q_R^2 \tag{E.36}$$

d_α	d_β	$\mathbf{r}_k\mathbf{r}_l$	$\langle d_\alpha\|\mathbf{r}_k\mathbf{r}_l\|d_\beta\rangle$ (Å^2)
d_{xy}	d_{yz}	xz	0.4
d_{xy}	d_{xz}	yz	0.4
d_{yz}	d_{xz}	xy	0.4
d_{yz}	$d_{x^2-y^2}$	yz	0.4
d_{xz}	$d_{x^2-y^2}$	xz	0.4
d_{xy}	$d_{z^2-r^2}$	xy	0.4
d_{yz}	$d_{z^2-r^2}$	yz	0.2
d_{xz}	$d_{z^2-r^2}$	xz	0.2

Table E.2: Matrix element $\langle \mathbf{r}_k\mathbf{r}_l\rangle$ between two $3d$ orbitals of Ti calculated using Slater type orbitals.

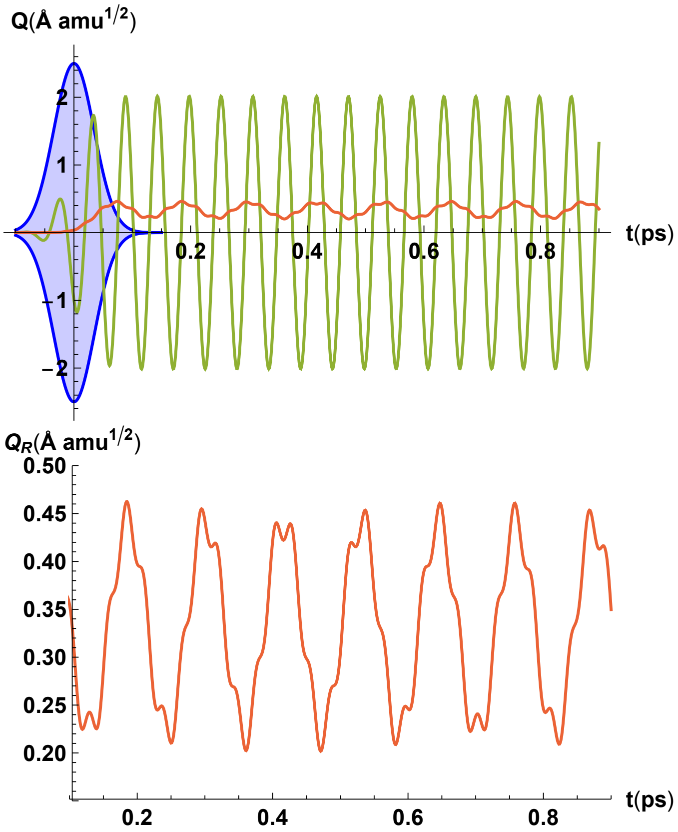

Figure E.6: Dynamics of phonon modes. Upper panel: Time evolution of Raman mode $A_g(25)$ (red curve) and IR active mode $B_{1u}(54)$(green) when excited by a resonant mid IR laser pulse of maximum amplitude $E = 0.5V/\text{Å}$ and pulse width $\sigma = 50/\sqrt{2}fs$ (shown in blue envelope for illustration purpose). Lower Panel: Magnified version of Raman mode and the lattice vibrations are almost sinusoidal. Here the amplitude of $A_g(25)$ mode is $Q_R \approx 0.12\text{Å}\sqrt{amu}$ and is proportional to the square of the amplitude of IR mode.

where $\omega_{R,IR}$ and $Q_{R,IR}$ are the frequencies and amplitudes of Raman and IR modes, respectively, as discussed in Ref. [124]. Here the mode amplitude Q is measured in $\AA\sqrt{amu}$, ω_R^2 in units of $eV/(\AA\sqrt{amu})^2$ ($521.471 cm^{-1} = 1 eV/\AA^2 amu$), g in units of $eV/(\AA\sqrt{amu})^3$, and $F(t) = CE\cos\omega t e^{-t^2/2\sigma^2}$ where E is measured in units of $V/\AA$ and $C = Z^*/\sqrt{m}$ depends on Born effective charge $Z^*$and $\sqrt{m}$ is the reduced mass of the mode. In the present scenario we can get the required rotation of oxygen octahedron by exciting $A_g(25)$ Raman mode. This mode couples strongly with IR mode $B_{1u}(54)$ with $g = 0.05$. Now, the amplitude of $A_g(25)$ Raman mode depends on a lot of factors like the coupling strength g, frequency ratio $\omega_{IR}/\omega R$, detuning $\omega - \omega_{IR}$, the pulse width σ. For the case of YTiO$_3$ and LaTiO$_3$, the time-evolution of above two equations for $E = 0.5 V/\text{Å}$ and $\sigma = 50/\sqrt{2} fs$ results in oscillations of amplitude $Q_R \approx 0.12\text{Å}\sqrt{amu}$ which correspondents to a lattice oscillation of amplitude $u_0 \approx 0.02\text{Å}$ as shown in Fig. E.6. We have ignored the damping terms as the damping would not affect the oscillations much for the time interval shown in Fig. E.6. Although the mode amplitude of IR active mode is large but since the other non-linear terms in Eq. E.36 are usually small ($a_3 \approx 0.008 eV/\text{Å}^2/\sqrt{amu}^{3/2}$, $b_4 \approx 0.08 eV/\text{Å}^4/(amu)^2$) for similar orthorhombic structures [335], so these non-linear terms are irrelevant for the time-evolution in the regime considered here.

Chapter 9

CONTROLLING LIGAND-MEDIATED EXCHANGE INTERACTIONS IN PERIODICALLY DRIVEN MAGNETIC MATERIALS

“The ability to perceive or think differently is more important than the knowledge gained.” – David Bohm

A periodic drive could alter the effective exchange interactions in magnetic materials. Here, we explore how exchange pathways affect the effective interactions of periodically driven magnetic materials. Aiming to apply Floquet engineering methods to two-dimensional magnetic materials, we consider realistic models and discuss the effect of a periodic drive on ligand-mediated exchange interactions. We show that depending on bond angles and the number of ligand ions involved in the exchange process, drive-induced changes can be very different from those calculated from direct-hopping models considered earlier. We study these effects and find that the presence of ligand ions must be taken into account, especially for TMTCs where ligand ion mediated next-neighbor interactions play a crucial role in determining the magnetic ground state of the system.

This chapter is based on the following reference:

Swati Chaudhary, Alon Ron, David Hsieh, and Gil Refael. “Controlling ligand-mediated exchange interactions in periodically driven magnetic materials.”
arXiv:2009.00813

9.1 Introduction

Periodic drives have been used extensively to tailor the properties of the Hamiltonians for ultracold gases in optical lattices, ranging from the generation of artificial gauge fields for neutral atoms in optical lattices to many-body localization [255, 178, 147, 208, 111, 351, 93, 16, 93, 97, 180, 122, 134, 135, 131, 24, 112, 139, 148, 236, 366, 275, 291, 340, 347, 29, 202, 390, 301, 156, 85, 263, 133, 2, 272, 350, 146, 339, 400, 58, 103, 252, 94, 387, 39, 83, 95, 388]. The evolution of such periodically-driven systems can be described by an effective time-independent Hamiltonian using Floquet theory [313]. The properties of this effective Hamiltonian can be controlled by changing the drive parameters like its frequency, amplitude, etc. Extending these methods to quantum materials seems very promising as it may allow us to realize new states of matter and manipulate the electronic and magnetic properties of these materials on demand [21, 256].

Previously, several works studied light-induced changes in the magnetic properties of transition metals compounds [175, 232, 230, 228, 230, 229, 40, 211, 137, 282, 283, 62, 293]. Recent works [228, 230, 229, 40, 211, 137, 282, 283, 62] have demonstrated the possibility of using periodic drives for manipulating the exchange interactions in extended antiferromagnetic (AFM) Mott insulators. These results can be applied to many transition metal (TM) compounds. Transition metal trichalcogenide (TMTC) monolayers are one of the prime candidates, where periodic drive could lead to interesting results. As shown in Ref. [318], the magnetic properties of such monolayers are very well described by the Heisenberg model on a honeycomb lattice with up to third nearest-neighbor interactions. Motivated by these materials, we study the effects of the periodic drive on a Fermi-Hubbard Model (FHM) on a honeycomb lattice, and study how the magnetic coupling strength can be modified by tuning different drive parameters. We further explore the consequences of the ligand ions and study how the changes in magnetic coupling strength depend not only on the drive parameters, but also on the bond angles and the orbital orientation of these intermediary ions.

9.2 Periodically driven Fermi Hubbard model

We study the effect of a periodic drive on the exchange interactions using a periodically driven Fermi Hubbard model (FHM) in the Mott regime at half-filling. Let us first review this model.

Review: Toy model for AFM coupling renormalization due to photo-modified tunneling

In the presence of a time-dependent electric field, the full Hamiltonian of the Fermi-Hubbard model is given by:

$$H = -t \sum_{<i,j>} c^{\dagger}_{i\sigma} c_{j\sigma} + \text{h.c} + U \sum_{i} n_{i\uparrow} n_{i\downarrow} + e\mathbf{E} \cdot \sum_{\mathbf{i},\sigma} n_{i\sigma} \mathbf{r_j} \cos(\omega \mathbf{t}). \tag{9.1}$$

After Peierls substitution, it becomes:

$$H' = -t \sum_{<i,j>} e^{i\left[\frac{e\mathbf{E}\cdot(\mathbf{r_j}-\mathbf{r}_i)}{\omega} \sin(\omega t)\right]} c^{\dagger}_{i\sigma} c_{j\sigma} + \text{h.c} + H_U = H'_t + H_U. \tag{9.2}$$

In the limit $U \gg t$, and for a non-resonant drive, the exchange coupling is given by:

$$J_i' = J_i U \sum_{n=-\infty}^{\infty} \frac{1}{U + n\omega} \mathcal{J}_n(\zeta_i)^2, \tag{9.3}$$

where, $J_i = \frac{4t^2}{U}$ is the magnetic coupling strength for the undriven case, $\mathcal{J}_n$ denotes n^{th} order Bessel function, and drive parameter

$$\zeta_i = \frac{e\mathbf{E} \cdot \Delta\mathbf{r}_i}{\omega}, \tag{9.4}$$

where $\Delta\mathbf{r}_i$ is the displacement between i^{th} neighbors. In the presence of this periodic drive, spin exchange interactions are affected mainly due to two factors: (a) change in the hopping parameter due to photon-assisted tunneling, and (b) virtual excitations between different Floquet sectors. The effective spin exchange interactions can thus be controlled by changing the frequency, polarization or intensity of the laser. Previous works [228, 230, 229, 40, 211, 137] have studied the periodically driven FHM extensively for both near-resonant and off-resonant cases. The above expression in Eq. (9.3) is valid only for a non-resonant drive where doublon sectors are well separated in energy from the single occupation sector. Near-resonant drive can be handled using a somewhat similar machinery of Floquet formalism as shown in Ref. [40] but in certain cases, real doublon-holon pairs can significantly affect the exchange interactions [210].

Driven FHM on honeycomb lattice

We are interested in controlling the properties of magnetic materials using light, and monolayer magnetic materials, e.g TMTC monolayers, provide a suitable platform for our exploration. The magnetic structure of these 2D magnetic materials is captured by the Heisenberg model on a honeycomb lattice with up to third nearest neighbor interactions. It exhibits numerous ground states depending on the relative signs and values of different neighbor exchange interactions [318]. So, before proceeding further, we briefly consider the effects of a non-resonant periodic drive on the exchange interactions in this model.

Consider the Fermi-Hubbard Model on a honeycomb lattice with up to third nearest neighbor hopping:

$$\begin{aligned} H =& H_U + H_t = U \sum_i \hat{n}_{i\uparrow}\hat{n}_{i\downarrow} + \sum_{\langle i,j\rangle\sigma} t_1 c^{\dagger}_{\mathbf{r_i}\sigma} c_{\mathbf{r_j}\sigma} \\ &+ \sum_{\langle\langle i,j,\sigma\rangle\rangle} t_2 c^{\dagger}_{\mathbf{r_i}\sigma} c_{\mathbf{r_j}\sigma} + \sum_{\langle\langle\langle i,j\rangle\rangle\rangle} t_3 c^{\dagger}_{\mathbf{r_i}\sigma} c_{\mathbf{r_j}\sigma} + \text{h.c} \end{aligned} \tag{9.5}$$

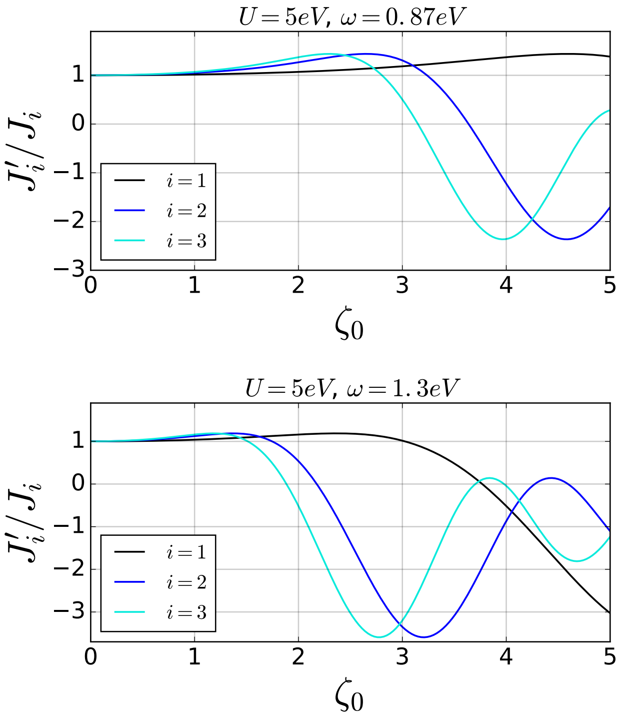

Figure 9.1: Periodic drive effect on magnetic coupling. Changes in the spin exchange interaction energy for different neighbors as a function of the drive parameter ζ_0 (in terms of E field magnitude, one unit on this scale can be read as $1V/$) for two different values of U/ω. The changes are larger for smaller values of U/ω as expected from Eq. 9.3.

where $U \gg t_i$. Adding a circularly polarized light beam gives rise to the following periodic drive:

$$H'(t) = \sum_i eE_0(\cos \omega t\, \hat{x} + \sin \omega t\, \hat{y}) \cdot \mathbf{r}_i \hat{n}_i \tag{9.6}$$

which results in a direction-independent modification of exchange interactions.

In the presence of this drive, the magnetic coupling strength between i^{th} neighbors is given by an expression similar to Eq. (9.3) with t replaced by t_i, and the changes with drive parameter $\zeta_0 = \frac{eE_0a}{\omega}$, where E_0 is the electric field amplitude, e is the electron charge and ω is the frequency of drive measured in units of eV, and a is the separation between the nearest neighbors on a honeycomb lattice, are shown in Fig. 9.1. This drive parameter is dimensionless. In most of the cases, $a \approx 1$ and $\omega \approx 1eV$, and thus $\zeta = 1$, roughly corresponds to an electric field amplitude of 1V/, i.e 100MV/cm. The changes in the coupling strength depend on both the drive parameter ζ_0, and the ratio U/ω. The main contribution in Eq. (9.3) comes from those values of n which

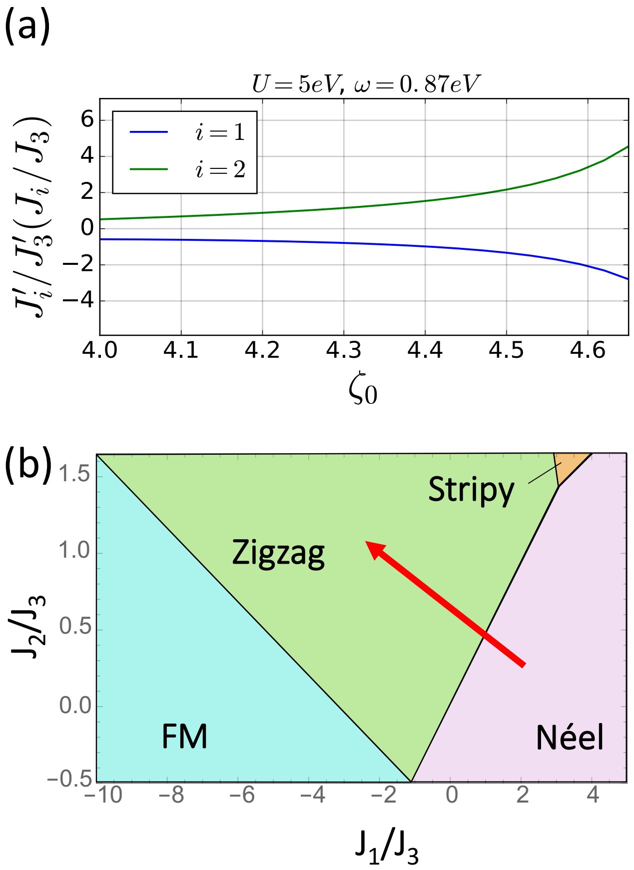

Figure 9.2: Magnetic ground state of effective Hamiltonian. (a) Change in the magnetic coupling strength ratio as a function of the drive parameter, and (b) same change shown by a red arrow on the phase diagram [318].

are close to U/ω. Roughly speaking, this change in the coupling constant behaves in the same manner as $\mathcal{J}_n(\zeta_i)$, and thus for large values of U/ω, the renormalization factor peaks at a higher value of the drive parameter, and its amplitude is also smaller as we notice in Fig. 9.1. This model is particularly interesting because depending on the drive parameter, the ground state of the effective time-independent Hamiltonian can be very different from the undriven case as shown in Fig. 9.2.

9.3 Applications to materials with ligand mediated magnetic interactions

Most of the previous works [228, 230, 229, 40, 211, 137] on the periodically driven FHM assumed direct hopping between two metal sites. In TM compounds, spin-exchange interactions are mostly mediated by ligand ions as shown in Fig. 9.3 for TMTC monolayers [318], and thus the exchange coupling depends on factors like bond lengths, bond angles, and the nature of orbitals involved in the exchange

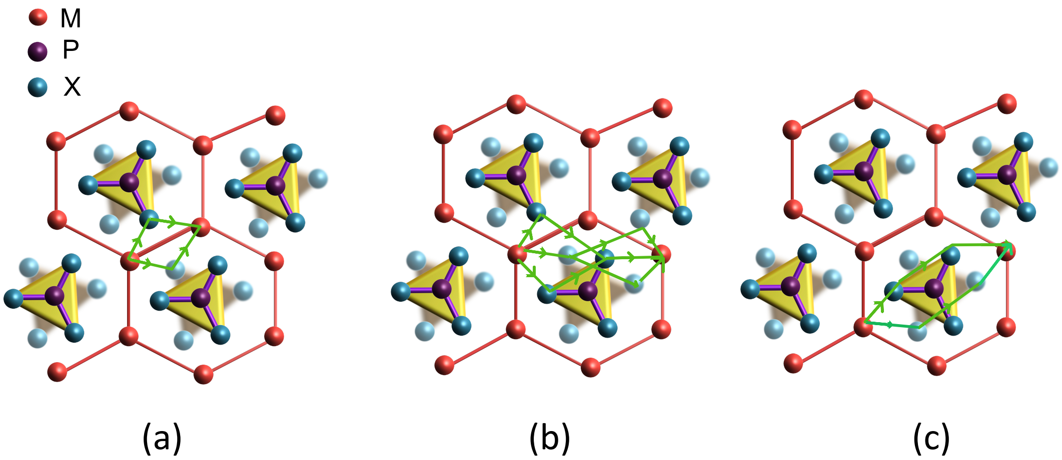

Figure 9.3: Exchange Pathways in TMTC monolayers. Top view of single layer metal phosphorus trichalcogenides (MPX_3) illustrating different paths responsible for spin exchange interaction: (a) Nearest neighbor interactions J_1 can occur via direct hopping or via one ligand ion, (b) Second nearest neighbor interactions are mediated by two intermediate ions, and there are five paths available for spin exchange, (c) Third nearest neighbor interactions occur via two intermediate ions and both belong to the same plane.

process. There are usually multiple pathways available for spin-exchange processes between two metal sites. Particularly for TMTC monolayers [318], the nearest neighbor interactions occur via direct hopping or via one ligand ion, second and third nearest neighbor interactions involve indirect hopping mediated by two ligand ions as shown in Fig. 9.3. In order to provide a more precise estimate of the change in coupling strength, one must take these factors into account. Below, we explore the consequences of periodic drive for different cases, and contrast them with the periodic drive effects for the direct-hopping case.

Case 1 : AF coupling via one intermediate ion with only one orbital

Consider a simple two-site model with one spin on each site, and with a non-magnetic (ligand) ion between the two metal sites, which mediates the spin exchange between two spins located at metal sites as shown in Fig. 9.4. This model can be described the following Hamiltonian:

$$H = -\sum_{i=1,2,\sigma} tc^{\dagger}_{i\sigma}c_{A\sigma} + \text{h.c } + E_A(\hat{n}_A - 2) + U\sum_{i=1,2} \hat{n}_{i\uparrow}\hat{n}_{i\downarrow}, \tag{9.7}$$

where i denotes the metals sites, A denotes the orbitals of non magnetic ions involved in the exchange process and its electronic energy E_A is negative, and the on-site interaction on metal sites is U. For the undriven case, the magnetic coupling strength is given by:

$$\text{J=}4t^4\left(\frac{1}{(E_d)^2U} + \frac{1}{(E_d)^3}\right), \tag{9.8}$$

where $E_d = |E_A|$+U is the energy of those virtual states where one electron has been transferred from the ligand orbital A to the metal ion [225]. Now, we apply a uniform AC electric field which adds an extra term H_p to above Hamiltonian where,

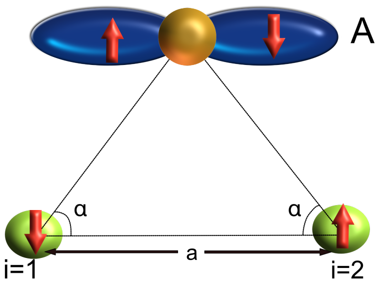

Figure 9.4: AF coupling via one ligand ion. Spin exchange between two sites (denoted by i) with one spin on each via orbital A of the ligand ion. There is no direct hopping between two metal sites, but the spin can hop between metal site and the orbital A for very small values of bond angle α. This superexchange mediated by a non-magnetic ion gives rise to AF interactions between two spins at sites denoted by i.

$$H_p = -\sum_i e\mathbf{E}(t)\cdot\mathbf{r}_i\hat{n}_i + e\mathbf{E}(t)\cdot\mathbf{r}_A\hat{n}_A \tag{9.9}$$

and $\mathbf{E}(t) = E_0(\cos\omega t\,\hat{x} + \sin\omega t\,\hat{y})$. Using fourth order perturbation theory, we show that in the non-resonant case, the new coupling strength is modified as follows:

$$\begin{aligned}
J_{\text{ex}} = 4t^4 \sum_{m_1,n_1,n} & \frac{1}{2(E_d+n_1\omega)(E_d+m_1\omega)(E_d+\frac{n}{2}\omega)} \\
& (\cos(2(n_1-m_1)\alpha)\mathcal{J}_{m_1}(\zeta_1)\mathcal{J}_{n_1}(\zeta_1)\mathcal{J}_{n_1-n}(\zeta_1)\mathcal{J}_{m_1-n}(\zeta_1)+ \\
& \cos(2(n-m_1-n_1)\alpha)\mathcal{J}_{n_1}(\zeta_1)\mathcal{J}_{m_1}(\zeta_2)\mathcal{J}_{n_1-n}(\zeta_1)\mathcal{J}_{m_1-n}(\zeta_2)) \\
& + \frac{1}{(E_d+n_1\omega)(E_d+m_1\omega)(U+n\omega)} \\
& \left(\cos(2(n_1-m_1)\alpha)\mathcal{J}_{m_1}(\zeta_1)\mathcal{J}_{n_1}(\zeta_1)\mathcal{J}_{n_1-n}(\zeta_2)\mathcal{J}_{m_1-n}(\zeta_2)\right)
\end{aligned} \tag{9.10}$$

where $\zeta_1 = -\zeta_2 = \frac{\zeta_0}{2\cos\alpha}$, and $\zeta_0 = \frac{eE_0a}{\omega}$. The resulting magnetic coupling strength is shown in Fig. 9.5 for different values of charge transfer gap E_d. We notice that the observed changes do not differ significantly from the direct hopping case if $E_d \gg U$ but the changes for $E_d \approx U$ can be much different.

In addition to the charge transfer gap, J_{ex} also depends on the bond angle α in Fig. 9.4, which is usually close to zero for AF coupling in most cases. In most of the transition metal compounds, only p type orbitals of the ligand ion are involved in this superexchange mechanism, and thus both metal sites should have finite overlap with the same orbital which is possible only if bond angle is very small. We study the effect of periodic drive on magnetic coupling for different bond angles. As shown in Fig. 9.6, the changes in magnetic coupling strength follows the same trend as the direct hopping case approaches the same value when E_d increases and $\alpha \ll 1$.

Case 2 : Effect of a periodic drive on FM coupling mediated by a ligand ion

In some cases, the ligand ion can also mediate FM interactions. When the spin exchange between two metal sites is not allowed but the two spins can still hop to two different ligand orbitals of the same ligand ion, then due to Hund's coupling, two spins align in the same direction. Even in this situation, the magnetic coupling strength depends on the hopping parameter, and thus can be tuned by a periodic drive to a certain extent. Consider a toy model shown in Fig. 9.7 with two TM ions (M) at sites $i = 1$ and $i = 2$, and a ligand ion (X) with two degenerate orbitals namely

A and B described by Hamiltonian:

$$\begin{aligned} H =& U \sum_{i=1,2} \hat{n}_{i\uparrow}\hat{n}_{i\downarrow} + J_H \sum_{\substack{\alpha=A,B,\\ \alpha\neq\alpha'}} c^{\dagger}_{\alpha\uparrow}c^{\dagger}_{\alpha'\downarrow}c_{\alpha\downarrow}c_{\alpha'\uparrow}+ \\ & \sum_{\substack{\alpha=\{A,B\},\\ \sigma=\{\uparrow,\downarrow\}}} E_A \hat{n}_{\alpha\sigma} - \sum_{\substack{i=\{1,2\},\\ \alpha=\{A,B\}}} t_{i\alpha}(c^{\dagger}_{i\sigma}c_{\alpha\sigma} + c^{\dagger}_{\alpha\sigma}c_{i\sigma}) \end{aligned} \tag{9.11}$$

where J_H is Hund's coupling and the hopping parameters, $t_{1A} = t_{2B} = t$, and $t_{2A} = t_{1B} = 0$ as the spins at $i = 1$, and at $i = 2$ hop to orbitals A and B, respectively.

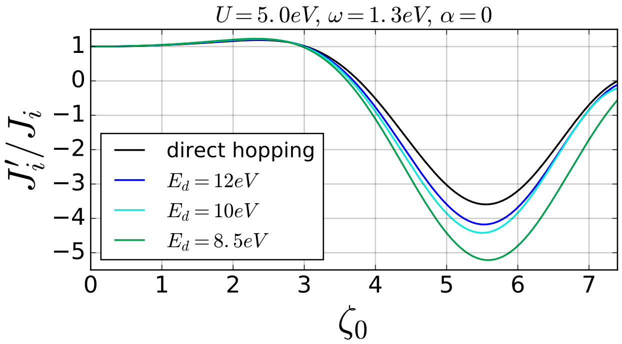

Figure 9.5: Effect of charge transfer gap. Changes in AFM coupling as a function of drive parameter for different values of charge transfer gap E_d, when the ligand ion lies at the line joining the two TM ions. The qualitative behavior of renormalized coupling is independent of E_d, but the quantitative predictions start to differ significantly as E_d decreases.

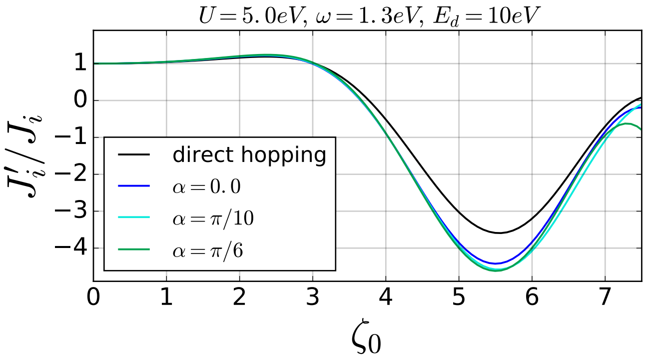

Figure 9.6: Effect of bond angle. Change in AF coupling as a function of drive parameter for different values of bond angle α in Fig. (9.4). This change follows the same trend as the direct hopping case, and approaches the direct hopping limit when $E_d \gg U$, $\alpha \to 0$.

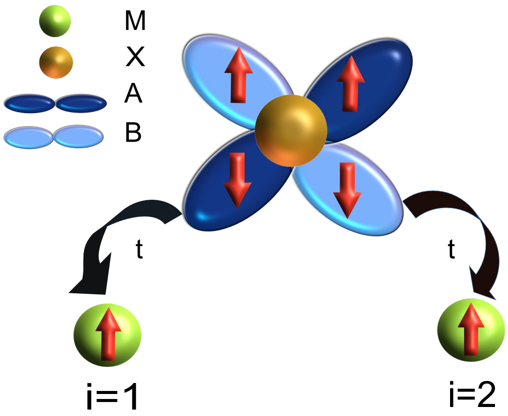

Figure 9.7: FM coupling via two orbitals of the ligand ion. FM interactions between spins mediated by a non-magnetic ion with two orbitals shown in different shades of blue. The electrons from each orbital of the ligand ion can hop to only one metal ion site so the intermediate state with same spin in two orbitals of the ligand ion is preferred due to Hund's coupling. This favors the parallel arrangement of the two spins at metal sites.

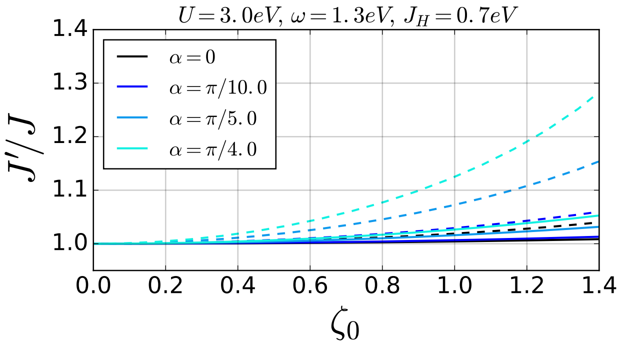

Figure 9.8: Effect of bond angle. Change in FM interactions as a function of drive parameter ζ_0 for charge transfer gap $E_d = 5eV$(dashed lines) and $E_d = 10eV$(solid lines) for different values of angle α, where α is the angle between the line joining the two TM ions and the projection of M-X bond on the plane containing these TM ions. In this case, changes depend on angle α and charge-transfer gap E_d.

In the presence of a circularly polarized light, the magnetic coupling strength is given by:

$$\begin{aligned} J = t^4 \sum_{m_1,n_1,n} & \frac{4J_H}{(E_d + m_1\omega)(E_d + n_1\omega)((2E_d + n\omega)^2 - J_H^2)} \\ & (\cos(2(m_1 - n_1)\alpha)\mathcal{J}_{n_1}(\zeta_{1a})\mathcal{J}_{m_1}(\zeta_{1a})\mathcal{J}_{n-n_1}(\zeta_{2b})\mathcal{J}_{n-m_1}(\zeta_{2b}) \\ & + \cos(2(n - m_1 - n_1)\alpha)\mathcal{J}_{n_1}(\zeta_{1a})\mathcal{J}_{m_1}(\zeta_{2b})\mathcal{J}_{n-n_1}(\zeta_{2b})\mathcal{J}_{n-m_1}(\zeta_{1a})) \end{aligned} \tag{9.12}$$

where $E_d = U - E_A$, $\zeta_{1a} = -\zeta_{2b} = \frac{\zeta_0}{2\cos\alpha}$, with $\zeta_0 = eE_0a/\omega$, a is the separation between two TM ions and α is the angle between the line joining the two TM ions and the projection of M-X bond on the plane containing these TM ions. We are using a circularly polarized drive to introduce a direction-independent modification of exchange interactions. As shown in Fig. 9.8, the change in FM interaction is sensitive to bond angle α and start to increase with the bond angle. Also, these changes are more significant when the charge transfer gap and drive frequency are of the same order.

Case 3: Effect of periodic drive on AF coupling mediated by two intermediate ligand ions

In some materials, especially in TMTC monolayers, second and third nearest neighbor interactions play a very important role in deciding the magnetic ground state. These kind of interactions are allowed only due to the presence of two or more intermediate ions available for spin exchange as shown in Fig. 9.3. In such cases, the effect of a periodic drive can be expected to be very different from the direct hopping case. We consider the toy model shown in Fig. 9.9, where the electron at site $i = 1$ can hop to orbital A, the electron at other metals site can hop to orbital B of the different ligand ion, and hopping between orbitals A and B is allowed. It can be described by the following Hamiltonian:

$$\begin{aligned} H = U\sum_i \hat{n}_{i\uparrow}\hat{n}_{i\downarrow} - \sum_{\substack{i=\{1,2\},\\ \alpha=\{A,B\},\\ \sigma=\{\uparrow,\downarrow\}}} t_{i\alpha}c^{\dagger}_{i\sigma}c_{\alpha\sigma} + \text{h.c } + E_A(\hat{n}_A - 2) \\ + E_B(\hat{n}_B - 2) - t_{AB}(c^{\dagger}_{A\sigma}c_{B\sigma} + c^{\dagger}_{B\sigma}c_{A\sigma}), \end{aligned} \tag{9.13}$$

where, E_A and E_B are the electronic energies of the orbitals A and B of the ligand ions, $t_{i\alpha}$ denotes the hopping parameter between orbital α of the ligand ion and metal site i, and $t_{1A} = t_{2B} = t$, while $t_{1B} = t_{2A} = 0$. Since in most cases, all ligand ions are similar so here we assume $E_A = E_B$. In the presence of a circularly polarized EM field, we calculate the changes in the effective spin-exchange interactions and observe that bond angles play a very important role as shown in Fig. 9.10.

Although Floquet engineering of the spin exchange interactions looks very promising, and changes in the effective spin exchange interactions have been demonstrated in some cold atom experiments [65, 119], in real materials, we need very large E fields (of the order of $1V/$) to make any significant changes, and we need to take into account the microscopic details of the spin exchange processes. In most cases, there

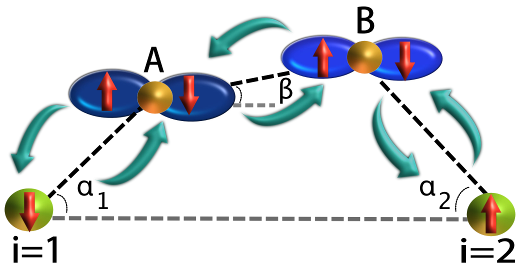

Figure 9.9: AF coupling via two ligand ions. AF coupling between two spins mediated by two ligand ions where no direct hopping is allowed between two metal sites. This system is represented by the Hamiltonian in Eq. (9.13).

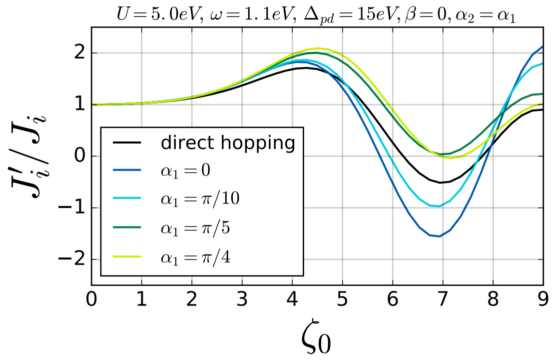

Figure 9.10: Effect of bond angles. Change in AF coupling strength as a function of drive parameter $\zeta_0 = \frac{eEa}{\omega}$, where a is the separation between two magnetic ions and the spin exchange is mediated by two intermediate ions in the presence of a periodic drive. This is one of the most important spin exchange pathway in TMTC monolayer, and the changes in spin exchange interactions are very different from direct hopping case.

are more than one competing mechanisms, and quantitatively precise predictions can be made only if the relative contributions from different exchange pathways are known a priori. Indeed, we find that the presence of intermediary ions can not be neglected, and must be taken into account, especially for materials like TMTCs where even the third nearest neighbor interactions play a crucial role in determining the magnetic ground state of the system. This section provided us an estimate of how depending on the exchange mechanism, changes in the magnetic coupling strength can be very different from the direct hopping case.

Implications for TMTC monolayers

The effect of ligand ions on the magnetic coupling renormalization depends on the material properties like bond length, bond angle and charge transfer gap. For TMTC

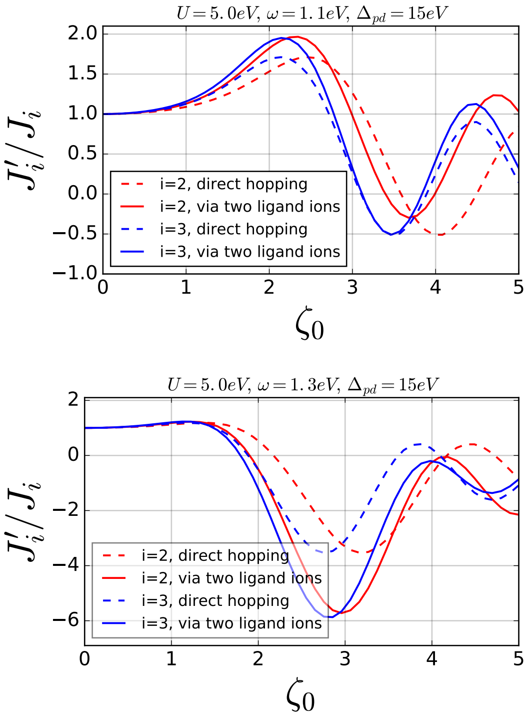

Figure 9.11: Effect of ligands on modified magnetic coupling in $MnPS_3$. Changes in magnetic coupling strength for the second nearest-neighbor ($i = 2$) and third nearest neighbor ($i = 3$) as a function of drive parameter $\zeta_0 = \frac{eEa}{\omega}$, where a is the distance between nearest-neighbor Mn ions (Here, $a \approx 3$ and $\omega \approx 1eV$, so electric field $E \approx \frac{\zeta_0}{3} eV/$)). We compare the results from a direct hopping model (Fig. 9.1) with a more realistic model with ligand ions. These changes were calculated mainly for $MnPS_3$ in Neel state for the bond parameters taken from Ref. [70]. For the second nearest neighbor case, spin exchange occurs via two different pathways: one involves the two X atoms attached to the same P atom while the other one occurs via two X atoms attached to different P atoms. For the purpose of this calculation, we focused on the first case.

monolayers, the ligand ions mainly affect the second and third nearest neighbor interactions (Fig. 9.3). As a result, the analysis shown in Fig. 9.1 and Fig. 9.2, where we assumed that all spin exchange processes were occurring as a result of direct hopping would be affected. In Fig. 9.11, we plot the changes in magnetic coupling strength for $MnPS_3$ by taking into account the different exchange mechanism and compare it to the direct-hopping case. We notice that, depending on the frequency, in certain cases even the qualitative behavior can be drastically different, for, e.g, when the drive frequency is $\omega = 1.1eV$, the second and third nearest-neighbor interactions, J_2 and J_3, change sign at some values of the drive parameter for direct-hopping, but they remain positive when the ligand ions are taken into account. This deviation from the results of direct-hopping model is significant as the ground state of the effective Floquet Hamiltonian has a very different magnetic order (Fig. 9.2) for the above two situations.

9.4 Conclusions

We studied the consequences of a periodic drive on the ligand mediated spin-exchange interactions in a model inspired by TMTCs . Although our calculations are not material specific, they capture the essential features of periodically driven magnetic materials where exchange interactions are mediated by non-magnetic ions. We showed that the modifications due to periodic drive depend on the exchange pathways, and in certain cases these changes can significantly differ from the changes predicted by the direct hopping models. This brings us a step closer to the experimental implementation of Floquet engineering in such materials.

We made several assumptions in order to understand the effects of periodic drive. Particularly, we restricted our analysis to a two-site toy model. Most of our calculations rely on the validity of perturbation methods in Floquet space, and hence we focused on off-resonant cases only. Furthermore, we restricted our analysis to a single orbital on each TM ion except for the FM case. As a result of these simplifications, these findings are applicable to only those cases where degeneracy between different d orbitals is lifted or the exchange process involves only one spin on each magnetic-ion site.

Also, our discussion was limited to the magnetic properties of Floquet Hamiltonians only. In practice, most of the observables also depend on the method used for switching on the drive. This analysis is valid only if the drive is turned on adiabatically. Additionally, the drive must be kept on for a long time to let the system adjust to the new effective Hamiltonian. In these spin systems, this time scale is roughly of the order of $1/J \approx 5ps$. As we observed in Fig. 9.2 , for certain values of the drive parameter, the effective Hamiltonian can have a very different magnetic ground state which can be measured directly from the changes in experimental quantities like reflectivity. While in other cases, the magnetic ground state might not change, but only the strength of magnetic coupling strength is modified. These kinds of changes should be reflected in the magnon spectrum or transition temperatures. In certain TMTCs like CrSiTe$_3$, where spin-lattice coupling is very strong [53], the modified exchange interactions can also affect the phonon frequency shifts which can be studied experimentally.

APPENDIX

F.1 Derivation for ligand-mediated AF coupling

For a two site-model considered in the main text, we have

$$H = E_A(\hat{n}_A - 2) + U \sum_{i=1,2} \hat{n}_{i\uparrow}\hat{n}_{i\downarrow} - \sum_{i=1,2,\sigma} t_A c^{\dagger}_{i\sigma} c_{A\sigma} + \text{h.c} \; = H_0 + H_{\text{hop}}, \tag{F.1}$$

where $\hat{n}_A = c^{\dagger}_{A\uparrow}c_{A\uparrow} + c^{\dagger}_{A\downarrow}c_{A\downarrow}$, i denotes the magnetic metal-ion sites, A is the orbital of the non-magnetic ion involved in the exchange process and its electronic energy E_A is negative, and the on-site interaction on metal sites is U. First, we'll calculate the exchange interactions in the static model where we have one spin on each magnetic ion and the ligand-orbital is completely filled. We can extract the AF coupling by focussing on $S_z = 0$ sector only, i.e by finding the energy difference between triplet and singlet configurations. We treat the hopping part as a perturbation. Within $S_z = 0$ subspace, H_0 has nine eigenstates which can be divided into following four sectors:

1. Magnetic-ion single-occupation sector P (two states)

$$|g_1\rangle = c^{\dagger}_{1\uparrow}c^{\dagger}_{2\downarrow}c^{\dagger}_{A\uparrow}c^{\dagger}_{A\downarrow}|0\rangle, \; |g_2\rangle = c^{\dagger}_{1\downarrow}c^{\dagger}_{2\uparrow}c^{\dagger}_{A\uparrow}c^{\dagger}_{A\downarrow}|0\rangle \tag{F.2}$$

   which has energy $E_P = 0$. This also happens to be the low-energy supspace of H_0 for $E_A < 0$ which is the case here.

2. Magnetic-ion double-occupation sector Q_1 (two states)

$$|Q^1_1\rangle = c^{\dagger}_{1\uparrow}c^{\dagger}_{1\downarrow}c^{\dagger}_{A\uparrow}c^{\dagger}_{A\downarrow}|0\rangle, \; |Q^2_1\rangle = c^{\dagger}_{2\uparrow}c^{\dagger}_{2\downarrow}c^{\dagger}_{A\uparrow}c^{\dagger}_{A\downarrow}|0\rangle \tag{F.3}$$

   with energy $E_{Q_1} = U$.

3. Ligand-ion single-occupation sector Q_2 (four states)

$$\begin{aligned} |Q^1_2\rangle &= c^{\dagger}_{1\uparrow}c^{\dagger}_{1\downarrow}c^{\dagger}_{A\uparrow}c^{\dagger}_{2\downarrow}|0\rangle, \; |Q^2_2\rangle = c^{\dagger}_{1\uparrow}c^{\dagger}_{1\downarrow}c^{\dagger}_{A\downarrow}c^{\dagger}_{2\uparrow}|0\rangle \\ |Q^3_2\rangle &= c^{\dagger}_{2\uparrow}c^{\dagger}_{2\downarrow}c^{\dagger}_{A\downarrow}c^{\dagger}_{1\uparrow}|0\rangle, \; |Q^4_2\rangle = c^{\dagger}_{2\uparrow}c^{\dagger}_{2\downarrow}c^{\dagger}_{A\uparrow}c^{\dagger}_{1\downarrow}|0\rangle \end{aligned} \tag{F.4}$$

   which has energy $E_{Q_2} = E_d = U - E_A$.

4. Ligand-ion zero-occupation sector Q_3 (one state)

$$|Q_3\rangle = c^{\dagger}_{1\uparrow}c^{\dagger}_{1\downarrow}c^{\dagger}_{2\uparrow}c^{\dagger}_{2\downarrow}|0\rangle \tag{F.5}$$

   which has energy $E_{Q_3} = 2E_d = 2U - 2E_A$.

In order to find the exchange interactions, we can write down an effective Hamiltonian for the ground state sector P by using Schrieffer-Wolf transformations [38]. In the model described above, the first contribution to exchange interactions comes from fourth-order corrections in low-energy effective Hamiltonian. This term arises because of virtual process which connects state $|g_1\rangle$ to $|g_2\rangle$ or vice-versa as shown in Fig. F.1. The contribution of fourth-order terms can be expressed as:

$$H^4_{\text{eff}} \approx \sum_{i,j,k=1,2,3} \frac{\hat{P}H_{\text{hop}}\hat{Q}_i H_{\text{hop}}\hat{Q}_j H_{\text{hop}}\hat{Q}_k H_{\text{hop}}\hat{P}}{(E_P - E_{Q_i})(E_P - E_{Q_j})(E_P - E_{Q_k})} \tag{F.6}$$

where $\hat{P}$ and $\hat{Q}_i$ denotes the projection operator on low-energy sector P and high-energy sector Q_i. We notice that

$$\hat{P}H_{\text{hop}}\hat{Q}_1 = \hat{P}H_{\text{hop}}\hat{Q}_3 = 0 \tag{F.7}$$

which reduces the above sum to

$$H^{(4)}_{\text{eff}} \approx -\sum_{j=1,3} \frac{\hat{P}H_{\text{hop}}\hat{Q}_2 H_{\text{hop}}\hat{Q}_j H_{\text{hop}}\hat{Q}_2 H_{\text{hop}}\hat{P}}{E_d^2 E_{Q_j}}, \tag{F.8}$$

and it takes the following form

$$H^{(4)}_{\text{eff}} \approx -\frac{2t_A^4}{E_d^2}\left(\frac{1}{U} + \frac{1}{E_d}\right) \sum_{i,j=1,2} (-1)^{i-j} |g_i\rangle \langle g_j| \tag{F.9}$$

for states $|g_1\rangle, |g_2\rangle$ of low-energy manifold (single-occupation sector P) of Hamiltonian H in Eq. F.1. A similar analysis for $S_z = \pm 1$ sector shows that $H^{(4)}_{\text{eff}} = 0$ indicating that the energy of this sector is equal to that of $S_z = 0$ triplet state $\frac{1}{\sqrt{2}}(|g_1\rangle + |g_2\rangle)$ as expected. This gives us a coupling strength:

$$J_{\text{ex}} = -\frac{4t_A^4}{E_d^2}\left(\frac{1}{U} + \frac{1}{E_d}\right). \tag{F.10}$$

Now, this analysis can be extended to include an off-resonant drive as well. For a driven system, after Peierls substitution, H_{hop} is replaced by:

$$H_{\text{hop}}(t) = -\sum_{i=1,2,\sigma} t_A e^{i\left[\frac{\mathbf{E}(t)\cdot\mathbf{r}_{iA}}{\omega}\right]} c^{\dagger}_{i\sigma} c_{A\sigma} + \text{h.c} \tag{F.11}$$

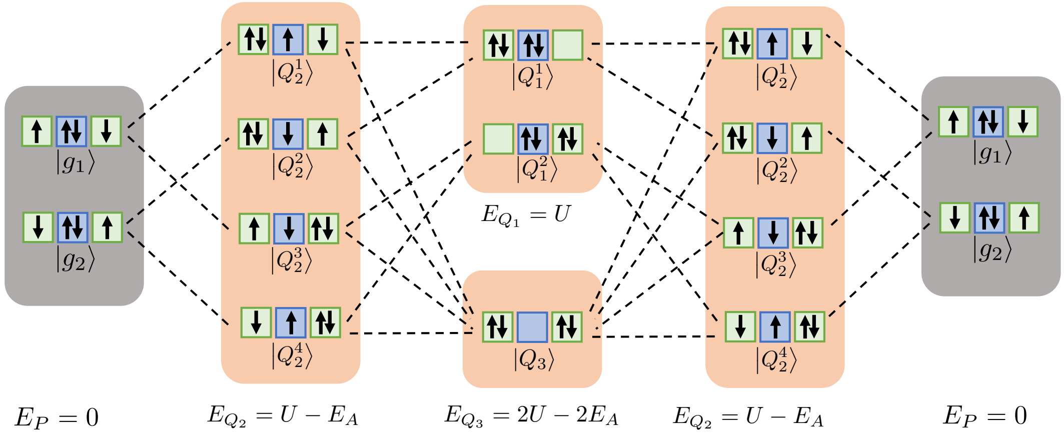

Figure F.1: This figure shows the different energy sectors of unperturbed Hamiltonian H_0 of Eq. F.1. It also shows all the fourth order perturbation terms which connect the low-energy subspace (shown on left) to the same sub-space (shown on right) after different virtual hoppings to high-energy sectors. All these virtual processes are captured by the effective Hamiltonian in H^4_{eff} in Eq. F.6. The low energy sector P is shown in gray and high-energy sectors Q_1, Q_2, Q_3 are shown in orange color. Each state in a given sector is represented by four spins placed in three boxes where green boxes indicate the magnetic ions site and the blue box indicates the ligand-ion site. All the hopping processes are shown by dashed lines. These hopping processes are responsible for the exchange interactions calculated in Eq. F.9.

where $\mathbf{r}_{iA} = \mathbf{r}_i - \mathbf{r}_A$ and ω is the frequency of EM field. For a circularly polarized light,

$$\mathbf{E}(t) \cdot \mathbf{r}_{iA} = Er_{iA} \cos(\alpha_{iA}) \cos \omega t + Er_{iA} \sin(\alpha_{iA}) \sin \omega t = Er_{iA} \cos(\omega t - \alpha_{iA}) \tag{F.12}$$

where α_{iA} is the angle between $\mathbf{r}_{iA}$ and $\hat{x}$ (we have chosen $\mathbf{r}_{12}$ as x direction). Now, using Jacob-Anger identity, we get

$$H_{\text{hop}}(t) = -\sum_{i=1,2,\sigma} t_A \mathcal{J}_n(\zeta_{iA}) e^{-in\alpha_{iA}} e^{in\omega t} c^\dagger_{i\sigma} c_{A\sigma} + \text{h.c} \tag{F.13}$$

where $\mathcal{J}_n$ denotes n^{th} order Bessel function and $\zeta_{iA} = Er_{iA}\text{Sign}(x_{iA})$. Now, we can use Floquet theory to express this Hamiltonian in a time-independent manner by extendind the original basis to include the photon degree of freedom. In this basis, the hooping part takes the following form

$$H_{\text{hop}} = \sum_{n,m} H^n_{\text{hop}} \otimes |m+n\rangle \langle m| + \text{h.c} \tag{F.14}$$

where $H^n_{\text{hop}} = -\sum_{i=1,2,\sigma} t_A \mathcal{J}_n(\zeta_{iA}) e^{-in\alpha_{iA}} \left(c^\dagger_{i\sigma} c_{A\sigma} + c^\dagger_{A\sigma} c_{i\sigma}\right)$ denotes the n photon-assisted hopping, and similarly the n^{th} sector of unperturbed part becomes

$$H^n_0 = (H_0 + n\omega) \otimes |n\rangle \langle n| \tag{F.15}$$

For an off-resonant drive, we can employ the same SW transformation technique in the extended Floquet basis which can account for all photo-assisted virtual processes. Here, again we notice that the lowest-order contribution to exchange splitting comes from the fourth-order terms and it is captured by the following term

$$H^{(4)}_{\text{eff}} \approx -\sum_{n_1,n,m_1} \sum_{j=1,3} \frac{\hat{P} H_{\text{hop}} \hat{Q}_{2,m_1} H^{m_1-n}_{\text{hop}} \hat{Q}_{j,n} H^{n-n_1}_{\text{hop}} \hat{Q}_{2,n_1} H^{n_1}_{\text{hop}} \hat{P}}{(E_d + m_1\omega)(E_{Q_j} + n\omega)(E_d + n_1\omega)}, \tag{F.16}$$

where $\hat{Q}_{i,n}$ denotes the n photon-dressed $\hat{Q}_i$ sector. By repeating the same steps as in the static case, we get

$$\begin{aligned} J_{\text{ex}} = 4t_A^4 \sum_{m_1,n_1,n} & \frac{1}{2(E_d + n_1\omega)(E_d + m_1\omega)(E_d + \frac{n}{2}\omega)} \\ & (\cos(2(n_1 - m_1)\alpha)\mathcal{J}_{m_1}(\zeta_1)\mathcal{J}_{n_1}(\zeta_1)\mathcal{J}_{n_1-n}(\zeta_1)\mathcal{J}_{m_1-n}(\zeta_1) + \\ & \cos(2(n - m_1 - n_1)\alpha)\mathcal{J}_{n_1}(\zeta_1)\mathcal{J}_{m_1}(\zeta_2)\mathcal{J}_{n_1-n}(\zeta_1)\mathcal{J}_{m_1-n}(\zeta_2)) + \\ & \frac{1}{(E_d + n_1\omega)(E_d + m_1\omega)(U + n\omega)} \\ & \left(\cos(2(n_1 - m_1)\alpha)\mathcal{J}_{m_1}(\zeta_1)\mathcal{J}_{n_1}(\zeta_1)\mathcal{J}_{n_1-n}(\zeta_2)\mathcal{J}_{m_1-n}(\zeta_2)\right) \end{aligned} \tag{F.17}$$

where $\zeta_1 = -\zeta_2 = \frac{\zeta_0}{2\cos\alpha}$, and $\zeta_0 = \frac{eE_0 a}{\omega}$ where $\alpha = \alpha_{1A} = -\alpha_{2A}$ and $a = |\mathbf{r}_{12}|$. A similar approach has been used to calculate the magnetic coupling strength for other cases based on an exchange mechanism involving two-ligand orbitals.

Chapter 10

ULTRAFAST ENHANCEMENT OF FERROMAGNETIC SPIN EXCHANGE INDUCED BY LIGAND-TO-METAL CHARGE TRANSFER

"I have spent many days stringing and unstringing my instrument while the song I came to sing remains unsung."– Rabindranath Tagore

In addition to the Floquet schemes discussed in the previous chapter, exchange interactions can also be modified by light induced charge transfer excitations. Such a process occurs only when the light is resonant with the given transition which modifies the charge distribution. In this chapter, we theoretically predict and experimentally demonstrate a nonthermal pathway to optically enhance superexchange interaction energies in a material based on exciting ligand-to-metal charge-transfer transitions, which introduces lower-order virtual hopping contributions that are absent in the ground state. We demonstrate this effect in the layered ferromagnetic insulator $CrSiTe_3$by exciting Te-to-Cr charge-transfer transitions using ultrashort laser pulses and detecting coherent phonon oscillations that are impulsively generated by superexchange enhancement via magneto-elastic coupling. This mechanism kicks in below the temperature scale where short-range in-plane spin correlations begin to develop and disappears when the excitation energy is tuned away from the charge-transfer resonance, consistent with our predictions. This protocol can potentially be broadly applied to dynamically engineer thermally inaccessible spin Hamiltonians in superexchange dominated magnets and to control magnetic transitions at ultrafast speeds.

This chapter is based on the following reference:

Alon Ron, Swati Chaudhary, Gufeng Zhang, Honglie Ning, Eli Zoghlin, Stephen Wilson, Richard Averitt, Gil Refael, and David Hsieh. "Ultrafast Enhancement of FerromagneticSpin Exchange Induced by Ligand-to-Metal Charge Transfer". Phys. Rev. Lett. **125**, 197203 (2020).

10.1 Introduction

Directly modifying spin exchange energies in a magnetic material with light can enable ultrafast nonthermal control of its magnetic states. Such a capability could potentially provide a pathway to engineer thermally inaccessible spin Hamiltonians, study out-of-equilibrium quantum many-body phenomena, and realize high-speed information processing technologies. Current approaches rely on tuning charge hopping amplitudes that mediate exchange inter-actions by optically exciting either virtual [230, 232, 22, 262, 76, 210, 63, 214, 405] or real [362, 129, 341] charge-transfer (CT) transitions between magnetic sites. In this work, we show that when an exchange interaction is mediated by a nonmagnetic ligand, optically exciting a real CT transition from the ligand to magneticsite enhances the exchange potentially several fold by introducing lower order virtual hopping contributions.Using a phase-resolved coherent phonon spectroscopy technique, we demonstrate this mechanism in $CrSiTe_3$, a prototypical superexchange dominated ferromagnetic insulator.

10.2 Mechanism

In superexchange dominated magnetic insulators, as is realized in many transition metal oxide and chalcogenide based materials, the superexchange energy J_{ex} between spins on neighboring metal sites depends on the number ofvirtual hopping processes that mediate the interaction. A simple illustrative model of ferromagnetic superexchange consists of two metal ions, each with a singly occupied d orbital, interacting via a ligand ion with fully occupied p_x and p_y orbitals in a 90° geometry [Fig. 10.4 (a)]. To leading order in perturbation theory $J_{ex} \propto -(\frac{t}{\Delta_{CT}})^4 J_H$ where t is the metal-to-ligand hopping energy, Δ_{CT} is the charge transfer energy between the ligand p- and metal d-orbital, and J_H is the Hund's coupling between the p-orbitals on the ligand site. This expression reflects the fact that the superexchange is ferromagnetic and is only sensitive to fourth-order virtual hopping processes. In contrast, for a CT excited state where an unpaired spin on a metal site moves to the ligand site (Fig. 1a), the leading order contribution is sensitive to second-order virtual hopping processes owing to the Hund's coupling on the ligand site and is given by $J_{ex} \propto -(\frac{t^2}{\Delta_{CT}^2 - J_H^2}) J_H$. Since Δ_{CT} can be several times larger than both t and J_H in these materials, one can in principle transiently enhance J_{ex} by exciting a CT transition with an ultrafast laser pulse.

Currently, there are two main experimental approaches to measuring ultrafast laser induced exchange (δJ_{ex}) modification. One is to detect δJ_{ex} induced coherent spin precession using THz emission [232] or magneto-optical Kerr spectroscopy [405]. Another is to resolve the transient renormalization of spin wave energies or exchange splitting energies using techniques such as femtosecond stimulated Raman scattering [22, 23] or photoemission spectroscopy [286, 51] respectively. Yet another is to measure the effects of δJ_{ex} on nonlinear responses such as the magneto-refractive effect[22] or magnetization-induced second harmonic generation[23,24]. We propose an alternative approach based on measuring δJ_{ex} induced displacive excitation of coherent phonons, dubbed spin-DECP. In conventional DECP [396], an ultrafast optical pulse instantaneously modifies the charge distribution in a material, which shifts the atomic coordinates of the potential energy minimum thereby producing a restoring Coulombic force $\vec{F}_C$ that initiates oscillatory lattice motion. In a superexchange system, the equilibrium metal-ligand-metal bonding angle θ is determined by a balance between the total elastic and total magnetic energies. The latter typically has the form $\sum_{ij} J_{ex}(\theta)\langle\vec{S}_i\cdot\vec{S}_j\rangle$, where $\langle\vec{S}_i\cdot\vec{S}_j\rangle$ is the spin correlator between metal sites i and j. An instantaneous change in magnetic energy due to δJ_{ex} shifts the potential energy minimum away from the equilibrium θ value, producing a restoring exchange force $\vec{F}_{ex}$ that initiates oscillatory motion (Fig. 1b). The advantage of using spin-DECP to detect δJ_{ex} over the aforementioned techniques is that it relies only on the existence of short-range ($\langle\vec{S}_i\cdot\vec{S}_j\rangle \neq 0$) and not long-range magnetic correlations ($\langle\vec{S}_i \neq 0\rangle$). This helps to disentangle δJ_{ex} from the many laser-induced processes that are known to affect magnetic order [176], and it can be applied to both antiferromagnetic (AFM) and ferromagnetic (FM) materials.

10.3 Experimental Results

An ideal material for demonstrating ultrafast ligand-to-metal CT induced enhancement of J_{ex} using spin-DECP is $CrSiTe_3$, a prototypical superexchange FM insulator with a layered honeycomb structure. In this material the magnetic ($S = 3/2$) degrees of freedom originate from half-filled Cr (metal) $3d\, t_{2g}$ orbitals, which interact predominantly with its nearest neighbors [368] within the honeycomb layer via FM superexchange mediated by the Te (ligand) 5p-orbitals. Direct AFM exchange between $Cr\ t_{2g}$ orbitals also exists but is expected to be weak due to the large Cr-Cr distance [53]. Owing to its quasi-two-dimensional structure, short-range intra-layer FM correlations in $CrSiTe_3$ persist up to $\sim 110K$ [368, 292], far above the Curie temperature $T_c = 33K$. Based on optical absorption [53] and density functional theory (DFT) calculations [67, 165], optical excitation across the direct bandgap of $CrSiTe_3$ primarily involves CT from the Te p- to Cr e_g-orbital (Fig. 2a), which, within our single d-orbital model, potentially leads to a $\sim$ 5-fold enhancement of J_{ex} using reported values of $\Delta_{CT} \sim 1eV$ and $t \sim 0.5eV$ for $CrSiTe_3$[165] and a typical value of $J_H \sim 0.5eV$[375]. The multi d-orbital nature of the magnetism in $CrSiTe_3$does not alter the conclusions drawn from our single d-orbital model (Fig.

1a) because the energies of the additional second-order virtual hopping processes introduced do not depend on the relative spin on the Cr sites. We note that CT excitation is also expected to weaken the AFM direct exchange, thus further enhancing the net FM exchange. This is because Coulomb repulsion from an additional electron in the e_g orbital suppresses virtual hopping between Cr t_{2g} orbitals, and because virtual hopping from a half-filled to empty e_g orbital gives rise to a FM exchange according to the Goodenough-Kanamori rules [116, 114, 163].

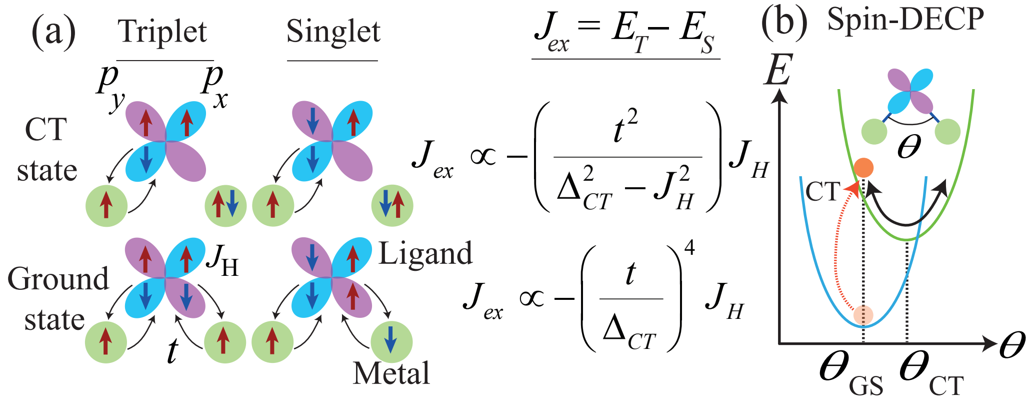

Figure 10.1: Ultrafast exchange enhancement and spin–DECP mechanisms. (a), Schematic showing the triplet and singlet spin configurations of our toy model before (bottom row) and after (top row) CT excitation. The superexchange energy J_{ex}, defined as the triplet and singlet energy splitting, is a function of the metal d-orbital to ligand $p_{x,y}$ orbital hopping energy t, the charge transfer energy Δ_{CT} and the Hund's coupling J_H between the ligand p-orbitals. Owing to the bond angle θ being near 90^o, hopping from the left (right) metal site to the $p_y(p_x)$ ligand orbital is neglected. Expressions for J_{ex} derived from a perturbative calculation in both the ground state (GS) and CT state are displayed to the right. (b), Schematic of the potential energy landscape of the nuclei as function of θ. The CT excitation (dotted red line) causes a sudden shift in the potential minimum due to an impulsive change in ex, launching coherent phonon oscillations about the new minimum.

To distinguish spin-DECP from conventional DECP effects, which is generally challenging because both contribute to exciting a coherent phonon [362], we target modes whose oscillation phase is sensitive to the excitation mechanism. An example is the A_g^2 optical phonon mode in CrSiTe$_3$which involves the periodic expansion and contraction of the Te octahedra that surround each Cr ion (Fig. 2a). An optical excitation that transfers an electron from the Te^{2-} to Cr^{3+} + ions launches this mode through DECP, primarily by reducing the electrostatic attraction between them, producing a repulsive $\vec{F}_C$ that causes an initial expansion of the Te octahedra. Importantly, the same CT excitation also increases J_{ex}, which launches the mode through spin-DECP by pushing θ towards 90^o where the FM superexchange is strongest according to the Goodenough-Kanamori rules [116, 114, 163]. Since, $\theta < 90^o$ in equilibrium [52], this produces an attractive $\vec{F}_{ex}$ that causes an initial contraction of the Te octahedra. Thus, DECP and spin-DECP drive the A_g^3 mode with opposite initial phase. We note that any contribution from impulsive heatingeffects would act in phase with DECP[14].

Phase-resolved coherent phonon spectroscopy of a bulk $CrSiTe_3$ single crystal was performed using ultrafast pump-probe optical reflectivity measurements (Fig. 2a). A typical reflectivity transient acquired using a pump photon energy resonant with Δ_{CT} is shown in Figure 2b, revealing an abrupt drop at delay time $t = 0$ followed by an exponential recovery on a $\tau \sim 2$ ps timescale, tracking the generation and relaxation of CT excitations, respectively. The periodic modulations atop the recovery arise from a coherent optical phonon with frequency f ~3.8 THz, which can be assigned to the A_g^3 mode based on Raman spectroscopy and DFT calculations [53, 205, 234]. A comparison of the oscillatory component $(\Delta R/R_osc)$, isolated by subtracting the exponential background from the data, acquired above and below T_c reveal a π phase difference (Fig. 2b). This suggests that A_g^3 mode excitation evolves from conventional DECP to spin-DECP dominated upon cooling.

To verify a spin-DECP mechanism at low temperature in $CrSiTe_3$, we note that pronounced growth of 2D FM correlations was detected below a temperature scale $T_{2D} \approx 110K$ by both neutron scattering and optical second harmonic generation. Therefore, one should expect spin-DECP effects to be present well above T_c. A complete temperature dependence of $\Delta R = R_{osc}$ and the optical second harmonic susceptibility of our sample are displayed in Figs.3(a) and 3(b). The phonon oscillation phase extracted from the $\Delta R = R_{osc}$ data undergoes a sharp change from 0 to π below $T 90K$ [Fig.3(c)], well inside the 2D correlated paramagnetic regime. To understand this behavior, we reanalyze the data with ϕ absorbed into the sign of the oscillation amplitude A_{ph}. This procedure is valid because must be either 0 or π, corresponding to positive and negative signs for A_{ph}, and helps visualize shifts in the relative weight of the DECP and spin-DECP contributions. As shown in Fig.3(c),A_{ph} is positive ($\phi = 0$) and temperature-independent for $T > T_{2D}$,consistent with the A_g^3 mode being driven exclusively by DECP. Below T_{2D} where $\langle \vec{S}_i \cdot \vec{S}_j \rangle$ begins to grow, a spin-DECP contribution with negative amplitude ($\phi = \pi$) starts to compete with DECP, causing A_{ph} to decrease and eventually change sign atT90K where $\vec{F}_{ex}$ becomes equal and opposite to $\vec{F}_C$. This crossover temperature has no measurable pump fluence dependence as expected since both the total $\vec{F}_{ex}$ and $\vec{F}_C$ should scale with the CT excitation density. As a control, we also measured coherento scillations of an E_g phonon using time-resolved secondharmonic generation under identical experimentalconditions. In contrast to the A_g^3 mode, the E_g mode can only be excited via impulsive stimulated Raman scatteringand not conventional or spin-DECP due to symmetry considerations. We verified that neither the amplitude nor phase of the E_g mode exhibit the aforementioned temperature dependence.

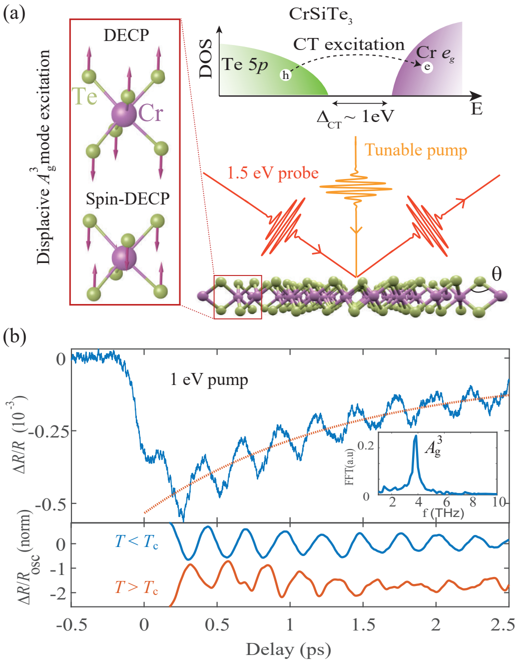

Figure 10.2: Spin-DECP detection method in CrSiTe$_3$. (a) Schematic of CrSiTe$_3$ density of states (DOS) showing that excitation with 1 eV light creates a hole in the Te 5p valence band and an electron in the Cr e_g conduction band. This excitation has the dual effect of reducing the electrostatic attraction between the Cr and Te ions and also enhancing J_{ex}, which acts to decrease and increase the Cr-Te-Cr bond angle θ, respectively, in turn launching the A_g^3 phonon mode with opposite initial directions as shown in the left panel. A schematic of the pump-probe optical reflectivity experiment used to detect the phase of the coherent A_g^3 mode is shown below. (b) (Top) Transient reflectivity of CrSiTe$_3$ following a 1 eV pump pulse taken at $T = 25K$. Inset shows the Fourier transform of the data with a clear peak at the A_g^3 mode frequency. (Bottom) Oscillatory component of the reflectivity transients ($\Delta R/R_{osc}$) taken at $T = 25K$ (blue) and $T = 125K$ (orange, vertically offset for clarity) obtained by subtracting a fitted exponential background (dashed orange line in top panel) from the raw data and then applying a moving average filter.

Below 90 K, A_{ph} becomes increasingly negative as $\langle \vec{S}_i \cdot \vec{S}_j \rangle$ continues to rise (Fig. 3a). However A_{ph} reaches a minimum around T_c, and then turns back towards

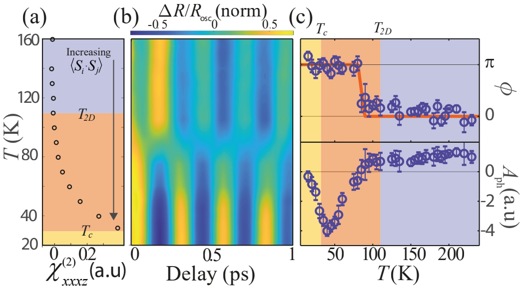

Figure 10.3: CT excitation of A_g^3 mode. (a) Temperature dependence of the $xxxz$ component of the electric quadrupole SHG response of CrSiTe$_3$, which is known to track the in-plane spin correlator $\langle \vec{S}_i \cdot \vec{S}_j \rangle$[292]. Spin correlations markedly increase below $T_{2D} \sim 110K$ and then diverge at $T_c = 33K$ when long-range order sets in. (b) Temperature dependence of the normalized oscillatory component of the reflectivity transients ($\Delta R/R_{osc}$) taken with 1 eV pump excitation after application of a moving average filter. (c) Temperature dependence of the A_g^3 phonon oscillation phase (top) and amplitude (bottom) extracted from the ($\Delta R/R_{osc}$) data. The former was extracted through fitting and the red line is a guide to the eye. The latter was extracted from the FFT amplitude, with a positive or negative sign denoting a 0 or π oscillation phase, respectively. Error bars on the phase and amplitude data are estimated based on the accuracy of determining peak locations in the $\Delta R/R$ data and the FFT spectra, respectively.

zero upon further cooling despite $\langle \vec{S}_i \cdot \vec{S}_j \rangle$ continuing to increase. This trend can be explained by a weakening of the spin-DECP contribution due to exchange striction below T_c . Previous x-ray diffraction studies [52] on CrSiTe$_3$ showed that below T_c there is a continual change in lattice parameters that brings θ closer to 90^o. This means that the separation in θ between the potential energy minima of the equilibrium and CT states become smaller (Fig.1b), progressively reducing $\vec{F}_{ex}$. Exchange striction must dominate the competing effect of increasing $\langle \vec{S}_i \cdot \vec{S}_j \rangle$, leading to a net decreasing spin-DECP to DECP ratio upon cooling below T_c.

To uniquely demonstrate that the observed ultrafast enhancement of J_{ex} is induced by a ligand-to-metal CT transition, we repeated our coherent phonon spectroscopy measurements with a pump photon energy of 0.14 eV, far below the indirect (0.4 eV) bandgap of CrSiTe$_3$[53], to suppress CT transitions between the Te and Cr ions. We note that the absorption edge of CrSiTe$_3$ is characterized by a long Urbach tail [193] that extends well below the indirect gap [53], allowing for finite absorption even at 0.14 eV. Given that the highest energy phonon mode in CrSiTe$_3$ lies at 0.06 eV [53], absorption at such low photon energies is likely to be dominated by transitions into mid-gap defect states30 rather than phonon assisted CT processes. In fact, DFT calculations have shown that it is energetically favorable to form Cr/Si anti-site defects in $CrSiTe_3$ [68] and scanning tunneling microscopy measurements on the closely related compound $CrGeTe_3$ have shown that this type of defect produces a finite density of in-gap states [130]. An optical CT excitation from the Te p- to Si defect orbitals should produce a Coulombic force between the Te and Cr atoms in the same direction as in the Te-Cr CT state due to increased charge negativity of the Te site. However, because the spin of the photo-hole on the Te site is independent of the spin on the Cr sites, second-order virtual hopping processes in the Te-Si CT state do not contribute to J_{ex}. In line with this scenario, Figure 4 shows that a 0.14 eV pump is indeed able to excite the A_g^3 mode well above T_c via conventional DECP, but that no phase change occurs down to 7 K. We note that while a renormalization of J_{ex} imparted by a photo-assisted virtual hopping (i.e. Floquet engineering) mechanism can in principle also drive spin-DECP, such effects are negligible ($< 1\%$) for the pump electric fields ($\sim 0.1V/\text{Å}$) used in our experiments.

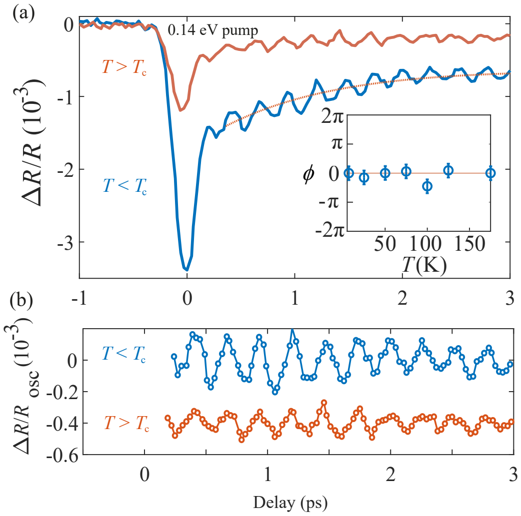

Figure 10.4: Sub-gap excitation of A_g^3 mode. (a) Transient reflectivity of $CrSiTe_3$ following a 0.14 eV pump pulse taken at $T = 25K$ (blue) and $T = 100K$ (orange) showing oscillations at the A_g^3 mode frequency. Inset shows the temperature dependence of the A_g^3 phonon oscillation phase extracted using the same method as described for the 1 eV pump case. Error bars are estimated based on the accuracy of determining peak locations in the $\Delta R/R$ data. (b) Oscillatory component of the reflectivity transients shown in panel a obtained by subtracting a fitted exponential background (dashed orange line in panel (a) from the raw data. Orange curve in panel (b) is vertically offset for clarity. No offsets were performed on the time axis.

10.4 Discussion

The ability to significantly enhance nearest-neighbor superexchange via ligand-to-metal CT excitation as we have demonstrated can potentially be harnessed to transiently manipulate magnetic materials in new ways. Examples include optically inducing FM order above T_c, switching between FM and AFM ordering patterns by altering the ratio of nearest-neighbor to further neighbor interactions, which are known to compete for example in transition-metal trichalcogenide materials such as $\mathrm{CrSiTe_3}$[318, 70], or inducing order in geometrically frustrated magnets by controlling the light polarization to generate anisotropic changes in J_{ex} that relieve frustration. Optically induced FM ordering above T_c was not achievable in our experiments because the stabilization of long-range FM orderng in $\mathrm{CrSiTe_3}$ depends predominantly on inter-layer exchange[368, 292], which is not enhanced by our pump. Moreover, owing to the intra- and inter-layer exchange time scales in $\mathrm{CrSiTe_3}$(h/J_{ex} ~4ps) being longer than the electron-hole recombination time (τ according to Fig.10.2b), there is likely insufficient time for global spin rearrangement. Realizing the aforementioned vision will therefore involve targeting exchange pathways in materials that most strongly affect magnetic order, engineering both materials and excitation protocols to extend $\tau J_{ex}/h$, and developing *ab initio* approaches to calculate J_{ex} in the CT state of complex solids to refine the molecular toy model estimates considered in this work.

Appendix G

APPENDIX

G.1 Details of perturbative calculations

In this section, we present the details of perturbative calculations employed to estimate the changes in FM exchange after the charge transfer process considered in the main text.

Calculation of J_{ex} before and after CT excitation

We consider a toy molecular model consisting of two metal ions ($i = 1, 2$) and one ligand ion, with a metal-ligand-metal bond angle close to 90°. We represent each metal ion by one singly occupied d-orbital and the ligand ion by two doubly occupied p-orbitals (X and Y). The p-orbitals mediate ferromagnetic superexchange interactions between the d-orbitals of the metal ions, which arise due to virtual hopping processes between the metal and ligand orbitals with hopping energies t_{X1}, t_{Y1},t_{X2}, and t_{Y2} (Fig. G.1). Owing to the near bond, we will assume that the $X(Y)$ orbital only has overlap with the d-orbital on metal ion 1(2) such that we can set $t_{X1} = t_{Y2} = t$ and $t_{X2} = t_{Y1} = 0$. We also assume a Hund's coupling J_H between the two p-orbitals of the ligand ion. Following the formalism outlined in Chapter 7 of Ref. [267], we explicitly calculate the superexchange interaction mediated by the ligand ion within our toy model, defined as the energy difference between the spin triplet and singlet states ($J_{ex} = E_T - E_S$), before and after charge transfer (CT) excitation. We ignore the antiferromagnetic direct exchange between the two metal

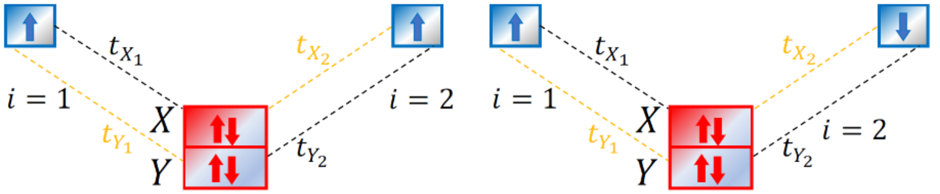

Figure G.1: Toy model consisting of two metal ions (i = 1,2) interacting via superexchange mediated by a ligand ion. The two ligand orbitals are denoted X and Y. The (left) triplet and (right) singlet configurations before CT excitation are shown. Dashed lines show the possible virtual hopping paths, with black (yellow) colors denoting paths with strong (weak) orbital overlap.

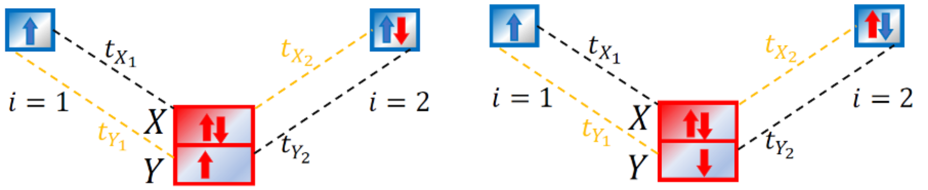

Figure G.2: Triplet (left) and singlet (right) configurations after CT excitation are shown. We ignore the case where an electron is excited from the ligand Y orbital to metal site 1 due to the 90° bond angle.

sites, which is not affected by the metal-ligand interactions.

In the equilibrium state before charge transfer (BCT), Ref. [267] showed that only fourth-order virtual processes contribute to superexchange, which is given by:

$$J_{ex}^{\mathrm{BCT}} = E_T - E_S = -\frac{4t^4}{\Delta_{CT}^2}\frac{2J_H}{4\Delta_{CT}^2 - J_H^2} \tag{G.1}$$

where the charge transfer gap $\Delta_{CT} = U_d + \varepsilon_d - \varepsilon_p$ is defined as the sum of the Coulomb repulsion energy between two electrons in a metal d-orbital (U_d) and the energy difference between the metal d and ligand p orbitals ($\varepsilon_d - \varepsilon_p$). For typical values of $\Delta_{CT} \approx 1eV$ and $J_H \approx 0.5eV$ found in transition metal oxide and chalcogenide materials, we make the approximation that $4\Delta_{CT}^2 - J_H^2 \approx 4\Delta_{CT}^2$, which yields the expression shown in the main text:

$$J_{ex}^{\mathrm{BCT}} = -2\left(\frac{t}{\Delta_{CT}}\right)^4 J_H. \tag{G.2}$$

Using appropriate estimates of $\Delta_{CT} \approx 1eV$, $t \approx 0.5eV$, and $J_H \approx 0.5eV$ for CrSiTe$_3$, Eq. G.2 gives $J_{ex}^{\mathrm{BCT}} \approx 60meV$, which is the same order of magnitude as that reported for CrSiTe$_3$using density functional calculations [67].

The triplet and singlet configurations of the system after charge transfer (ACT) are shown in Fig. G.2. In contrast to the BCT case, one can directly see that the energy of a second-order virtual hopping process between metal ion 1 and the ligand ion depends on the initial spin configuration due to Hund's coupling on the ligand site. This produces a finite second-order contribution to the superexchange that is absent in the BCT case. More explicitly, the triplet energy is given by:

$$E_T = -\frac{t_{X1}^2}{\Delta_{CT} - J_H} + \frac{t_{Y2}^2}{\Delta_{CT}}, \tag{G.3}$$

while the singlet energy is given by:

$$E_T = -\frac{t_{X1}^2}{\Delta_{CT} + J_H} + \frac{t_{Y2}^2}{\Delta_{CT}}. \tag{G.4}$$

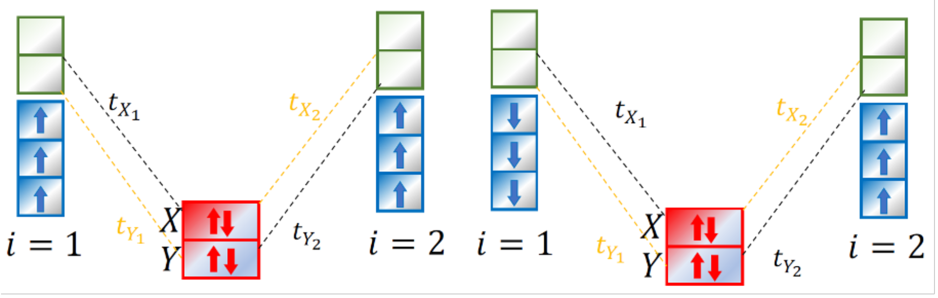

Figure G.3: Multi-orbital model consisting of two metal ions each with three unpaired spins in $t2g$ orbitals (shown in blue) and fully occupied ligand orbitals X and Y (shown in red). This figure shows the (left) triplet and (right) singlet configurations before the charge transfer process. As before, we assume a near 90° bond angle such that the metal 1(2) orbitals have a very large overlap with the ligand $X(Y)$ orbital.

As a result, we arrive at the expression for the triplet-singlet energy splitting that is shown in the main text:

$$J_{ex}^{ACT} = -2\left(\frac{t^2}{\Delta_{CT}^2 - J_H^2}\right) J_H. \tag{G.5}$$

Using again the previous values of $\Delta_{CT} \approx 1eV$, $t \approx 0.5eV$, and J_H $0.5eV$ forCrSiTe$_3$we find that $J_{ex}^{ACT} \approx 300meV$, a roughly five-fold increase compared to the BCT case where the spin-dependent triplet-singlet energy difference was only sensitive to fourth-order virtual processes.

Multi *d*-orbital effects

The toy model considered above very well captures the change in the superexchange energy between the BCT and ACT states in CrSiTe$_3$. A more detailed model may account for the fact that the Cr^{3+} ion has three unpaired electrons in t_2g orbitals, and the fact that CT excitation moves an electron from the Te p orbital to Cr e_g orbital, but the main effects derived from our single d-orbital model remain unchanged as we explain below.

In the BCT state of the multi-orbital model (Fig. G.3), the virtual hopping energies are dictated by Hund's coupling within the ligand p-orbitals as well as the strong Hund's coupling within the d-orbitals. Therefore the ligand mediated superexchange interactions again favor a FM state with a strength that depends on fourth-order virtual hopping processes. In the ACT state (Fig. G.4), the spin of the electron transferred from ligand to metal depends on the spin of the other unpaired electrons

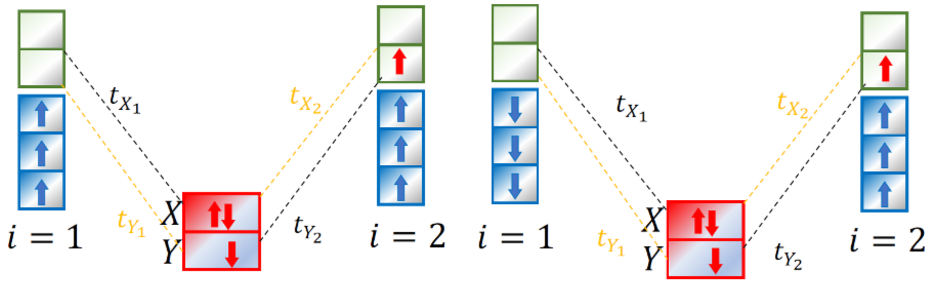

Figure G.4: Triplet (left) and singlet (right) cases after the charge transfer process. This is one of the two possibilities for charge transfer associated with 1 eV excitation in CrSiTe$_3$where an electron is moved from the Y to e_g orbital (shown in green) at site 2. In this case, the transferred spin is parallel to the spin of the unpaired electrons at the metal 2 site because of Hund's coupling within the d-orbitals.

present in the t_2g orbitals due to the large Hund's coupling within the d-orbitals. This is corroborated by first principles calculations that show it is the parallel spin e_g states that lie above the charge transfer gap of $\Delta_{CT} \approx 1eV$. The opposite spin states lie much higher in energy due to Hund's coupling within the d-orbitals. Therefore the unpaired spin left on the ligand Y orbital after CT excitation must be anti-parallel to the spins on the t_{2g} orbital of metal site 2. Similar to our single d-orbital model (Fig. G.2), virtual hopping processes between the ligand X orbital and metal site 1 then become sensitive to the initial spin configuration by virtue of Hund's coupling on the ligand site, once again introducing second-order contributions to the superexchange.

Numerical force estimate for CrSiTe$_3$

Now, we calculate the exchange force arising due to enhanced exchange interactions and compare it to the Coulombic force arising due to redistribution of charges after the charge transfer excitation.

Exchange force.The total change in superexchange coupling before and after CT excitation in our single d-orbital model is given by:

$$\Delta J_{ex} = J_{ex}^{ACT} - J_{ex}^{BCT} = -2\left(\frac{t^2}{\Delta_{CT}^2 - J_H^2} J_H\right) + 2\left(\frac{t}{\Delta_{CT}}\right)^4 J_H. \tag{G.6}$$

The exchange energy depends on magnetic coupling and spin correlations. This gives rise to an exchange force, $\vec{F}_{ex}$, that can be calculated by evaluating the gradient of the change in exchange energy ΔJ_{ex} as:

$$\Delta E_{ex} = \Delta J_{ex} \left\langle \vec{S}_1 \cdot \vec{S}_2 \right\rangle \tag{G.7}$$

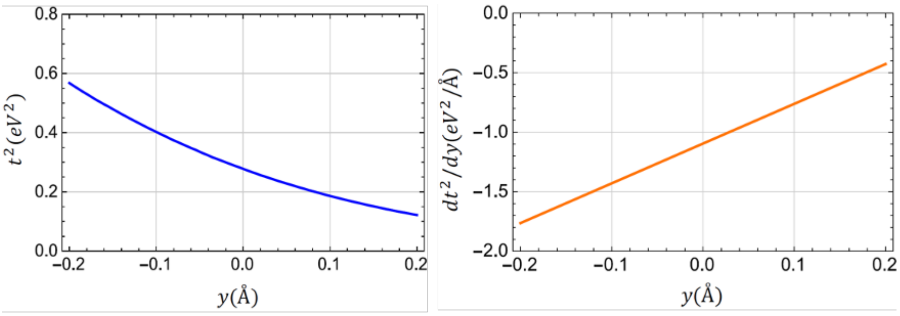

Figure G.5: Change in hopping parameter t and its derivative as a function of the displacement along y direction calculated using a Slater orbital model.

and

$$\vec{F}_{ex} = \nabla\left(\Delta E_{ex}\right). \tag{G.8}$$

For CrSiTe3, we are specifically interested in understanding the force along the phonon coordinate y, the direction along the perpendicular from the Te ion to the line joining two Cr ions. This depends on how the hopping parameters change as a function of y, with $y = 0$ being the equilibrium value. To quantitatively estimate, $\vec{F}_{ex}$, we compute the y dependence of the hopping parameters using Slater type orbitals [321] – with an effective charge slightly higher than the one given by the Slater method in order to match the expected value of hopping parameter – and the reported bond lengths for CrSiTe$_3$. In agreement with the intuitive arguments outlined in the main text, our calculations (Fig. G.5) show that $\vec{F}_{ex}$ tries to increase the bond angle from its equilibrium value which is less than 90° and thus pushes the Te ion towards the Cr ions. To calculate the magnitude of the force, we keep only the second-order contribution to ΔJ_{ex} and use a quantitative estimate for the gradient of the hopping energy based on our Slater orbital model ($\partial_y t^2|_{y=0} = -1eV^2/\text{Å}$) (Fig. G.5) together with the previously used values of $\Delta_{CT} \approx 1eV$, $t \approx 0.5eV$ and $J_H \approx 0.5eV$ for CrSiTe$_3$. Plugging this into our expression for $\vec{F}_{ex}$ yields:

$$F^y_{ex} = -\frac{1}{3}\left\langle \vec{S}_1 \cdot \vec{S}_2 \right\rangle \tag{G.9}$$

in units of $eV/\text{Å}$.

Coulomb force. Next, we estimate the additional Coulombic force $\vec{F}_C$ on a Te atom in the ACT state compared to the BCT state due to changes in the spatial charge distribution. Based on the reported local magnetic moment value of 3.87 μ_B on the Cr^{3+} ions [165] in the BCT state, we estimate that there is an extra -0.87e charge on the Cr ions, which is reportedly due to Cr-Te *dp*-hybridization. Therefore

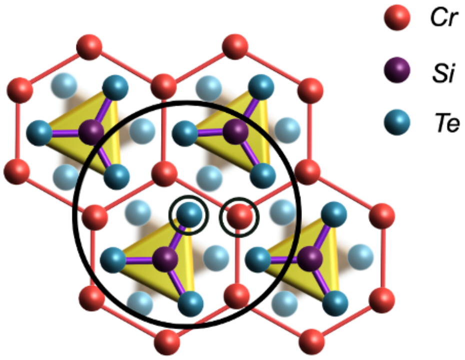

Figure G.6: The top view of a CrSiTe3 monolayer. Cr atoms are arranged on a honeycomb lattice with a layer of Te atoms above and below. Based on x-ray structure refinements, in our model we use a Cr-Te bond length of 2.753 Å where the vertical distance is 1.67 Å and the horizontal distance is 2.189 Å, and a Si-Te bond length of 2.477 Å with vertical distance of 0.567 Å and a horizontal distance 2.4119 Å. The y-direction points out of the page.

we infer that the charge on the Cr ion is +2.13e. The extra charge of +0.87e is shared among three Te^{2-} ions based on the $CrSiTe_3$stoichiometry, and thus each Te atom has an extra charge of +(0.87/3)e, making the charge on each Te ion equal to $(-2+0.87/3)e \approx -1.7e$. For simplicity, we assume that the CT process involves the transfer of one electron from a Te ion to its neighboring Cr ion, which are located by the small black circles in Fig. G.6. For the purpose of this simple calculation we ignore the changes in charge distribution on other Cr and Te ions inside the larger circle in Fig. G.6. The vertical (y) component (perpendicular to the honeycomb plane) of the Coulombic force, F_C^y on the encircled Te ion arises mainly due to a reduction in attractive forces from oppositely charged Cr ions. However, a modified charge on the encircled Te ion also affects the Coulombic repulsion from other Te ions. In order to estimate $\vec{F}_C$ after the CT process, we treat all these ions as point charges and calculate $\vec{F}_C$ on the encircled Te ion using the expression:

$$\vec{F}_C = \sum_i \frac{q_{Te}^f q_i^f - q_{Te}^0 q_i^0}{r_i^2} \hat{r}_i \tag{G.10}$$

where q_i^f and q_i^0 denotes the charge on the i^{th} ion in the ACT and BCT state, respectively, $\vec{r}_i$ is a vector pointing from the i^{th} ion to the Te ion, and the index i runs over all the Cr and Te atoms inside the large circle in Fig. G.6. In this approximation, we calculate $F_C^y \approx +2eV/\text{Å}$, denoting repulsion of the encircled Te ion away from the Cr layer.

Net force. Combining our results for the exchange and Coulomb contributions to the y-component of force on the encircled Te ion in Fig. G.6, we get the expression:

$$F^y = F^y_C + F^y_{ex} \approx \left(2 - \frac{1}{3}\left\langle \vec{S}_1 \cdot \vec{S}_2 \right\rangle\right). \tag{G.11}$$

We see that the exchange force competes with the Coulombic force, and thus the total force should change from being positive to naegative as $\left\langle \vec{S}_1 \cdot \vec{S}_2 \right\rangle$ increases. This explains the observed trend in the amplitude of the coherent A^2_g phonon mode as spin correlations increases upon cooling. We note that our calculations present a very rough estimate and that the Coulombic force is likely overestimated given that we ignored the shielding effect from electron clouds and also assumed that the CT process involves the transfer of one electron from the Te ion to the Cr ion. Model Hamiltonian calculations have shown that $\left\langle \vec{S}_1 \cdot \vec{S}_2 \right\rangle \approx 0.1$ at $T = 90K$ in CrSiTe$_3$ [292], where we observe the coherent A^2_g amplitude and thus F^y to cross zero. This is consistent with the value of F^y_c being overestimated in our model.

G.2 Calculation of Floquet engineering effects

A time-periodic electric (E) field can modify exchange interactions due to hopping renormalization. In CrSiTe$_3$, the FM interactions arise due to virtual hopping between ligand Te ions and metal Cr ions. The two magnetic site model introduced in Section S1 can be described by the following tight-binding Hamiltonian:

$$H = U_d \sum_{i=1,2} \hat{n}_{i\uparrow}\hat{n}_{i\downarrow} + J_H \sum_{\substack{\alpha=X,Y,\\ \alpha\neq\alpha'}} c^\dagger_{\alpha\uparrow}c^\dagger_{\alpha'\downarrow}c^\dagger_{\alpha\downarrow}c^\dagger_{\alpha'\uparrow} + \sum_{\substack{\alpha=X,Y,\\ \sigma=\uparrow,\downarrow}} \varepsilon_p \hat{n}_{\alpha\sigma} + \sum_{\substack{i=1,2,\\ \alpha=X,Y}} t_{\alpha i}\left(c^\dagger_{i\sigma}c_{\alpha\sigma} + c^\dagger_{\alpha\sigma}c_{i\sigma}\right) \tag{G.12}$$

where $i = 1, 2$ are the two Cr sites, X, Y denote the two orbitals of the Te ion, ε_p is the electronic energy of the Te p-orbitals, J_H is the Hund's coupling between these orbitals, and U_d denotes the Coulombic repulsion for electrons in the Cr d-orbitals. In this case, the charge transfer gap, $\Delta_{CT} = U_d - \varepsilon_p$ where all energies are measured with respect to the energy of Cr d-orbitals. As before, owing to the 90° bond angle, we use $t_{X1} = t_{Y2} = t$ and $t_{X2} = t_{Y1} = 0$. The effect of a circularly polarized A.C electric field can be incorporated by making a Peierls' substitution that results in photo-assisted hopping, and thus allows virtual excitations to many different Floquet sectors. By applying fourth-order perturbation theory, we calculate the magnetic

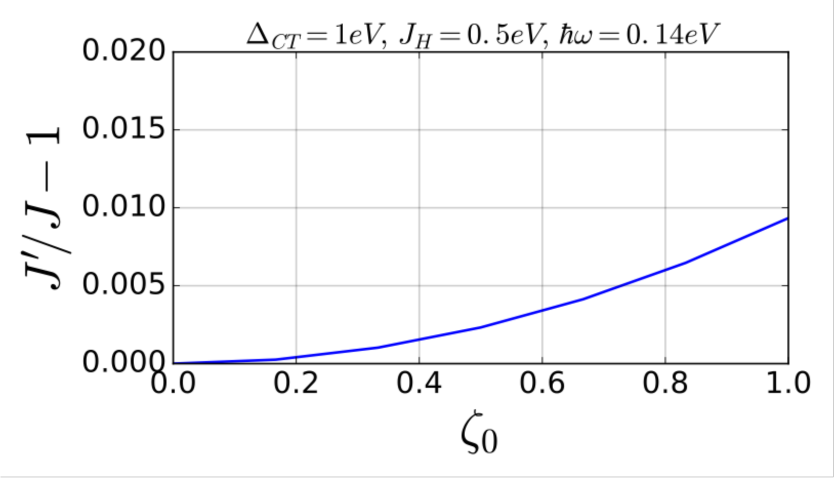

Figure G.7: Calculated fractional change in FM exchange energy without (J) and with driving (J') as a function of the Floquet parameter, ζ_0. Summation was carried out over the range $-12 \leq n, n_1, m_1 \leq 12$. An electric field of $E \approx 0.1\text{V}/\text{Å}$ corresponds roughly to $\zeta_0 = 1$, and thus imparts a change of only about 1% to the exchange.

coupling strength for the Floquet Hamiltonian:

$$\begin{aligned} J_{ex} = t^4 \sum_{m_1,n_1,n} & \frac{4J_H}{(\Delta_{CT} + m_1\omega)(\Delta_{CT} + n_1\omega)((\Delta_{CT} + n\omega)^2 - J_H^2)} \\ & (\cos(2(m_1 - n_1))\, \mathcal{J}_{n_1}(\zeta_{X1})\mathcal{J}_{m_1}(\zeta_{X1})\mathcal{J}_{n-n_1}(\zeta_{Y2})\mathcal{J}_{n-m_1}(\zeta_{Y2}) \\ & \cos(2(n - m_1 - n_1))\, \mathcal{J}_{n_1}(\zeta_{X1})\mathcal{J}_{m_1}(\zeta_{Y2})\mathcal{J}_{n-n_1}(\zeta_{Y2})\mathcal{J}_{n-m_1}(\zeta_{X1})) \end{aligned} \tag{G.13}$$

where $\mathcal{J}_n$ is the n^{th} order Bessel function and the drive parameter is $\eta_{X1} = -\zeta_{Y2} = \frac{\zeta_0}{2\cos\alpha}$, with $\eta_0 = eEa/\hbar$, where e is the electron charge, a is the separation between two Cr ions, $\hbar\omega$ is the driving photon energy, α and is the angle between the line joining the two Cr ions and the component of the Cr-Te bond in the plane containing the Cr ions. The resulting changes in FM coupling are shown in Fig. G.7, which show that such Floquet engineering effects are significant only for $E \approx 1\text{V}/\text{Å}$. In our 0.14 eV pump experiments, the pump fluence is of order $10mJ/cm^2$ and the pulse width is roughly 100 fs, giving a field strength $E \approx 0.1\text{V}/\text{Å}$, which corresponds to a negligible enhancement in the magnetic coupling strength (< 1%).

BIBLIOGRAPHY

[1] D Afanasiev et al. “Ultrafast control of magnetic interactions via light-driven phonons”. In: *Nature Materials* (2021), pp. 1–5. URL: `https://www.nature.com/articles/s41563-021-00922-7`.

[2] Adhip Agarwala and Diptiman Sen. “Effects of local periodic driving on transport and generation of bound states”. In: *Phys. Rev. B* 96 (10 Sept. 2017), p. 104309. DOI: `10.1103/PhysRevB.96.104309`. URL: `https://link.aps.org/doi/10.1103/PhysRevB.96.104309`.

[3] Y. Aharonov and J. Anandan. “Phase change during a cyclic quantum evolution”. In: *Phys. Rev. Lett.* 58 (16 Apr. 1987), pp. 1593–1596. DOI: `10.1103/PhysRevLett.58.1593`. URL: `https://link.aps.org/doi/10.1103/PhysRevLett.58.1593`.

[4] Y. Aharonov and D. Bohm. “Significance of Electromagnetic Potentials in the Quantum Theory”. In: *Phys. Rev.* 115 (3 Aug. 1959), pp. 485–491. DOI: `10.1103/PhysRev.115.485`. URL: `https://link.aps.org/doi/10.1103/PhysRev.115.485`.

[5] Junyeong Ahn, Guang-Yu Guo, and Naoto Nagaosa. “Low-Frequency Divergence and Quantum Geometry of the Bulk Photovoltaic Effect in Topological Semimetals”. In: *Phys. Rev. X* 10 (4 Nov. 2020), p. 041041. DOI: `10.1103/PhysRevX.10.041041`. URL: `https://link.aps.org/doi/10.1103/PhysRevX.10.041041`.

[6] Junyeong Ahn et al. “Riemannian Geometry of Resonant Optical Responses”. In: *arXiv preprint arXiv:2103.01241* (2021). URL: `https://arxiv.org/abs/2103.01241`.

[7] Haoqiang Ai et al. “1T Transition-Metal Dichalcogenides: Strong Bulk Photovoltaic Effect for Enhanced Solar-Power Harvesting”. In: *The Journal of Physical Chemistry C* 124.20 (2020), pp. 11221–11228. URL: `https://pubs.acs.org/doi/abs/10.1021/acs.jpcc.0c02498`.

[8] M Aidelsburger et al. “Measuring the Chern number of Hofstadter bands with ultracold bosonic atoms”. In: *Nat. Phys.* 11 (2015), p. 162. URL: `https://www.nature.com/articles/nphys3171`.

[9] Monika Aidelsburger et al. “Realization of the Hofstadter Hamiltonian with ultracold atoms in optical lattices”. In: *Physical review letters* 111.18 (2013), p. 185301. URL: `https://journals.aps.org/prl/abstract/10.1103/PhysRevLett.111.185301`.

[10] Andrew A. Allocca, Dmitry K. Efimkin, and Victor M. Galitski. “Fingerprints of Berry phases in the bulk exciton spectrum of a topological insulator”. In: *Phys. Rev. B* 98 (4 July 2018), p. 045430. DOI: `10.1103/`

PhysRevB.98.045430. URL: https://link.aps.org/doi/10.1103/PhysRevB.98.045430.

[11] Alexander Altland and Martin R. Zirnbauer. “Nonstandard symmetry classes in mesoscopic normal-superconducting hybrid structures”. In: *Phys. Rev. B* 55 (2 Jan. 1997), pp. 1142–1161. DOI: 10.1103/PhysRevB.55.1142. URL: https://link.aps.org/doi/10.1103/PhysRevB.55.1142.

[12] P. W. Anderson. “Ordering and Antiferromagnetism in Ferrites”. In: *Phys. Rev.* 102 (4 May 1956), pp. 1008–1013. DOI: 10.1103/PhysRev.102.1008. URL: https://link.aps.org/doi/10.1103/PhysRev.102.1008.

[13] Eva Y Andrei et al. “The marvels of moiré materials”. In: *Nature Reviews Materials* (2021), pp. 1–6. URL: https://www.nature.com/articles/s41578-021-00284-1.

[14] S. H. Autler and C. H. Townes. “Stark Effect in Rapidly Varying Fields”. In: *Phys. Rev.* 100 (2 Oct. 1955), pp. 703–722. DOI: 10.1103/PhysRev.100.703. URL: https://link.aps.org/doi/10.1103/PhysRev.100.703.

[15] Joseph E Avron, Daniel Osadchy, and Ruedi Seiler. “A topological look at the quantum Hall effect”. In: *Physics today* 56.8 (2003), pp. 38–42. URL: https://physicstoday.scitation.org/doi/10.1063/1.1611351.

[16] Eyal Bairey, Gil Refael, and Netanel H. Lindner. “Driving induced many-body localization”. In: *Phys. Rev. B* 96 (2 July 2017), p. 020201. DOI: 10.1103/PhysRevB.96.020201. URL: https://link.aps.org/doi/10.1103/PhysRevB.96.020201.

[17] CJ Ballhausen and Andrew D Liehr. “Intensities in inorganic complexes: III. Octahedral complexes of Ni (II) and V (III)”. In: *Molecular Physics* 2.2 (1959), pp. 123–128. URL: https://www.tandfonline.com/doi/abs/10.1080/00268975900100111.

[18] CJ Ballhausen and Andrew D Liehr. “Intensities in inorganic complexes: Part II. Tetrahedral complexes”. In: *Journal of Molecular Spectroscopy* 2.1-6 (1958), pp. 342–360. URL: https://www.sciencedirect.com/science/article/pii/0022285258900869.

[19] Ralph von Baltz and Wolfgang Kraut. “Theory of the bulk photovoltaic effect in pure crystals”. In: *Phys. Rev. B* 23.10 (1981), p. 5590. DOI: 10.1103/PhysRevB.23.5590. URL: https://link.aps.org/doi/10.1103/PhysRevB.23.5590.

[20] M. M. S. Barbeau et al. “Optical control of competing exchange interactions and coherent spin-charge coupling in two-orbital Mott insulators”. In: *SciPost Phys.* 6 (3 2019), p. 27. DOI: 10.21468/SciPostPhys.6.3.027. URL: https://scipost.org/10.21468/SciPostPhys.6.3.027.

[21] DN Basov, RD Averitt, and D Hsieh. “Towards properties on demand in quantum materials”. In: *Nature materials* 16.11 (2017), pp. 1077–1088. URL: `https://www.nature.com/articles/nmat5017`.

[22] G Batignani et al. “Probing ultrafast photo-induced dynamics of the exchange energy in a Heisenberg antiferromagnet”. In: *Nature Photonics* 9.8 (2015), p. 506.

[23] Giovanni Batignani et al. “Modeling the Ultrafast Response of Two-Magnon Raman Excitations in Antiferromagnets on the Femtosecond Timescale”. In: *Annalen der Physik* 531.12 (2019), p. 1900439.

[24] Yuval Baum, Evert PL van Nieuwenburg, and Gil Refael. “From Dynamical Localization to Bunching in interacting Floquet Systems”. In: *arXiv preprint arXiv:1802.08262* (2018). URL: `https://arxiv.org/pdf/1802.08262.pdf`.

[25] VI Belinicher, EL Ivchenko, and BI Sturman. “Kinetic theory of the displacement photovoltaic effect in piezoelectrics”. In: *Zh Eksp Teor Fiz* 83 (1982), pp. 649–661. URL: `http://jetp.ac.ru/cgi-bin/dn/e_056_02_0359.pdf`.

[26] Maxime Ben Dahan et al. “Bloch Oscillations of Atoms in an Optical Potential”. In: *Phys. Rev. Lett.* 76 (24 June 1996), pp. 4508–4511. DOI: `10.1103/PhysRevLett.76.4508`. URL: `https://link.aps.org/doi/10.1103/PhysRevLett.76.4508`.

[27] Wladimir A Benalcazar, B Andrei Bernevig, and Taylor L Hughes. “Quantized electric multipole insulators”. In: *Science* 357.6346 (2017), pp. 61–66. URL: `https://science.sciencemag.org/content/357/6346/61`.

[28] Wladimir A. Benalcazar, B. Andrei Bernevig, and Taylor L. Hughes. “Electric multipole moments, topological multipole moment pumping, and chiral hinge states in crystalline insulators”. In: *Phys. Rev. B* 96 (24 Dec. 2017), p. 245115. DOI: `10.1103/PhysRevB.96.245115`. URL: `https://link.aps.org/doi/10.1103/PhysRevB.96.245115`.

[29] M. Benito et al. “Floquet engineering of long-range p-wave superconductivity”. In: *Phys. Rev. B* 90 (20 Nov. 2014), p. 205127. DOI: `10.1103/PhysRevB.90.205127`. URL: `https://link.aps.org/doi/10.1103/PhysRevB.90.205127`.

[30] Oleg L. Berman and Roman Ya. Kezerashvili. “Superfluidity of dipolar excitons in a transition metal dichalcogenide double layer”. In: *Phys. Rev. B* 96 (9 Sept. 2017), p. 094502. DOI: `10.1103/PhysRevB.96.094502`. URL: `https://link.aps.org/doi/10.1103/PhysRevB.96.094502`.

[31] B Andrei Bernevig and Taylor L Hughes. *Topological insulators and topological superconductors*. Princeton University Press, 2013.

[32] B. A. Bernevig, T. L. Hughes, and S.-C. Zhang. “Quantum Spin Hall Effect and Topological Phase Transition in HgTe Quantum Wells”. In: *Science* 314.5806 (Dec. 2006), pp. 1757–1761. ISSN: 1095-9203. DOI: 10.1126/science.1133734. eprint: cond-mat/0611399. URL: http://dx.doi.org/10.1126/science.1133734.

[33] Michael Victor Berry. “Quantal phase factors accompanying adiabatic changes”. In: *Proceedings of the Royal Society of London. A. Mathematical and Physical Sciences* 392.1802 (1984), pp. 45–57. URL: https://royalsocietypublishing.org/doi/abs/10.1098/rspa.1984.0023.

[34] Michael Victor Berry. “Quantum phase corrections from adiabatic iteration”. In: *Proceedings of the Royal Society of London. A. Mathematical and Physical Sciences* 414.1846 (1987), pp. 31–46. URL: https://royalsocietypublishing.org/doi/abs/10.1098/rspa.1987.0131.

[35] Rafi Bistritzer and Allan H MacDonald. “Moiré bands in twisted double-layer graphene”. In: *Proceedings of the National Academy of Sciences* 108.30 (2011), pp. 12233–12237. URL: https://www.pnas.org/content/108/30/12233.short.

[36] Raditya Weda Bomantara and Jiangbin Gong. “Measurement-only quantum computation with Floquet Majorana corner modes”. In: *Phys. Rev. B* 101 (8 Feb. 2020), p. 085401. DOI: 10.1103/PhysRevB.101.085401. URL: https://link.aps.org/doi/10.1103/PhysRevB.101.085401.

[37] Raditya Weda Bomantara et al. “Coupled-wire construction of static and Floquet second-order topological insulators”. In: *Phys. Rev. B* 99 (4 Jan. 2019), p. 045441. DOI: 10.1103/PhysRevB.99.045441. URL: https://link.aps.org/doi/10.1103/PhysRevB.99.045441.

[38] Sergey Bravyi, David P DiVincenzo, and Daniel Loss. “Schrieffer–Wolff transformation for quantum many-body systems”. In: *Annals of physics* 326.10 (2011), pp. 2793–2826. URL: https://www.sciencedirect.com/science/article/pii/S0003491611001059.

[39] Leda Bucciantini et al. “Emergent Weyl nodes and Fermi arcs in a Floquet Weyl semimetal”. In: *Phys. Rev. B* 96 (4 July 2017), p. 041126. DOI: 10.1103/PhysRevB.96.041126. URL: https://link.aps.org/doi/10.1103/PhysRevB.96.041126.

[40] Marin Bukov, Michael Kolodrubetz, and Anatoli Polkovnikov. “Schrieffer-Wolff Transformation for Periodically Driven Systems: Strongly Correlated Systems with Artificial Gauge Fields”. In: *Phys. Rev. Lett.* 116.12 (2016), pp. 1–6. ISSN: 10797114. DOI: 10.1103/PhysRevLett.116.125301. arXiv: 1510.02744.

[41] Michele Buzzi et al. “Probing dynamics in quantum materials with femtosecond X-rays”. In: *Nature Reviews Materials* 3.9 (2018), pp. 299–311. URL: `https://www.nature.com/articles/s41578-018-0024-9`.

[42] E. V. Calman et al. “Indirect excitons in van der Waals heterostructures at room temperature”. In: *Nature Communications* 9.1 (May 2018). ISSN: 2041-1723. DOI: `10.1038/s41467-018-04293-7`. URL: `http://dx.doi.org/10.1038/s41467-018-04293-7`.

[43] Hernán L. Calvo et al. “Robust edge states induced by electron-phonon interaction in graphene nanoribbons”. In: *Phys. Rev. B* 98 (3 July 2018), p. 035423. DOI: `10.1103/PhysRevB.98.035423`. URL: `https://link.aps.org/doi/10.1103/PhysRevB.98.035423`.

[44] Jinlyu Cao, H.A Fertig, and Luis Brey. “Quantum Geometric Exciton Drift Velocity”. In: (2020). eprint: `arXiv:2008.00259`. URL: `https://arxiv.org/pdf/2008.00259.pdf`.

[45] Ting Cao, Meng Wu, and Steven G. Louie. “Unifying Optical Selection Rules for Excitons in Two Dimensions: Band Topology and Winding Numbers”. In: *Phys. Rev. Lett.* 120 (8 Feb. 2018), p. 087402. DOI: `10.1103/PhysRevLett.120.087402`. URL: `https://link.aps.org/doi/10.1103/PhysRevLett.120.087402`.

[46] Ting Cao et al. “Valley-selective circular dichroism of monolayer molybdenum disulphide”. In: *Nature communications* 3.1 (2012), pp. 1–5. URL: `https://www.nature.com/articles/ncomms1882`.

[47] Yuan Cao et al. “Correlated insulator behaviour at half-filling in magic-angle graphene superlattices”. In: *Nature* 556 (Mar. 2018), pp. 80–84. URL: `https://doi.org/10.1038/nature26154`.

[48] Yuan Cao et al. “Correlated insulator behaviour at half-filling in magic-angle graphene superlattices”. In: *Nature* 556 (Mar. 2018), 80 EP -. URL: `https://doi.org/10.1038/nature26154`.

[49] Yuan Cao et al. “Unconventional superconductivity in magic-angle graphene superlattices”. In: *Nature* 556 (Mar. 2018), pp. 43–50. URL: `https://doi.org/10.1038/nature26160`.

[50] Yuan Cao et al. “Unconventional superconductivity in magic-angle graphene superlattices”. In: *Nature* 556 (Mar. 2018), p. 43. URL: `https://doi.org/10.1038/nature26160`.

[51] Robert Carley et al. “Femtosecond laser excitation drives ferromagnetic gadolinium out of magnetic equilibrium”. In: *Physical review letters* 109.5 (2012), p. 057401.

[52] V Carteaux et al. “Magnetic structure of the new layered ferromagnetic chromium hexatellurosilicate Cr2Si2Te6”. In: *Journal of magnetism and magnetic materials* 94.1-2 (1991), pp. 127–133.

[53] LD Casto et al. “Strong spin-lattice coupling in CrSiTe3”. In: *APL materials* 3.4 (2015), p. 041515. URL: `https://aip.scitation.org/doi/abs/10.1063/1.4914134`.

[54] A. H. Castro Neto et al. “The electronic properties of graphene”. In: *Rev. Mod. Phys.* 81 (1 Jan. 2009), pp. 109–162. DOI: `10.1103/RevModPhys.81.109`. URL: `https://link.aps.org/doi/10.1103/RevModPhys.81.109`.

[55] Tommaso Cea and Francisco Guinea. “Coulomb interaction, phonons, and superconductivity in twisted bilayer graphene”. In: *arXiv:2103.01815* (2021). URL: `https://arxiv.org/abs/2103.16132`.

[56] Tommaso Cea, Niels R. Walet, and Francisco Guinea. “Electronic Band Structure and Pinning of Fermi Energy to Van Hove Singularities in Twisted Bilayer Graphene: A Self-Consistent Approach”. In: *Physical Review B* 100.20 (Nov. 2019), p. 205113. DOI: `10.1103/PhysRevB.100.205113`.

[57] Ching-Kit Chan et al. “Photocurrents in Weyl semimetals”. In: *Phys. Rev. B* 95 (4 Jan. 2017), p. 041104. DOI: `10.1103/PhysRevB.95.041104`. URL: `https://link.aps.org/doi/10.1103/PhysRevB.95.041104`.

[58] Ching-Kit Chan et al. “Type-II Weyl cone transitions in driven semimetals”. In: *Phys. Rev. B* 94 (12 Sept. 2016), p. 121106. DOI: `10.1103/PhysRevB.94.121106`. URL: `https://link.aps.org/doi/10.1103/PhysRevB.94.121106`.

[59] Ming-Che Chang and Qian Niu. “Berry phase, hyperorbits, and the Hofstadter spectrum: Semiclassical dynamics in magnetic Bloch bands”. In: *Phys. Rev. B* 53 (11 Mar. 1996), pp. 7010–7023. DOI: `10.1103/PhysRevB.53.7010`. URL: `https://link.aps.org/doi/10.1103/PhysRevB.53.7010`.

[60] AV Chaplik and MV Entin. “Charged impurities in very thin layers(Electrons and ionized impurities interaction in thin quantizing layers, discussing donor activation energy and kinetic characteristics)”. In: *Zhurnal Eksperimental’noi i Teoreticheskoi Fiziki* 61 (1971), pp. 2496–2503.

[61] Swati Chaudhary, Manuel Endres, and Gil Refael. “Berry electrodynamics: Anomalous drift and pumping from a time-dependent Berry connection”. In: *Phys. Rev. B* 98 (6 Aug. 2018), p. 064310. DOI: `10.1103/PhysRevB.98.064310`.

[62] Swati Chaudhary, David Hsieh, and Gil Refael. “Orbital Floquet engineering of exchange interactions in magnetic materials”. In: *Phys. Rev. B* 100 (22 Dec. 2019), p. 220403. DOI: `10.1103/PhysRevB.100.220403`. URL: `https://link.aps.org/doi/10.1103/PhysRevB.100.220403`.

[63] **Swati Chaudhary**, David Hsieh, and Gil Refael. “Orbital Floquet engineering of exchange interactions in magnetic materials”. In: *Phys. Rev. B* 100 (22 Dec. 2019), p. 220403. DOI: `10.1103/PhysRevB.100.220403`.

[64] **Swati Chaudhary**, Christina Knapp, and Gil Refael. “Anomalous exciton transport in response to a uniform in-plane electric field”. In: *Phys. Rev. B* 103 (16 Apr. 2021), p. 165119. DOI: 10.1103/PhysRevB.103.165119.

[65] Yu-Ao Chen et al. “Controlling Correlated Tunneling and Superexchange Interactions with ac-Driven Optical Lattices”. In: *Phys. Rev. Lett.* 107 (21 Nov. 2011), p. 210405. DOI: 10.1103/PhysRevLett.107.210405. URL: https://link.aps.org/doi/10.1103/PhysRevLett.107.210405.

[66] Hailong Chen et al. “Ultrafast formation of interlayer hot excitons in atomically thin MoS 2/WS 2 heterostructures”. In: *Nature communications* 7.1 (2016), pp. 1–8. URL: https://www.nature.com/articles/ncomms12512.

[67] Xiaofang Chen, Jingshan Qi, and Daning Shi. “Strain-engineering of magnetic coupling in two-dimensional magnetic semiconductor CrSiTe3: Competition of direct exchange interaction and superexchange interaction”. In: *Physics Letters A* 379.1-2 (2015), pp. 60–63.

[68] Haixia Cheng et al. “Robust two-dimensional bipolar magnetic semiconductors by defect engineering”. In: *Journal of Materials Chemistry C* 6.31 (2018), pp. 8435–8443.

[69] Ran Cheng. “Quantum geometric tensor (Fubini-study metric) in simple quantum system: A pedagogical introduction”. In: *arXiv:1012.1337* (2010). URL: https://arxiv.org/abs/1012.1337.

[70] Bheema Lingam Chittari et al. “Electronic and magnetic properties of single-layer MPX_3 metal phosphorous trichalcogenides”. In: *Phys. Rev. B* 94 (18 Nov. 2016), p. 184428. DOI: 10.1103/PhysRevB.94.184428. URL: https://link.aps.org/doi/10.1103/PhysRevB.94.184428.

[71] Ching-Kai Chiu, Hong Yao, and Shinsei Ryu. “Classification of topological insulators and superconductors in the presence of reflection symmetry”. In: *Phys. Rev. B* 88 (7 Aug. 2013), p. 075142. DOI: 10.1103/PhysRevB.88.075142. URL: https://link.aps.org/doi/10.1103/PhysRevB.88.075142.

[72] Ching-Kai Chiu et al. “Classification of topological quantum matter with symmetries”. In: *Rev. Mod. Phys.* 88 (3 Aug. 2016), p. 035005. DOI: 10.1103/RevModPhys.88.035005. URL: https://link.aps.org/doi/10.1103/RevModPhys.88.035005.

[73] Youngjoon Choi et al. “Correlation-driven topological phases in magic-angle twisted bilayer graphene”. In: *Nature* 589.7843 (2021), pp. 536–541. URL: https://www.nature.com/articles/s41586-020-03159-7.

[74] Youngjoon Choi et al. “Interaction-driven Band Flattening and Correlated Phases in Twisted Bilayer Graphene”. In: (2021). arXiv: 2102.02209 [cond-mat.str-el].

[75] Alberto Ciarrocchi et al. "Polarization switching and electrical control of interlayer excitons in two-dimensional van der Waals heterostructures". In: *Nature Photonics* 13.2 (Dec. 2018), pp. 131–136. ISSN: 1749-4893. DOI: 10.1038/s41566-018-0325-y. URL: http://dx.doi.org/10.1038/s41566-018-0325-y.

[76] Martin Claassen et al. "Dynamical time-reversal symmetry breaking and photo-induced chiral spin liquids in frustrated Mott insulators". In: *Nature communications* 8.1 (2017), p. 1192.

[77] Alexandr I. Cocemasov, Denis L. Nika, and Alexander A. Balandin. "Phonons in twisted bilayer graphene". In: *Phys. Rev. B* 88 (3 July 2013), p. 035428. DOI: 10.1103/PhysRevB.88.035428. URL: https://link.aps.org/doi/10.1103/PhysRevB.88.035428.

[78] Tyler L Cocker et al. "An ultrafast terahertz scanning tunnelling microscope". In: *Nature Photonics* 7.8 (2013), pp. 620–625. URL: https://www.nature.com/articles/nphoton.2013.151.pdf?draft=marketing.

[79] Ashley M Cook et al. "Design principles for shift current photovoltaics". In: *Nature communications* 8.1 (2017), pp. 1–9. URL: https://www.nature.com/articles/ncomms14176.

[80] Adrien P Cote et al. "Porous, crystalline, covalent organic frameworks". In: *science* 310.5751 (2005), pp. 1166–1170. URL: https://science.sciencemag.org/content/310/5751/1166.full.

[81] Pierluigi Cudazzo, Ilya V. Tokatly, and Angel Rubio. "Dielectric screening in two-dimensional insulators: Implications for excitonic and impurity states in graphane". In: *Phys. Rev. B* 84 (8 Aug. 2011), p. 085406. DOI: 10.1103/PhysRevB.84.085406. URL: https://link.aps.org/doi/10.1103/PhysRevB.84.085406.

[82] Alexandre Dauphin and Nathan Goldman. "Extracting the Chern number from the dynamics of a Fermi gas: Implementing a quantum Hall bar for cold atoms". In: *Phys. Rev. Lett.* 111.13 (2013), p. 135302. DOI: 10.1103/PhysRevLett.111.135302. URL: https://link.aps.org/doi/10.1103/PhysRevLett.111.135302.

[83] Oindrila Deb and Diptiman Sen. "Generating surface states in a Weyl semimetal by applying electromagnetic radiation". In: *Phys. Rev. B* 95 (14 Apr. 2017), p. 144311. DOI: 10.1103/PhysRevB.95.144311. URL: https://link.aps.org/doi/10.1103/PhysRevB.95.144311.

[84] Roberto B Diener et al. "Intrinsic self-rotation of BEC Bloch wave packets". In: *arXiv:* 0306184 (2003). URL: https://arxiv.org/abs/cond-mat/0306184.

[85] Kai-He Ding et al. “Quantum Hall effect in ac driven graphene: From the half-integer to the integer case”. In: *Phys. Rev. B* 97 (3 Jan. 2018), p. 035123. DOI: 10.1103/PhysRevB.97.035123. URL: https://link.aps.org/doi/10.1103/PhysRevB.97.035123.

[86] Ankit S. Disa et al. “Orbital Engineering in Symmetry-Breaking Polar Heterostructures”. In: *Phys. Rev. Lett.* 114 (2 Jan. 2015), p. 026801. DOI: 10.1103/PhysRevLett.114.026801. URL: https://link.aps.org/doi/10.1103/PhysRevLett.114.026801.

[87] Liang Dong and Qian Niu. “Geometrodynamics of electrons in a crystal under position and time dependent deformation”. In: *arXiv:* 1802.02887 (2018). URL: https://arxiv.org/abs/1802.02887.

[88] Lucia Duca et al. “An Aharonov-Bohm interferometer for determining Bloch band topology”. In: *Science* 347.6219 (2015), pp. 288–292. URL: http://science.sciencemag.org/content/347/6219/288.

[89] André Eckardt. “Colloquium: Atomic quantum gases in periodically driven optical lattices”. In: *Reviews of Modern Physics* 89.1 (2017), p. 011004. URL: https://journals.aps.org/rmp/abstract/10.1103/RevModPhys.89.011004.

[90] André Eckardt. “Colloquium: Atomic quantum gases in periodically driven optical lattices”. In: *Rev. Mod. Phys.* 89 (1 Mar. 2017), p. 011004. DOI: 10.1103/RevModPhys.89.011004. URL: https://link.aps.org/doi/10.1103/RevModPhys.89.011004.

[91] André Eckardt et al. “Exploring dynamic localization with a Bose-Einstein condensate”. In: *Physical Review A* 79.1 (2009), p. 013611. URL: https://journals.aps.org/pra/abstract/10.1103/PhysRevA.79.013611.

[92] Martin Eckstein, Johan H Mentink, and Philipp Werner. “Designing spin and orbital exchange hamiltonians with ultrashort electric field transients”. In: *arXiv preprint arXiv:1703.03269* (2017). URL: https://arxiv.org/abs/1703.03269.

[93] Motohiko Ezawa. “Photoinduced Topological Phase Transition and a Single Dirac-Cone State in Silicene”. In: *Phys. Rev. Lett.* 110 (2 Jan. 2013), p. 026603. DOI: 10.1103/PhysRevLett.110.026603. URL: https://link.aps.org/doi/10.1103/PhysRevLett.110.026603.

[94] Motohiko Ezawa. “Photoinduced topological phase transition from a crossing-line nodal semimetal to a multiple-Weyl semimetal”. In: *Phys. Rev. B* 96 (4 July 2017), p. 041205. DOI: 10.1103/PhysRevB.96.041205. URL: https://link.aps.org/doi/10.1103/PhysRevB.96.041205.

[95] Motohiko Ezawa. “Photoinduced topological phase transition from a crossing-line nodal semimetal to a multiple-Weyl semimetal”. In: *Phys. Rev. B* 96 (4 July 2017), p. 041205. DOI: 10.1103/PhysRevB.96.041205. URL: https://link.aps.org/doi/10.1103/PhysRevB.96.041205.

[96] Hui Fang et al. “Strong interlayer coupling in van der Waals heterostructures built from single-layer chalcogenides”. In: *Proceedings of the National Academy of Sciences* 111.17 (2014), pp. 6198–6202. DOI: 10.1073/pnas.1405435111.

[97] Daniele Fausti et al. “Light-induced superconductivity in a stripe-ordered cuprate”. In: *science* 331.6014 (2011), pp. 189–191. URL: http://science.sciencemag.org/content/sci/331/6014/189.full.pdf?sid=7ab2aa67-2776-4d79-accd-2670edd5f0f4.

[98] N Fläschner et al. “Experimental reconstruction of the Berry curvature in a Floquet Bloch band”. In: *Science* 352.6289 (2016), pp. 1091–1094. URL: http://science.sciencemag.org/content/352/6289/1091.

[99] MM Fogler, LV Butov, and KS Novoselov. “High-temperature superfluidity with indirect excitons in van der Waals heterostructures”. In: *Nature communications* 5.1 (2014), pp. 1–5. URL: https://www.nature.com/articles/ncomms5555?origin=ppub.

[100] Benjamin M. Fregoso, Takahiro Morimoto, and Joel E. Moore. “Quantitative relationship between polarization differences and the zone-averaged shift photocurrent”. In: *Phys. Rev. B* 96 (7 Aug. 2017), p. 075421. DOI: 10.1103/PhysRevB.96.075421. URL: https://link.aps.org/doi/10.1103/PhysRevB.96.075421.

[101] VM Fridkin. “Bulk photovoltaic effect in noncentrosymmetric crystals”. In: *Crystallogr. Rep.* 46.4 (2001), pp. 654–658. URL: https://link.springer.com/article/10.1134%2F1.1387133.

[102] Liang Fu. “Topological Crystalline Insulators”. In: *Phys. Rev. Lett.* 106 (10 Mar. 2011), p. 106802. DOI: 10.1103/PhysRevLett.106.106802. URL: https://link.aps.org/doi/10.1103/PhysRevLett.106.106802.

[103] Pei-Hao Fu et al. “Phase transitions in three-dimensional Dirac semimetal induced by off-resonant circularly polarized light”. In: *Physics Letters A* 381.40 (2017), pp. 3499–3504. URL: https://www.sciencedirect.com/science/article/pii/S0375960117308149?via%3Dihub.

[104] Shiyuan Gao, Li Yang, and Catalin D Spataru. “Interlayer coupling and gate-tunable excitons in transition metal dichalcogenide heterostructures”. In: *Nano letters* 17.12 (2017), pp. 7809–7813. URL: https://pubs.acs.org/doi/abs/10.1021/acs.nanolett.7b04021?casa_token=fPogixOzStQAAAAA:4CNfWn6PgL_YYOfVSZXj6XbG1tqoFGY_8TA2znFTElBgdTrQeHWDnDFBA4E1_NvvFaMFQtKp7OCWY70.

[105] Max Geier et al. “Second-order topological insulators and superconductors with an order-two crystalline symmetry”. In: *Phys. Rev. B* 97 (20 May 2018), p. 205135. DOI: 10.1103/PhysRevB.97.205135. URL: https://link.aps.org/doi/10.1103/PhysRevB.97.205135.

[106] Andre K Geim and Irina V Grigorieva. “Van der Waals heterostructures”. In: *Nature* 499.7459 (2013), pp. 419–425. URL: https://www.nature.com/articles/nature12385.

[107] Iann C. Gerber et al. “Interlayer excitons in bilayer MoS_2 with strong oscillator strength up to room temperature”. In: *Phys. Rev. B* 99 (3 Jan. 2019), p. 035443. DOI: 10.1103/PhysRevB.99.035443. URL: https://link.aps.org/doi/10.1103/PhysRevB.99.035443.

[108] A Gianfrate et al. “Measurement of the quantum geometric tensor and of the anomalous Hall drift”. In: *Nature* 578.7795 (2020), pp. 381–385. URL: https://www.nature.com/articles/s41586-020-1989-2.

[109] Roland Gillen and Janina Maultzsch. “Interlayer excitons in $MoSe_2/WSe_2$ heterostructures from first principles”. In: *Phys. Rev. B* 97 (16 Apr. 2018), p. 165306. DOI: 10.1103/PhysRevB.97.165306. URL: https://link.aps.org/doi/10.1103/PhysRevB.97.165306.

[110] Feliciano Giustino et al. “The 2021 quantum materials roadmap”. In: *Journal of Physics: Materials* 3.4 (2021), p. 042006. URL: https://iopscience.iop.org/article/10.1088/2515-7639/abb74e/meta.

[111] N. Goldman and J. Dalibard. “Periodically Driven Quantum Systems: Effective Hamiltonians and Engineered Gauge Fields”. In: *Phys. Rev. X* 4 (3 Aug. 2014), p. 031027. DOI: 10.1103/PhysRevX.4.031027. URL: https://link.aps.org/doi/10.1103/PhysRevX.4.031027.

[112] Nathan Goldman et al. “Light-induced gauge fields for ultracold atoms”. In: *Reports on Progress in Physics* 77.12 (2014), p. 126401. URL: http://iopscience.iop.org/article/10.1088/0034-4885/77/12/126401/meta.

[113] JB Goodenough. *Magnetism and the Chemical Bond, Interscience(Wiley)*. 1963.

[114] John B Goodenough. “An interpretation of the magnetic properties of the perovskite-type mixed crystals La1- xSrxCoO3- λ”. In: *Journal of Physics and Chemistry of Solids* 6.2-3 (1958), pp. 287–297.

[115] John B Goodenough. “Goodenough-Kanamori rule”. In: *Scholarpedia* 3.10 (2008), p. 7382.

[116] John B Goodenough. “Theory of the role of covalence in the perovskite-type manganites [La, M (II)] Mn O 3”. In: *Physical Review* 100.2 (1955), p. 564.

[117] Zachary A. H. Goodwin et al. “Hartree Theory Calculations of Quasiparticle Properties in Twisted Bilayer Graphene”. In: *arXiv:2004.14784 [cond-mat]* (July 2020). arXiv: 2004.14784 [cond-mat].

[118] Zachary AH Goodwin et al. “Hartree theory calculations of quasiparticle properties in twisted bilayer graphene”. In: *arXiv:2004.14784* (2020). URL: https://arxiv.org/pdf/2004.14784.pdf.

[119] Frederik Görg et al. “Enhancement and sign change of magnetic correlations in a driven quantum many-body system”. In: *Nature* 553.7689 (2018), p. 481. URL: `https://www.nature.com/articles/nature25135`.

[120] Christoph W Groth et al. “Kwant: a software package for quantum transport”. In: *New Journal of Physics* 16.6 (2014), p. 063065. URL: `https://iopscience.iop.org/article/10.1088/1367-2630/16/6/063065/meta`.

[121] Fabian Grusdt, Dmitry Abanin, and Eugene Demler. “Measuring Z 2 topological invariants in optical lattices using interferometry”. In: *Phys. Rev. A* 89.4 (2014), p. 043621. URL: `https://journals.aps.org/pra/abstract/10.1103/PhysRevA.89.043621`.

[122] Adolfo G. Grushin, Álvaro Gómez-León, and Titus Neupert. “Floquet Fractional Chern Insulators”. In: *Phys. Rev. Lett.* 112 (15 Apr. 2014), p. 156801. DOI: `10.1103/PhysRevLett.112.156801`. URL: `https://link.aps.org/doi/10.1103/PhysRevLett.112.156801`.

[123] Mingqiang Gu and James M. Rondinelli. “Nonlinear phononic control and emergent magnetism in Mott insulating titanates”. In: *Phys. Rev. B* 98 (2 July 2018), p. 024102. DOI: `10.1103/PhysRevB.98.024102`. URL: `https://link.aps.org/doi/10.1103/PhysRevB.98.024102`.

[124] Mingqiang Gu and James M. Rondinelli. “Nonlinear phononic control and emergent magnetism in Mott insulating titanates”. In: *Phys. Rev. B* 98 (2 July 2018), p. 024102. DOI: `10.1103/PhysRevB.98.024102`. URL: `https://link.aps.org/doi/10.1103/PhysRevB.98.024102`.

[125] Satya N Guin et al. “2D-Berry-Curvature-Driven Large Anomalous Hall Effect in Layered Topological Nodal-Line MnAlGe”. In: *Advanced Materials* (2021), p. 2006301.

[126] Francisco Guinea and Niels R Walet. “Electrostatic effects, band distortions, and superconductivity in twisted graphene bilayers”. In: *Proceedings of the National Academy of Sciences* 115.52 (2018), pp. 13174–13179. URL: `https://www.pnas.org/content/115/52/13174.short`.

[127] Francisco Guinea and Niels R. Walet. “Electrostatic Effects, Band Distortions, and Superconductivity in Twisted Graphene Bilayers”. In: *Proceedings of the National Academy of Sciences* 115.52 (Dec. 2018), pp. 13174–13179. ISSN: 0027-8424, 1091-6490. DOI: `10.1073/pnas.1810947115`.

[128] F. D. M. Haldane. “Model for a Quantum Hall Effect without Landau Levels: Condensed-Matter Realization of the "Parity Anomaly"”. In: *Phys. Rev. Lett.* 61 (18 Oct. 1988), pp. 2015–2018. DOI: `10.1103/PhysRevLett.61.2015`. URL: `https://link.aps.org/doi/10.1103/PhysRevLett.61.2015`.

[129] IP Handayani et al. “Dynamics of photo-excited electrons in magnetically ordered TbMnO3”. In: *Journal of Physics: Condensed Matter* 25.11 (2013), p. 116007.

[130] Zhenqi Hao et al. “Atomic scale electronic structure of the ferromagnetic semiconductor Cr2Ge2Te6”. In: *Science Bulletin* 63.13 (2018), pp. 825–830.

[131] Fenner Harper and Rahul Roy. “Floquet Topological Order in Interacting Systems of Bosons and Fermions”. In: *Phys. Rev. Lett.* 118 (11 Mar. 2017), p. 115301. DOI: `10.1103/PhysRevLett.118.115301`. URL: `https://link.aps.org/doi/10.1103/PhysRevLett.118.115301`.

[132] M. Z. Hasan and C. L. Kane. “Colloquium: Topological insulators”. In: *Rev. Mod. Phys.* 82 (4 Nov. 2010), pp. 3045–3067. DOI: `10.1103/RevModPhys.82.3045`. URL: `https://link.aps.org/doi/10.1103/RevModPhys.82.3045`.

[133] Mehedi Hasan et al. “Topological edge-state engineering with high-frequency electromagnetic radiation”. In: *Phys. Rev. B* 96 (20 Nov. 2017), p. 205127. DOI: `10.1103/PhysRevB.96.205127`. URL: `https://link.aps.org/doi/10.1103/PhysRevB.96.205127`.

[134] Mehedi Hasan et al. “Topological edge-state engineering with high-frequency electromagnetic radiation”. In: *Phys. Rev. B* 96 (20 Nov. 2017), p. 205127. DOI: `10.1103/PhysRevB.96.205127`. URL: `https://link.aps.org/doi/10.1103/PhysRevB.96.205127`.

[135] Philipp Hauke et al. “Non-Abelian Gauge Fields and Topological Insulators in Shaken Optical Lattices”. In: *Phys. Rev. Lett.* 109 (14 Oct. 2012), p. 145301. DOI: `10.1103/PhysRevLett.109.145301`. URL: `https://link.aps.org/doi/10.1103/PhysRevLett.109.145301`.

[136] Ke He, Yayu Wang, and Qi-Kun Xue. “Topological materials: quantum anomalous Hall system”. In: *Annual Review of Condensed Matter Physics* 9 (2018), pp. 329–344. URL: `https://www.annualreviews.org/doi/pdf/10.1146/annurev-conmatphys-033117-054144`.

[137] Kasra Hejazi, Jianpeng Liu, and Leon Balents. “Floquet spin and spin-orbital Hamiltonians and doublon-holon generations in periodically driven Mott insulators”. In: *Phys. Rev. B* 99 (20 May 2019), p. 205111. DOI: `10.1103/PhysRevB.99.205111`. URL: `https://link.aps.org/doi/10.1103/PhysRevB.99.205111`.

[138] A. Hichri, S. Jaziri, and M. O. Goerbig. “Charged excitons in two-dimensional transition metal dichalcogenides: Semiclassical calculation of Berry curvature effects”. In: *Phys. Rev. B* 100 (11 Sept. 2019), p. 115426. DOI: `10.1103/PhysRevB.100.115426`. URL: `https://link.aps.org/doi/10.1103/PhysRevB.100.115426`.

[139] Martin Holthaus. “Floquet engineering with quasienergy bands of periodically driven optical lattices”. In: *Journal of Physics B: Atomic, Molecular and Optical Physics* 49.1 (2015), p. 013001. URL: `http://iopscience.iop.org/article/10.1088/0953-4075/49/1/013001/meta`.

[140] Pavan Hosur. “Circular photogalvanic effect on topological insulator surfaces: Berry-curvature-dependent response”. In: *Phys. Rev. B* 83 (3 Jan. 2011), p. 035309. DOI: `10.1103/PhysRevB.83.035309`. URL: `https://link.aps.org/doi/10.1103/PhysRevB.83.035309`.

[141] Hannes Hübener, Umberto De Giovannini, and Angel Rubio. “Phonon driven Floquet matter”. In: *Nano letters* 18.2 (2018), pp. 1535–1542. URL: `https://pubs.acs.org/doi/full/10.1021/acs.nanolett.7b05391`.

[142] Taylor L. Hughes, Emil Prodan, and B. Andrei Bernevig. “Inversion-symmetric topological insulators”. In: *Phys. Rev. B* 83 (24 June 2011), p. 245132. DOI: `10.1103/PhysRevB.83.245132`. URL: `https://link.aps.org/doi/10.1103/PhysRevB.83.245132`.

[143] M. N. Iliev et al. “Phonons and magnetic excitations in the Mott insulator $LaTiO_3$”. In: *Phys. Rev. B* 69 (17 May 2004), p. 172301. DOI: `10.1103/PhysRevB.69.172301`. URL: `https://link.aps.org/doi/10.1103/PhysRevB.69.172301`.

[144] M. N. Iliev et al. “Raman spectroscopy of orthorhombic perovskitelike $YMnO_3$ and $LaMnO_3$”. In: *Phys. Rev. B* 57 (5 Feb. 1998), pp. 2872–2877. DOI: `10.1103/PhysRevB.57.2872`. URL: `https://link.aps.org/doi/10.1103/PhysRevB.57.2872`.

[145] Stefan Imhof et al. “Topolectrical-circuit realization of topological corner modes”. In: *Nature Physics* 14.9 (2018), p. 925. URL: `https://www.nature.com/articles/s41567-018-0246-1`.

[146] Jun-ichi Inoue. “Floquet Engineered Quadri-partite Lattice System as an Extension of the Topological Haldane Model”. In: *Journal of the Physical Society of Japan* 87.3 (2018), p. 034711. URL: `https://journals.jps.jp/doi/10.7566/JPSJ.87.034711`.

[147] Jun-ichi Inoue and Akihiro Tanaka. “Photoinduced Transition between Conventional and Topological Insulators in Two-Dimensional Electronic Systems”. In: *Phys. Rev. Lett.* (1 June 2010), p. 017401. DOI: `10.1103/PhysRevLett.105.017401`. URL: `https://link.aps.org/doi/10.1103/PhysRevLett.105.017401`.

[148] AP Itin and MI Katsnelson. “Effective hamiltonians for rapidly driven many-body lattice systems: induced exchange interactions and density-dependent hoppings”. In: *Phys. Rev. Lett.* 115.7 (2015), p. 075301. URL: `https://journals.aps.org/prl/abstract/10.1103/PhysRevLett.115.075301`.

[149] Dieter Jaksch and Peter Zoller. “Creation of effective magnetic fields in optical lattices: the Hofstadter butterfly for cold neutral atoms”. In: *New Journal of Physics* 5.1 (2003), p. 56. URL: `https://iopscience.iop.org/article/10.1088/1367-2630/5/1/356/meta`.

[150] Jean-Marc Jancu et al. “Empirical spds* tight-binding calculation for cubic semiconductors: General method and material parameters”. In: *Phys. Rev. B* 57 (11 Mar. 1998), pp. 6493–6507. DOI: `10.1103/PhysRevB.57.6493`. URL: `https://link.aps.org/doi/10.1103/PhysRevB.57.6493`.

[151] Luis A Jauregui and Philip Kim. “2D materials: Curved paths of electron–hole pairs”. In: *Nature Materials* 16.12 (2017), pp. 1169–1170. URL: `https://www.nature.com/articles/nmat5046`.

[152] Wei Ji, Kui Yao, and Yung C. Liang. “Evidence of bulk photovoltaic effect and large tensor coefficient in ferroelectric $BiFeO_3$ thin films”. In: *Phys. Rev. B* 84 (9 Sept. 2011), p. 094115. DOI: `10.1103/PhysRevB.84.094115`. URL: `https://link.aps.org/doi/10.1103/PhysRevB.84.094115`.

[153] Wei Jiang, Huaqing Huang, and Feng Liu. “A Lieb-like lattice in a covalent-organic framework and its Stoner ferromagnetism”. In: *Nature communications* 10.1 (2019), p. 2207. URL: `https://www.nature.com/articles/s41467-019-10094-3`.

[154] Chenhao Jin et al. “Imaging of pure spin-valley diffusion current in WS2-WSe2 heterostructures”. In: *Science* 360.6391 (2018), pp. 893–896. URL: `https://science.sciencemag.org/content/360/6391/893.abstract`.

[155] Gregor Jotzu et al. “Experimental realization of the topological Haldane model with ultracold fermions”. In: *Nature* 515.7526 (2014), pp. 237–240. URL: `https://www.nature.com/articles/nature13915`.

[156] Gregor Jotzu et al. “Experimental realization of the topological Haldane model with ultracold fermions”. In: *Nature* 515.7526 (2014), p. 237. URL: `https://www.nature.com/articles/nature13915`.

[157] Fernando de Juan et al. “Quantized circular photogalvanic effect in Weyl semimetals”. In: *Nature communications* 8.1 (2017), pp. 1–7. URL: `https://www.nature.com/articles/ncomms15995`.

[158] Fernando de Juan et al. “Quantized circular photogalvanic effect in Weyl semimetals”. In: *Nature communications* 8.1 (2017), pp. 1–7. URL: `https://www.nature.com/articles/ncomms15995`.

[159] A. Julku et al. “Superfluid weight and Berezinskii-Kosterlitz-Thouless transition temperature of twisted bilayer graphene”. In: *Phys. Rev. B* 101 (6 Feb. 2020), p. 060505. DOI: `10.1103/PhysRevB.101.060505`. URL: `https://link.aps.org/doi/10.1103/PhysRevB.101.060505`.

[160] Dominik M. Juraschek and Sebastian F. Maehrlein. “Sum-frequency ionic Raman scattering”. In: *Phys. Rev. B* 97 (17 May 2018), p. 174302. DOI: `10.1103/PhysRevB.97.174302`. URL: `https://link.aps.org/doi/10.1103/PhysRevB.97.174302`.

[161] Høgni C Kamban and Thomas G Pedersen. "Interlayer excitons in van der Waals heterostructures: Binding energy, Stark shift, and field-induced dissociation". In: *Scientific Reports* 10.1 (2020), pp. 1–10. URL: `https://www.nature.com/articles/s41598-020-62431-y`.

[162] J Kanamori. "J. Kanamori, Prog. Theor. Phys. 30, 275 (1963)." In: *Prog. Theor. Phys.* 30 (1963), p. 275. URL: `https://academic.oup.com/ptp/article/30/3/275/1865799`.

[163] Junjiro Kanamori. "Superexchange interaction and symmetry properties of electron orbitals". In: *Journal of Physics and Chemistry of Solids* 10.2-3 (1959), pp. 87–98.

[164] Ngeywo Tolbert Kaner et al. "Enhanced Shift Currents in Monolayer 2D GeS and SnS by Strain-Induced Band Gap Engineering". In: *ACS omega* 5.28 (2020), pp. 17207–17214. URL: `https://pubs.acs.org/doi/abs/10.1021/acsomega.0c01319`.

[165] Sungmo Kang, Seungjin Kang, and Jaejun Yu. "Effect of Coulomb Interactions on the Electronic and Magnetic Properties of Two-Dimensional CrSiTe 3 and CrGeTe 3 Materials". In: *Journal of Electronic Materials* 48.3 (2019), pp. 1441–1445.

[166] Daniel Kaplan, Tobias Holder, and Binghai Yan. "Momentum shift current at terahertz frequencies in twisted bilayer graphene". In: *arXiv:2101.07539* (2021). URL: `https://arxiv.org/abs/2101.07539`.

[167] LV Keldysh. "Coulomb interaction in thin semiconductor and semimetal films". In: *Soviet Journal of Experimental and Theoretical Physics Letters* 29 (1979), p. 658. URL: `http://www.jetpletters.ac.ru/ps/1458/article_22207.shtml`.

[168] Eslam Khalaf. "Higher-order topological insulators and superconductors protected by inversion symmetry". In: *Phys. Rev. B* 97 (20 May 2018), p. 205136. DOI: `10.1103/PhysRevB.97.205136`. URL: `https://link.aps.org/doi/10.1103/PhysRevB.97.205136`.

[169] Eslam Khalaf et al. "Symmetry Indicators and Anomalous Surface States of Topological Crystalline Insulators". In: *Phys. Rev. X* 8 (3 Sept. 2018), p. 031070. DOI: `10.1103/PhysRevX.8.031070`. URL: `https://link.aps.org/doi/10.1103/PhysRevX.8.031070`.

[170] DI Khomskii. "Role of orbitals in the physics of correlated electron systems". In: *Physica Scripta* 72.5 (2005), p. CC8. URL: `http://iopscience.iop.org/article/10.1238/Physica.Regular.072a00CC8/meta`.

[171] DI Khomskii and GA Sawatzky. "Interplay between spin, charge and orbital degrees of freedom in magnetic oxides". In: *Solid state communications* 102.2-3 (1997), pp. 87–99.

[172] Kun Woo Kim, Takahiro Morimoto, and Naoto Nagaosa. "Shift charge and spin photocurrents in Dirac surface states of topological insulator". In: *Phys. Rev. B* 95.3 (2017), p. 035134. DOI: `10.1103/PhysRevB.95.035134`. URL: `https://link.aps.org/doi/10.1103/PhysRevB.95.035134`.

[173] So Yeun Kim et al. "Charge-Spin Correlation in van der Waals Antiferromagnet $NiPS_3$". In: *Phys. Rev. Lett.* 120 (13 Mar. 2018), p. 136402. DOI: `10.1103/PhysRevLett.120.136402`. URL: `https://link.aps.org/doi/10.1103/PhysRevLett.120.136402`.

[174] Tae Wu Kim et al. "Ultrafast charge transfer coupled with lattice phonons in two-dimensional covalent organic frameworks". In: *Nature communications* 10.1 (2019), pp. 1–10. URL: `https://www.nature.com/articles/s41467-019-09872-w.pdf`.

[175] Andrei Kirilyuk, Alexey V Kimel, and Theo Rasing. "Ultrafast optical manipulation of magnetic order". In: *Rev. Mod. Phys.* 82.3 (2010), p. 2731. URL: `https://journals.aps.org/rmp/abstract/10.1103/RevModPhys.82.2731`.

[176] Andrei Kirilyuk, Alexey V Kimel, and Theo Rasing. "Ultrafast optical manipulation of magnetic order". In: *Reviews of Modern Physics* 82.3 (2010), p. 2731.

[177] Alexei Kitaev. "Periodic table for topological insulators and superconductors". In: *AIP Conf. Proc.* 1134 (2009), p. 22. URL: `https://aip.scitation.org/doi/abs/10.1063/1.3149495?journalCode=apc`.

[178] Takuya Kitagawa et al. "Transport properties of nonequilibrium systems under the application of light: Photoinduced quantum Hall insulators without Landau levels". In: *Phys. Rev. B* 84 (23 Dec. 2011), p. 235108. DOI: `10.1103/PhysRevB.84.235108`. URL: `https://link.aps.org/doi/10.1103/PhysRevB.84.235108`.

[179] Lennart Klebl et al. "Importance of long-ranged electron-electron interactions for the magnetic phase diagram of twisted bilayer graphene". In: (2020). arXiv: `2012.14499 [cond-mat.str-el]`.

[180] Jelena Klinovaja, Peter Stano, and Daniel Loss. "Topological Floquet Phases in Driven Coupled Rashba Nanowires". In: *Phys. Rev. Lett.* 116 (17 Apr. 2016), p. 176401. DOI: `10.1103/PhysRevLett.116.176401`. URL: `https://link.aps.org/doi/10.1103/PhysRevLett.116.176401`.

[181] Sergej Konschuh, Martin Gmitra, and Jaroslav Fabian. "Tight-binding theory of the spin-orbit coupling in graphene". In: *Phys. Rev. B* 82 (24 Dec. 2010), p. 245412. DOI: `10.1103/PhysRevB.82.245412`. URL: `https://link.aps.org/doi/10.1103/PhysRevB.82.245412`.

[182] Andor Kormányos et al. “Tunable Berry curvature and valley and spin Hall effect in bilayer MoS_2”. In: *Phys. Rev. B* 98 (3 July 2018), p. 035408. DOI: `10.1103/PhysRevB.98.035408`. URL: `https://link.aps.org/doi/10.1103/PhysRevB.98.035408`.

[183] Mikito Koshino et al. “Maximally Localized Wannier Orbitals and the Extended Hubbard Model for Twisted Bilayer Graphene”. In: *Phys. Rev. X* 8 (3 Sept. 2018), p. 031087. DOI: `10.1103/PhysRevX.8.031087`. URL: `https://link.aps.org/doi/10.1103/PhysRevX.8.031087`.

[184] V. M. Kovalev and I. G. Savenko. “Quantum anomalous valley Hall effect for bosons”. In: *Phys. Rev. B* 100 (12 Sept. 2019), p. 121405. DOI: `10.1103/PhysRevB.100.121405`. URL: `https://link.aps.org/doi/10.1103/PhysRevB.100.121405`.

[185] Daichi Kozawa et al. “Evidence for fast interlayer energy transfer in MoSe2/WS2 heterostructures”. In: *Nano letters* 16.7 (2016), pp. 4087–4093. URL: `https://pubs.acs.org/doi/abs/10.1021/acs.nanolett.6b00801`.

[186] VK Kozin et al. “Anomalous exciton Hall effect”. In: *arXiv:2006.08717* (2020).

[187] Petr Král. “Quantum kinetic theory of shift-current electron pumping in semiconductors”. In: *J. Phys. Condens. Matter* 12.22 (2000), p. 4851. URL: `http://iopscience.iop.org/article/10.1088/0953-8984/12/22/317`.

[188] Petr Král, E. J. Mele, and David Tománek. “Photogalvanic Effects in Heteropolar Nanotubes”. In: *Phys. Rev. Lett.* 85 (7 Aug. 2000), pp. 1512–1515. DOI: `10.1103/PhysRevLett.85.1512`. URL: `https://link.aps.org/doi/10.1103/PhysRevLett.85.1512`.

[189] Shun-ichi Kuga, Shuichi Murakami, and Naoto Nagaosa. “Spin Hall effect of excitons”. In: *Phys. Rev. B* 78 (20 Nov. 2008), p. 205201. DOI: `10.1103/PhysRevB.78.205201`. URL: `https://link.aps.org/doi/10.1103/PhysRevB.78.205201`.

[190] KI Kugel and DI Khomskii. “Crystal-structure and magnetic properties of substances with orbital degeneracy”. In: *Zh. Eksp. Teor. Fiz* 64 (1973), pp. 1429–1439.

[191] Anshuman Kumar et al. “Chiral plasmon in gapped Dirac systems”. In: *Physical Review B* 93.4 (2016), p. 041413. URL: `https://journals.aps.org/prb/abstract/10.1103/PhysRevB.93.041413`.

[192] Jens Kunstmann et al. “Momentum-space indirect interlayer excitons in transition-metal dichalcogenide van der Waals heterostructures”. In: *Nature Physics* 14.8 (2018), pp. 801–805. URL: `https://www.nature.com/articles/s41567-018-0123-y`.

[193] MV Kurik. “Urbach rule”. In: *physica status solidi (a)* 8.1 (1971), pp. 9–45.

[194] A. V. Kuznetsov and C. J. Stanton. “Theory of Coherent Phonon Oscillations in Semiconductors”. In: *Phys. Rev. Lett.* 73 (24 Dec. 1994), pp. 3243–3246. DOI: 10.1103/PhysRevLett.73.3243. URL: https://link.aps.org/doi/10.1103/PhysRevLett.73.3243.

[195] Yves H Kwan et al. “Exciton band topology in spontaneous quantum anomalous Hall insulators: applications to twisted bilayer graphene”. In: (2020). eprint: arXiv:2003.11560. URL: https://arxiv.org/abs/2003.11560.

[196] Josias Langbehn et al. “Reflection-Symmetric Second-Order Topological Insulators and Superconductors”. In: *Phys. Rev. Lett.* 119 (24 Dec. 2017), p. 246401. DOI: 10.1103/PhysRevLett.119.246401. URL: https://link.aps.org/doi/10.1103/PhysRevLett.119.246401.

[197] Simone Latini et al. “Interlayer excitons and band alignment in MoS2/hBN/WSe2 van der Waals heterostructures”. In: *Nano letters* 17.2 (2017), pp. 938–945.

[198] Akash Laturia, Maarten L Van de Put, and William G Vandenberghe. “Dielectric properties of hexagonal boron nitride and transition metal dichalcogenides: from monolayer to bulk”. In: *npj 2D Materials and Applications* 2.1 (2018), pp. 1–7. URL: https://www.nature.com/articles/s41699-018-0050-x.

[199] Cyprian Lewandowski, Stevan Nadj-Perge, and Debanjan Chowdhury. “Does filling-dependent band renormalization aid pairing in twisted bilayer graphene?” In: *arXiv:2102.05661* (2021). URL: https://arxiv.org/abs/2102.05661.

[200] Tracy Li et al. “Bloch state tomography using Wilson lines”. In: *Science* 352.6289 (2016), pp. 1094–1097. URL: http://science.sciencemag.org/content/352/6289/1094.

[201] Yun-Mei Li et al. “Light-Induced Exciton Spin Hall Effect in van der Waals Heterostructures”. In: *Phys. Rev. Lett.* 115 (16 Oct. 2015), p. 166804. DOI: 10.1103/PhysRevLett.115.166804. URL: https://link.aps.org/doi/10.1103/PhysRevLett.115.166804.

[202] Zeng-Zhao Li, Chi-Hang Lam, and J. Q. You. “Floquet engineering of long-range p-wave superconductivity: Beyond the high-frequency limit”. In: *Phys. Rev. B* 96 (15 Oct. 2017), p. 155438. DOI: 10.1103/PhysRevB.96.155438. URL: https://link.aps.org/doi/10.1103/PhysRevB.96.155438.

[203] Zhi Li et al. “Second-harmonic generation in noncentrosymmetric phosphates”. In: *Phys. Rev. B* 96 (3 July 2017), p. 035205. DOI: 10.1103/PhysRevB.96.035205. URL: https://link.aps.org/doi/10.1103/PhysRevB.96.035205.

[204] Andrew D Liehr and CJ Ballhausen. “Intensities in inorganic complexes”. In: *Physical Review* 106.6 (1957), p. 1161. URL: https://journals.aps.org/pr/pdf/10.1103/PhysRev.106.1161.

[205] Ming-Wei Lin et al. “Ultrathin nanosheets of CrSiTe 3: a semiconducting two-dimensional ferromagnetic material”. In: *Journal of Materials Chemistry C* 4.2 (2016), pp. 315–322.

[206] Pei Lin et al. “Piezo-phototronic effect for enhanced flexible MoS2/WSe2 van der Waals photodiodes”. In: *Advanced Functional Materials* 28.35 (2018), p. 1802849. URL: https://onlinelibrary.wiley.com/doi/abs/10.1002/adfm.201802849.

[207] Netanel H Lindner, Gil Refael, and Victor Galitski. “Floquet topological insulator in semiconductor quantum wells”. In: *Nature Physics* 7.6 (2011), pp. 490–495. URL: https://www.nature.com/articles/nphys1926.

[208] Netanel H Lindner, Gil Refael, and Victor Galitski. “Floquet topological insulator in semiconductor quantum wells”. In: *Nat. Phys.* 7.6 (2011), p. 490. URL: https://www.nature.com/articles/nphys1926.

[209] Jianpeng Liu and Xi Dai. “Anomalous Hall effect, magneto-optical properties, and nonlinear optical properties of twisted graphene systems”. In: *npj Computational Materials* 6.1 (2020), pp. 1–10. URL: https://www.nature.com/articles/s41524-020-0299-4.

[210] Jianpeng Liu, Kasra Hejazi, and Leon Balents. “Floquet engineering of multi-orbital Mott insulators: applications to orthorhombic titanates”. In: (). arXiv: 1801.00401. URL: http://arxiv.org/abs/1801.00401.

[211] Jianpeng Liu, Kasra Hejazi, and Leon Balents. “Floquet Engineering of Multiorbital Mott Insulators: Applications to Orthorhombic Titanates”. In: *Phys. Rev. Lett.* 121 (10 Sept. 2018), p. 107201. DOI: 10.1103/PhysRevLett.121.107201. URL: https://link.aps.org/doi/10.1103/PhysRevLett.121.107201.

[212] J. M. B. Lopes dos Santos, N. M. R. Peres, and A. H. Castro Neto. “Graphene Bilayer with a Twist: Electronic Structure”. In: *Phys. Rev. Lett.* 99 (25 Dec. 2007), p. 256802. DOI: 10.1103/PhysRevLett.99.256802. URL: https://link.aps.org/doi/10.1103/PhysRevLett.99.256802.

[213] J. M. B. Lopes dos Santos, N. M. R. Peres, and A. H. Castro Neto. “Graphene Bilayer with a Twist: Electronic Structure”. In: *Phys. Rev. Lett.* 99 (25 Dec. 2007), p. 256802. DOI: 10.1103/PhysRevLett.99.256802. URL: https://link.aps.org/doi/10.1103/PhysRevLett.99.256802.

[214] Juan M Losada, Arne Brataas, and Alireza Qaiumzadeh. “Ultrafast Control of Spin Interactions in Honeycomb Antiferromagnetic Insulators”. In: *arXiv preprint arXiv:1904.01270* (2019).

[215] Daniel Loss, Paul Goldbart, and A. V. Balatsky. "Berry's phase and persistent charge and spin currents in textured mesoscopic rings". In: *Phys. Rev. Lett.* 65 (13 Sept. 1990), pp. 1655–1658. DOI: `10.1103/PhysRevLett.65.1655`. URL: `https://link.aps.org/doi/10.1103/PhysRevLett.65.1655`.

[216] Xiaobo Lu et al. "Superconductors, orbital magnets and correlated states in magic-angle bilayer graphene". In: *Nature* 574.7780 (2019), pp. 653–657. DOI: `10.1038/s41586-019-1695-0`. URL: `https://doi.org/10.1038/s41586-019-1695-0`.

[217] Qiong Ma, Adolfo G. Grushin, and Kenneth S. Burch. "Topology and geometry under the nonlinear electromagnetic spotlight". In: *arXiv:2103.03269* (2021). URL: `https://arxiv.org/abs/2103.03269`.

[218] Qiong Ma et al. "Observation of the nonlinear Hall effect under time-reversal-symmetric conditions". In: *Nature* 565.7739 (2019), pp. 337–342. URL: `https://www.nature.com/articles/s41586-018-0807-6`.

[219] Kin Fai Mak et al. "Control of valley polarization in monolayer MoS_2 by optical helicity". In: *Nature nanotechnology* 7.8 (2012), pp. 494–498. URL: `https://www.nature.com/articles/nnano.2012.96`.

[220] Kin Fai Mak et al. "The valley Hall effect in MoS_2 transistors". In: *Science* 344.6191 (2014), pp. 1489–1492. URL: `https://science.sciencemag.org/content/344/6191/1489.abstract`.

[221] Ivar Martin, Gil Refael, and Bertrand Halperin. "Topological Frequency Conversion in Strongly Driven Quantum Systems". In: *Phys. Rev. X* 7 (4 Oct. 2017), p. 041008. DOI: `10.1103/PhysRevX.7.041008`. URL: `https://link.aps.org/doi/10.1103/PhysRevX.7.041008`.

[222] M Ramezani Masir, P Vasilopoulos, and FM Peeters. "Wavevector filtering through single-layer and bilayer graphene with magnetic barrier structures". In: *Applied Physics Letters* 93.24 (2008), p. 242103. URL: `https://aip.scitation.org/doi/pdf/10.1063/1.3049600`.

[223] S Mathias et al. "Time and angle resolved photoemission spectroscopy using femtosecond visible and high-harmonic light". In: *Journal of Physics: Conference Series*. Vol. 148. 1. IOP Publishing. 2009, p. 012042. URL: `https://iopscience.iop.org/article/10.1088/1742-6596/148/1/012042/pdf`.

[224] Fumihiro Matsukura, Yoshinori Tokura, and Hideo Ohno. "Control of magnetism by electric fields". In: *Nature nanotechnology* 10.3 (2015), pp. 209–220. URL: `https://www.nature.com/articles/nnano.2015.22`.

[225] Daniel C Mattis. *The theory of magnetism made simple: an introduction to physical concepts and to some useful mathematical methods*. World Scientific Publishing Company, 2006.

[226] James W McIver et al. “Light-induced anomalous Hall effect in graphene”. In: *Nature physics* 16.1 (2020), pp. 38–41. URL: https://www.nature.com/articles/s41567-019-0698-y.

[227] J. H. Mentink, K. Balzer, and M. Eckstein. “Ultrafast and reversible control of the exchange interaction in Mott insulators”. In: *Nat. Commun.* 6 (2015), pp. 1–8. ISSN: 20411723. DOI: 10.1038/ncomms7708. URL: http://dx.doi.org/10.1038/ncomms7708.

[228] J. H. Mentink and M. Eckstein. “Ultrafast Quenching of the Exchange Interaction in a Mott Insulator”. In: *Phys. Rev. Lett.* 113.5 (Jan. 2014). ISSN: 10797114. DOI: 10.1103/PhysRevLett.113.057201. arXiv: 1401.5308. URL: http://dx.doi.org/10.1103/PhysRevLett.113.057201.

[229] JH Mentink. “Manipulating magnetism by ultrafast control of the exchange interaction”. In: *Journal of Physics: Condensed Matter* 29.45 (2017), p. 453001. URL: http://iopscience.iop.org/article/10.1088/1361-648X/aa8abf/meta.

[230] JH Mentink, Karsten Balzer, and Martin Eckstein. “Ultrafast and reversible control of the exchange interaction in Mott insulators”. In: *Nat. Commun.* 6 (2015), p. 6708. URL: https://www.nature.com/articles/ncomms7708.

[231] Philipp Merkl et al. “Ultrafast transition between exciton phases in van der Waals heterostructures”. In: *Nature materials* 18.7 (2019), pp. 691–696. URL: https://www.nature.com/articles/s41563-019-0337-0.

[232] RV Mikhaylovskiy et al. “Ultrafast optical modification of exchange interactions in iron oxides”. In: *Nat. Commun.* 6 (2015), p. 8190. URL: https://www.nature.com/articles/ncomms9190.

[233] Bastian Miller et al. “Long-lived direct and indirect interlayer excitons in van der Waals heterostructures”. In: *Nano letters* 17.9 (2017), pp. 5229–5237. URL: https://pubs.acs.org/doi/abs/10.1021/acs.nanolett.7b01304.

[234] A Milosavljević et al. “Evidence of spin-phonon coupling in CrSiTe 3”. In: *Physical Review B* 98.10 (2018), p. 104306.

[235] Hongki Min et al. “Intrinsic and Rashba spin-orbit interactions in graphene sheets”. In: *Phys. Rev. B* 74 (16 Oct. 2006), p. 165310. DOI: 10.1103/PhysRevB.74.165310. URL: https://link.aps.org/doi/10.1103/PhysRevB.74.165310.

[236] Tridev Mishra et al. “Floquet topological phase transitions in a kicked Haldane-Chern insulator”. In: *Phys. Rev. B* 97 (8 Feb. 2018), p. 085405. DOI: 10.1103/PhysRevB.97.085405. URL: https://link.aps.org/doi/10.1103/PhysRevB.97.085405.

[237] A. Molina-Sánchez and L. Wirtz. “Phonons in single-layer and few-layer MoS_2 and WS_2”. In: *Phys. Rev. B* 84 (15 Oct. 2011), p. 155413. DOI: 10.1103/PhysRevB.84.155413. URL: https://link.aps.org/doi/10.1103/PhysRevB.84.155413.

[238] J. E. Moore and J. Orenstein. “Confinement-Induced Berry Phase and Helicity-Dependent Photocurrents”. In: *Phys. Rev. Lett.* 105 (2 July 2010), p. 026805. DOI: 10.1103/PhysRevLett.105.026805. URL: https://link.aps.org/doi/10.1103/PhysRevLett.105.026805.

[239] Takahiro Morimoto and Naoto Nagaosa. “Topological aspects of nonlinear excitonic processes in noncentrosymmetric crystals”. In: *Phys. Rev. B* 94 (3 July 2016), p. 035117. DOI: 10.1103/PhysRevB.94.035117. URL: https://link.aps.org/doi/10.1103/PhysRevB.94.035117.

[240] Takahiro Morimoto and Naoto Nagaosa. “Topological nature of nonlinear optical effects in solids”. In: *Science advances* 2.5 (2016), e1501524. URL: https://advances.sciencemag.org/content/2/5/e1501524.

[241] Takahiro Morimoto, Hoi Chun Po, and Ashvin Vishwanath. “Floquet topological phases protected by time glide symmetry”. In: *Phys. Rev. B* 95 (19 May 2017), p. 195155. DOI: 10.1103/PhysRevB.95.195155. URL: https://link.aps.org/doi/10.1103/PhysRevB.95.195155.

[242] Michael V Moskalets. *Scattering matrix approach to non-stationary quantum transport*. World Scientific, 2012.

[243] Erich J Mueller. “Artificial electromagnetism for neutral atoms: Escher staircase and Laughlin liquids”. In: *Physical Review A* 70.4 (2004), p. 041603. URL: https://journals.aps.org/pra/abstract/10.1103/PhysRevA.70.041603.

[244] Shankari Nadupalli, Jens Kreisel, and Torsten Granzow. “Increasing bulk photovoltaic current by strain tuning”. In: *Science advances* 5.3 (2019), eaau9199. URL: https://advances.sciencemag.org/content/5/3/eaau9199.abstract.

[245] Naoto Nagaosa and Takahiro Morimoto. “Concept of Quantum Geometry in Optoelectronic Processes in Solids: Application to Solar Cells”. In: *Adv. Mater.* 29.25 (2017), p. 1603345. DOI: 10.1002/adma.201603345. URL: https://onlinelibrary.wiley.com/doi/abs/10.1002/adma.201603345.

[246] Philipp Nagler et al. “Interlayer exciton dynamics in a dichalcogenide monolayer heterostructure”. In: *2D Materials* 4.2 (2017), p. 025112. URL: https://iopscience.iop.org/article/10.1088/2053-1583/aa7352/meta.

[247] CS Naiman. “Interpretation of the absorption spectra of K3Fe (CN) 6”. In: *The Journal of Chemical Physics* 35.1 (1961), pp. 323–328. URL: https://aip.scitation.org/doi/pdf/10.1063/1.1731909?class=pdf.

[248] Shuta Nakajima et al. “Topological Thouless pumping of ultracold fermions”. In: *Nature Physics* 12.4 (2016), pp. 296–300. URL: https://www.nature.com/articles/nphys3622.

[249] D. Nandi et al. “Exciton condensation and perfect Coulomb drag”. In: *Nature* 488.7412 (Aug. 2012), pp. 481–484. ISSN: 1476-4687. DOI: 10.1038/nature11302. URL: http://dx.doi.org/10.1038/nature11302.

[250] Ajaya K Nayak et al. “Large anomalous Hall effect driven by a nonvanishing Berry curvature in the noncolinear antiferromagnet Mn3Ge”. In: *Science advances* 2.4 (2016), e1501870. URL: https://advances.sciencemag.org/content/2/4/e1501870.short.

[251] Xiang Ni et al. “Observation of higher-order topological acoustic states protected by generalized chiral symmetry”. In: *Nature materials* 18.2 (2019), p. 113. URL: https://www.nature.com/articles/s41563-018-0252-9.

[252] Zhi Ping Niu and Xueshi Wu. “Tunable anisotropic anomalous Nernst effect and orbital magnetization in Floquet Weyl semimetals”. In: *Physics Letters A* (2018). URL: https://www.sciencedirect.com/science/article/pii/S0375960118300070.

[253] N. Ogawa et al. “Shift current in the ferroelectric semiconductor SbSI”. In: *Phys. Rev. B* 96 (24 Dec. 2017), p. 241203. DOI: 10.1103/PhysRevB.96.241203. URL: https://link.aps.org/doi/10.1103/PhysRevB.96.241203.

[254] Takashi Oka and Hideo Aoki. “Photovoltaic Hall effect in graphene”. In: *Phys. Rev. B* 79 (8 Feb. 2009), p. 081406. DOI: 10.1103/PhysRevB.79.081406. URL: https://link.aps.org/doi/10.1103/PhysRevB.79.081406.

[255] Takashi Oka and Hideo Aoki. “Photovoltaic Hall effect in graphene”. In: *Phys. Rev. B* 79 (8 Feb. 2009), p. 081406. DOI: 10.1103/PhysRevB.79.081406. URL: https://link.aps.org/doi/10.1103/PhysRevB.79.081406.

[256] Takashi Oka and Sota Kitamura. “Floquet Engineering of Quantum Materials”. In: *arXiv preprint arXiv:1804.03212* (2018). URL: https://arxiv.org/pdf/1804.03212.pdf.

[257] Takashi Oka and Sota Kitamura. “Floquet engineering of quantum materials”. In: *Annual Review of Condensed Matter Physics* 10 (2019), pp. 387–408. URL: https://www.annualreviews.org/doi/abs/10.1146/annurev-conmatphys-031218-013423.

[258] Masaru Onga et al. “Exciton Hall effect in monolayer MoS 2”. In: *Nature materials* 16.12 (2017), pp. 1193–1197. URL: https://www.nature.com/articles/nmat4996?proof=t.

[259] J Orenstein et al. “Topology and Symmetry of Quantum Materials via Nonlinear Optical Responses”. In: *Annual Review of Condensed Matter Physics* 12 (2021), pp. 247–272. URL: https://www.annualreviews.org/doi/full/10.1146/annurev-conmatphys-031218-013712.

[260] Gavin B Osterhoudt et al. “Colossal mid-infrared bulk photovoltaic effect in a type-I Weyl semimetal”. In: *Nature materials* 18.5 (2019), pp. 471–475. URL: https://www.nature.com/articles/s41563-019-0297-4.

[261] Simon Ovesen et al. “Interlayer exciton dynamics in van der Waals heterostructures”. In: *Communications Physics* 2.1 (2019), pp. 1–8. URL: https://www.nature.com/articles/s42005-019-0122-z.pdf.

[262] SA Owerre. “Magnetic order in laser-irradiated kagome antiferromagnets”. In: *Journal of Physics Communications* 1.2 (2017), p. 021001.

[263] SA Owerre. “Photoinduced Topological Phase Transitions in Topological Magnon Insulators”. In: *Scientific reports* 8.1 (2018), p. 4431. URL: https://www.nature.com/articles/s41598-018-22779-8.

[264] Tomoki Ozawa, Hannah M. Price, and Iacopo Carusotto. “Quantum Hall effect in momentum space”. In: *Phys. Rev. B* 93 (19 May 2016), p. 195201. DOI: 10.1103/PhysRevB.93.195201. URL: https://link.aps.org/doi/10.1103/PhysRevB.93.195201.

[265] Shivaramakrishnan Pancharatnam. “Generalized theory of interference and its applications”. In: 44.6 (1956), pp. 398–417. URL: https://link.springer.com/article/10.1007/BF03046050.

[266] Daniel E. Parker et al. “Diagrammatic approach to nonlinear optical response with application to Weyl semimetals”. In: *Phys. Rev. B* 99 (4 Jan. 2019), p. 045121. DOI: 10.1103/PhysRevB.99.045121. URL: https://link.aps.org/doi/10.1103/PhysRevB.99.045121.

[267] Eva Pavarini et al. “Correlated electrons: from models to materials”. In: *Reihe Modeling and Simulation* 2 (2012).

[268] Oleg E. Peil, Michel Ferrero, and Antoine Georges. “Orbital polarization in strained LaNiO$_3$: Structural distortions and correlation effects”. In: *Phys. Rev. B* 90 (4 July 2014), p. 045128. DOI: 10.1103/PhysRevB.90.045128. URL: https://link.aps.org/doi/10.1103/PhysRevB.90.045128.

[269] Yang Peng. “Floquet higher-order topological insulators and superconductors with space-time symmetries”. In: *Phys. Rev. Research* 2 (1 Feb. 2020), p. 013124. DOI: 10.1103/PhysRevResearch.2.013124. URL: https://link.aps.org/doi/10.1103/PhysRevResearch.2.013124.

[270] Yang Peng, Yimu Bao, and Felix von Oppen. “Boundary Green functions of topological insulators and superconductors”. In: *Phys. Rev. B* 95 (23 June 2017), p. 235143. DOI: 10.1103/PhysRevB.95.235143. URL: https://link.aps.org/doi/10.1103/PhysRevB.95.235143.

[271] Yang Peng and Gil Refael. "Floquet Second-Order Topological Insulators from Nonsymmorphic Space-Time Symmetries". In: *Phys. Rev. Lett.* 123 (1 July 2019), p. 016806. DOI: `10.1103/PhysRevLett.123.016806`. URL: `https://link.aps.org/doi/10.1103/PhysRevLett.123.016806`.

[272] Anastasiia A. Pervishko, Dmitry Yudin, and Ivan A. Shelykh. "Impact of high-frequency pumping on anomalous finite-size effects in three-dimensional topological insulators". In: *Phys. Rev. B* 97 (7 Feb. 2018), p. 075420. DOI: `10.1103/PhysRevB.97.075420`. URL: `https://link.aps.org/doi/10.1103/PhysRevB.97.075420`.

[273] Christopher W Peterson et al. "A quantized microwave quadrupole insulator with topologically protected corner states". In: *Nature* 555.7696 (2018), p. 346. URL: `https://www.nature.com/articles/nature25777`.

[274] Patrick J. Phillips et al. "Experimental verification of orbital engineering at the atomic scale: Charge transfer and symmetry breaking in nickelate heterostructures". In: *Phys. Rev. B* 95 (20 May 2017), p. 205131. DOI: `10.1103/PhysRevB.95.205131`. URL: `https://link.aps.org/doi/10.1103/PhysRevB.95.205131`.

[275] Kirill Plekhanov, Guillaume Roux, and Karyn Le Hur. "Floquet engineering of Haldane Chern insulators and chiral bosonic phase transitions". In: *Phys. Rev. B* 95 (4 Jan. 2017), p. 045102. DOI: `10.1103/PhysRevB.95.045102`. URL: `https://link.aps.org/doi/10.1103/PhysRevB.95.045102`.

[276] LI Podobedova, DE Kelleher, and WL Wiese. "Critically evaluated atomic transition probabilities for Sulfur SI–S XV". In: *Journal of Physical and Chemical Reference Data* 38.2 (2009), pp. 171–439.

[277] Hannah M Price, Tomoki Ozawa, and Iacopo Carusotto. "Quantum mechanics with a momentum-space artificial magnetic field". In: *Phys. Rev. Lett.* 113.19 (2014), p. 190403. URL: `https://journals.aps.org/prl/pdf/10.1103/PhysRevLett.113.190403`.

[278] HM Price and NR Cooper. "Mapping the Berry curvature from semiclassical dynamics in optical lattices". In: *Phys. Rev. A* 85.3 (2012), p. 033620. URL: `https://journals.aps.org/pra/abstract/10.1103/PhysRevA.85.033620`.

[279] Xiao-Liang Qi and Shou-Cheng Zhang. "Topological insulators and superconductors". In: *Rev. Mod. Phys.* 83 (4 Oct. 2011), pp. 1057–1110. DOI: `10.1103/RevModPhys.83.1057`. URL: `https://link.aps.org/doi/10.1103/RevModPhys.83.1057`.

[280] Wei Qin, Bo Zou, and Allan H. MacDonald. "Critical magnetic fields and electron-pairing in magic-angle twisted bilayer graphene". In: (2021). arXiv: `2102.10504`.

[281] Diana Y. Qiu, Ting Cao, and Steven G. Louie. “Nonanalyticity, Valley Quantum Phases, and Lightlike Exciton Dispersion in Monolayer Transition Metal Dichalcogenides: Theory and First-Principles Calculations”. In: *Phys. Rev. Lett.* 115 (17 Oct. 2015), p. 176801. DOI: 10.1103/PhysRevLett.115.176801. URL: https://link.aps.org/doi/10.1103/PhysRevLett.115.176801.

[282] VL Quito and Rebecca Flint. “Floquet engineering magnetic materials with polarized and unpolarized light”. In: *arXiv preprint arXiv:2003.04272* (2020). URL: https://arxiv.org/abs/2003.04272.

[283] VL Quito and Rebecca Flint. “Polarization as a tuning parameter for Floquet engineering: magnetism in the honeycomb, square, and triangular Mott insulators”. In: *arXiv preprint arXiv:2003.05933* (2020). URL: https://arxiv.org/abs/2003.05933.

[284] Louk Rademaker, Dmitry A. Abanin, and Paula Mellado. “Charge Smoothening and Band Flattening Due to Hartree Corrections in Twisted Bilayer Graphene”. In: *Physical Review B* 100.20 (Nov. 2019), p. 205114. DOI: 10.1103/PhysRevB.100.205114. URL: https://journals.aps.org/prb/abstract/10.1103/PhysRevB.100.205114.

[285] Tonatiuh Rangel et al. “Large Bulk Photovoltaic Effect and Spontaneous Polarization of Single-Layer Monochalcogenides”. In: *Phys. Rev. Lett.* 119 (6 Aug. 2017), p. 067402. DOI: 10.1103/PhysRevLett.119.067402. URL: https://link.aps.org/doi/10.1103/PhysRevLett.119.067402.

[286] H-S Rhie, HA Dürr, and W Eberhardt. “Femtosecond Electron and Spin Dynamics in N i/W (110) Films”. In: *Physical review letters* 90.24 (2003), p. 247201.

[287] Pasqual Rivera et al. “Interlayer valley excitons in heterobilayers of transition metal dichalcogenides”. In: *Nature nanotechnology* 13.11 (2018), pp. 1004–1015. URL: https://www.nature.com/articles/s41565-018-0193-0.pdf.

[288] Pasqual Rivera et al. “Observation of long-lived interlayer excitons in monolayer MoSe 2–WSe 2 heterostructures”. In: *Nature communications* 6.1 (2015), pp. 1–6. URL: https://www.nature.com/articles/ncomms7242?page=3.

[289] Pasqual Rivera et al. “Valley-polarized exciton dynamics in a 2D semiconductor heterostructure”. In: *Science* 351.6274 (2016), pp. 688–691. URL: https://science.sciencemag.org/content/351/6274/688.abstract.

[290] Martin Rodriguez-Vega, Abhishek Kumar, and Babak Seradjeh. “Higher-order Floquet topological phases with corner and bulk bound states”. In: *Physical Review B* 100.8 (2019), p. 085138. URL: https://journals.aps.org/prb/abstract/10.1103/PhysRevB.100.085138.

[291] Pedro Roman-Taboada and Gerardo G. Naumis. “Topological edge states on time-periodically strained armchair graphene nanoribbons”. In: *Phys. Rev. B* 96 (15 Oct. 2017), p. 155435. DOI: 10.1103/PhysRevB.96.155435. URL: https://link.aps.org/doi/10.1103/PhysRevB.96.155435.

[292] A Ron et al. “Dimensional crossover in a layered ferromagnet detected by spin correlation driven distortions”. In: *Nature communications* 10.1 (2019), p. 1654.

[293] A Ron et al. “Ultrafast enhancement of ferromagnetic spin exchange induced by ligand-to-metal charge transfer”. In: *arXiv preprint arXiv:1910.06376* (2019). URL: https://arxiv.org/abs/1910.06376.

[294] A. Ron, **S. Chaudhary**, G. Zhang, H. Ning, E. Zoghlin, S. D. Wilson, R. D. Averitt, G. Refael, and D. Hsieh. “Ultrafast enhancement of ferromagnetic spin exchange induced by ligand-to-metal charge transfer”. In: *Phys. Rev. Lett.* 125 (19 Nov. 2020), p. 197203. DOI: 10.1103/PhysRevLett.125.197203.

[295] Jason S Ross et al. “Interlayer exciton optoelectronics in a 2D heterostructure p–n junction”. In: *Nano letters* 17.2 (2017), pp. 638–643. URL: https://pubs.acs.org/doi/abs/10.1021/acs.nanolett.6b03398.

[296] Jan R. Rubbmark et al. “Dynamical effects at avoided level crossings: A study of the Landau-Zener effect using Rydberg atoms”. In: *Phys. Rev. A* 23 (6 June 1981), pp. 3107–3117. DOI: 10.1103/PhysRevA.23.3107. URL: https://link.aps.org/doi/10.1103/PhysRevA.23.3107.

[297] Mark S Rudner and Netanel H Lindner. “Band structure engineering and non-equilibrium dynamics in Floquet topological insulators”. In: *Nature reviews physics* 2.5 (2020), pp. 229–244. URL: https://www.nature.com/articles/s42254-020-0170-z.

[298] David A Ruiz-Tijerina, Isaac Soltero, and Francisco Mireles. “Theory of moiré localized excitons in transition-metal dichalcogenide heterobilayers”. In: (2020). eprint: arXiv:2007.03754. URL: https://arxiv.org/abs/2007.03754.

[299] David A. Ruiz-Tijerina and Vladimir I. Fal’ko. “Interlayer hybridization and moiré superlattice minibands for electrons and excitons in heterobilayers of transition-metal dichalcogenides”. In: *Phys. Rev. B* 99 (12 Mar. 2019), p. 125424. DOI: 10.1103/PhysRevB.99.125424. URL: https://link.aps.org/doi/10.1103/PhysRevB.99.125424.

[300] Shinsei Ryu et al. “Topological insulators and superconductors: tenfold way and dimensional hierarchy”. In: *New Journal of Physics* 12.6 (2010), p. 065010. URL: https://iopscience.iop.org/article/10.1088/1367-2630/12/6/065010/meta.

[301] Siddhartha Saha, Shankar N. Sivarajan, and Diptiman Sen. "Generating end modes in a superconducting wire by periodic driving of the hopping". In: *Phys. Rev. B* 95 (17 May 2017), p. 174306. DOI: `10.1103/PhysRevB.95.174306`. URL: `https://link.aps.org/doi/10.1103/PhysRevB.95.174306`.

[302] Joseph Samuel and Rajendra Bhandari. "General Setting for Berry's Phase". In: *Phys. Rev. Lett.* 60 (23 June 1988), pp. 2339–2342. DOI: `10.1103/PhysRevLett.60.2339`. URL: `https://link.aps.org/doi/10.1103/PhysRevLett.60.2339`.

[303] Aaron M Schankler, Lingyuan Gao, and Andrew M Rappe. "Large Bulk Piezophotovoltaic Effect of Monolayer 2 H-MoS2". In: *The Journal of Physical Chemistry Letters* 12.4 (2021), pp. 1244–1249. URL: `https://pubs.acs.org/doi/abs/10.1021/acs.jpclett.0c03503`.

[304] Frank Schindler et al. "Higher-order topological insulators". In: *Sci. Adv.* 4.6 (2018), eaat0346. URL: `https://advances.sciencemag.org/content/4/6/eaat0346`.

[305] Frank Schindler et al. "Higher-order topology in bismuth". In: *Nature Physics* 14.9 (2018), p. 918. URL: `https://www.nature.com/articles/s41567-018-0224-7`.

[306] F Schmitt et al. "Ultrafast electron dynamics in the charge density wave material TbTe3". In: *New Journal of Physics* 13.6 (2011), p. 063022. URL: `https://iopscience.iop.org/article/10.1088/1367-2630/13/6/063022`.

[307] Andreas P. Schnyder et al. "Classification of topological insulators and superconductors in three spatial dimensions". In: *Phys. Rev. B* 78 (19 Nov. 2008), p. 195125. DOI: `10.1103/PhysRevB.78.195125`. URL: `http://link.aps.org/doi/10.1103/PhysRevB.78.195125`.

[308] M Serlin et al. "Intrinsic quantized anomalous Hall effect in a moiré heterostructure". In: *Science* 367.6480 (2020), pp. 900–903. URL: `https://science.sciencemag.org/content/367/6480/900.abstract`.

[309] Marc Serra-Garcia et al. "Observation of a phononic quadrupole topological insulator". In: *Nature* 555.7696 (2018), p. 342. URL: `https://pubmed.ncbi.nlm.nih.gov/29334685/`.

[310] Aaron L. Sharpe et al. "Emergent ferromagnetism near three-quarters filling in twisted bilayer graphene". In: *Science* 365.6453 (2019), pp. 605–608. ISSN: 0036-8075. DOI: `10.1126/science.aaw3780`. URL: `https://science.sciencemag.org/content/365/6453/605`.

[311] Li-kun Shi and Justin C. W. Song. "Symmetry, spin-texture, and tunable quantum geometry in a WTe_2 monolayer". In: *Phys. Rev. B* 99 (3 Jan. 2019), p. 035403. DOI: `10.1103/PhysRevB.99.035403`. URL: `https://link.aps.org/doi/10.1103/PhysRevB.99.035403`.

[312] Ken Shiozaki and Masatoshi Sato. "Topology of crystalline insulators and superconductors". In: *Phys. Rev. B* 90 (16 Oct. 2014), p. 165114. DOI: `10.1103/PhysRevB.90.165114`. URL: `https://link.aps.org/doi/10.1103/PhysRevB.90.165114`.

[313] Jon H. Shirley. "Solution of the Schrödinger Equation with a Hamiltonian Periodic in Time". In: *Phys. Rev.* 138 (4B May 1965), B979–B987. DOI: `10.1103/PhysRev.138.B979`. URL: `https://link.aps.org/doi/10.1103/PhysRev.138.B979`.

[314] Edbert J Sie et al. "Time-resolved XUV ARPES with tunable 24–33 eV laser pulses at 30 meV resolution". In: *Nature communications* 10.1 (2019), pp. 1–11. URL: `https://www.nature.com/articles/s41467-019-11492-3`.

[315] Edbert J Sie et al. "Valley-selective optical Stark effect in monolayer WS 2". In: *Nature Materials* 14.3 (2015), pp. 290–294. URL: `https://www.nature.com/articles/nmat4156`.

[316] Barry Simon. "Holonomy, the Quantum Adiabatic Theorem, and Berry's Phase". In: *Phys. Rev. Lett.* 51 (24 Dec. 1983), pp. 2167–2170. DOI: `10.1103/PhysRevLett.51.2167`. URL: `https://link.aps.org/doi/10.1103/PhysRevLett.51.2167`.

[317] J. E. Sipe and A. I. Shkrebtii. "Second-order optical response in semiconductors". In: *Phys. Rev. B* 61 (8 Feb. 2000), pp. 5337–5352. DOI: `10.1103/PhysRevB.61.5337`. URL: `https://link.aps.org/doi/10.1103/PhysRevB.61.5337`.

[318] Nikhil Sivadas et al. "Magnetic ground state of semiconducting transition-metal trichalcogenide monolayers". In: *Phys. Rev. B* 91 (23 June 2015), p. 235425. DOI: `10.1103/PhysRevB.91.235425`. URL: `https://link.aps.org/doi/10.1103/PhysRevB.91.235425`.

[319] J. C. Slater. "Atomic Shielding Constants". In: *Phys. Rev.* 36 (1 July 1930), pp. 57–64. DOI: `10.1103/PhysRev.36.57`. URL: `https://link.aps.org/doi/10.1103/PhysRev.36.57`.

[320] J. C. Slater and G. F. Koster. "Simplified LCAO Method for the Periodic Potential Problem". In: *Phys. Rev.* 94 (6 June 1954), pp. 1498–1524. DOI: `10.1103/PhysRev.94.1498`. URL: `https://link.aps.org/doi/10.1103/PhysRev.94.1498`.

[321] John C Slater. "Atomic shielding constants". In: *Physical Review* 36.1 (1930), p. 57.

[322] J. A. Sobota et al. "Ultrafast Optical Excitation of a Persistent Surface-State Population in the Topological Insulator Bi_2Se_3". In: *Phys. Rev. Lett.* 108 (11 Mar. 2012), p. 117403. DOI: `10.1103/PhysRevLett.108.117403`. URL: `https://link.aps.org/doi/10.1103/PhysRevLett.108.117403`.

[323] Inti Sodemann and Liang Fu. "Quantum Nonlinear Hall Effect Induced by Berry Curvature Dipole in Time-Reversal Invariant Materials". In: *Phys. Rev. Lett.* 115 (21 Nov. 2015), p. 216806. DOI: `10.1103/PhysRevLett.115.216806`. URL: `https://link.aps.org/doi/10.1103/PhysRevLett.115.216806`.

[324] H. Soifer et al. "Band-Resolved Imaging of Photocurrent in a Topological Insulator". In: *Phys. Rev. Lett.* 122 (16 Apr. 2019), p. 167401. DOI: `10.1103/PhysRevLett.122.167401`. URL: `https://link.aps.org/doi/10.1103/PhysRevLett.122.167401`.

[325] IV Solovyev. "Lattice distortion and magnetism of 3 d- t 2 g perovskite oxides". In: *Phys. Rev. B* 74.5 (2006), p. 054412. URL: `https://journals.aps.org/prb/abstract/10.1103/PhysRevB.74.054412`.

[326] Joolee Son et al. "Strain Engineering of the Berry Curvature Dipole and Valley Magnetization in Monolayer MoS 2". In: *Physical review letters* 123.3 (2019), p. 036806. URL: `https://journals.aps.org/prl/abstract/10.1103/PhysRevLett.123.036806`.

[327] Justin CW Song and Mark S Rudner. "Chiral plasmons without magnetic field". In: *Proceedings of the National Academy of Sciences* 113.17 (2016), pp. 4658–4663. URL: `https://www.pnas.org/content/113/17/4658`.

[328] Zhida Song, Zhong Fang, and Chen Fang. "$d-2$-Dimensional Edge States of Rotation Symmetry Protected Topological States". In: *Phys. Rev. Lett.* 119 (24 Dec. 2017), p. 246402. DOI: `10.1103/PhysRevLett.119.246402`. URL: `https://link.aps.org/doi/10.1103/PhysRevLett.119.246402`.

[329] Ajit Srivastava and Ata c Imamo ğlu. "Signatures of Bloch-Band Geometry on Excitons: Nonhydrogenic Spectra in Transition-Metal Dichalcogenides". In: *Phys. Rev. Lett.* 115 (16 Oct. 2015), p. 166802. DOI: `10.1103/PhysRevLett.115.166802`. URL: `https://link.aps.org/doi/10.1103/PhysRevLett.115.166802`.

[330] Ady Stern. "Berry's phase, motive forces, and mesoscopic conductivity". In: *Phys. Rev. Lett.* 68.7 (1992), p. 1022. DOI: `10.1103/PhysRevLett.68.1022`. URL: `https://link.aps.org/doi/10.1103/PhysRevLett.68.1022`.

[331] Sergey V Streltsov and Daniil I Khomskii. "Orbital physics in transition metal compounds: new trends". In: *arXiv:1711.05409* (2017). URL: `https://arxiv.org/abs/1711.05409`.

[332] J. Struck et al. "Tunable Gauge Potential for Neutral and Spinless Particles in Driven Optical Lattices". In: *Phys. Rev. Lett.* 108 (22 May 2012), p. 225304. DOI: `10.1103/PhysRevLett.108.225304`. URL: `https://link.aps.org/doi/10.1103/PhysRevLett.108.225304`.

[333] Boris Itskhakovich Sturman. “Ballistic and shift currents in the bulk photovoltaic effect theory”. In: *Physics-Uspekhi* 63.4 (2020), p. 407. URL: https://iopscience.iop.org/article/10.3367/UFNe.2019.06.038578.

[334] Alaska Subedi, Andrea Cavalleri, and Antoine Georges. “Theory of nonlinear phononics for coherent light control of solids”. In: *Phys. Rev. B* 89 (22 June 2014), p. 220301. DOI: 10.1103/PhysRevB.89.220301. URL: https://link.aps.org/doi/10.1103/PhysRevB.89.220301.

[335] Alaska Subedi, Andrea Cavalleri, and Antoine Georges. “Theory of nonlinear phononics for coherent light control of solids”. In: *Phys. Rev. B* 89 (22 June 2014), p. 220301. DOI: 10.1103/PhysRevB.89.220301. URL: https://link.aps.org/doi/10.1103/PhysRevB.89.220301.

[336] S. Sugano and R. G. Shulman. “Covalency Effects in $KNiF_3$. III. Theoretical Studies”. In: *Phys. Rev.* 130 (2 Apr. 1963), pp. 517–530. DOI: 10.1103/PhysRev.130.517. URL: https://link.aps.org/doi/10.1103/PhysRev.130.517.

[337] Ganesh Sundaram and Qian Niu. “Wave-packet dynamics in slowly perturbed crystals: Gradient corrections and Berry-phase effects”. In: *Phys. Rev. B* 59.23 (1999), p. 14915. DOI: 10.1103/PhysRevB.59.14915. URL: https://link.aps.org/doi/10.1103/PhysRevB.59.14915.

[338] Ganesh Sundaram and Qian Niu. “Wave-packet dynamics in slowly perturbed crystals: Gradient corrections and Berry-phase effects”. In: *Phys. Rev. B* 59 (23 June 1999), pp. 14915–14925. DOI: 10.1103/PhysRevB.59.14915. URL: https://link.aps.org/doi/10.1103/PhysRevB.59.14915.

[339] Kazuaki Takasan, Masaya Nakagawa, and Norio Kawakami. “Laser-irradiated Kondo insulators: Controlling the Kondo effect and topological phases”. In: *Phys. Rev. B* 96 (11 Sept. 2017), p. 115120. DOI: 10.1103/PhysRevB.96.115120. URL: https://link.aps.org/doi/10.1103/PhysRevB.96.115120.

[340] Kazuaki Takasan et al. “Laser-induced topological superconductivity in cuprate thin films”. In: *Phys. Rev. B* 95 (13 Apr. 2017), p. 134508. DOI: 10.1103/PhysRevB.95.134508. URL: https://link.aps.org/doi/10.1103/PhysRevB.95.134508.

[341] Diyar Talbayev et al. “Spin-dependent polaron formation dynamics in Eu 0.75 Y 0.25 MnO 3 probed by femtosecond pump-probe spectroscopy”. In: *Physical Review B* 91.6 (2015), p. 064420.

[342] Liang Z Tan et al. “Shift current bulk photovoltaic effect in polar materials—hybrid and oxide perovskites and beyond”. In: *Npj Computational Materials* 2.1 (2016), pp. 1–12. URL: https://www.nature.com/articles/npjcompumats201626.

[343] Liang Z. Tan and Andrew M. Rappe. “Enhancement of the Bulk Photovoltaic Effect in Topological Insulators”. In: *Phys. Rev. Lett.* 116 (23 June 2016), p. 237402. DOI: 10.1103/PhysRevLett.116.237402. URL: https://link.aps.org/doi/10.1103/PhysRevLett.116.237402.

[344] Liang Z. Tan et al. “Shift current bulk photovoltaic effect in polar materials–hybrid and oxide perovskites and beyond”. In: *NPJ Comput. Mater.* 2 (Aug. 2016), p. 16026. URL: https://www.nature.com/articles/npjcompumats201626.

[345] Leticia Tarruell et al. “Creating, moving and merging Dirac points with a Fermi gas in a tunable honeycomb lattice”. In: *Nature* 483.7389 (2012), pp. 302–305. URL: https://www.nature.com/articles/nature10871.

[346] Jeffrey C. Y. Teo and C. L. Kane. “Topological defects and gapless modes in insulators and superconductors”. In: *Phys. Rev. B* 82 (11 Sept. 2010), p. 115120. DOI: 10.1103/PhysRevB.82.115120. URL: http://link.aps.org/doi/10.1103/PhysRevB.82.115120.

[347] Manisha Thakurathi, Daniel Loss, and Jelena Klinovaja. “Floquet Majorana fermions and parafermions in driven Rashba nanowires”. In: *Phys. Rev. B* 95 (15 Apr. 2017), p. 155407. DOI: 10.1103/PhysRevB.95.155407. URL: https://link.aps.org/doi/10.1103/PhysRevB.95.155407.

[348] D. J. Thouless. “Quantization of particle transport”. In: *Phys. Rev. B* 27 (10 May 1983), pp. 6083–6087. DOI: 10.1103/PhysRevB.27.6083. URL: https://link.aps.org/doi/10.1103/PhysRevB.27.6083.

[349] D. J. Thouless et al. “Quantized Hall Conductance in a Two-Dimensional Periodic Potential”. In: *Phys. Rev. Lett.* 49 (6 Aug. 1982), pp. 405–408. DOI: 10.1103/PhysRevLett.49.405. URL: https://link.aps.org/doi/10.1103/PhysRevLett.49.405.

[350] Daniel Thuberg et al. “Perfect Spin Filter by Periodic Drive of a Ferromagnetic Quantum Barrier”. In: *Phys. Rev. Lett.* 119 (26 Dec. 2017), p. 267701. DOI: 10.1103/PhysRevLett.119.267701. URL: https://link.aps.org/doi/10.1103/PhysRevLett.119.267701.

[351] Paraj Titum et al. “Anomalous Floquet-Anderson Insulator as a Nonadiabatic Quantized Charge Pump”. In: *Phys. Rev. X* 6 (2 May 2016), p. 021013. DOI: 10.1103/PhysRevX.6.021013. URL: https://link.aps.org/doi/10.1103/PhysRevX.6.021013.

[352] R. I. Tobey et al. “Ultrafast Electronic Phase Transition in $La_{1/2}Sr_{3/2}MnO_4$ by Coherent Vibrational Excitation: Evidence for Nonthermal Melting of Orbital Order”. In: *Phys. Rev. Lett.* 101 (19 Nov. 2008), p. 197404. DOI: 10.1103/PhysRevLett.101.197404. URL: https://link.aps.org/doi/10.1103/PhysRevLett.101.197404.

[353] Y Tokura and N Nagaosa. “Orbital physics in transition-metal oxides”. In: *science* 288.5465 (2000), pp. 462–468. URL: `http://science.sciencemag.org/content/288/5465/462`.

[354] Yoshinori Tokura, Masashi Kawasaki, and Naoto Nagaosa. “Emergent functions of quantum materials”. In: *Nature Physics* 13.11 (2017), pp. 1056–1068. URL: `https://www.nature.com/articles/nphys4274`.

[355] G. E. Topp et al. *Light-matter coupling and quantum geometry in moiré materials*. 2021. arXiv: `2103.04967 [physics.optics]`. URL: `https://arxiv.org/abs/2103.04967`.

[356] Alberto de la Torre et al. “Nonthermal pathways to ultrafast control in quantum materials”. In: *arXiv preprint arXiv:2103.14888* (2021). URL: `https://arxiv.org/abs/2103.14888`.

[357] Engin Torun et al. “Interlayer and intralayer excitons in MoS_2/WS_2 and $MoSe_2/WSe_2$ heterobilayers”. In: *Phys. Rev. B* 97 (24 June 2018), p. 245427. DOI: `10.1103/PhysRevB.97.245427`. URL: `https://link.aps.org/doi/10.1103/PhysRevB.97.245427`.

[358] Luka Trifunovic and Piet W. Brouwer. “Higher-Order Bulk-Boundary Correspondence for Topological Crystalline Phases”. In: *Phys. Rev. X* 9 (1 Jan. 2019), p. 011012. DOI: `10.1103/PhysRevX.9.011012`. URL: `https://link.aps.org/doi/10.1103/PhysRevX.9.011012`.

[359] Ari M. Turner, Yi Zhang, and Ashvin Vishwanath. “Entanglement and inversion symmetry in topological insulators”. In: *Phys. Rev. B* 82 (24 Dec. 2010), p. 241102. DOI: `10.1103/PhysRevB.82.241102`. URL: `https://link.aps.org/doi/10.1103/PhysRevB.82.241102`.

[360] M. Van der Donck and F. M. Peeters. “Interlayer excitons in transition metal dichalcogenide heterostructures”. In: *Phys. Rev. B* 98 (11 Sept. 2018), p. 115104. DOI: `10.1103/PhysRevB.98.115104`. URL: `https://link.aps.org/doi/10.1103/PhysRevB.98.115104`.

[361] David Vanderbilt. *Berry Phases in Electronic Structure Theory: Electric Polarization, Orbital Magnetization and Topological Insulators*. Cambridge University Press, 2018.

[362] S Wall et al. “Ultrafast coupling between light, coherent lattice vibrations, and the magnetic structure of semicovalent LaMnO 3”. In: *Physical review letters* 103.9 (2009), p. 097402.

[363] Botao Wang, F. Nur Ünal, and André Eckardt. “Floquet Engineering of Optical Solenoids and Quantized Charge Pumping along Tailored Paths in Two-Dimensional Chern Insulators”. In: *Phys. Rev. Lett.* 120 (24 June 2018), p. 243602. DOI: `10.1103/PhysRevLett.120.243602`. URL: `https://link.aps.org/doi/10.1103/PhysRevLett.120.243602`.

[364] Gang Wang et al. “Colloquium: Excitons in atomically thin transition metal dichalcogenides”. In: *Rev. Mod. Phys.* 90 (2 Apr. 2018), p. 021001. DOI: `10.1103/RevModPhys.90.021001`. URL: `https://link.aps.org/doi/10.1103/RevModPhys.90.021001`.

[365] Hua Wang and Xiaofeng Qian. “Ferroicity-driven nonlinear photocurrent switching in time-reversal invariant ferroic materials”. In: *Science advances* 5.8 (2019), eaav9743.

[366] L. C. Wang, X. P. Li, and C. F. Li. “Effect of periodic kicking on Chern insulators”. In: *Phys. Rev. B* 95 (10 Mar. 2017), p. 104308. DOI: `10.1103/PhysRevB.95.104308`. URL: `https://link.aps.org/doi/10.1103/PhysRevB.95.104308`.

[367] Frank Wilczek. “Quantum Mechanics of Fractional-Spin Particles”. In: *Phys. Rev. Lett.* 49 (14 Oct. 1982), pp. 957–959. DOI: `10.1103/PhysRevLett.49.957`. URL: `https://link.aps.org/doi/10.1103/PhysRevLett.49.957`.

[368] Travis J Williams et al. “Magnetic correlations in the quasi-two-dimensional semiconducting ferromagnet CrSiTe 3”. In: *Physical Review B* 92.14 (2015), p. 144404.

[369] Martin Wimmer et al. “Experimental measurement of the Berry curvature from anomalous transport”. In: *Nat. Phys.* 13.6 (2017), p. 545. URL: `https://www.nature.com/articles/nphys4050`.

[370] Dillon Wong et al. “Cascade of electronic transitions in magic-angle twisted bilayer graphene”. In: *arXiv e-prints*, arXiv:1912.06145 (Dec. 2019), arXiv:1912.06145. arXiv: `1912.06145 [cond-mat.mes-hall]`.

[371] Fengcheng Wu, Timothy Lovorn, and A. H. MacDonald. “Theory of optical absorption by interlayer excitons in transition metal dichalcogenide heterobilayers”. In: *Phys. Rev. B* 97 (3 Jan. 2018), p. 035306. DOI: `10.1103/PhysRevB.97.035306`. URL: `https://link.aps.org/doi/10.1103/PhysRevB.97.035306`.

[372] Fengcheng Wu, Timothy Lovorn, and A.H. MacDonald. “Topological Exciton Bands in Moiré Heterojunctions”. In: *Physical Review Letters* 118.14 (Apr. 2017). ISSN: 1079-7114. DOI: `10.1103/physrevlett.118.147401`. eprint: `arXiv:1610.03855`. URL: `http://dx.doi.org/10.1103/PhysRevLett.118.147401`.

[373] Fengcheng Wu et al. “Hubbard Model Physics in Transition Metal Dichalcogenide Moiré Bands”. In: *Phys. Rev. Lett.* 121 (2 July 2018), p. 026402. DOI: `10.1103/PhysRevLett.121.026402`. URL: `https://link.aps.org/doi/10.1103/PhysRevLett.121.026402`.

[374] Liang Wu et al. “Giant anisotropic nonlinear optical response in transition metal monopnictide Weyl semimetals”. In: *Nature Physics* 13.4 (2017), pp. 350–355. URL: `https://www.nature.com/articles/nphys3969`.

[375] Meng Wu et al. "Physical origin of giant excitonic and magneto-optical responses in two-dimensional ferromagnetic insulators". In: *Nature communications* 10.1 (2019), p. 2371.

[376] B Wunsch, F Guinea, and F Sols. "Dirac-point engineering and topological phase transitions in honeycomb optical lattices". In: *New J. Phys.* 10.10 (2008), p. 103027. URL: `http://iopscience.iop.org/article/10.1088/1367-2630/10/10/103027/meta`.

[377] Di Xiao, Ming-Che Chang, and Qian Niu. "Berry phase effects on electronic properties". In: *Rev. Mod. Phys.* 82 (3 July 2010), pp. 1959–2007. DOI: `10.1103/RevModPhys.82.1959`. URL: `https://link.aps.org/doi/10.1103/RevModPhys.82.1959`.

[378] Di Xiao, Ming-Che Chang, and Qian Niu. "Berry phase effects on electronic properties". In: *Rev. Mod. Phys.* 82 (3 July 2010), pp. 1959–2007. DOI: `10.1103/RevModPhys.82.1959`. URL: `https://link.aps.org/doi/10.1103/RevModPhys.82.1959`.

[379] Di Xiao, Junren Shi, and Qian Niu. "Berry Phase Correction to Electron Density of States in Solids". In: *Phys. Rev. Lett.* 95 (13 Sept. 2005), p. 137204. DOI: `10.1103/PhysRevLett.95.137204`. URL: `https://link.aps.org/doi/10.1103/PhysRevLett.95.137204`.

[380] Fang Xie et al. "Topology-Bounded Superfluid Weight in Twisted Bilayer Graphene". In: *Phys. Rev. Lett.* 124 (16 Apr. 2020), p. 167002. DOI: `10.1103/PhysRevLett.124.167002`. URL: `https://link.aps.org/doi/10.1103/PhysRevLett.124.167002`.

[381] Ming Xie and Allan H. MacDonald. "Weak-Field Hall Resistivity and Spin/Valley Flavor Symmetry Breaking in MAtBG". In: *arXiv:2010.07928 [cond-mat]* (Oct. 2020). arXiv: `2010.07928 [cond-mat]`.

[382] Ying Xiong, Li-kun Shi, and Justin CW Song. "Atomic configuration controlled photocurrent in van der Waals homostructures". In: *2D Materials* 8.3 (2021), p. 035008. URL: `https://iopscience.iop.org/article/10.1088/2053-1583/abe762/meta`.

[383] Su-Yang Xu et al. "Electrically switchable Berry curvature dipole in the monolayer topological insulator WTe 2". In: *Nature Physics* 14.9 (2018), pp. 900–906. URL: `https://www.nature.com/articles/s41567-018-0189-6`.

[384] Haoran Xue et al. "Acoustic higher-order topological insulator on a kagome lattice". In: *Nature materials* 18.2 (2019), p. 108. URL: `https://www.nature.com/articles/s41563-018-0251-x`.

[385] Touru Yamauchi et al. "Pressure-Induced Mott Transition Followed by a 24-K Superconducting Phase in $BaFe_2S_3$". In: *Phys. Rev. Lett.* 115 (24 Dec. 2015), p. 246402. DOI: `10.1103/PhysRevLett.115.246402`. URL: `https://link.aps.org/doi/10.1103/PhysRevLett.115.246402`.

[386] Zhongbo Yan, Fei Song, and Zhong Wang. “Majorana Corner Modes in a High-Temperature Platform”. In: *Phys. Rev. Lett.* 121 (9 Aug. 2018), p. 096803. DOI: 10.1103/PhysRevLett.121.096803. URL: https://link.aps.org/doi/10.1103/PhysRevLett.121.096803.

[387] Zhongbo Yan and Zhong Wang. “Floquet multi-Weyl points in crossing-nodal-line semimetals”. In: *Phys. Rev. B* 96 (4 July 2017), p. 041206. DOI: 10.1103/PhysRevB.96.041206. URL: https://link.aps.org/doi/10.1103/PhysRevB.96.041206.

[388] Zhongbo Yan and Zhong Wang. “Tunable Weyl Points in Periodically Driven Nodal Line Semimetals”. In: *Phys. Rev. Lett.* 117 (8 Aug. 2016), p. 087402. DOI: 10.1103/PhysRevLett.117.087402. URL: https://link.aps.org/doi/10.1103/PhysRevLett.117.087402.

[389] Ming-Min Yang, Dong Jik Kim, and Marin Alexe. “Flexo-photovoltaic effect”. In: *Science* 360.6391 (2018), pp. 904–907. URL: https://science.sciencemag.org/content/360/6391/904.abstract.

[390] Xiaosen Yang, Beibing Huang, and Zhengling Wang. “Floquet Topological Superfluid and Majorana Zero Modes in Two-Dimensional Periodically Driven Fermi Systems”. In: *Scientific reports* 8.1 (2018), p. 2243. URL: https://www.nature.com/articles/s41598-018-20604-w.

[391] Matthew Yankowitz et al. “Tuning superconductivity in twisted bilayer graphene”. In: *Science* 363.6431 (2019), pp. 1059–1064. ISSN: 0036-8075. DOI: 10.1126/science.aav1910. URL: https://science.sciencemag.org/content/363/6431/1059.

[392] Wang Yao and Qian Niu. “Berry Phase Effect on the Exciton Transport and on the Exciton Bose-Einstein Condensate”. In: *Phys. Rev. Lett.* 101 (10 Sept. 2008), p. 106401. DOI: 10.1103/PhysRevLett.101.106401. URL: https://link.aps.org/doi/10.1103/PhysRevLett.101.106401.

[393] Steve M. Young and Andrew M. Rappe. “First Principles Calculation of the Shift Current Photovoltaic Effect in Ferroelectrics”. In: *Phys. Rev. Lett.* 109 (11 Sept. 2012), p. 116601. DOI: 10.1103/PhysRevLett.109.116601. URL: https://link.aps.org/doi/10.1103/PhysRevLett.109.116601.

[394] Hongyi Yu et al. “Anomalous Light Cones and Valley Optical Selection Rules of Interlayer Excitons in Twisted Heterobilayers”. In: *Phys. Rev. Lett.* 115 (18 Oct. 2015), p. 187002. DOI: 10.1103/PhysRevLett.115.187002. URL: https://link.aps.org/doi/10.1103/PhysRevLett.115.187002.

[395] Yifei Yu et al. “Equally efficient interlayer exciton relaxation and improved absorption in epitaxial and nonepitaxial MoS2/WS2 heterostructures”. In: *Nano letters* 15.1 (2015), pp. 486–491. URL: https://pubs.acs.org/doi/abs/10.1021/nl5038177.

[396] HJ Zeiger et al. “Theory for displacive excitation of coherent phonons”. In: *Physical Review B* 45.2 (1992), p. 768.

[397] Alessandro Zenesini et al. “Coherent control of dressed matter waves”. In: *Physical review letters* 102.10 (2009), p. 100403. URL: https://journals.aps.org/prl/abstract/10.1103/PhysRevLett.102.100403.

[398] A. Zenkevich et al. “Giant bulk photovoltaic effect in thin ferroelectric $BaTiO_3$ films”. In: *Phys. Rev. B* 90 (16 Oct. 2014), p. 161409. DOI: 10.1103/PhysRevB.90.161409. URL: https://link.aps.org/doi/10.1103/PhysRevB.90.161409.

[399] Jingdi Zhang and Richard Douglas Averitt. “Dynamics and control in complex transition metal oxides”. In: *Annual Review of Materials Research* 44 (2014), pp. 19–43. URL: https://www.annualreviews.org/doi/abs/10.1146/annurev-matsci-070813-113258?journalCode=matsci.

[400] Xiao-Xiao Zhang, Tze Tzen Ong, and Naoto Nagaosa. “Theory of photoinduced Floquet Weyl semimetal phases”. In: *Phys. Rev. B* 94 (23 Dec. 2016), p. 235137. DOI: 10.1103/PhysRevB.94.235137. URL: https://link.aps.org/doi/10.1103/PhysRevB.94.235137.

[401] Xiaoou Zhang, Wen-Yu Shan, and Di Xiao. “Optical Selection Rule of Excitons in Gapped Chiral Fermion Systems”. In: *Phys. Rev. Lett.* 120 (7 Feb. 2018), p. 077401. DOI: 10.1103/PhysRevLett.120.077401. URL: https://link.aps.org/doi/10.1103/PhysRevLett.120.077401.

[402] Yang Zhang, Yan Sun, and Binghai Yan. “Berry curvature dipole in Weyl semimetal materials: An ab initio study”. In: *Phys. Rev. B* 97 (4 Jan. 2018), p. 041101. DOI: 10.1103/PhysRevB.97.041101. URL: https://link.aps.org/doi/10.1103/PhysRevB.97.041101.

[403] Yang Zhang et al. “Photogalvanic effect in Weyl semimetals from first principles”. In: *Phys. Rev. B* 97 (24 June 2018), p. 241118. DOI: 10.1103/PhysRevB.97.241118. URL: https://link.aps.org/doi/10.1103/PhysRevB.97.241118.

[404] Yuanbo Zhang et al. “Experimental observation of the quantum Hall effect and Berry’s phase in graphene”. In: *Nature* 438.7065 (2005), pp. 201–204. URL: https://www.nature.com/articles/nature04235.

[405] HB Zhao et al. “Coherent spin precession via photoinduced antiferromagnetic interactions in La 0.67 Ca 0.33 MnO 3”. In: *Physical review letters* 107.20 (2011), p. 207205.

[406] Jianhui Zhou et al. “Berry Phase Modification to the Energy Spectrum of Excitons”. In: *Phys. Rev. Lett.* 115 (16 Oct. 2015), p. 166803. DOI: 10.1103/PhysRevLett.115.166803. URL: https://link.aps.org/doi/10.1103/PhysRevLett.115.166803.

[407] Uri Zondiner et al. “Cascade of Phase Transitions and Dirac Revivals in Magic Angle Graphene”. In: *arXiv e-prints*, arXiv:1912.06150 (Dec. 2019), arXiv:1912.06150. arXiv: `1912.06150 [cond-mat.mes-hall]`. URL: `https://ui.adsabs.harvard.edu/abs/2019arXiv191206150Z`.

[408] A. A. Zyuzin and A. A. Burkov. “Topological response in Weyl semimetals and the chiral anomaly”. In: *Phys. Rev. B* 86 (11 Sept. 2012), p. 115133. DOI: `10.1103/PhysRevB.86.115133`. URL: `https://link.aps.org/doi/10.1103/PhysRevB.86.115133`.